# Cyclotron Designs for Ion Beam Therapy with Cyclinacs

THÈSE N<sup>O</sup> 5156 (2011)

## ÉCOLE POLYTECHNIQUE FÉDÉRALE DE LAUSANNE

POUR L'OBTENTION DU GRADE DE DOCTEUR ÈS SCIENCES

PAR

## Adriano GARONNA

ÉCOLE POLYTECHNIQUE
FÉDÉRALE DE LAUSANNE

Suisse
2011

# Abstract

This thesis presents new superconducting *compact* (as opposed to *separated-sector*) cyclotron designs for injection in CABOTO, a linac developed by the TERA Foundation delivering $C^{6+}/H_2^+$ beams up to 400 MeV/u for ion beam therapy. This association of a variable energy linac injected by a fixed energy cyclotron is called *cyclinac*. Two superconducting cyclotron designs are compared under the same design constraints and methods: a synchrocyclotron and an isochronous cyclotron, both at the highest possible magnetic field and with an output energy of 230 MeV/u. This energy allows to use the cyclotron as a stand-alone accelerator for protontherapy. Once the optimal cyclotron is determined, lower energy cyclotrons can easily be designed.

The short pulse length (1.5 $\mu$s), fast repetition rate (100-300 Hz) and small beam transmission of the cyclinac (0.2%) require intense pulsed ion sources. To deliver the desired clinical dose rate, the average pulse current of 60 e$\mu$A of $C^{6+}$ at 300 Hz can be produced by three commercial EBIS (EBIS-SC by Dreebit Gmbh) operating at 100 Hz and connected to the beamline in alternating mode. A multicusp ion source is sufficient to produce compatible $H_2^+$ beams.

The synchrocyclotron design features a central magnetic field of 5 T, an axisymmetric pole and a constant field index of 0.02. The beam is injected axially with a spiral inflector ($K = 1.4$). A static magnetic perturbation of 0.1 T and 5° width boosts the beam radial gain per turn (with no emittance degradation) by exciting the first radial integer resonance and thus allows beam ejection with moderate beam losses (30%). The RF system operates in first harmonic ($Q = 2500$). The 180° *Dee* provides 28 kV peak voltage and the RF is modulated (30-38 MHz) by a rotating capacitor (90-900 pF). The synchrocyclotron's best features are the simple and compact magnet (300 tons) and the low RF power requirements (30 kW power supply).

The isochronous cyclotron design features a 3.2 T central magnetic field, four sectors and a pole characterized by elliptical gaps in the hills (3-30 mm) and in the valleys (11-50 cm). Spiraling is minimized (80° total hill axis rotation) and beam ejection is achieved with a single electrostatic deflector placed inside an empty valley. The two RF cavities operate in fourth harmonic at 98 MHz ($Q = 7100$). The RF system provides peak voltages of 70-120 kV and is powered by a single 100 kW unit.

The synchrocyclotron reliability is brought into question by the need of a rotating capacitor and by the complexity of the injection and ejection systems. However, the isochronous cyclotron requires a much more complex magnet. Overall, the isochronous cyclotron is a better solution compared to the synchrocyclotron, because it is as compact but more reliable.

To quantitatively determine the industrial and clinical optimum for the CABOTO injection energy, three complementary isochronous cyclotrons of 70, 120 and 170 MeV/u are studied, based on the 230 MeV/u design. The optimal cyclotron energy strongly depends on the clinical aim of the facility. For a dual proton and carbon ion centre, the best compromise between clinical flexibility, accelerator size and power consumption is to accelerate particles up to 150 MeV/u in the cyclotron.

In this configuration, the 150 MeV/u isochronous cyclotron has similar weight and spiraling as the most widely used cyclotron for protontherapy (C235 by IBA S.A.), CABOTO is 24 m long and the overall power consumption of the cyclinac is 650 kW. Adding to these characteristics, the property of fast energy variation of the linac makes the cyclinac presented in this thesis a strongly competitive accelerator for dual proton and carbon ion therapy.

Keywords: carbon ion therapy, cyclinac, hadrontherapy, particle therapy, superconducting cyclotron, superconducting synchrocyclotron

# Sintesi

Questa tesi presenta nuovi disegni di ciclotroni *compatti* (e non a *settori separati*) super-conduttori come iniettori di CABOTO, un linac sviluppato dalla Fondazione TERA che accelera fasci di $C^{6+}/H_2^+$ fino a 400 MeV/u per l'adroterapia. Questa associazione di un linac a energia variabile iniettato da un ciclotrone a energia fissa è chiamata *cyclinac*. Due disegni di ciclotroni superconduttori sono comparati con gli stessi vincoli tecnici e metodi di calcolo: un sincrociclotrone e un ciclotrone isocrono. Una volta determinato il disegno ottimale, un disegno a energia più bassa può essere facilmente prodotto.

L'impulso breve (1.5 $\mu$s), l'alto tasso di ripetizione (100-300 Hz) e la ridotta trasmissione del fascio (0.2 %) del cyclinac richiedono potenti sorgenti di ioni impulsate. Per consentire l'irraggiamento clinico richiesto, la corrente media nell'impulso di 60 e$\mu$A $C^{6+}$ a 300 Hz può essere prodotta da tre sorgenti commerciali di tipo *EBIS* (EBIS-SC, Dreebit Gmbh), operanti a 100 Hz in modo alternato. La corrente per $H_2^+$ può invece essere fornita da una sorgente continua di tipo *multicusp*.

Il disegno del sincrociclotrone è caratterizzato da un campo magnetico centrale di 5 T, un polo a simmetria assiale e un indice di campo costante di 0.02. Il fascio è iniettato assialmente tramite un inflettore a spirale ($K = 1.4$). Una perturbazione magnetostatica di 0.1 T e 5° di larghezza permette di aumentare il guadagno radiale per giro del fascio (senza degradare l'emittanza), eccitando la prima risonanza radiale intera, e quindi di estrarre il fascio con perdite di fascio moderate (30 %). Il sistema RF opera in prima armonica ($Q = 2500$). Il *Dee* a 180° fornisce tensioni di picco di 28 kV e la RF è modulata (30-38 MHz) da un condensatore rotante (90-900 pF). Le caratteristiche le più attrattive del sincrociclotrone sono il magnete semplice e compatto (300 tonnellate) e il basso consumo di potenza RF (30 kW di potenza installata).

Il disegno del ciclotrone isocrono è caratterizzato da un campo magnetico centrale di 3.2 T,
quattro settori e un polo caratterizzato da aperture ellittiche del magnete in collina (3-30 mm) e nelle valli (11-50 cm). Lo *spiraling* è minimizzato (rotazione totale dell'asse di collina di 80°) e il fascio è estratto con un unico deflettore elettrostatico posto all'interno di una valle libera. Le due cavità RF operano in quarta armonica a 98 MHz (Q=7100). Il sistema RF fornisce tensioni di picco di 70-120 kV e richiede un solo alimentatore da 100 kW.

L'affidabilità del sincrociclotrone è messa in discussione dalla necessità di un condensatore rotativo e dalla complessità dei sistemi di iniezione ed estrazione del fascio. Tuttavia, il ciclotrone isocrono richiede un magnete molto più complesso. Complessivamente, il ciclotrone isocrono è una soluzione migliore rispetto al sincrociclotrone, perché altrettanto

compatta ma più affidabile.

Per determinare in modo quantitativo la soluzione industrialmente e clinicamente ottimale per l'energia d'iniezione di CABOTO, tre disegni complementari di ciclotroni isocroni a 70, 120 e 170 MeV/u sono stati studiati. La scelta dell'energia del ciclotrone è fortemente legata agli scopi clinici del centro di terapia. Per un centro duale di adroterapia con protoni e ioni carbonio, il migliore compromesso fra la flessibilità clinica e le dimensioni e consumi dell'acceleratore è di adoperare un'energia di iniezione in CABOTO di 150 MeV/u.

In questa configurazione, il ciclotrone isocrono da 150 MeV/u ha un peso e uno *spiraling* simili al ciclotrone più usato per la protonterapia (C235 della IBA S.A.), CABOTO ha 24 m di lunghezza e il consumo totale di potenza del cyclinac è di 650 kW. Se si aggiunge la proprietà unica di variazione di energia veloce del linac, il cyclinac risulta molto competitivo come acceleratore per un centro duale di adroterapia.

Parole chiave: adroterapia, ciclotrone superconduttore, cyclinac, sincrociclotrone superconduttore, terapia con ioni carbonio, terapia con particelle

# Acknowledgments

First of all, I thank Prof. Ugo Amaldi for giving me so much responsibility and for supporting my work and education. His leadership based on trust and enthusiasm (or 'cosmic optimism', as he calls it) truly inspired me to always give my best. Indeed, 'physics is beautiful ... and useful'!

I thank also Prof. Leonid Rivkin for accepting me as his PhD student and for the concrete help he gave me in times of need: for arranging and financing my stay at PSI for the experimental project which is part of this thesis, for supporting my attendance to the USPAS school and for putting me in contact with Dr. Werner Joho and Prof. Jacobus Maarten Schippers.

I am endebted to Phys. Eng. André Laisné for his supervision of the cyclotron designs, for the computer codes and all the knowledge he has shared with me. The discussions and hard work during our meetings in Paris and Geneva have been extremely valuable to me. His constant support reassured me in times of distress and I will always have good memories of his 'summer school' in Oméel.

I thank Phys. Eng. Luciano Calabretta for his advice and for taking the time to share his vast experience on cyclotrons with me. I also thank Dr. Daniela Campo for her work on the synchrocyclotron inflector design and Dr. Mario Maggiore for his valuable remarks.

I express my gratitude to Marco Schippers for his supervision of my work at PSI, his feedback and help with my research, as well as the whole COMET technical team.

I thank Dr. Günther Zschornack for arranging the measurements at his laboratory, Dr. Falk Ulmann for supervising them and the whole team at the Rossendorf Research Center.

My gratitude goes to Phys. Marie-Paule Bourgarel for her initial help on the inflector design and injection beam line.

I am grateful to Eng. Samuel Meyroneinc and Phys. Bernard Launé who invited me to the Orsay Therapy Center at the very beginning of my thesis, gave me critical feedback at various stages of my work, lent me documents on the Orsay synchrocyclotron and put me in contact with André Laisné. Their help was crucial!

I thank Werner Joho for his advice and bibliographic help at the beginning of my thesis.

I thank Ugo Amaldi, André Laisné, Phys. Giulio Magrin and Phys. Bénédicte Demaurex for their meticulous proof-reading of this thesis.

I thank all the people who contributed in their own way to my work (in alphabetical order): Dr. Bernard Auchmann, Dr. Saverio Braccini, Dr. Daniel Brandt, Dr. Frédéric

# Contents

# Abbreviations

| | |
|---|---|
| $\frac{q}{A}$ | Charge-over-mass ratio |
| **C235 / C400** | Cyclone 235 / Cyclone 400 cyclotrons |
| **CABOTO** | CArbon Booster for Therapy in Oncology |
| **CNAO** | Italian National Center for Oncological Hadrontherapy |
| **COMET** | Compact Medical Therapy Cyclotron |
| **EBIS** | Electron Beam Ion Sources |
| **ECRIS** | Electron Cyclotron Resonance Ion Sources |
| **ESS** | Energy Selection System |
| **FWHM** | Full Width at Half Maximum |
| **HIMAC** | Heavy Ion Medical Accelerator in Chiba |
| **HIT** | Heidelberg Ion Therapy Center |
| **IBA** | Ion Beam Applications S.A. |
| **IC** | Isochronous Cyclotron |
| **JINR** | Russian Joint Institute for Nuclear Research |
| **LNS** | Italian National Southern Laboratories |
| **PSI** | Paul Scherrer Institute |
| $Q$**-value** | Quality factor |
| **RF** | Radio Frequency |
| **rms** | Root-Mean-Square |
| **RotCo** | Rotating Capacitor |
| **SC** | Synchrocyclotron |
| **SCENT** | Superconducting Cyclotron for Exotic Nuclei and Therapy |
| **TERA** | Research Foundation for Oncological Hadrontherapy |

# Introduction

*Ion beam therapy* and *Hadrontherapy* are types of external beam radiotherapy, that use beams of fast ions and hadrons. Over the years, various particles have been used for radiotherapy. Recently, the vast majority of patients have been treated with protons and carbon ions, which is why this study focuses only on these two particles. The basics of protontherapy and carbon ion therapy are reviewed in Chap.1.

In this context, the Italian research Foundation for Oncological Hadrontherapy (TERA[1]) is developing fast-cycling accelerators, dubbed *cyclinacs* and composed of a fixed energy *compact* (as opposed to *separated-sector*) cyclotron followed by a high-gradient high Radio Frequency (RF) linac boosting the beam energy up to the maximum needed for medical therapy. The linac has the unique property of allowing a fast electronic beam energy variation, which opens the way to the most advanced tumor treatment techniques. The different accelerator systems specifically developed for hadrontherapy are presented in Chap.2.

The aim of this study is to determine the optimal ion sources and compact cyclotron providing carbon ion ($C^{6+}$) beams (and $H_2^+$ or protons) to be injected in the high-gradient booster linac studied by TERA and called CABOTO[2]. CABOTO is pulsed at high repetition rate (300 Hz) and accelerates short beam pulses (1.5 $\mu s$) up to energies of 400 MeV/u.

As part of this thesis, an experimental project was carried out at the Paul Scherrer Institute (PSI), under the supervision of Prof. Jacobus Maarten Schippers. The proton-therapy at PSI is based on a superconducting 250 MeV cyclotron. In order to change the penetration of the beam, its energy must be continuously adjusted and that is done via passive degraders. The aim of the project was to study the correct alignment of the elements in the part of the beamline that immediately follows the cyclotron, where the beam energy degradation takes place. This is crucial for the fast-scanning delivery of the new Gantry2, requiring the beam to have stable intensity at all energies. The measurements and analysis are presented in Chap.3.

The performance of the ion sources currently used in hadrontherapy centers, as well as that of other potential candidate sources for CABOTO are investigated in Chap.4. The special beam characteristics of CABOTO are compatible to those of the beams produced by Electron Beam Ion Sources (EBIS). To investigate their possible use with cyclinacs, the maximum number of ions needed to deliver the desired clinical dose rate are computed,

---

[1]in Italian, *Fondazione per Adroterapia Oncologica*
[2]CArbon BOoster for Therapy in Oncology

based on the total beam losses and the special beam delivery technique foreseen to be used with cyclinacs.

The injector for CABOTO should be adapted to medical therapy: this green (low consumption) and light (small weight) accelerator should be reliable and industrially viable. The cyclotron energy should lie between 70 MeV/u (for protontherapy of ocular tumors) and 230 MeV/u (for protontherapy of deep-seated tumors with passive degraders). However, the existing *compact* (as opposed to *separated-sector*) cyclotrons can only reach up to 200 MeV/u (K1200 of Michigan State University). Therefore, new cyclotron designs have been produced and are here presented. Once the optimal cyclotron at 230 MeV/u is determined, lower energy cyclotrons can easily be designed.

The underlying philosophy of the designs is, when possible, to use simplified models, in order to avoid the precise but complex and time-consuming process of three-dimensional modeling. The method and computational tools used in the designs are detailed in Chap.5.

A 230 MeV/u superconducting synchrocyclotron (SC) is first investigated as a possible injector for CABOTO. This type of cyclotron is a good candidate because: it can be designed at very high magnetic field and can be pulsed at the same repetition rate as the linac. However, its characteristic low acceleration voltage combined with the high magnetic field implies challenges linked to the injection and ejection systems. The design of the SC is detailed in Chap.6.

As an alternative solution for injection in CABOTO, a 230 MeV/u superconducting IC is studied. The isochronous cyclotron is potentially interesting because it is a reliable, wide-spread and compact accelerator. However, the IC suffers from the very complex geometries of the poles and of the RF cavities. The design for CABOTO aims at the highest possible central magnetic field and the simplest reliable solution, resulting in reduced spiraling and a simplified ejection system. The design is presented in Chap.7.

Based on the designs studied, the SC and IC solutions are compared in Chap.8 mainly in terms of operation reliability, magnet compactness and RF power. This comparison is unique in its kind, because the two designs were computed used similar design methods and constraints. It is concluded that the IC is, overall, a better solution.

The cyclotron output energy is an important quantity because it strongly influences the size and cost of the whole accelerator complex. The optimal cyclotron output energy for a cyclinac is studied in detail in terms of industrial and medical criteria, by studying complementary ICs at 70, 120 and 170 MeV/u, based on the 230 MeV/u design. The optimal cyclotron energy strongly depends on the clinical aim of the facility. The best compromise between clinical capability, accelerator size and power consumption for a dual proton and carbon ion cyclinac center is based on a 150 MeV/u isochronous cyclotron and a 24 meter long CABOTO.

# Chapter 1

# Ion Beam Therapy

The use of ion beams in tumor treatment was first proposed more than 60 years ago, when the depth-dose characteristics of proton beams were investigated[Wilson, 1946]. Since then, ion beam therapy has evolved and significantly expanded. This chapter gives an overview of the historical developments and current status, specific to the world of protontherapy and carbon ion therapy.

## 1.1 Sixty Years of History

The most updated statistics[1] (end of 2010) indicate a total of 28 medical facilites offering protontherapy and 4 facilities offering carbon ion therapy. Since the early 50's, more than 70 000 patients have been treated with protons and around 7 000 patients with carbon ions. The following section briefly overviews the historical milestones from the early days in the United States, to the pioneering work in Japan and the research successes in Europe. For sake of completeness, it should be stated that other centers are and have been delivering hadrontherapy treatments with success in Canada, South Africa, China and South Korea.

### 1.1.1 Developments in the United States

The first treatments on human patients were delivered with proton beams in 1954 at a nuclear physics research facility, the Lawrence Berkeley National Laboratory (LBNL). Treatment with other ions started three years later. Although the accelerator beam time dedicated to medical research was only 30 %, around 2 500 patients were treated.

In parallel, since 1961, proton therapy technology and clinical practice started to be studied by the Massachusetts General Hospital in collaboration with the Harvard Cyclotron Laboratory. This strong research background led to the world's first hospital-based proton therapy center built in 1990 at the Loma Linda University Medical Center (LLUMC). In 2001, the Northeast Proton Therapy Center at the Massachusetts General Hospital was also brought online. The past years have seen the flourishing of proton treatment centers in the USA. At the time of writing, eight centers offer proton therapy and five

---

[1]taken from the Particle Therapy Cooperative Group (PTCOG) website: `http://ptcog.web.psi.ch/Archive/Patientenzahlen-updateMay2011.pdf`

more are under construction. On the contrary, the research on heavier ions stopped with the shutdown of the Berkeley accelerator in 1993.

### 1.1.2 Japanese Development

After nearly 20 years of research in neutron and proton therapy, the National Institute of Radiological Sciences (NIRS) created in 1994 the Heavy Ion Medical Accelerator in Chiba (HIMAC), the first medical center dedicated to the treatment of cancers with carbon ions.

The center was developed using similar technical concepts as those pioneered at Berkeley. Until today, it detains by far the worldwide record in the number of patients treated with carbon ions (almost 7 000 in 15 years). Continuous developments in the technology and clinical practice make this center a reference in the field.

The Proton Medical Research Center at the University of Tsukuba also developed extensive experience with proton therapy since 1983, first using an accelerator used for high energy physics and successively a dedicated accelerator. The successes of NIRS sparked the creation of four other dedicated proton therapy centers, one dual carbon-proton treatment center, the Hyogo Ion Beam Medical Center (HIBMC) and one carbon ion treatment center, the Gunma University Heavy Ion Medical Center (GHMC).

### 1.1.3 European Development

In Europe, as elsewhere, the first treatments were performed with particle accelerators built for physics research, as was the case at the Uppsala University in 1957. In the early 90's and almost in parallel, two prestigious physics research centers started ambitious particle therapy programs developing sophisticated innovative techniques, significantly different from those used by Berkeley and HIMAC. These are the PSI working on proton therapy and the Helmholtz Center for Heavy Ion Research (GSI[2]) working on carbon ion therapy, with first patient treatments in 1996 and 1997, respectively. The successes of these two research projects led to the creation of: PROSCAN, a dedicated facility featuring a modern proton accelerator and a fast scanning gantry and the Heidelberg Ion Therapy Center (HIT), the first combined proton and heavy ion (carbon as the primary element but with the possibility of using also oxygen and helium among others) therapy facility in Europe. HIT treated the first patient in the fall of 2009.

TERA proposed in 1993 a dual proton and carbon ion center and initiated, in 1995, a collaborative study with the European Organization for Nuclear Research (CERN), MedAustron and Oncology2000 called the Proton Ion Medical Machine Study (PIMMS). Its mandate was to design a light ion hadrontherapy center made of a combination of systems, optimized for the medical application, without any financial and/or space limitation. In 2000-2003, TERA adapted the PIMMS design so as to reduce its cost and space requirements and obtained the approval of the Italian Health Ministry. The construction of the National Center for Oncological Hadrontherapy (CNAO) was entrusted to the CNAO Foundation (formed by five hospitals of the Lumbardy region and TERA), which obtained the technical help of the National Institute for Nuclear Physics (INFN) for the construction of the accelerator. The first patient is expected to be treated in the

---

[2]in German, *Gesellschaft für Schwerionenforschung*

fall of 2011.

A strong pan-european cooperation spirit led to the creation of many collaborative research projects and most importantly, to ENLIGHT[3], established in 2002 with the aim of a coordinated effort towards ion beam research in the European Union. Finally, at the time of writing, three proton centers are operating in Russia, two in France and one in Sweden, England, Germany and Italy.

## 1.2 Multidisciplinary Rationale

Hadrontherapy is a unique field at the border between physics, biology and medecineAmaldi and Larsson [1994]. Indeed, its potential advantages over conventional radiotherapy arise from these three science domains.

### 1.2.1 Physical Rationale

**Finite Range**

The finite range in matter of charged particles is the main advantage offered by hadrons compared to conventional radiotherapy treatments with X-rays (photons). A comparison of depth-dose curves for photon, proton and carbon ion beams is shown in Fig.1.1.
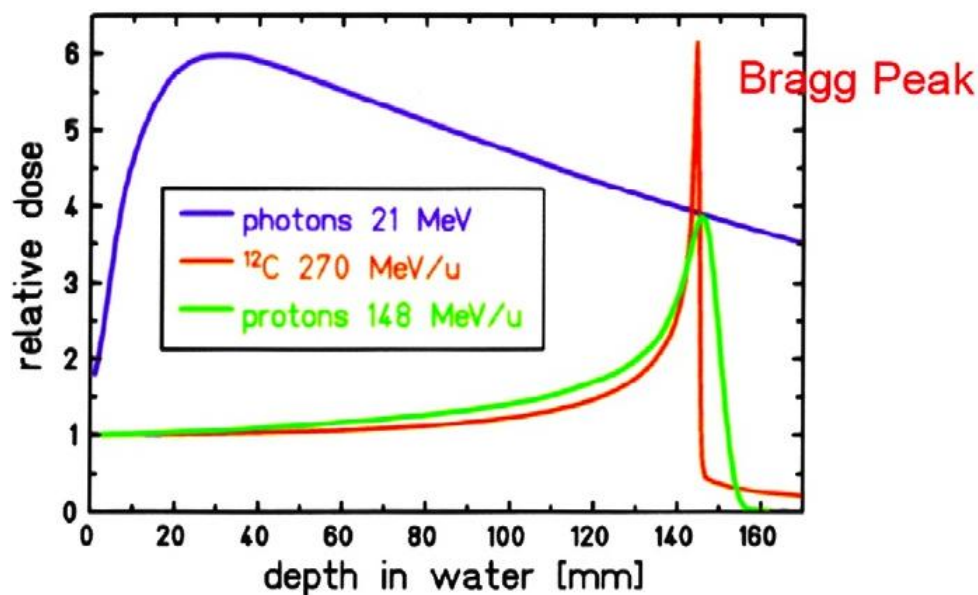


Figure 1.1: Dose-depth curve for monoenergetic photons, protons and carbon ions (courtesy of GSI)

The energy loss curve has a peak (the so-called *Bragg* peak) at the end of the particle path, a few millimeters before all the particles stop so that the highest dose is deposited in a localized region. The depth reached depends on the initial energy of the particle and on the irradiated material[Ziegler et al., 2008]. In tissue, protons and carbon ions need respective energies of 200 MeV and 4800 MeV to reach 27 cm depth. Their ranges at different energies are shown in Fig.1.2.

---

[3]European Network for LIGht ion Hadron Therapy
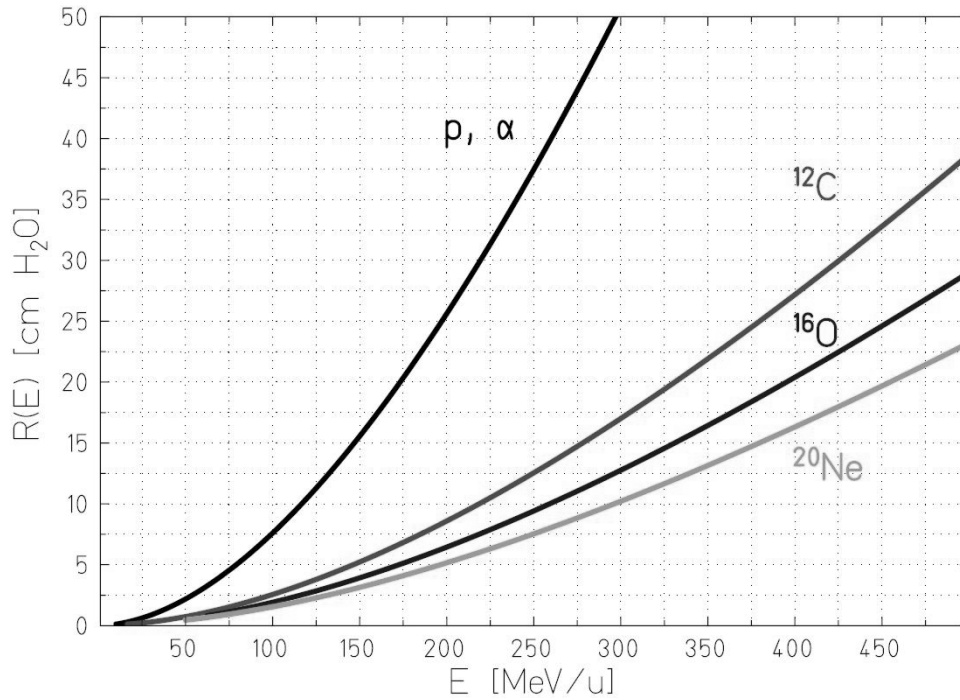
Figure 1.2: Mean range in water of proton ($p$), helium ($\alpha$), carbon ($C$), oxygen ($O$) and neon ($Ne$) ions in water[Schardt et al., 2010]

At these energies, charged hadrons release their energy mainly via inelastic collisions with the electrons of the medium. Since the energy dissipated in each electronic collision is very small, the energy loss of the projectile is practically continuous. The mean energy loss is described by the Bethe-Bloch formula[Fano, 1963]. It is also called *stopping power* and (unrestricted) Linear Energy Transfer (LET$_{(\infty)}$). The intrinsic difference between stopping power and LET resides in the fact that some secondary electrons created by the incident particle have sufficient energy to travel away from the interaction point and to deposit their energy in a different area. Their contribution to the main particle energy loss is then only included in the LET if their energy is lower than the subscript of the LET. Within the range of therapeutic energies, the Bethe-Bloch formula is to a good approximation dominated by $\frac{1}{\beta^2}$, which determines the increase of the stopping power with decreasing projectile energy, resulting in the Bragg peak. In addition, for a given particle velocity, LET depends quadratically on the projectile electric charge, thus carbon ions have much higher LET than protons.

Since the energy loss against atomic electrons is a stochastic process, a spread in energy always occurs after a monoenergetic beam has passed through a given target thickness. The energy spread leads to range *straggling*, defined as the fluctuation in path length for individual particles of the same initial energy. Straggling is also partly due to the scattering experienced by the particles traversing a material. The range spread amounts to about 1 % of the range for protons and only 0.3 % for carbon ions, because of the $\frac{1}{\sqrt{A}}$ dependence on the mass.

Along their path, carbon ions are affected by fragmentation. The ranges of the fragments scale (at the same velocity) to a good approximation as $\frac{A}{q^2}$. This has the negative effect of creating a dose tail beyond the Bragg peak in the energy loss curve. On the other hand,

some of the fragments produced are positron emitting nuclei which, as will be explained in Sec.1.4.2, allow the monitoring of the primary particle range by Positron Emission Tomography (PET).

**Spread-Out Bragg Peak**

The spatial selectivity of ion beams entails that to treat a tumor with a certain width, different Bragg peaks need to be cumulated to create a so-called Spread-Out Bragg Peak (SOBP), as shown in Fig.1.3. In the case of a proton irradiation, the weighting function $W$ of the figure must be determined such that the resulting dose distribution $DSOBP$ is uniform in the given depth interval $[da; db]$. For carbon ions, the creation of a volume of uniform clinical effects is more complex because of the Radiobiological Effectiveness (RBE), which is larger towards the end of the range, as explained in the next section.
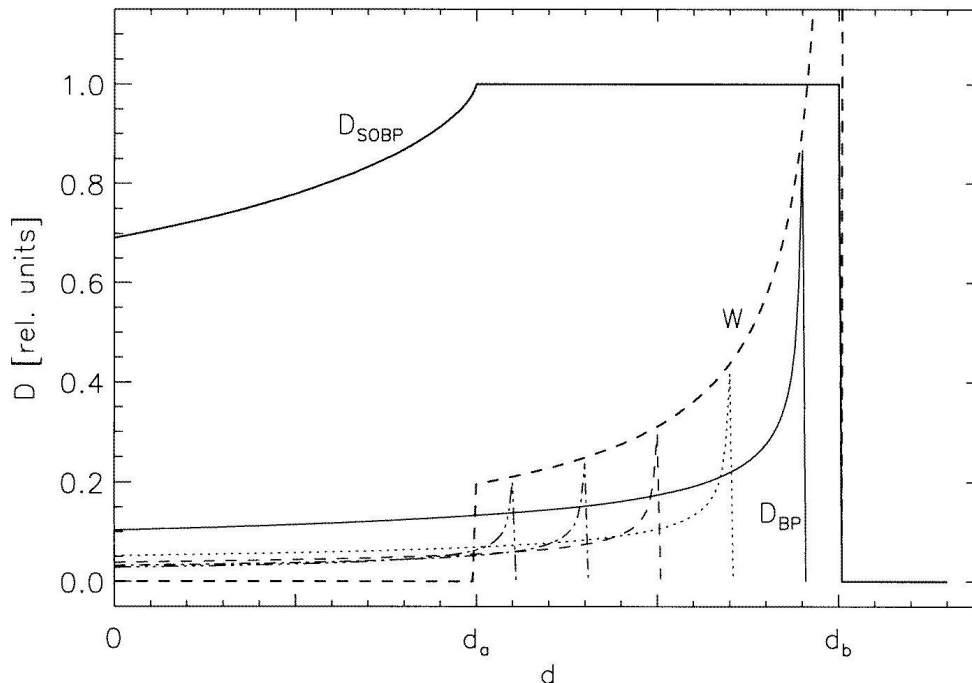


Figure 1.3: Weighted superposition of elementary Bragg peaks DBP at different depths[Bortfeld and Schlegel, 1996]

The comparison between the dose deposition from photons and the SOBP from protons and carbon ions reveals that the entrance dose given to healthy tissues is significantly reduced with particles. This is shown in Fig.1.4, in the case of only one field of irradiation. Note that the *biologically effective* dose is obtained by multiplying the physical dose by the RBE.
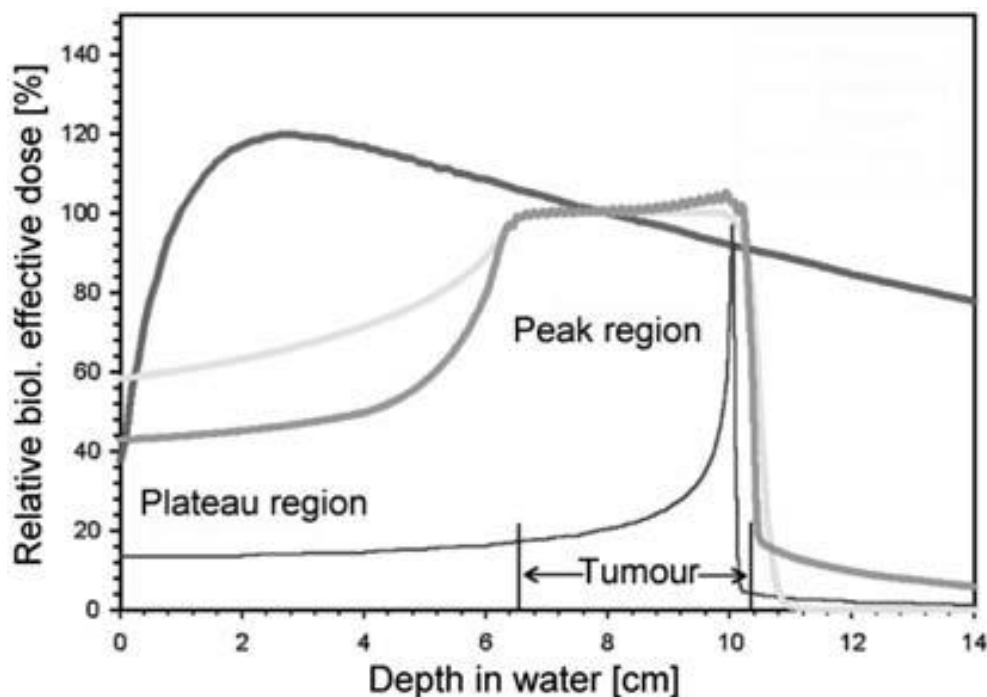
Figure 1.4: Biologically effective dose, as a function of the penetration depth in water, for a 15 MV photon beam (dark grey thick line), a 220 MeV/u carbon ion Bragg peak (black thin line) and SOBPs of 120 MeV protons (thick light grey line) and 220 MeV/u carbon ions (thick dark grey line)[Jäkel, 2009]. The dose is expressed in relative units, normalised to the dose at a depth of 8 cm

**Lateral Spread**

The comparison of beam widths of photon, carbon ion and proton beams, as shown in Fig.1.5.
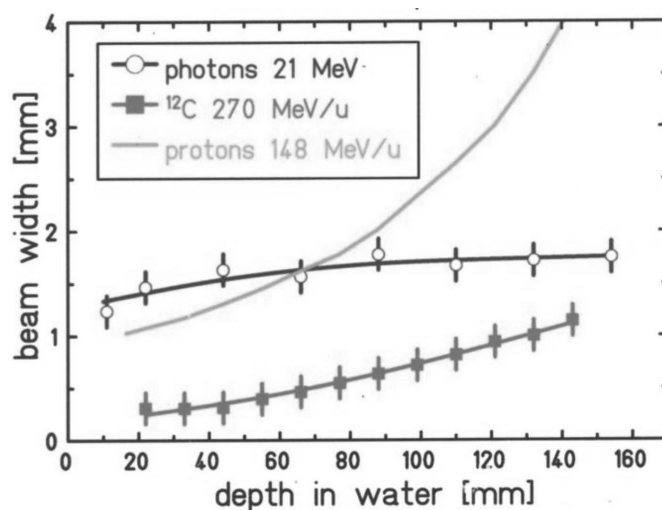


Figure 1.5: Beam width at different depths in water of photons, protons and carbon ions[Kraft, 2000]

The lateral beam spread is mainly caused by the elastic Coulomb interactions with the medium nuclei, which cause multiple discrete deviations of the particle path. This scatter

affects the lateral margins of the beam (penumbra) and is an important aspect affecting the conformity of radiotherapy beams. Similarly to the longitudinal distribution described earlier, the lateral beam width of charged hadrons increases by a factor 3 moving from carbon ions to protons. Fig.1.5 reveals that carbon ions have the best lateral characteristics and that protons have a worse lateral spread than well collimated photon beams, at depths larger than 10 cm.

## 1.2.2 Radiobiological Rationale

The radiobiological specificities of protons and carbon ions are here briefly introduced. The interested reader can find more comprehensive and detailed information in the bibliography[Hall, 2002].

### Radiobiological Effectiveness

The basis of radiation therapy is to deliver a lethal dose to the tumor cells, while preserving the healthy cells. Indeed, during deep-seated tumor radiation therapy, healthy tissue cells in the beam path and/or close to the tumor site are also subject to radiation and compromises have to made between the increased tumor damage linked to an increased delivered dose and the decreased normal tissue damage linked to a reduced delivered dose.

Radiation lethality is strongly related to the damage induced on the deoxyribonucleic acid (DNA) chain in the cell. This damage can be of two main types: direct (with radiation disrupting ions and chemical bonds in the DNA chain) and indirect (via radiation-induced free radicals). In normal conditions, these damages are restored by complex repair mechanisms. However, for various reasons, some of these mechanisms are often impaired in tumor cells. Therefore, a different lethality from the same radiation exposure arises between tumor cells and normal cells.

Moreover, different types of radiation have, for the same dose delivered to the target volume, a different effectiveness in killing tumor cells, as shown in Fig.1.6.



Figure 1.6: Typical cell survival curves and graphical definition of RBE[Kraft, 2000]

This is expressed by the RBE, cited earlier, which is defined, as given in Eq.1.1, as the ratio between the absorbed dose of a reference radiation (generally the 1.2 MeV photons emitted by $^{60}$Co) and that of the test radiation, required to produce the same biological

effect in a certain type of cell. The doses $D$ are often taken at the 10 % cell survival level.

$$RBE_{particle} = \frac{D_{reference}}{D_{particle}}\bigg|_{isoeffect} \qquad (1.1)$$

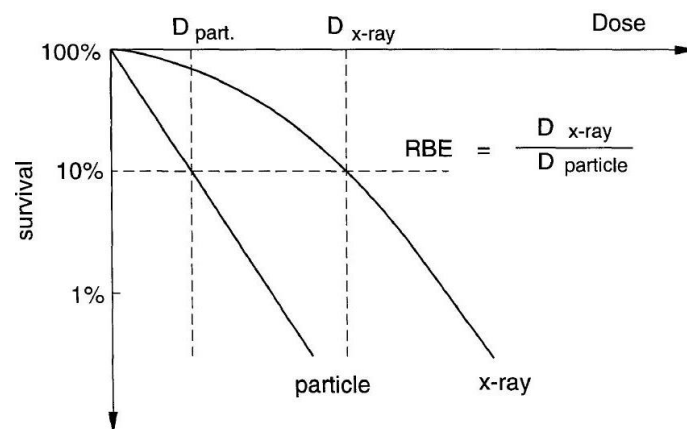The RBE of protons is assumed to be 1.1 over the full clinical range. This means that proton beams produce practically the same lethal damage as conventional photon beams. This has strongly simplified the clinical development of protontherapy since treatment protocols for proton therapy and conventional radiotherapy can be simply compared, by scaling the prescribed doses.

For carbon ions, the RBE can range between 2 and 5 and it increases in the last few centimeters before the stopping of the ion at the end of the range. The reason for the higher RBE is that the ionization density produced by a carbon ion traversing a cell is twenty times larger than the one of a proton having the same range and in particular, the fact that more than one ionization is produced in the few nanometer width of the DNA molecule. This entails more disruptive damages to the DNA.

In addition to the particle type, RBE depends on many parameters such as the particle LET, the dose, the tissue and tumor type, among others. The complex mechanisms hidden behind the value of the RBE are still a controversial topic in radiobiology. The research led at GSI also included the development of a radiobiological model to compute the RBE of carbon ions. This is called the Local Effect Model and is currently the basis for the treatment planning softwares used at HIT[Schardt et al., 2010].

**Oxygen Enhancement Ratio**

Another important characteristic of light ions is the weak dependence of the RBE on the oxygen content in the tumor. In the case of sparsely ionizing radiation, like photons and protons, the radiosensitivity of a biological system can be affected by external agents. Oxygen is a well known radiosensitizer that plays a crucial rule in radiation oncology, so that low vascularized tumors can become *radioresistant*.

This effect is quantified by the oxygen enhancement ratio (OER), defined by Eq.1.2.

$$OER_{particle} = \frac{D_{anoxic}}{D_{oxic}}\bigg|_{isoeffect} \qquad (1.2)$$

The OER decreases as LET increases. Thus, the OER of carbon ions is close to 1, while it can be as large as 3 for photon (or proton) beams. This may be explained by the difference in DNA damage between carbon ions and photons. This is a very important factor since it extends the range of tumor indications that can be successfully treated by radiation and is one of the strongest arguments in support of carbon ion therapy, compared to protontherapy, as discussed in the next section.

### 1.2.3 Clinical Rationale

The use of gantries for delivering the particle beams allows to irradiate from any angle, sparing the organs at risk distal to the tumor and the healthy tissues proximal to the tumor. This advantage can be either used to lower the complication probability or to increase the tumor control rate, as it allows to increase the dose to the tumor while maintaining the same complication probability. In general terms, proton beams offer very good tumor dose distributions and are simple to implement in the consolidated clinical practice because, as said before, they have a radiobiological effect similar to the photon beams used in conventional radiotherapy[Slater et al., 2009]. Thus, protons are suited for the irradiation of deep-seated solid tumors which being close to critical organs, cannot receive a large enough dose with photons with a consequent unsatisfactory tumor control.

Carbon ions are indicated for the treatment of radioresistant tumors because of their increased RBE[Suit et al., 2009]. Several treatment protocols have determined the advantages of therapy with carbon ions but more clinical studies, in which carbon and proton effects are compared, are still needed to determine other tumors, which would be beneficially treated with carbon ions in terms of tumor control and patient lifetime. This is one of the goals of the ENLIGHT collaboration.

A complete review of the results obtained by irradiating patients and of the future prospects is outside the scope of this section. The interested reader will find relevant information in the papers[Baron et al., 2004; Krengli and Orecchia, 2004; Mayer et al., 2004] published in the framework of ENLIGHT. The conclusion was that, in the medium term, 12 % (3 %) of the European patients treated every year with photons would profit from the use of proton (carbon ion) beams. Since the average number of photon patients is 20 000 per 10 million inhabitants, this corresponds to about 2 400 proton patients and about 600 carbon ion patients per year.

## 1.3 Beam Delivery Techniques

In addition to the accelerators and ion sources which will be detailed in Chap.2 and Chap.4, special beam delivery techniques are needed to conform the delivered dose to the tumor volume and to spare the surrounding healthy tissues and critical structures. Two different types of dose delivery systems are used: the *passive* scanning (or *broad-beam* technique) and *active* scanning (or *pencil-beam* technique).

### 1.3.1 Passive Scanning

This dose delivery system is based on a spread-out particle beam that transversally irradiates the whole target. In the simplest and most commonly used setups, this is a passive system in which the beam is scattered in two successive targets and shaped with filters, scatterers and patient-specific collimators[Koehler et al., 1977].

As shown in Fig.1.7, the beam is first scattered on a single (or double) target.
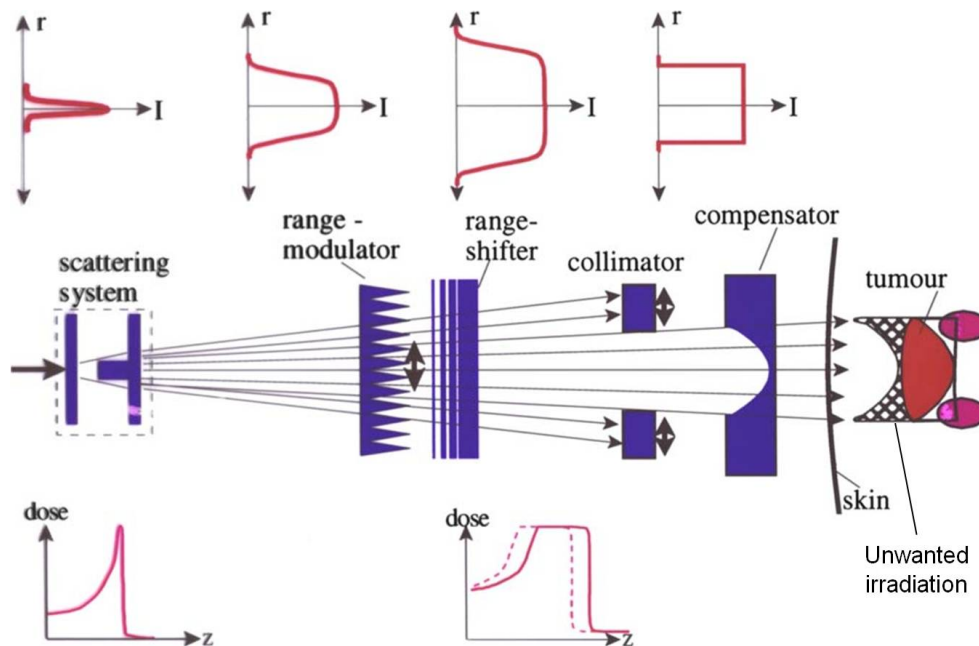
Figure 1.7: Sketch of a fully passive beam shaping system[Schardt et al., 2010]

Pictures of a compensator and a collimator are shown in Fig.1.8.
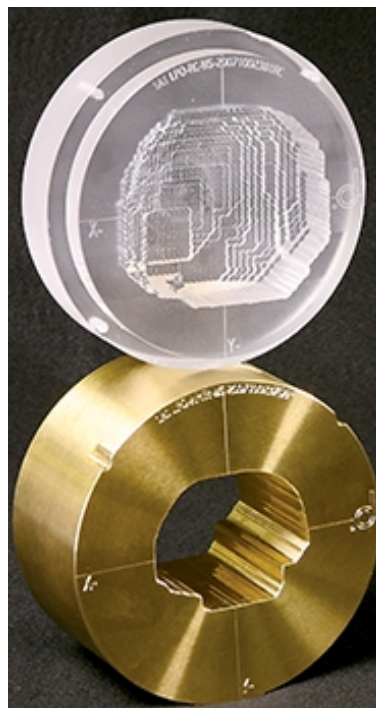


Figure 1.8: Picture of a compensator (top) and a collimator (bottom), taken from `www.oncolink.org`

The initially narrow beam is broadened by a scattering system and adapted to the target volume by various passive beam shaping devices: the range *modulator/shifter* transform the monoenergetic beam in a beam with a wide energy spread, resulting in a SOBP in the patient centered at the right penetration depth. A collimator, usually made of brass,

shapes transversally the beam. Finally, a *compensator*, made of wax or acrylic, shapes the far edge of the beam according to the distal geometry of the tumor. This results however in unwanted normal-tissue dose in the proximal part (indicated by the doubly hatched area in the figure). The collimator and compensator are made specifically for each patient's tumor treatment plan. This technique allows to irradiate the whole tumor region at the same time, imposing only moderate requirements on the accelerator control system. However, it implies a large amount of material traversed by the beam near the patient resulting in considerable beam intensity and energy loss, which requires more powerful accelerators and increases the activation by secondary neutrons. As a partial remedy, at NIRS, beam-wobbling magnets cover the tumor cross-section with thinner scattering targets[Yonai et al., 2008].

In the simplest setups, the dose cannot be tailored to the proximal end of the target volume and an undesirable dose is delivered to the adjacent normal tissue (see Fig.1.7). To counteract this effect, NIRS uses the *layer-stacking* method, in which the beam energy is changed in steps by moving a specific number of degrader plates into the beam and dynamically controlling the beam-modifying devices to adapt to the tumor shape at each energy[Kanai et al., 2006]. Future plans foresee making these step changes faster by electronically reducing the energy of the ejected beam from the (synchrotron) accelerator[Iwata et al., 2010].

## 1.3.2 Active Scanning

A scheme of the active scanning technique is shown in Fig.1.9.
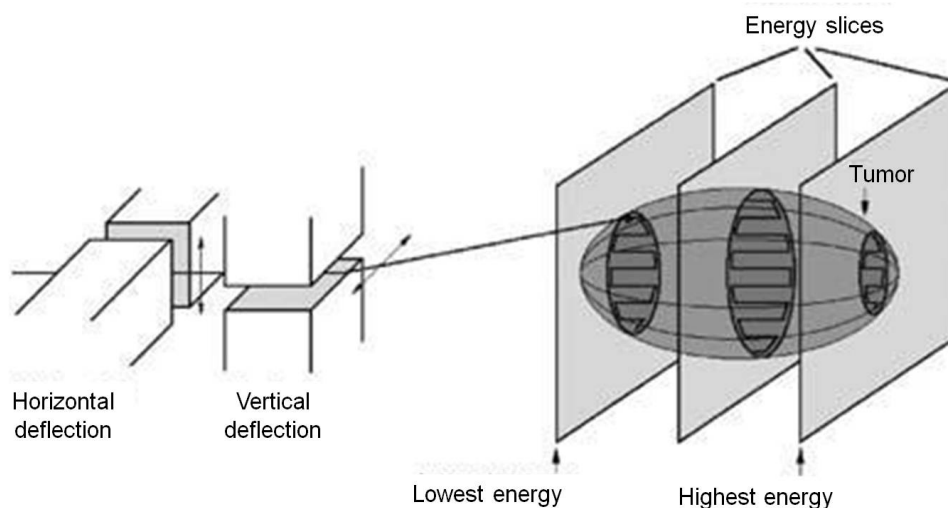


Figure 1.9: Scheme of the active beam delivery of GSI[Jäkel, 2009]

It is a more advanced delivery system is based on a pencil beam, which is moved point-by-point to cover the whole target volume. This is an active system in which the transverse position of the beam is scanned in the tumor cross-section by two bending magnets. In parallel, the longitudinal position of the spot, corresponding to the range of incident particles, is varied either by mechanically moving absorbers or by adjusting accelerator parameters. This removes the need for patient specific devices, increases the dose target volume conformity and allows the accurate modulation of the dose within the target

region[Lomax, 1999]. Moreover, neutron activation is reduced.

Two facilities have pioneered the pencil beam method for clinical use and used it to treat hundreds of patients: the PSI with the *spot* scanning technique for protons[Pedroni et al., 1995] and the GSI with the *raster* scanning technique for ions[Haberer et al., 1993].

Pencil beam scanning is presently also used with protons at the Francis H. Burr Proton Therapy Center, the MD Anderson Cancer Center, the Rinecker Proton Therapy Center and the University of Florida Proton Therapy Institute and with carbon ions and protons at HIT.

At PSI, the 8-10 mm Full Width at Half Maximum (FWHM) spot is moved in relatively large steps: 75 % of the spot FWHM. After irradiation of a voxel, the beam is turned off (for 5 $\mu$s) and moved to the next voxel. In the Gantry1 system, each of the three axes is scanned with a separate device to keep the system simple, safe and reliable[Pedroni et al., 2001]. The first transversal and most often used motion is given by a sweeper magnet before the last 90° bending magnet. The motion in the longitudinal direction is given by placing a range shifter device in the beam, allowing to vary sequentially the proton range in water in single steps of 4.5 mm. Finally, the slowest and least frequently used motion is given by the patient table itself. In the new Gantry2, both transverse movements are made by scanning magnets. More importantly, range shifting is done with a degrader system and beam line magnets: a step in range of 5 mm is done in 80 ms[4].

At the pilot project of GSI, a pencil beam of 4-10 mm FWHM was moved in the transverse plane almost continuously in steps equal to 30 % of the spot FWHM. Indeed, the beam was not switched off between close points. This requires fast scanning magnets to keep the dose applied between two points at an acceptable level. The *painting* of successive layers is obtained by varying the ejection beam energy of the (synchrotron) accelerator in typical steps of a second or more.

## 1.4 Future Prospects: a Selection of Modern Research Topics

The specificities of hadrontherapy sparked an impressive research effort in techniques to fully exploit the potential of ion beams. The following section presents some of the newest and most promising research topics, which are crucial for the further development and success of hadrontherapy in the coming years.

### 1.4.1 Moving Organs

One of the main challenges in modern hadrontherapy is the irradiation of moving tumors[Langen and Jones, 2001]. Organ motion during dose delivery can occur from respiration and heart pulsation among others. For therapy of moving targets in the thorax region, two techniques are frequently proposed: synchronization of irradiation and breathing (*gating*) and repeated irradiation (*multipainting*). Gating consists in measuring the breathing cycle and irradiating the target only during exhalation. This simple approach is used with good results in many centers but comes at the expense of a five-fold increase

---

[4]see Chap.3

in treatment time.

The more advanced multipainting technique proposes instead to split the dose delivery to each point of the target in many subdose deliveries, to statistically average out the errors due to over- or under-dosage.

Ideally, to overcome the challenge of treating moving organs, important technological developments are needed in[Amaldi et al., 2010b]:

1. devices to detect the instantaneous position of the tumor and produce signals to be used in (either 2D or 3D) feedback loops connected with the systems of point 2;

2. systems to actively scan in 3D with a pencil beam and continuously correct the spot position taking into account the (2D or 3D) information of point 1;

3. instruments capable of continuously monitoring the distribution of the dose in the body of the patient.

It has to be noted that the cyclinac accelerator is designed to produce a beam, which is especially suited for multipainting combined with a three dimensional feedback system. The characteristics of this accelerator are detailed in Chap.2.

## 1.4.2 Dose Monitoring

Although it is clear that the physical properties of hadrons allow a dose deposition very conformal to the 3D structure of the tumor, in order to take advantage of this feature, advanced imaging techniques are needed to delineate the tumor before the treatment and to control that the dose is delivered where it should be. In this perspective, two techniques look very promising : proton computed tomography (CT) and *in-beam* PET.

**Proton Radiography**

The idea to use charged particles (and in particular, protons) for imaging dates back to the 60's[Hanson et al., 1981]. The principle is to measure the residual energy and position of a monoenergetic beam after passing through a target. The residual range of the particle is a function of material electron density and the stopping power it has encountered in its path. It is thus possible to obtain a 2D radiography of the target.

With the recent development in proton therapy, the prospect of using this method as a diagnostic and quality assurance tool is very appealing. The potential advantage over conventional X-ray imaging lies in the use of the same radiation for both treatment and in situ imaging. Indeed, the current practice is to calculate proton doses based on X-ray CT and this implies some uncertainties on the proton ranges. In addition, a proton-CT would have the advantage of delivering a dose to the patient much lower than the conventional X-ray CT, for the same resolution level.

Many simulation studies have been performed and different solutions for the construction of a proton radiograph are under study in various research groups[Braccini et al., 2010; Talamonti et al., 2010]. For example, the TERA Foundation has developed a prototype called Proton Range Telescope (PRT10)[Amaldi et al., 2011]. The tests of this small-size prototype showed a sub-millimeter accuracy and an energy resolution of a few percent.

At the time of writing, a new device with identical design and larger acceptance (30 x 30 cm$^2$) is under construction.

Much more research is still ahead to meet the stringent medical requirements and solve the specific reconstruction algorithms linked to proton tomography[Schulte et al., 2004].

**In-beam PET**

*In-beam* PET was successfully applied at the pilot project of GSI to monitor the fractionated irradiation of more than 400 patients[Enghardt et al., 2004]. For the greatest part of treated patients, no deviations between the real and the expected activity maps were encountered, so that an overall accuracy of 1 mm was obtained in the determination of the longitudinal dose profile.

The employed technique exploited the activation of the target induced by the primary $^{12}C$ beam. In the fragmentation reactions of projectile carbon ions with target nuclei, the resulting fragments can have a neutron defect, so that they can undergo a $\beta+$ decay. The positron emitters created in these conditions are mainly $^{11}C$, $^{10}C$ and $^{15}O$. The first two species result from fragmentation of both the projectile and the target carbon nuclei. The latter can only be produced by target fragmentation, which means that the atoms are nearly at rest and carry information on the lateral width of the carbon beam.

Because fragmentation reactions leading to positron emitter creation do not occur at high rate, the final activity of 200 Bq Gy$^{-1}$ cm$^{-3}$ is a factor $10^3$ lower than the typical activity injected in patients for standard PET acquisitions.

An alternative approach, proposed by HIMAC, makes use of radioactive $^{11}C$ or $^{10}C$ beams. These radioactive beams deliver to the irradiated volume an activity of up to $10^5$ Bq Gy$^{-1}$ cm$^{-3}$[Enghardt et al., 2004]. $^{11}C$, $^{10}C$ and $^{15}O$ have a half-life of respectively 1 200, 120 and 2 s. The last two are so short that there are severe limits to the possibility of a post-treatment acquisition with the patient moved to a standard PET tomograph. Furthermore, in-beam PET can be performed only for a limited time after the irradiation because the biological lifetime due to the blood washing of the radioisotopes is 5 min.

## 1.5 Chapter Summary

Proton and carbon ion therapies offer attractive radiobiological, physical and clinical advantages compared to conventional photon radiotherapy treatments. They can provide very conformal dose deliveries on the tumor, sparing surrounding critical regions and offer an increased radiobiological effectiveness, which extends the limits of the tumors treatable with radiation. This explains their recent development around the world, with new clinical centers opening every year.

The beam delivery systems used can involve passive or active scanning. These techniques are inherently linked to the performance of the particle accelerator: medicine and engineering come together to determine the best compromise between the best possible treatment modality and the most reliable technical solution. This field of research is very active and will strongly influence the future of ion beam therapy. The particle accelerators used in hadrontherapy, as well as the possible future newcomers are presented in the next chapter.

# Chapter 2

# Hadrontherapy Accelerators

At the heart of a hadrontherapy center, the accelerator contributes by 20 to 30 % to the total investment cost of the facility[Amaldi et al., 2010b]. It also occupies a major share in its running costs, bringing its burden of maintenance, electrical power consumption and specialized staff, among others. As medical and commercial interests rise, there is increasing pressure on the scientific community to deliver dedicated accelerators, providing the best possible treatment modalities at the lowest possible investment and running costs. For example, in Europe a proton treatment costs about three times more than an advanced X-ray treatment (Intensity Modulated Radiation Therapy). The future of protontherapy would be very successful if more affordable centers could be made commercially available.

This chapter reviews the main accelerator elements specific to hadrontherapy. The novice to accelerator physics can find relevant information in the bibliography[Wiedemann, 2007]. Recent and complete reviews of all accelerators for medical application can be found in the second volume (2009) of Reviews of Accelerator Science and Technology[1]. A more specific review of all modern types of cyclotrons for various applications is also provided in the bibliography[Joho, 1986].

The requirements imposed on the accelerator vary quite significantly depending on the beam delivery techniques used[Chu et al., 1993; Wieszczycka and Schaf, 2001]. As an example, the beam specifications for the CNAO dual proton/carbon ion synchrotron, currently under commissioning, are given in Tab.2.1.

---

[1]http://www.worldscinet.com/rast/

Table 2.1: Clinical performance specifications for CNAO[Rossi, 2006] (*: at isocentre or, for fixed beam, at normal treatment distance)

| | |
|---|---|
| **Beam Particle Species** | p, $C^{6+}$, (possibly $He^{2+}$, $Li^{3+}$, $Be^{4+}$, $B^{5+}$, $O^{8+}$) |
| **Beam Particle Switching Time** | $\leq$ 10 min |
| **Beam Range** | 1.0 g/cm$^2$ to 27 g/cm$^2$ in one treatment room <br> 3 g/cm$^2$ to 27 g/cm$^2$ elsewhere <br> up to 20 g/cm$^2$ for $O^{8+}$ ions |
| **Bragg Peak Modulation Steps** | 0.1 g/cm$^2$ |
| **Range Adjustment** | 0.1 g/cm$^2$ |
| **Adjustment / Modulation Accuracy** | $\leq \pm$ 0.025 g/cm$^2$ |
| **Average Dose Rate** | 2 Gy/min (for treatment volumes of 1 L) |
| **Delivery Dose Precision** | $\leq \pm$ 2.5 % |
| **Beam Axis Height (above floor)** | 150 cm (head and neck beam line), <br> 120 cm (elsewhere) |
| **Beam Size*** | 4 to 10 mm FWHM for each direction independently |
| **Beam Size Step** | 1.0 mm |
| **Beam Size Accuracy*** | $\leq \pm$ 0.2 mm |
| **Beam Position Step*** | 0.8 mm |
| **Beam Position Accuracy*** | $\leq \pm$ 0.05 mm |
| **Field Size*** | 5 mm to 34 mm (diameter for ocular treatments), <br> 2 x 2 cm$^2$ to 20 x 20 cm$^2$ (for H and V fixed beams) |
| **Field Position Accuracy*** | $\leq \pm$ 0.5 mm |
| **Field Dimension Step*** | 1 mm |
| **Field Size Accuracy*** | $\leq \pm$ 0.5 mm |

# 2.1 Protontherapy

## 2.1.1 State-of-the-art: Normal Conducting Cyclotron

The vast majority of protontherapy centers around the world are based on a normal conducting isochronous cyclotron called Cyclone 235 (C235) from Ion Beam Applications S.A. (IBA, Belgium). Its main characteristics[Walter, 2001] are presented in Tab.2.2.

Table 2.2: Technical parameters of the C235. Note that these values were compiled from various publications and private communications. They should thus be taken as indicative

| Accelerated Particles | Protons (H$^+$, $\frac{q}{A} = 1$) |
|---|---|
| Central Magnetic Field | 1.7 T |
| Number of Sectors | 4 |
| Pole Radius | 1.12 m |
| Hill Vertical Gap | Elliptical: $\pm$ 96 mm to $\pm$ 9 mm |
| Hill Azimuthal Width | 38° to 53° |
| Valley Vertical Gap | constant: $\pm$ 60 cm |
| Max. Sector Azimuthal Rotation | 60 ° |
| Betatron Radial Tune | 1-1.37 |
| Betatron Vertical Tune | 0-0.28 |
| Main Coil Current | 0.5 Millon A turns |
| Magnet Coil Power Consumption | 190 kW |
| Yoke Diameter | 5.5 m |
| Yoke Height | 2.4 m |
| Iron Weight | 210 tons |
| Number of RF cavities | 2 |
| RF Harmonic Mode | 4 |
| RF Frequency | 106 MHz |
| Peak Voltage at Injection | 55 kV |
| Peak Voltage at Ejection | 150 kV |
| RF Power Consumption | 60 kW total |
| Ion source | Internal |
| Ejection Method | Electrostatic Deflector (14-17 MV/m) |
| Ejection Efficiency | 30 % |
| Output Kinetic Energy | 230 MeV |
| Max. Output Current | 300 nA |
| Output Emittance | 5 $\pi$ mm mrad |

A particular feature of this cyclotron is its elliptical hill gap, which as will be explained in more detail in Chap.7, minimizes pole spiraling and simplifies beam ejection. The ejected beam has a fixed energy so that absorbers are needed to vary the beam energy and perform tumor depth scanning. By adjusting the width of material through which the beam passes, the beam energy is reduced. These are called *degraders*. A range modulator wheel (IBA) or range wedge (PSI) transform the monoenergetic beam in a

beam with a wide energy spread, resulting in a SOBP[2] in the patient. The degraded beam energies vary virtually from zero up to the initial energy of the beam before the degrader. The beam transmission through these degraders typically varies between 0.1 % and 10 %. A range variation of 5 mm is achieved in 80 ms. The new beam coming out of the degrader has also a wider transverse size and is highly divergent. Specific mechanical beam-modifying devices are introduced to give the beam the required characteristics of beam size and divergence. In addition, a bending magnet and adjustable collimating slits at high dispersion points filter the desired beam energy and energy spread, to match the momentum acceptance of the beam lines (around 1.25 %). This comes at the cost of beam loss, which leads to neutron activation. These devices constitute the Energy Selection System (ESS), which is typically 15 m long. A study on the beam properties in the section of the PSI protontherapy beamline, where the degrader is located, is presented in Chap.3.

A picture of the cyclotron is shown in Fig.2.1.
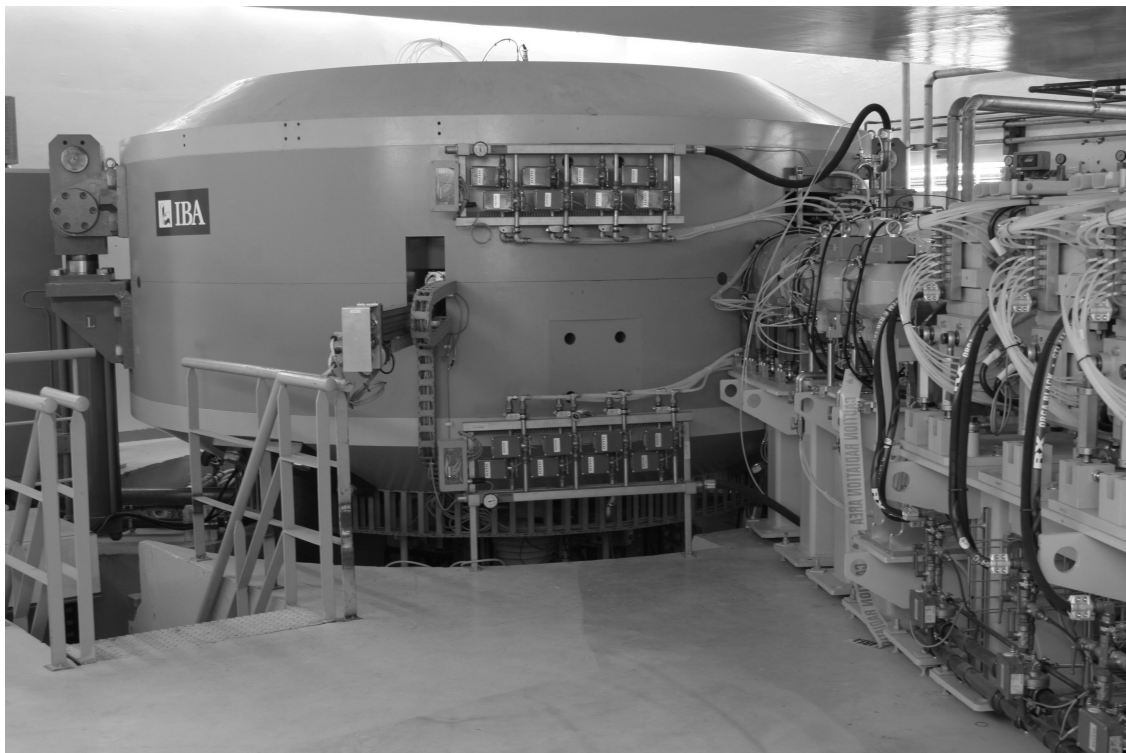


Figure 2.1: Picture of the C235 protontherapy cyclotron, taken from `http://www.pennmedicine.org/`

## 2.1.2   State-of-the-art: Synchrotron

The accelerator at LLUMC[3] was designed and built by Fermilab. It is a weak-focusing, 6 m diameter synchrotron accelerating protons from the 2 MeV delivered by the Radio Frequency Quadrupole to a maximum energy of 250 MeV. The minimum ejection energy is 70 MeV[Coutrakon et al., 1994]. This accelerator is important because as the first pro-

---

[2]see Chap.1
[3]see Chap.1

ton therapy accelerator used in a hospital environment, it set the standards for successive centers. A scheme of the main accelerator components is shown in Fig.2.2.
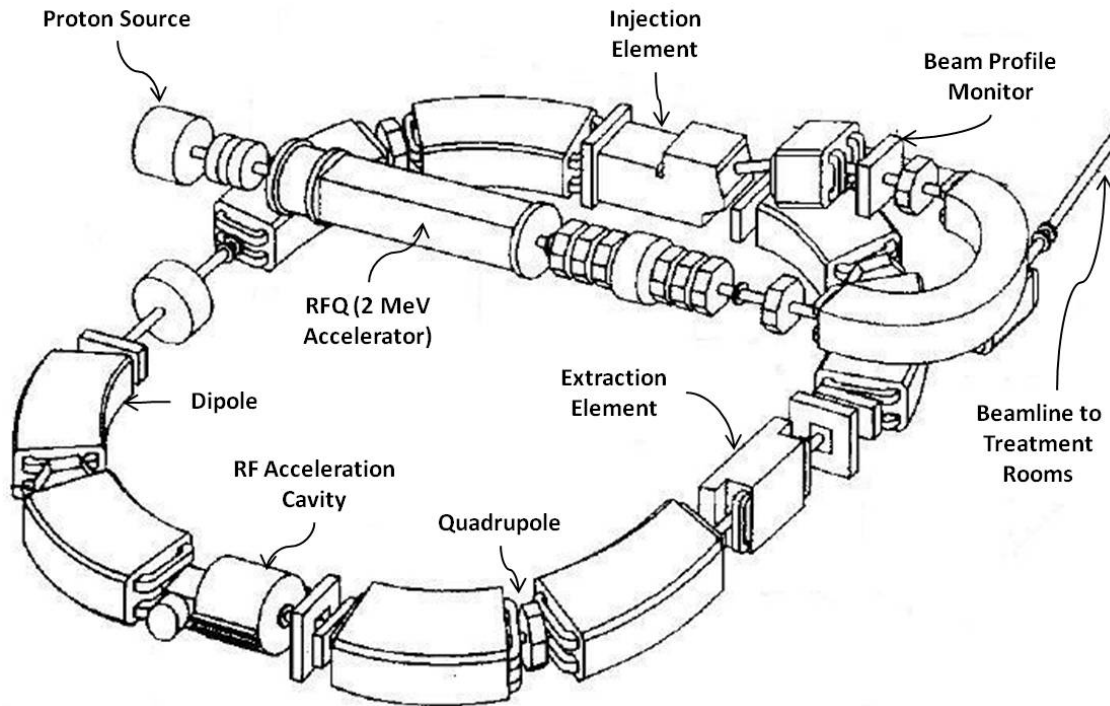


Figure 2.2: Layout of the LLUMC proton synchrotron[Coutrakon et al., 1994]

Another synchrotron design exclusively dedicated to protontherapy is installed in three centers in Japan (National Cancer Center Hospital East at Kashiwa, Wakasa Wan Energy Research Center and Proton Medical Research Center of the University of Tsukuba) and one in the USA (MD Anderson Cancer Center). The Hitachi Ltd. (Japan) synchrotron has a larger diameter than the LLUMC synchrotron (7 m) and produces a five times higher dose rate with $10^{11}$ protons per spill.

Synchrotrons offer a reliable and versatile technology, which needs to be handled by specialized and well-trained personnel. They offer the advantage of a variable beam energy, which allows both passive and active scanning. However, the repetition rate is quite low for fast depth scanning (at most 1 Hz).

### 2.1.3  State-of-the-art: Superconducting Cyclotron

At the time of writing, the only superconducting cyclotron used for protontherapy is the COMET (Compact Medical Therapy Cyclotron) isochronous cyclotron installed at PSI and at the Rinecker Protontherapy Center. Its design originates from a study led by Dr. Henry Blosser at Michigan State University in the 90's[Blosser and Team, 1993].

Its best features are the superconducting magnet, enabling low power consumption and reduced magnet size, and the high number of RF cavities which limits the beam losses during acceleration and at ejection (resulting in a low activation of the cyclotron). Finally, COMET features a fast beam intensity modulation of maximum 100% within 50 $\mu$s[4], via

---

[4]private communication, M. Schippers (PSI)

vertical electrostatic deflectors in the cyclotron central region.

The COMET characteristics are summarized in Tab.2.3 and a schematic view of COMET is shown in Fig.2.3.

Table 2.3: Parameters of COMET. Note that these values were compiled from various publications[Blosser and Team, 1993; Geisler et al., 2007; Schillo et al., 2001] and should be taken as indicative

| | |
|---|---|
| **Accelerated Particles** | Protons (H$^+$, $\frac{q}{A} = 1$) |
| **Central Magnetic Field** | 2.4 T |
| **Number of Sectors** | 4 |
| **Pole Radius** | 90 cm |
| **Hill Vertical Gap** | Constant: $\pm$ 27 mm |
| **Hill Azimuthal Width** | 27° to 44° |
| **Valley Vertical Gap** | Constant: $\pm$ 27 cm |
| **Max. Sector Azimuthal Rotation** | 80° |
| **Betatron Radial Tune** | 1-1.3 |
| **Betatron Vertical Tune** | 0.1-0.9 |
| **Rated Cryogenic Power** | 40 kW |
| **Total Coil Current** | 1 Million A turns |
| **Yoke Diameter** | 3.2 m |
| **Yoke Height** | 1.6 m |
| **Iron Weight** | 90 tons |
| **Number of RF cavities** | 4 |
| **RF Harmonic Mode** | 2 |
| **RF Frequency** | 73 MHz |
| **Peak Voltage at Injection** | 80 kV |
| **Peak Voltage at Ejection** | 130 kV |
| **RF Power Consumption** | 120 kW |
| **Ion source** | Internal |
| **Ejection Method** | Two Electrostatic Deflectors |
| **Ejection Efficiency** | 80 % |
| **Output Kinetic Energy** | 250 MeV |
| **Max. Output Current** | 1 $\mu$A |
| **Output Momentum Spread** | $\pm$ 0.2 % |
| **Output Emittance** | 2-4 $\pi$ mm mrad (normalized, 2$\sigma$) |

Figure 2.3: Model cut view of COMET with lifted upper pole cap

## 2.1.4 Future: Radio-Frequency Linacs

A complete overview of high-frequency linacs for hadrontherapy is given in the bibliography[Amaldi et al., 2009]. Four particular designs are here presented. These are LIBO[5], IDRA, ACLIP and TOP-IMPLART. They differ almost exclusively by their initial acceleration scheme. The first uses a 62 MeV cyclotron, the second and the third a 30 MeV cyclotron with a 3 m long linac[Amaldi, 2007; Vaccaro et al., 2007] and the fourth a linac[Picardi and Ronsivalle, 2004].

LIBO was designed by the TERA Foundation. It is a side-coupled linac operating at 3 GHz, the same frequency as all electron linacs used for conventional radiotherapy. LIBO boosts the energy of protons up to 200 MeV in a total length of around 13.5 m. The main advantages of this linear accelerating solution are the possibility of sharing the cyclotron resources already present in some hospitals, the smaller transverse beam emittances compared to the ones of cyclotrons and synchrotrons and the possibility to

---

[5]LInac BOoster

vary the output beam energy in only a few milliseconds, which opens the possibility of combining the spot scanning technique with multipainting and tracking of a moving tumor. These advantages will be discussed in more detail in Sec.2.3. The average beam current needed for therapy is small (nanoamperes) compared to the output current of the cyclotron, thus the low $10^{-3}$ duty cycle of the linac is not a limit. In collaboration with INFN and CERN, a prototype of LIBO was constructed and tested by TERA[Amaldi et al., 2004], accelerating protons from 62 to 73 MeV. A picture of the prototype is shown in Fig.2.4.



Figure 2.4: Cut section of the prototype of LIBO (courtesy of TERA)

The first LIBO proposal foresaw a 30 MeV cyclotron as injector, which could also be used to produce radiopharmaceuticals. Since at low energies, the efficiency of cell coupled linacs is small, the first prototype was designed and built for the 62 MeV cyclotron of the Clatterbridge center. After the very positive results obtained with the prototype of Fig.2.4, a center based on a 30 MeV cyclotron was designed. Its *First Unit*, which accelerates protons from 30 to 41 MeV, was later built by Applications of Detectors and Accelerators in Medicine (ADAM S.A., Switzerland) and power tested. A picture is shown in Fig.2.5.

The TOP-IMPLART initial acceleration scheme is composed of a 450 MHz Radio-Frequency Quadrupole followed by a 450 MHz Drift-Tube Linac (DTL) up to 7 MeV and a 10 m-long 3 GHz Side-Coupled DTL up to 40 MeV. TOP-IMPLART thus constitutes an all-linac solution. In 2010, the Lazio region in Italy approved the financing of the construction of the accelerator.

Figure 2.5: Picture of the First Unit, built and power tested at CERN (courtesy of ADAM)

## 2.1.5 Future: FFAG

The principles behind Fixed-Field Alternating Gradient (FFAG) accelerators date back from the 50's[Symon et al., 1956]. Detailed reviews of FFAGs[Craddock and Symon, 2008; Trbojevic, 2009] and a comparative study between FFAGs and RF linacs[Andrés, 2011] are found in the bibliography.

FFAGs are fixed-field accelerators with a variable particle revolution time/RF. There is an external source and injection with pre-acceleration. The magnets are arranged as a lattice of focusing and defocusing radial (or spiral) sector magnets, as shown in Fig.2.6.
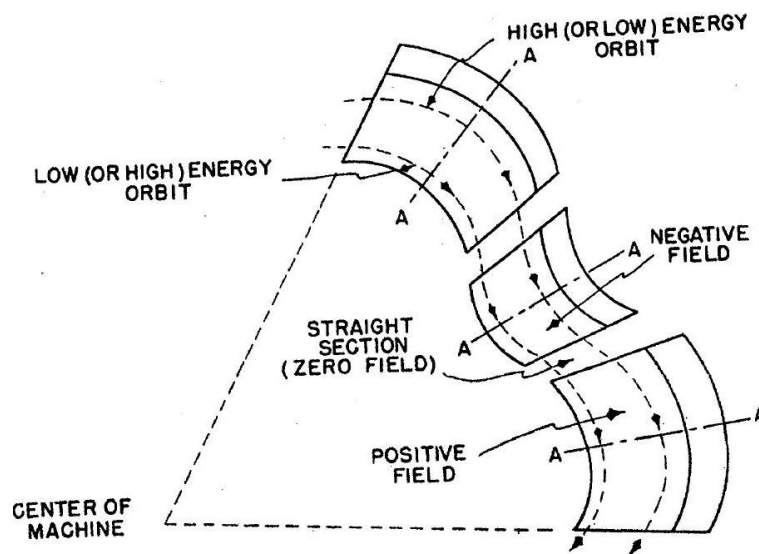


Figure 2.6: Plan view of a FFAG sector magnet and beam orbits at different energies[Symon et al., 1956]

The magnetic field is characterized by a strong radial gradient reducing the radial orbit excursion from injection to ejection. This reduces the size of the magnets (but increases their complexity) and allows a variable energy ejection with fast kickers.

The other main specificities of the FFAGs are the large acceptance, high beam current and fast repetition rate.

The so-called *scaling* FFAGs are characterized by the constancy of the magnetic field index and thus of the betatron tunes (see Chap.5). They were studied and electron models were built by the Midwest University Research Association fifty years ago. The first proton version was built in 2000 at the High Energy Accelerator Research Organization KEK.

A first non-scaling FFAG, the Electron Model for Many Applications (EMMA), was recently built and is currently under commissioning. This novel concept entails smaller and more affordable magnets at the expense of a complicated beam optics with many resonance crossings during acceleration.

Many designs for hadrontherapy applications have been proposed and this is a very active field of research. Both the variable energy and the high repetition rate (in the kHz range) are interesting for the multipainting of tumors (see Chap.1). Moreover, FFAGs can be more compact than synchrotrons if the non-scaling design is adopted. However, non-scaling hadron FFAGs have never been built and there are various technical uncertainties related to magnet complexity, ejection techniques and the broad-band high-gradient RF cavities needed for acceleration.

## 2.1.6 Future: Single-room Proton Facility

Interest has recently increased towards the development of proton, so-called single-room facilities.

A 250 MeV superconducting synchrocyclotron based on earlier design studies at Michigan State University has been built and is currently being tested by Still River Systems (USA). The very high magnetic field of 9 Tesla allows to reduce the magnet weight to 20 tons and to mount the accelerator on a rotating gantry[Friesel and Antaya, 2009]. The features of this system are an internal proton source, a rotating capacitor to provide the RF modulation and a passive beam scanning system for beam delivery. This kind of accelerator will be further detailed in Chap.6.

TERA is working on TULIP[6], a high-gradient proton linac mounted on a rotating stand[Amaldi et al., 2010b].

In addition, two new technologies have been proposed: the Dielectric Wall Accelerator[Caporaso et al., 2009] and the Laser-Driven Accelerator[Tajima et al., 2009]. The first is being studied by the Lawrence Livermore National Laboratory. It is an induction linac employing a novel insulating beam tube to impress a longitudinal electric field with strong accelerating gradients of the order of 100 MV/m in nanosecond pulses.

Research on Laser-Driven accelerators is pursued by many research groups around the world. The basic operational principle is the following: a high-intensity laser irradiates

---

[6]TUrning LInac for Protontherapy

the front surface of a solid target, electrons in the surface of the plasma are heated to high energies, they propagate through the target and emerge from the rear surface. This induces large electrostatic fields, which accelerate ions in the target. The accelerator is thus able to produce pulsed beams with a wide spectrum of energies and very short pulse lengths.

Both Laser-Driven and Dielectric Wall Accelerators look promising and could play an important role in the longer term future. But the technological problems are very challenging and research is only in the initial stage.

## 2.2 Carbon Ion Therapy

### 2.2.1 State-of-the-art: Synchrotron

At present, only five centers treat deep-seated tumors with carbon ions worldwide. These are: HIMAC, HIT, HIBMC, GHMC and the Institute of Modern Physics in China[7]. All of them use synchrotrons. A synchrotron ring for carbon ion therapy is typically about 20 m in diameter and can deliver beams with variable energy but with a dead time of 1-2 seconds because of the cycling magnetic field. Maximal carbon ion energies used for the treatment of deep-seated tumors range from 320 MeV/u (Hyogo) to 430 MeV/u (HIT).

Four more centers are presently under construction. The construction of CNAO is completed, as is the construction of the Siemens AG (Germany) Medical Center in Marburg. Siemens is also constructing a center in Kiel and one in Shanghai.

The synchrotrons have different designs. Without going into detail, the present section focuses on the design of CNAO, which serves as the basis for the final design of the MedAustron dual hadrontherapy center, whose construction recently started. CNAO was designed[Amaldi, 2001; Bazzano and CNAO-Collaboration, 2010] by TERA based on PIMMS[Bryant et al., 1999], as explained in Chap.1. The characteristics of the CNAO synchrotron[Amaldi et al., 2010a] are summarized in Tab.2.4 and the facility layout is shown in Fig.2.7.

Its specificity is the *betatron core*, which allows to produce a stable ejected beam. Indeed, because of the slow ejection and the ripples in magnet power supplies, the beams ejected from synchrotrons present large fluctuations in beam current inside the spill.

---

[7]see Chap.1

Table 2.4: Main parameters of CNAO for protons and carbon ions

| Accelerated Particles | $H^+$ | $C^{6+}$ |
|---|---|---|
| Mean Ring Diameter | 24.5 m | |
| Typical Repetition Rate | 0.5 Hz | |
| Injection Energy | 7 MeV/u | |
| Injection Scheme | multi-turn | |
| Revolution Frequency at Injection | 0.48 MHz | 0.47 MHz |
| Ejection Energy | 60-250 MeV/u | 120-400 MeV/u |
| Ejection Scheme | Resonant - Betatron Core | |
| Output Emittance [$\pi$ mm mrad (normalized, 4-rms)] | 2.1 | 3.0 |
| Estimated Particle Losses | 30 %, from ion source to patient | |
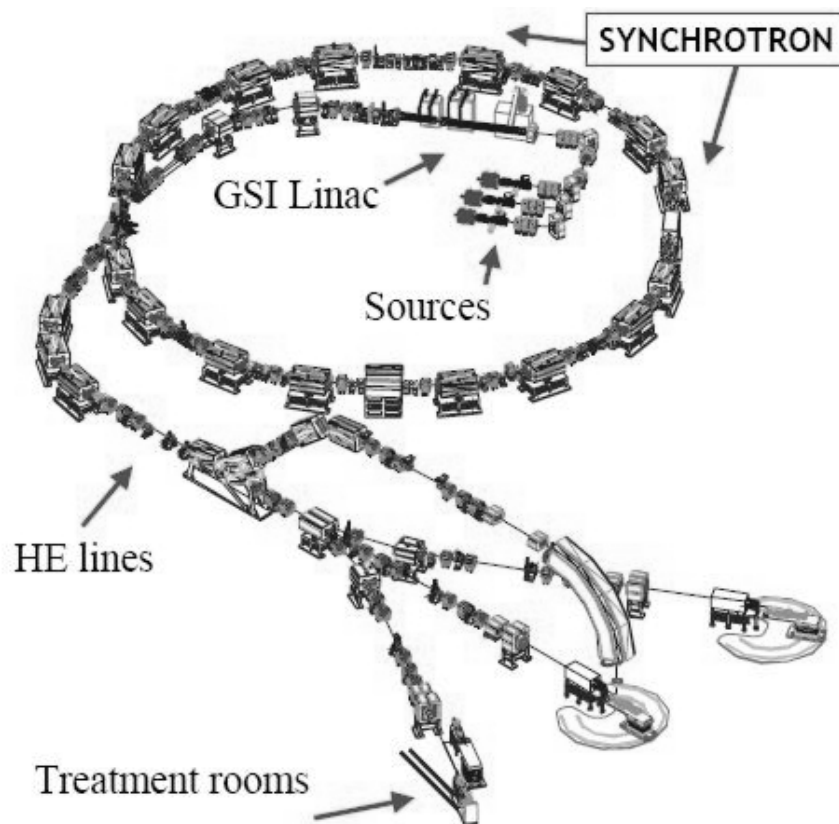


Figure 2.7: Layout of the CNAO accelerators and beam transport lines[Rossi, 2006]. The figure shows the possibility of adding a third source

## 2.2.2 Future: *Compact* Cyclotron

Note that the denomination *compact* qualifies single magnet cyclotrons, as opposed to separated-sector cyclotrons and is not related to the size of their magnet.

**SCENT**

The Superconducting Cyclotron for Exotic Nuclei and Therapy (SCENT) was designed at Italian National Southern Laboratories (LNS[8]) under the direction of Phys. Eng. Luciano Calabretta. The design is based on the existing K800 cyclotron at LNS and is characterized by a constant magnetic pole gap, strong spiraling and small iron yoke. A picture of the cyclotron and its beam ejection system is shown in Fig.2.8. The cyclotron main parameters[Calabretta et al., 2006] are listed in Tab.2.5.
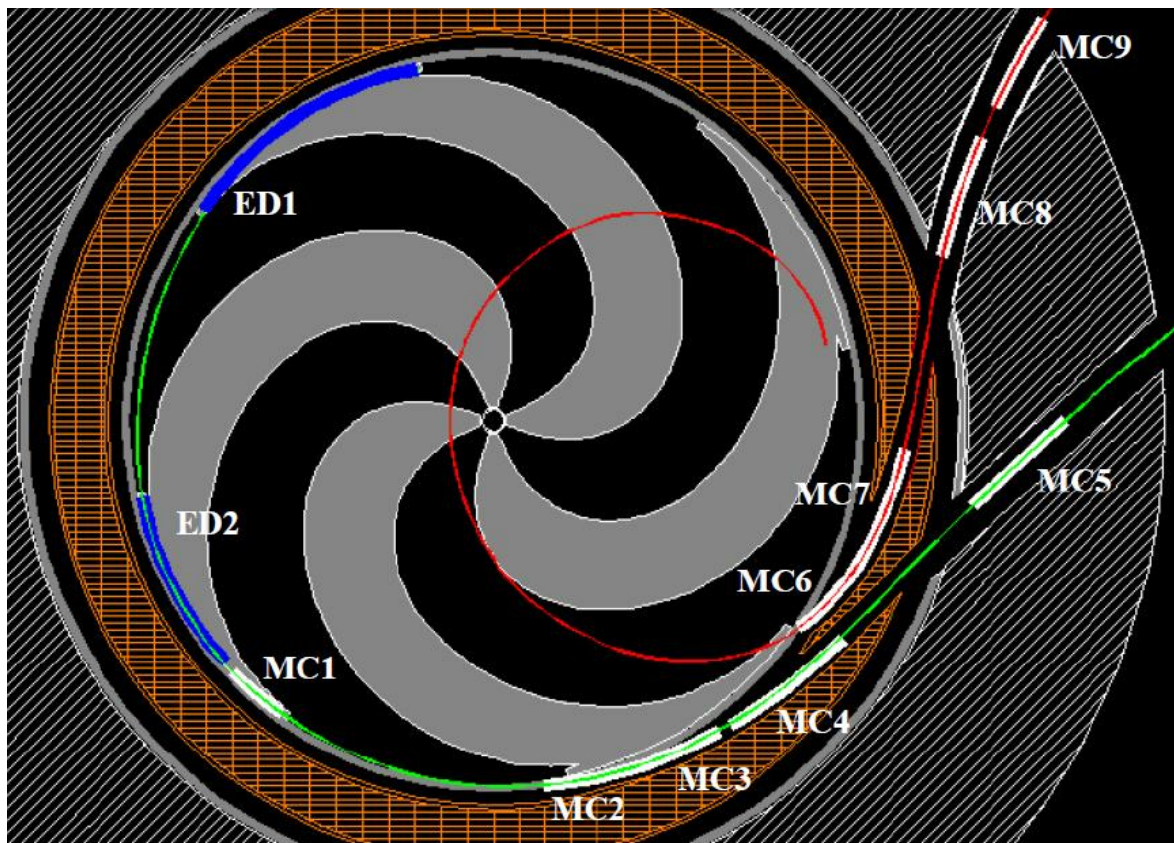


Figure 2.8: View of the SCENT cyclotron[Campo, 2010b]. The ejection trajectories for the carbon beam (green line) and for the proton beam (red line). The positions of the electrostatic deflector (ED) and of the ten magnetic channels (MC) are also shown

---

[8]in Italian, *Laboratori Nazionali del Sud*

Table 2.5: Design parameters of SCENT. Note that these values should be taken as indicative since they were collected from publications dated from 2006 to 2009, corresponding to various stages of design (the final design report is not publicly available)

| | |
|---|---|
| **Accelerated Particles** | $^{12}C^{6+}$, $H_2^+$ $(\frac{q}{A} = \frac{1}{2})$ |
| **Central Magnetic Field** | 3.2 T |
| **Number of Sectors** | 4 |
| **Pole Radius** | 1.33 m |
| **Hill Vertical Gap** | Constant: $\pm$ 25 mm |
| **Hill Azimuthal Width** | 34° to 44° |
| **Valley Vertical Gap** | Constant: $\pm$ 53 cm |
| **Max. Sector Azimuthal Rotation** | 140° |
| **Max. Spiral Angle** | 82 ° |
| **Betatron Radial Tune** | 1-0.8 |
| **Betatron Vertical Tune** | 0.2-1.1 |
| **Yoke Diameter** | 5 m |
| **Yoke Height** | 3 m |
| **Iron Weight** | 350 tons |
| **Number of RF cavities** | 4 |
| **RF Harmonic Mode** | 4 |
| **RF Frequency** | 98 MHz |
| **Peak Voltage at Injection** | 70 kV |
| **Peak Voltage at Ejection** | 120 kV |
| **RF Power Consumption** | 50-70 kW per cavity |
| **Ion Source** | 2 (external) |
| **Injection Type** | Axial, spiral inflector |
| **Injection Energy** | 25 keV/u |
| **Proton Ejection Method and Efficiency** | Stripper Foil, 100 % |
| **Ion Ejection Method and Efficiency** | 2 Electrostatic Deflectors (120 MV/m), 70 % |
| **Total Beam Transmission** | 10 % |
| **Output Momemtum Spread** | 0.1 % |
| **Output Kinetic Energy** | 260 MeV (protons) , 300 MeV/u (ions) |

**C400**

The superconducting isochronous cyclotron Cyclone 400 (C400)[Jongen et al., 2010] has been designed by IBA in collaboration with the Joint Institute for Nuclear Research (JINR) in Russia. The main characteristics of the cyclotron are presented in Tab.2.6.

Table 2.6: Technical parameters of the C400

| | |
|---|---|
| **Accelerated Particles** | $^{12}C^{6+}$, $H_2^+$, $^4He^{2+}$ ($^6Li^{3+}$, $^{10}B^{5+}$) |
| **Central Magnetic Field** | 2.4 T |
| **Number of Sectors** | 4 |
| **Pole Radius** | 1.87 m |
| **Hill Vertical Gap** | Elliptical: $\pm$ 60 mm to $\pm$ 6 mm |
| **Hill Azimuthal Width** | 23.5° to 45° |
| **Valley Vertical Gap** | constant: $\pm$ 60 cm |
| **Max. Sector Azimuthal Rotation** | 142° |
| **Max. Spiral Angle** | 68 ° |
| **Betatron Radial Tune** | 1-1.35 (protons), 1-1.65 (ions) |
| **Betatron Vertical Tune** | 0-0.25 (protons), 0-0.45 (ions) |
| **Yoke Diameter** | 6.6 m |
| **Yoke Height** | 3.4 m |
| **Iron Weight** | 700 tons |
| **Ion source** | 3 (external) |
| **Number of RF cavities** | 2 |
| **RF Harmonic Mode** | 4 |
| **RF Frequency** | 75 MHz |
| **Peak Voltage at Injection** | 80 kV |
| **Peak Voltage at Ejection** | 160 kV |
| **RF Power Consumption per Cavity** | 50 kW |
| **Proton Ejection Method and Efficiency** | Stripper Foil, 100 % |
| **Ion Ejection Method and Efficiency** | Electrostatic Deflector (150 MV/m), 70 % |
| **Total Beam Transmission** | 13 % |
| **Output Radial/Vertical Emittance [$\pi$ mm mrad]** | 10 / 4 (carbon), 3 / 1 (proton) |
| **Output Momentum Spread** | 0.1 % |
| **Output Kinetic Energy** | 400 MeV/u (ions), 265 MeV (protons) |

The cyclotron is foreseen to operate within the framework of the Archade project in Northern France, in collaboration with the physics research center GANIL[9]. When operational, it will be the first cyclotron in the world capable of delivering protons, carbon and helium ions for cancer treatment.

The main drawbacks of this accelerator are the large magnet size, the strong spiraling and the requirement of an ESS to vary the beam energy (see Chap.1).

The layout of the cyclotron is shown in Fig.2.9.
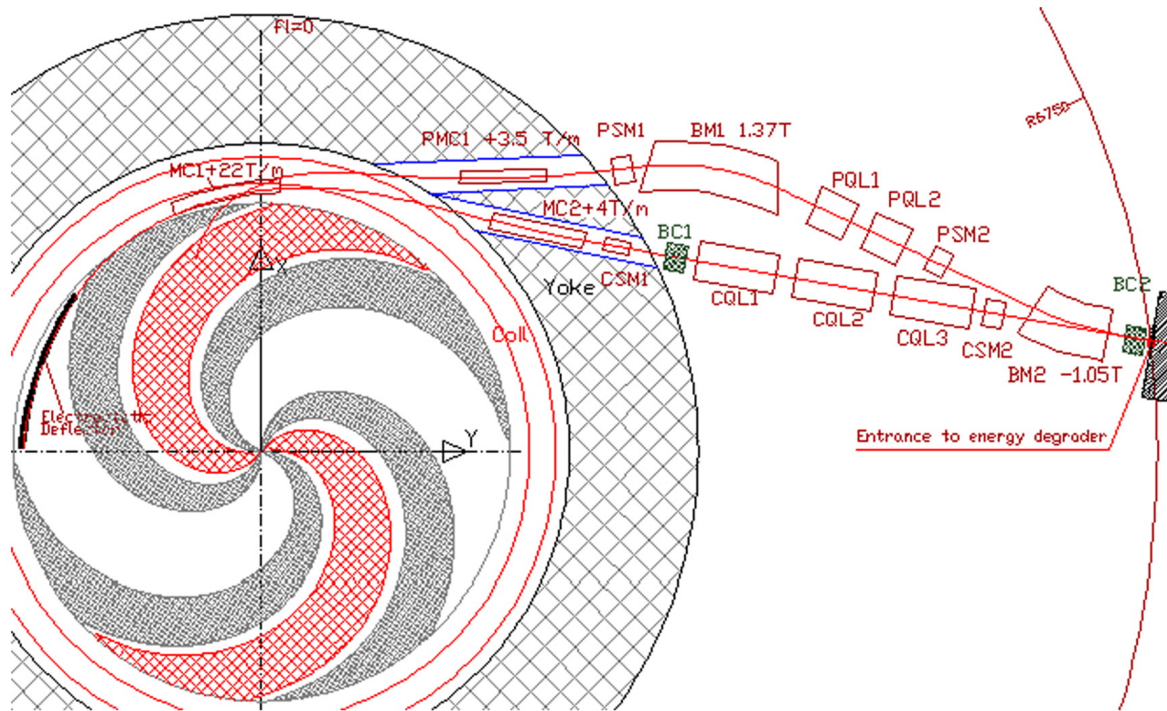


Figure 2.9: Layout of the C400 cyclotron with two ejection lines[Jongen et al., 2010]

### 2.2.3 Future: Separated-Sector Cyclotron and FFAG

**Separated-Sector Isochronous Cylotron**

Following the experience of the high-current 590 MeV proton ring cyclotron at PSI and the superconducting K2500 sector cyclotron at RIKEN, preliminary design studies for a carbon ion therapy accelerator were carried out at PSI[Schippers et al., 2009]. The concept is based on an accelerator system of two coupled cyclotrons, accelerating particles with $\frac{q}{A} = \frac{1}{2}$.

The first cyclotron provides protons (and helium ions), which can be used for the full spectrum of treatments and low energy carbon ions, with a range of 12.7 cm in water for a subset of tumors and radiobiological experiments. For treatments of all tumor sites with carbon ions, the carbon ions can be boosted subsequently up to 450 MeV/u in a separated-sector cyclotron, consisting of six sector magnets with superconducting coils and three RF cavities. This responds to a desire for hospitals with a two phased approach: treatment with protons in a first phase and upgrade to carbon ions in a second phase.

---

[9]in French, *Grand Accélérateur National d'Ions Lourds*

The first cyclotron has an output energy of 250 MeV/u and would be a compact superconducting cyclotron, with a design similar to SCENT and COMET. The second cyclotron would have a diameter of 12 m and a total magnet weight of around 500 tons. The advantage of the separated-sector cyclotron is the ample space available for simple injection/ejection elements operating at low magnetic field and the ample space for the RF cavities, which can be made with very high quality factor ($Q \geq 30000$) and high accelerating voltage (600 kV).

**FFAG**

FFAGs for carbon ion therapy differ from the proton FFAGs of the previous section. Indeed, their required energy range, RF variation, magnet size and number of magnet rings are larger. The broad-band cavities enabling large frequency swings are limited by the electric potential they can produce. This means that the number of acceleration turns is large and this makes resonance crossing troublesome.

Five detailed designs have been proposed: two scaling and three non-scaling. For illustration, the most compact design is here introduced: it is the Johnstone-Koscielniak Tune-Stabilized Non Linear Non Scaling FFAG[Johnstone et al., 2009]. It consists in a pair of nested 8-cell triplet rings, forming a multi-ion cancer treatment accelerator. The inner ring (orbit radii 2.75-3.39 m) takes protons from 30 to 250 MeV, and acts as injector to the outer ring (5.5-6.9 m) taking carbon ions from 65 MeV/u to 400 MeV/u. The magnets are superconducting with fields around 4 T. The particular magnet geometry produces nearly flat tunes and large dynamic apertures. Ongoing research aims at achieving nearly isochronous orbits, to avoid the need of RF modulation.

A scheme of the magnet ring is shown in Fig.2.10.
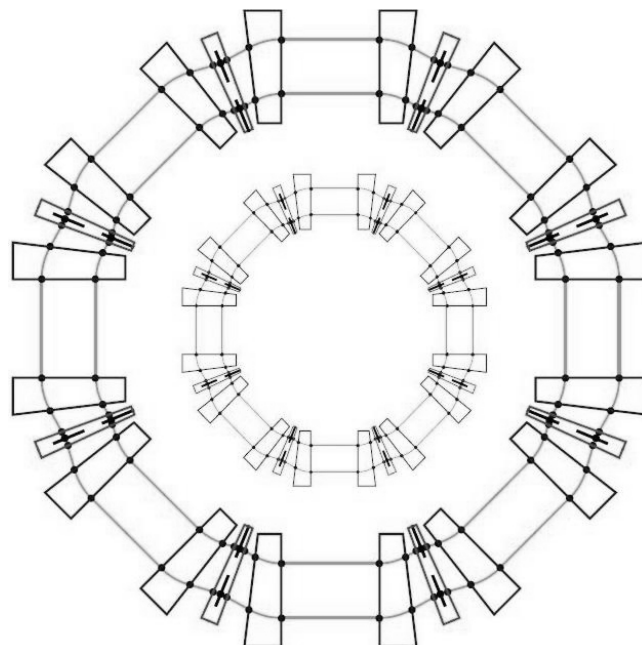


Figure 2.10: FFAG magnet rings for proton and carbon ion therapy[Johnstone et al., 2009]: the inner ring has a diameter of 7 m, the outer ring has a diameter between 11 and 13.8 m with 2 m long straight sections between the triplets

## 2.3   CABOTO

Serious alternative accelerators to FFAGs and superconducting cyclotrons for carbon ion therapy are the high-frequency linacs[Amaldi et al., 2009]. Overall, one can state that, for hadrontherapy, hadron linacs are closer to realization than FFAGs and offer a more versatile beam (in terms of energy modulation) compared to isochronous cyclotrons[Andrés, 2011].

The application of the cyclinac concept, introduced earlier, to carbon ion therapy is called CABOTO. Its main feature is the possibility to have intensity and energy modulated carbon ion beams, well adapted to the treatment of moving organs with a 4D multipainting spot scanning technique, in which the fourth dimension (the time) expresses the capability of the system to follow on-line the movements of the tumor. Indeed, the energy can be changed in a few milliseconds so that, even at high repetition rate, the depth reached by the beam can be adjusted at will, within the momentum acceptance of the magnetic transport line. If this acceptance is equal to $\pm$ 2 %, the range is adjustable by $\pm$ 7 %, from one spot to the next[Amaldi et al., 2010b].

The same linac accelerates $H_2^+$ molecules, which can be stripped after acceleration to obtain proton beams.

### 2.3.1   High-Gradient Linac Technology

The length of the linac could be reduced if higher accelerating gradients were achieved. The main focus of TERA's recent research is thus to achieve accelerating gradients larger than the one of LIBO (15-20 MV/m), without compromising the machine reliability. Indeed, increasing the electric field in the acceleration gaps of the linac increases the probability of electrical breakdowns in the cavity, inducing the loss of the beam.

In this context, TERA is collaborating with the CLIC[10] group at CERN, which works on high-gradient linacs for a future electron-positron collider. Determining the appropriate frequency at which the structure has to operate is an issue, as the frequency influences not only the beam dynamics and the cost of the machine but also, more importantly, the maximum accelerating gradient that can be achieved in the structure. Recently, different experiments have shown that the breakdown model used by Kilpatrick (which gives a maximum value for the surface electric field) does not apply, that the maximum surface field is not the proper parameter to look at and that Kilpatrick's limitation was too conservative at high RF frequencies[Grudiev et al., 2009].

To experimentally measure the high gradient limitation of high frequency RF cavities suitable for hadron accelerators, a 3 GHz single-cell cavity was designed, built and tested by a group of TERA researchers[Andrés et al., 2010]. These first observations were encouraging and a more precise test will soon be performed. In addition, a 5.7 GHz single cavity is under construction to bridge the gap between the experience at low frequencies and the experiments already performed by CLIC at 12 and 30 GHz.

---

[10]Compact LInear Collider

## 2.3.2   Latest CABOTO Design

The latest CABOTO design is based on a 120 MeV/u injector, followed by a 5.7 GHz Cell Coupled Linac which boosts the beam energy up to 400 MeV/u[Amaldi et al., 2010b; Garonna et al., 2010]. The main parameters of the linac are collected in Tab.2.7.

Table 2.7: Technical parameters of CABOTO[Amaldi et al., 2010b]

| | |
|---|---|
| **Accelerated Particles** | $C^{6+}$, $H_2^+$ ($\frac{q}{A} = \frac{1}{2}$) |
| **RF Frequency** | 5.7 GHz |
| **Length of the Linac** | 25 m |
| **Repetition Rate** | 300 Hz |
| **Carbon Ion Pulse Duration** | 1.5 $\mu$s |
| **Max. Axial Electric Field** | 41 MV/m |
| **Max. Surface Electric Field** | 185 MV/m |
| **Cells per Tank , Tanks per Module** | 21-17 , 3 |
| **Number of Accelerating Modules/Klystrons** | 18 |
| **Beam Hole Diameter** | 3.0 mm |
| **Synchronous Phase** | -17° |
| **Number of Permanent Magnetic Quadrupoles** | 54 |
| **Quadrupole Length and Gradient** | 60 mm ; 195 T/m |
| **Effective Shunt Impedance** | 115 - 150 M$\Omega$/m |
| **RF Duty Cycle (with 0.7 $\mu$s linac filling time)** | 0.1 % |
| **Peak Power per Module** | 9.5 MW (with 15 % losses) |
| **Klystron Peak Power** | 12 MW |
| **Total Peak RF Power** | 220 MW |
| **Linac Plug Power at 300 Hz** | 400 kW + 100 kW auxiliaries |
| **Output Transverse Emittance** | 1 $\pi$ mrad mm (normalized, 4-rms) |

The linac accelerating units are made of copper, each one subdivided into three tanks (shown in Fig.2.11) with a different number of cells. As in all linacs, the lengths of the cell (and thus of the tanks) are increasing as $\beta\lambda$ to keep the RF field in synchronism with the accelerated particles. The average length of each module is 1.3 m, for an average axial field in the tanks of 40 MV/m. Permanent Magnet Quadrupoles are placed between each tank to focus the beam along the structure.
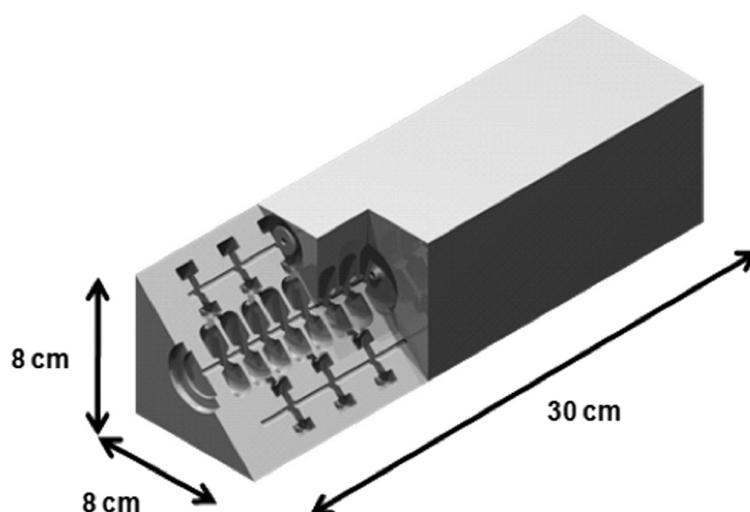
Figure 2.11: Sketch of a CABOTO tank[Amaldi et al., 2010b]

## 2.3.3   Energy Modulation

The main feature of CABOTO is the possibility to vary the energy of the hadron beam electronically by switching off a certain number of klystrons and by changing the amplitude and phase of the drive signal sent to the last active klystron. An illustration of this is presented in Fig.2.12.
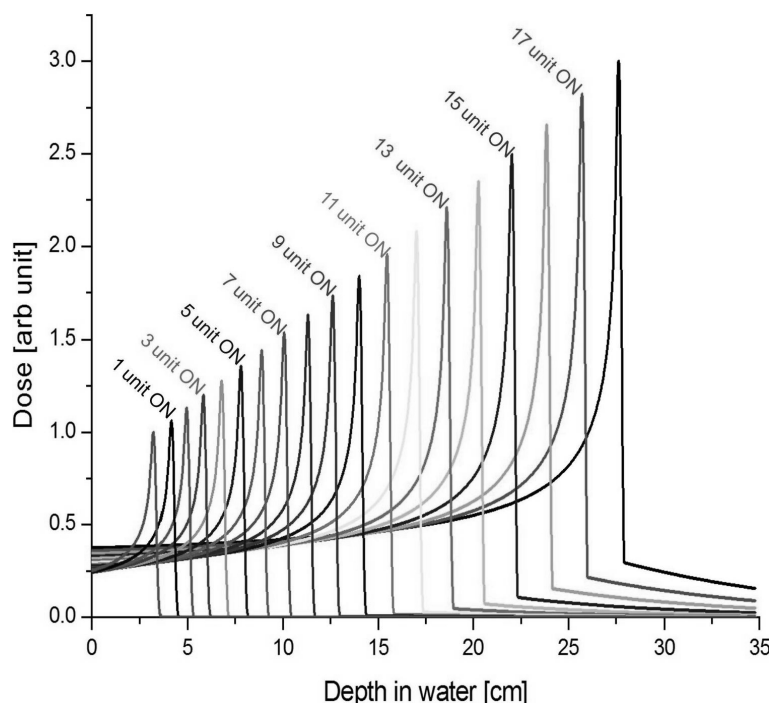


Figure 2.12: Beam range variation by increasing the number of active units[Garonna et al., 2010]. Note that intermediate ranges can be also obtained by modulating the power (and/or the phase) of the last active unit between the two extremes: *ON* and *OFF*

This means that the range of the particles can be changed actively on a time scale that is estimated to be as low as a couple of milliseconds without using passive absorbers. In

order to sweep all the intermediate energies, a cyclinac requires a large number of low power klystrons in the range of 7-15 MW, in contrast with the high power (50 MW) requirement of all high frequency linacs used for research.

The fast and continuous energy variation makes the cyclinac beam more suited to the spot scanning technique with tumor multipainting than the one produced by a cyclotron - in which the intermediate energies are obtained using passive absorbers which need about 100 ms to change the energy, cause fragmentation and need a long ESS (see Fig.8.4) - and by a synchrotron, in which the energy can be varied electronically, but on a time scale of the order of one second. The cyclinac beam is instead conceived to track the tumor (with an appropriate monitoring and feedback system) and paint it in a treatment session about 10 times in three dimensions[11] so that any over-dosages and/or under-dosages can be corrected in the next painting of the same volume[Amaldi et al., 2009].

### 2.3.4 Beam Focusing

The possibility to actively modulate the energy is a unique feature offered by the modularity of the linac but implies a delicate balance between the length of the tanks (i.e. the distance between successive PMQs forming the focusing FODO structure), the number of tanks powered by a single klystron and the peak power of the available klystrons. Because of the interplay between these quantities, the most important design limitation, when considering different RF frequencies, is given by the availability of compact and cheap RF sources for the required power.

Since the magnetic gradient of the quadrupoles cannot be changed during operation, the lattice is designed in such a way that a beam arriving with an energy lower than the reference one can still be transported along the linac without significant losses, even when many modules are switched off. In addition, the beam transverse characteristics remains stable, as shown in Fig.2.13.
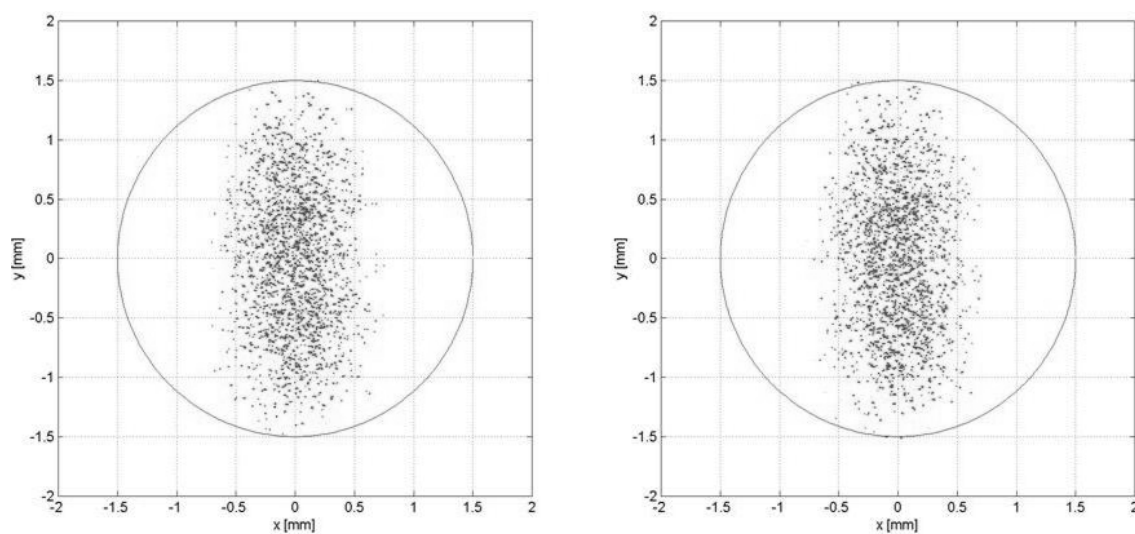


Figure 2.13: Beam transverse profile at the end of the linac with the 14th unit off (left) and on (right), corresponding to beam energies of 317 MeV/u and 334 MeV/u[Garonna et al., 2010]

---

[11]see Chap.1 and Chap.4

## 2.4 Chapter Summary

The spread of advanced beam delivery systems is partly inhibited by the performance limitations of current accelerators. On one hand, the cyclotrons used for protontherapy have the disadvantage of requiring a passive energy degradation system which leads to neutron activation. Chap.3 presents an experimental study of the beamline, at the prestigious protontherapy center of PSI, and more precisely, the beamline section where the degrader is. The study highlights the typical components of cyclotron-based therapy beamlines and some of the challenges linked to the energy degradation.

On the other hand, the synchrotrons suffer from the fluctuations of the extracted beam current and the low repetition rate at which the energy of the beam can be changed. Other accelerators like the FFAGs and the RF linacs are variable energy fast cycling solutions aiming to overcome the present limits.

In particular, TERA developed the *cyclinac*: an accelerator composed of a variable energy linac injected by a fixed energy *compact* (as opposed to *separated-sectors*) cyclotron. The focus of this PhD thesis is the quantitative assessment of the optimal injector to CABOTO: a 400 MeV/u high-gradient high RF linac delivering $C^{6+}/H_2^+$ beams with short pulse length (1.5 $\mu$s) and fast repetition rates (300 Hz).

The first crucial step is to determine the appropriate ion source to provide enough ions to deliver the desired clinical dose rate. The sources currently used in hadrontherapy are reviewed in Chap.4. Their performance reveals that more adapted types of ion sources need to be investigated and more precisely, the use of a new commercial superconducting EBIS is detailed.

# Chapter 3

# Beam Line Study at PSI

The year 2010 has seen the commissioning of a new eye treatment room (OPTIS2) and a second gantry room, called Gantry 2[Schippers et al., 2007] at PSI. The new Gantry2 treatment delivery room was at the time of this study (November-December 2009) still under commissioning[Pedroni et al., 2001]. For its new fast-scanning method, Gantry2 requires the beam current to be as stable as possible for every beam energy. To achieve this, it is crucial to ensure that the beamline elements are well aligned in the part of the beamline that immediately follows the cyclotron, as this affects considerably the degrader efficiency. This is the focus of the experimental work described in this chapter. After an initial introduction on the beamline and its instrumentation, results are presented in a chronological order, to give better understanding of the choices made and the difficulties encountered. The study was particularly challenging because of the very limited beam time available for the measurements. A new measurement protocol was specially elaborated to study the misalignments of the beamline, by increasing the accuracy of the beam measurements, with respect to the standard protocol of the Control Room. After the analysis, specific recommandations on the PROSCAN beamline alignment have been formulated.

## 3.1 PROSCAN Beamline Instrumentation

PSI has been a pioneer in hadrontherapy, since the early days of pion treatment. The successful treatment of the eye cancers (OPTIS project) and the international interest generated in the innovative technologies and techniques employed, led to the birth of the PROSCAN project[Schippers et al., 2006] in 2000. With the installation and commissioning tests of the COMET superconducting cyclotron, the PROSCAN system came on stream in 2007 for all-year patient therapy with the pre-existing eye therapy treatment room and the isocentric gantry (Gantry1) room. A scheme of the beamline is shown in the Fig.3.1.
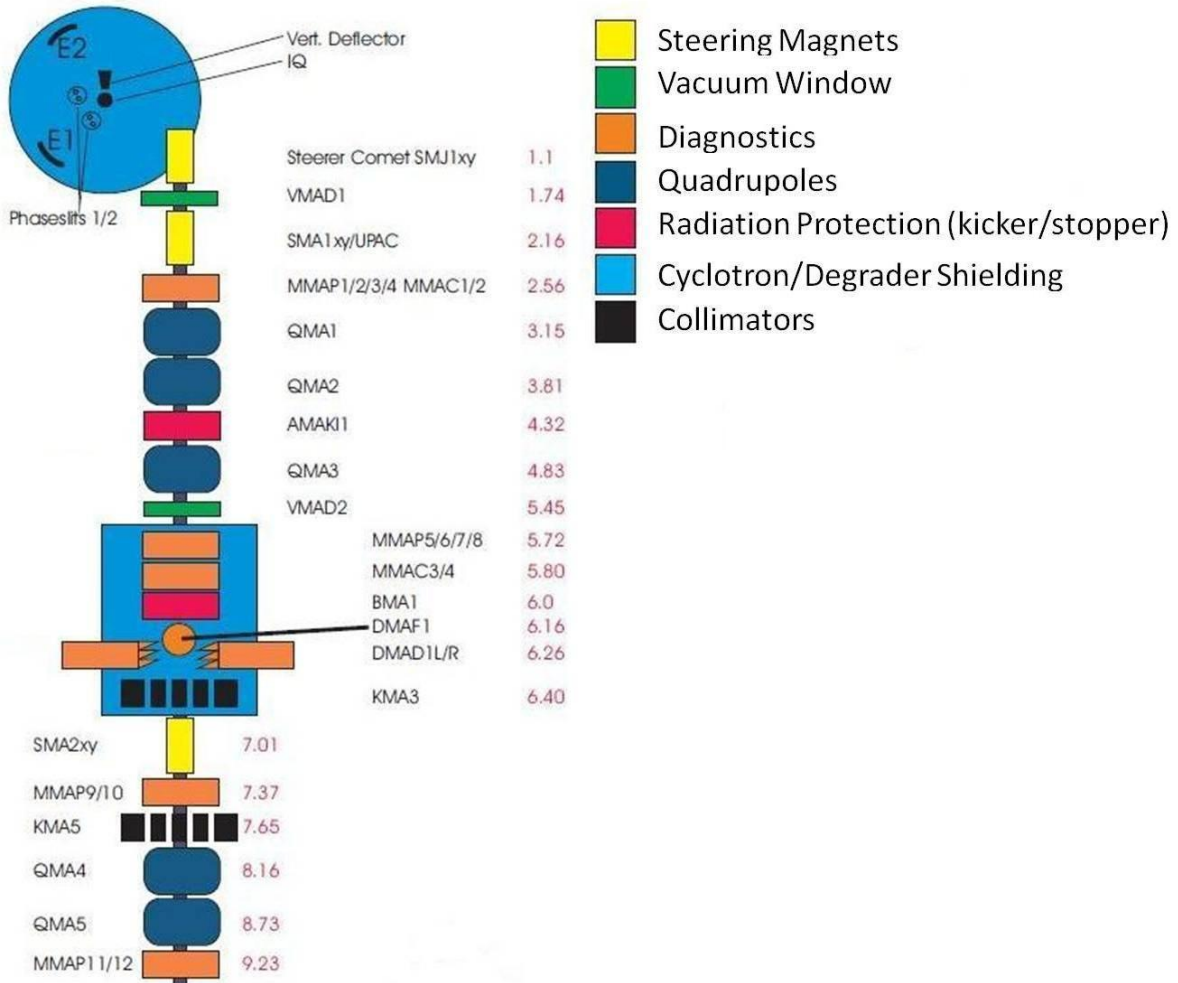
Figure 3.1: PROSCAN Beamline (courtesy M. Schippers, PSI)

### 3.1.1   Modeling

The beam transport through the different beamline elements is modeled using programs TRANSPORT[Rohrer, 2007a] and TURTLE[Rohrer, 2007b]. These programs are updated graphic versions of old CERN/SLAC/FERMILAB codes written in portable FORTRAN-77. They have been used and upgraded extensively for the last 30 years at PSI and in other nuclear physics research centers. They share the same core structure and thus have very similar input files.

TRANSPORT is a charged particle beam transport code, which: defines for each beamline element the respective transfer matrix (or $R$ matrix)[Reiser, 2008], characterizes its optical properties on the beam and calculates the evolution of the beam envelopes through the beamline. TURTLE is a Monte Carlo program tracking individual ray trajectories of many particles of a given initial beam. It investigates particular beam properties like particle losses, phase space and momentum acceptances and beam profiles.

### 3.1.2 Quadrupoles

The quadrupole triplet (QMA1-3) focuses the beam, exiting from the cyclotron, on the degrader[Schippers, 2001]. After the degrader unit, two quadrupoles (QMA4-5) focus the beam on the entrance of the AMA1 dipole magnet which directs the beam towards the different treatment rooms. All quadrupoles are modeled in TRANSPORT and TURTLE with an effective length of 35 cm and a half-aperture radius of 5 cm.

### 3.1.3 Degrader

The degrader[Reist et al., 2003] allows the reduction of the energy of the incoming 250 MeV beam in the range 70-238 MeV, at a rate of 2 % in 80 ms (5 mm in range). It is composed of carbon wedges positioned at both left and right sides of the beam axis. The overlap of the wedges is controlled by a motor and determines the amount of carbon material in the beam path and thus the beam degradation. An illustration of the degrader is shown in Fig.3.2.
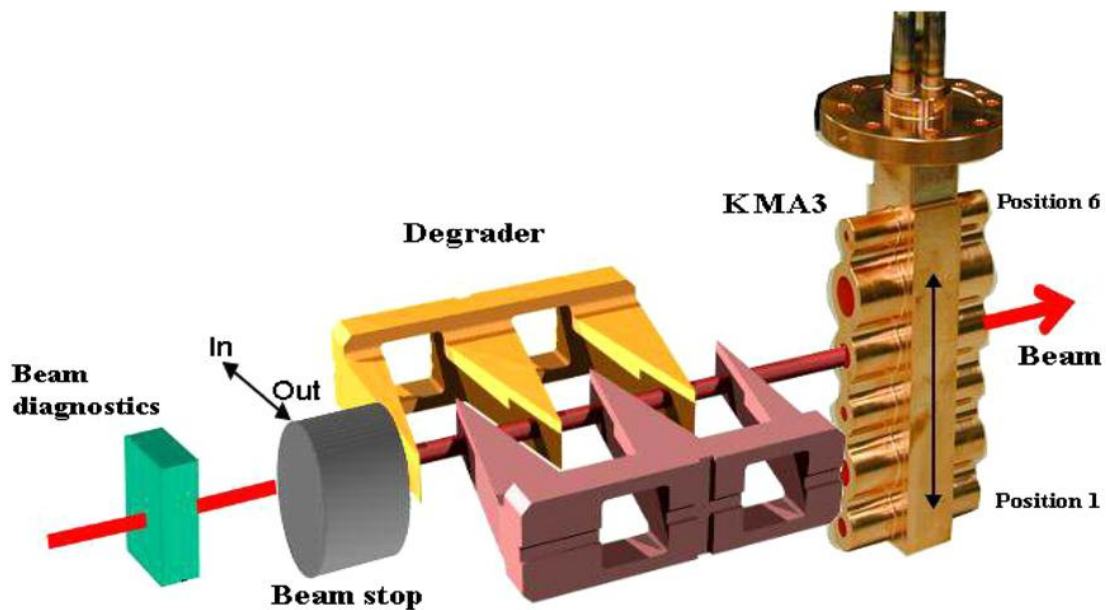


Figure 3.2: Schematic drawing of the PSI carbon wedge degrader layout[Goethem et al., 2009]. The red arrow indicates the proton beam direction (not to scale)

### 3.1.4 Collimators

Three collimators give the required shape to the spread out beam that comes out of the degrader. These are KMA3-5. KMA3 and KMA5 are copper collimators with multiple exchangeable positions corresponding to different apertures (six different radii of circular aperture from 0.5 mm to 6.5 mm for KMA3 and four elliptical and one circular aperture from 7.5 mm to 15 mm for KMA5). KMA4 is instead made of carbon and has only one fixed circular aperture of 6.5 mm. This collimation system defines the new beam size and width (the accepted part of the degraded beam). Finally, collimator KMA4 is always in the beam whereas, collimators KMA3 and KMA5 can be taken out (*off* position). Illustrations of the collimators are shown in Fig.3.2.

### 3.1.5 Profile Monitors

Profile monitors are present in the first part of the beamline near the cyclotron, both as permanently inserted devices or as devices introducible into the beam by compressed-air actuators. They are multi-strip ionisation chambers, with 32 strips arranged in a *1 broader + 30 regular + 1 broader* pattern, where the broad strip is 30 mm wide and the regular strip is 1 mm wide. These devices monitor the beam center position, width and current.

### 3.1.6 Control Room User Interface

From the Control Room, an operator can control all components of the cyclotron and the beamline. This includes: changing the current applied to steering magnets and quadrupoles, moving profile monitors and collimators in and out of the beam path and adjusting the degrader settings. The display allows to visualize the real-time profiles and beam center positions, along the beamline. It is also possible to acquire data from the profile monitors from the interface program. Two different acquisition modes were used in this study: the *single-shot* and *harfen-trace* modes. In the *single-shot* mode, a single reading from a single profile monitor is exported. The beam profiles are reconstructed from the current signal of each detector strip and interpreted as a constant line-current density over the strip width for regular strips and with a special extrapolation method for outer broad strips[Doelling, 2004]. The program automatically exports a text file with two columns: one for the position and the other for the current. In the *harfen-trace* mode, data from multiple profile monitors (in this work, up to four) can be acquired and multiple data samples (in this work, up to ten) are recorded in the same data file. The file contains the strip center positions and the measured current. No pre-processing of the data occurs in this particular acquisition mode. These are the raw data.

### 3.1.7 Sign Conventions

As it is often the case, every workgroup has its own coordinate axis conventions. In order to avoid confusion, the conventions for the coordinate axis and magnetic fields for beamline elements, survey and TRANSPORT/TURTLE have to be carefully taken into account. All results presented in this report follow the TRANSPORT/TURTLE convention, which is a cartesian coordinate system where the Y-axis is vertical and pointing upwards, the X-axis is horizontal and pointing to the right (when looking in the same direction as the beam trajectory) and the Z-axis points in a direction opposite to the beam path[1].

## 3.2 Results

### 3.2.1 Initial Measurements

First measurements were carried out at the Control Room by monitoring the profile monitors (MMAP1x,2y,5x,6y,7x,8y,9x,10y,11x,12y) and varying the steering magnets (SMJ1xy and SMA1xy), the quadrupoles (QMA1-5), the degrader and the collimators (KMA3,5).

---

[1]For profile monitors' acquisition programs, the Y-axis is defined in the opposite direction and for survey measurements the X-axis is defined in the opposite direction

## Initial Conditions

For a particular setting of steering magnets and quadrupoles, a beam whose position was within 0.4 mm from the center of profile monitors MMAP1x to MMAP8y was obtained. The beam was then considered to be aligned.

## Quadrupole Alignment

In order to test the alignment of the first quadrupole triplet (QMA1-3), all magnet currents were put to zero (corresponding to a negligible pole tip field of 3.7 mT) and the steering magnets were set up so that the beam was well centered on MMAP1x/2y and MMAP5x/6y. For each quadrupole, the current was then varied and the consequent displacement of the beam center on MMAP5x/6y was manually recorded, based on the readings from the Control Room Panel. Indeed, if the center of the quadrupole is not exactly aligned with the center of the beamline, a dipolar magnetic component appears in the center of the beamline and results in a displacement of the beam transverse position, with an amplitude proportional to the quadrupole strength.

The data was then analyzed using TRANSPORT. A screenshot from TRANSPORT is shown in Fig.3.3. It was assumed that the profile monitors were aligned in the beamline. The elements of the beamline were defined and misaligments of a quadrupole were simulated until obtaining the same beam displacements as in the measurements.
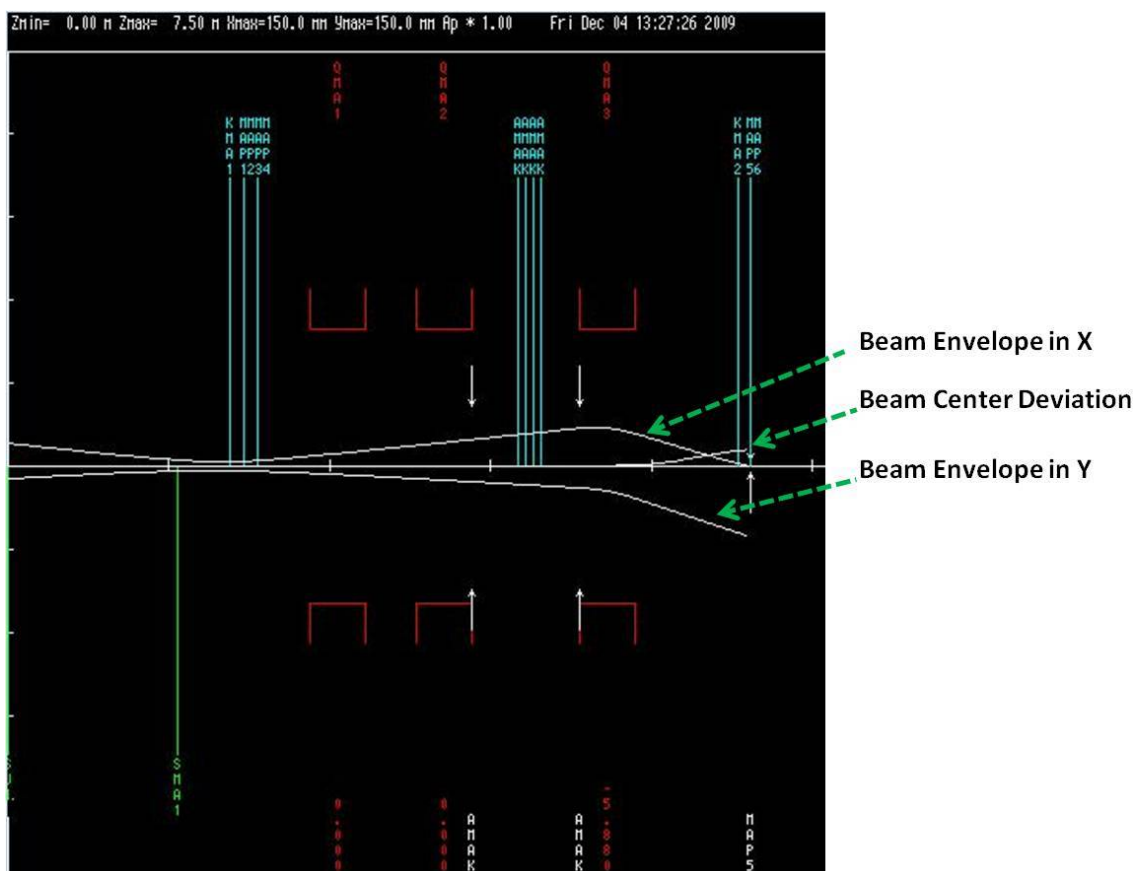


Figure 3.3: Screenshot from TRANSPORT showing X and Y beam envelopes and the deviation of the beam caused by the misalignment of quadrupole QMA3

Using this method, the possible misalignments of the quadrupoles were found (Fig.3.4).
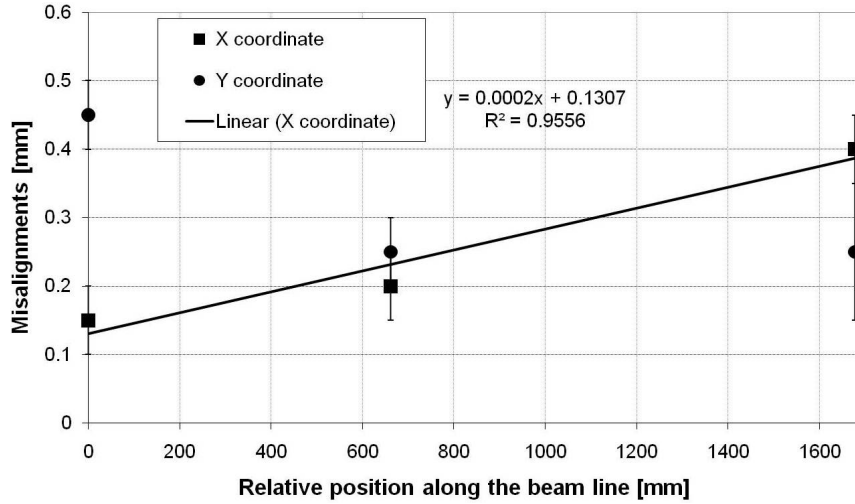


Figure 3.4: Quadrupole misalignments from TRANSPORT analysis

Knowing that the quadrupoles of the triplet share the same mechanical support, their potential misalignments must be correlated. The results suggest that the beamline section longitudinal direction axis is rotated by an angle of 0.2 mrad (along the vertical axis) with respect to the beam axis and that it also has a vertical shift of +0.3 mm.

## 3.2.2 Second Measurement Session

A second measurement session was held in the Control Room.

**Transmission Measurements**

The beam transmissions between MMAC3 and MMAP9/10 for all the possible KMA3 settings were measured for three different energies: 100 MeV, 160 MeV and 215 MeV. The beam losses take place on the degrader, KMA3 and KMA4. The values for KMA3 at position 5 (corresponding to a radius of 6.5 mm) can be compared with published measurements[Goethem et al., 2009]. In Fig.7 of the reference, the beam losses on the different elements of the PROSCAN beamline for various beam energies are presented. The present measurements revealed much higher transmissions, compared with the reference, as shown in Fig.3.5.

This improvement in beam transmission could be explained by the improved beam emittance from the cyclotron and perhaps, better focusing conditions before the degrader (indeed, experience tells that the sensitivity of the losses in the degrader is quite high to the incoming beam conditions)[2].

**KMA5 Alignment**

For this measurement, the beam was centered on profile monitors MMAP9x/10y, with KMA5 on *off* position and no degrader or KMA3 collimation. The settings of KMA5 were sequentially changed and the beam positions were measured on profile monitors MMAP9x/10y (and MMAP11x/12y). The beam profiles were noticeably altered by the

---

[2]private communication, M. Schippers (PSI)
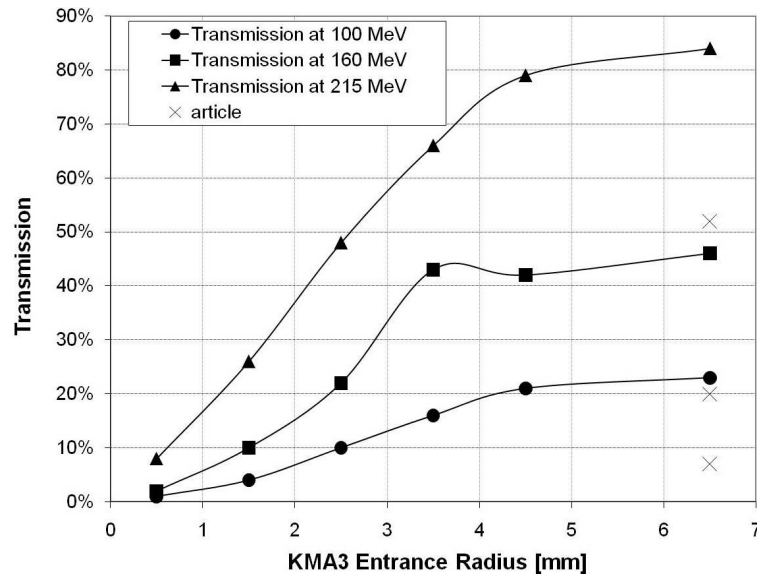
Figure 3.5: Measured beam transmission through KMA3, KMA4 and the degrader

size of the KMA5 collimator but the beam offcentering was always lower than 0.1 mm. It can thus be concluded that KMA5 is well centered with respect to profile monitors MMAP9/10/11/12.

**KMA3 and KMA4 Alignment**

The correct alignment of KMA3 was tentatively verified by inserting the collimator, changing the apertures and checking for any deviation of the beam center on profile monitors MMAP9x/10y with a narrow beam at 250 MeV. In average, no deviation occurred: the average beam position is at center and standard deviations are 0.2 mm in X and 0.4 mm in Y.

To see if the beam width would have an influence on the results, the degrader was set to an energy of 150 MeV. Results are shown in Fig.3.6.
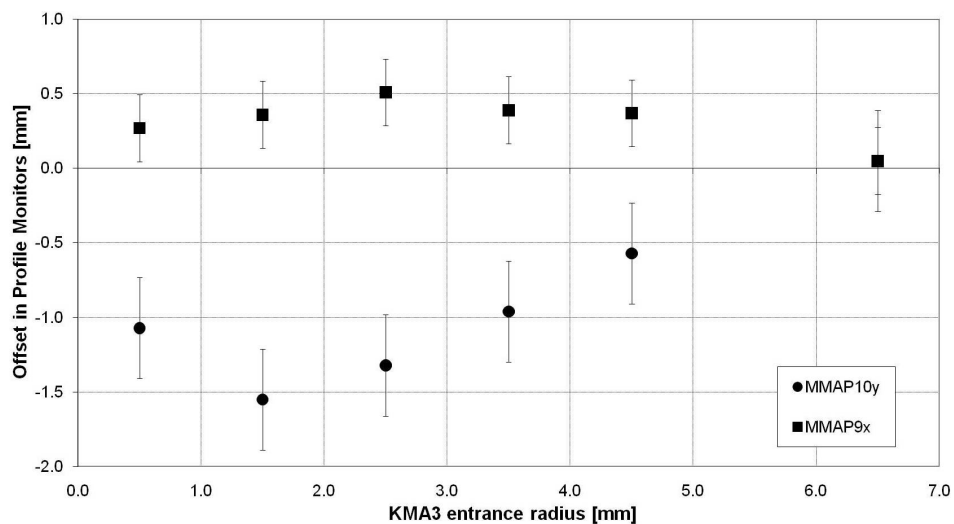


Figure 3.6: Beam centroid deviations as a function of KMA3 entrance radius

In this case, average deviations of 0.3 mm in X and -0.9 mm in Y were observed. The most plausible explanation is a misalignment of the KMA4 collimator. To verify this hypothesis, the program TURTLE was used. The appropriate beam characteristics at the exit of the degrader were first determined. This was done by trying to match the measured losses in KMA3 and KMA4 with those stated in the literature[Goethem et al., 2009]. For a 150 MeV beam, the expected losses in KMA3 and KMA4 should be, respectively 28 % and 52 % (for KMA3 in position 5). This corresponds to an input beam in TURTLE having a $2\sigma$ distribution of 5.25 mm in width and 110 mrad in divergence (X and Y)[3]. For a lower energy of 100 MeV, the losses of 45 % and 43 % were found to correspond to an initial beam of 6.0 mm width and 145 mrad divergence. This procedure was quite delicate: indeed, varying the initial beam width and divergence by a small amount resulted in important changes in the losses on the collimators. Furthermore, the results stated in the article did not exactly correspond to the recently measured values, as indicated in the previous section. This sheds some doubt on the accuracy of the results.

The effect of misaligning the KMA4 collimator for beams of two different energies (100 and 150 MeV) corresponding to beams of different widths was investigated, for the two extremal positions of KMA3 collimation (position 5, the widest and position 6, the narrowest). A typical screenshot from TURTLE is shown in Fig.3.7.
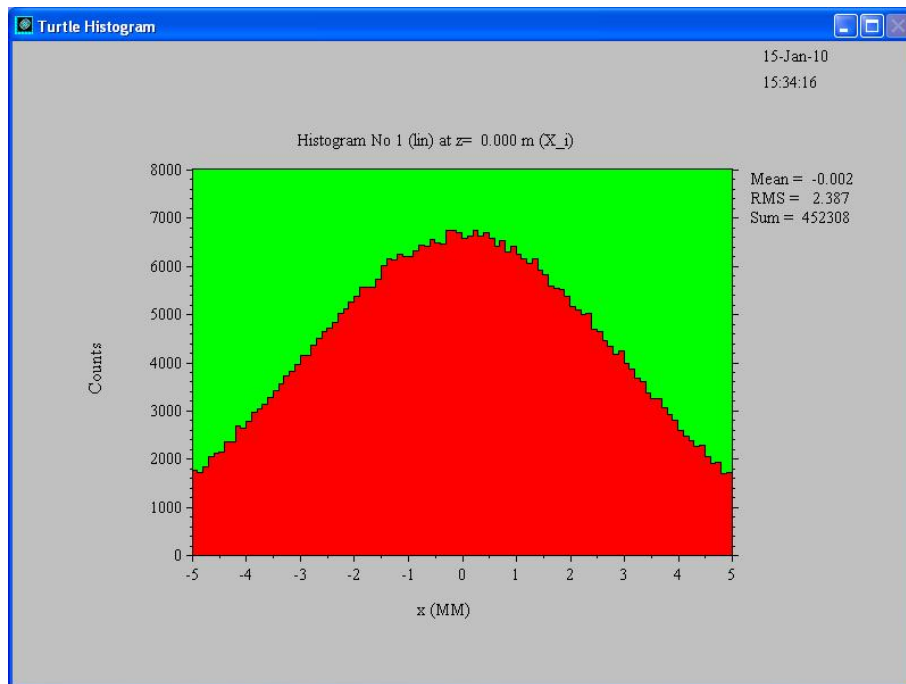


Figure 3.7: Screenshot from the program TURTLE

The first thing to determine was the minimum number of particles to simulate to obtain a final beam with a continuous distribution (average final position within $\pm$ 0.1 mm for aligned KMA4). These ranged between $10^5$ and $10^7$ particles. KMA4 was then displaced by $\pm$ 1 mm in each transverse coordinate. The average beam offsets were small: $\pm$ 0.2 mm for 150 MeV and $\pm$ 0.1 mm for 100 MeV. The measurements on the beam at 150

---

[3]the starting conditions for the beam given by M. Schippers were 12 mm in width and 120 mrad in divergence

MeV roughly corresponded to a displacement of +1 mm in X for KMA3 on position 5. However, no correspondence was found for the measurement with KMA3 on position 6.

**Improvement of the Measurement Protocol**

The beam being very broad in the measurement of the previous section, the protocol was modified to increase the precision of the measurements: instead of simply writing down the beam centroid readings of the Control Room screens, the readings from the profile monitors were exported in the *single-shot* mode, which extrapolates the current measured for each detector strip of the profile monitor to have equally spaced data points in the position coordinate.

To calculate the centroid positions from the exported data files, a Matlab[4] script was written to automatically import the values from the text files, plot and fit the curve by least squares method to a Gaussian curve of four parameters (A, B, C, D) as in Eq.3.1.

$$y = A + B \, e^{-\frac{(x-C)^2}{2 \, D^2}} \tag{3.1}$$

The result is shown in Fig.3.8.
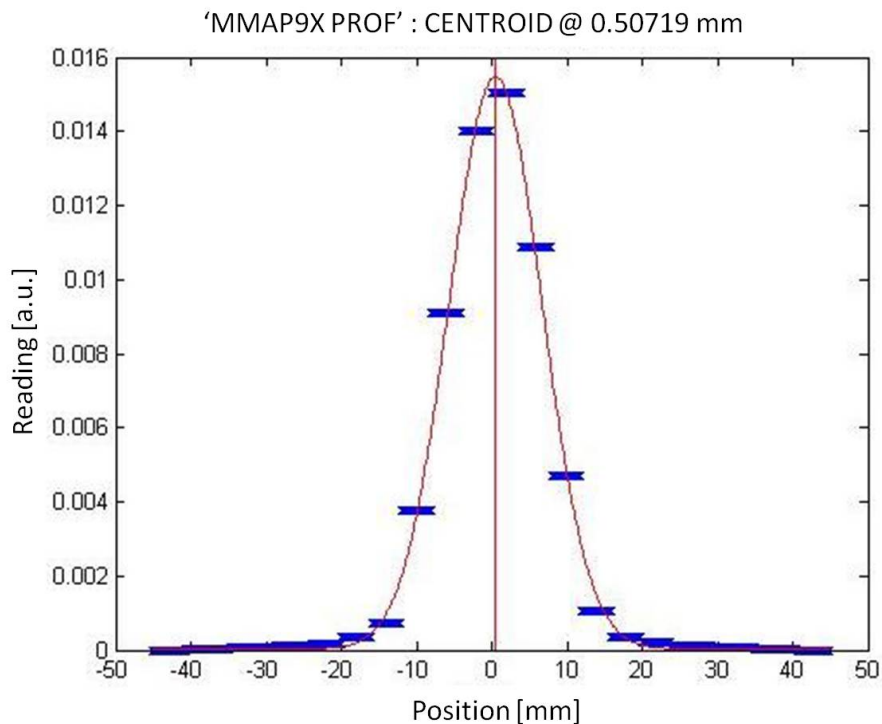


Figure 3.8: Beam profile in *single-shot* mode (in blue) with fit of all data points (in red). The vertical red line shows the centroid calculated from the fit

However, as explained previously in Sec.3.1.6, the control room software outputs a data file with processed raw data. Thus, an accurate fit is subject to the user defining a region of interest. This was implemented in Matlab, where the user can exclude part of the data by defining a *window* in the abscissa corresponding to ordinates higher than a

---

[4]MathWorks, version 7.8.0.347 (r2009a), http://www.mathworks.com/products/matlab/

certain ratio of the peak. More clearly, by taking a ratio to the peak of 0.5, the window corresponds to the FWHM. All the data inside this window is used for the fit and the rest of the data is discarded. An example is shown in Fig.3.9.
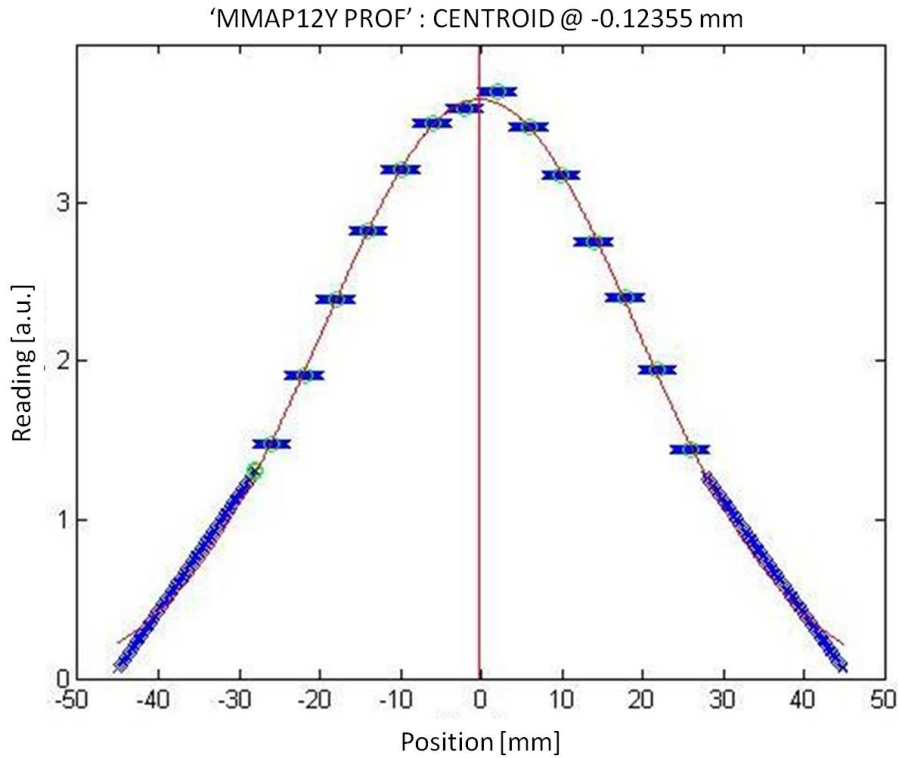


Figure 3.9: Beam profile in *single-shot* mode (in blue and green) with fit *window* corresponds to ordinates higher than 35 % of the peak value (in red). The vertical red line shows the beam centroid calculated from the fit

### 3.2.3   Third Measurement Session

To confirm the results of Fig.3.4, another measurement session focused on studying quadrupole misalignment using the new measurement protocol.

**Quadrupole Alignment**

Profiles from profile monitors MMAP1x/2y and MMAP5x/6y were acquired. The data was analyzed using TRANSPORT by taking into account the initial readings of MMAP1x/2y (defining the initial beam position) and of MMAP5x/6y (defining the initial beam divergence).

Results are shown in Fig.3.10. Compared to the previous findings, misalignments do not really match. The origin of the problem was assumed to come from the readings from the profile monitors.
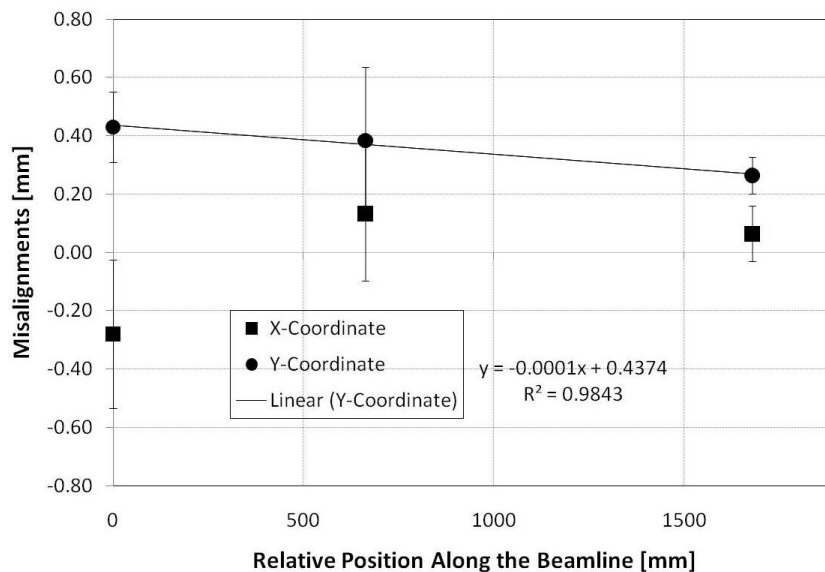
Figure 3.10: Quadrupole misalignments from TRANSPORT analysis

### Variability of Profile Monitor Readings

The readings from MMAP1x/2y (which should in principle remain constant, since the profile monitors are placed before the quadrupoles) were also analyzed. The standard deviations of these readings were 0.2 mm. This value is definitely too big to accurately estimate the misalignment of the quadrupoles. This variability of the readings may thus explain the discordance of the previous two separate analysis.

## 3.2.4   Final Measurement Session

### Survey Measurements

A survey analysis was carried out on the beamline quadrupoles and profile monitors. The results are compared, in Tab.3.1, with those of the two analyses made with TRANSPORT.

Table 3.1: Comparison of quadrupole misalignments ($\Delta$X/$\Delta$Y) measured in the survey and analytically predicted by TRANSPORT (Analysis 1/2)

| Element | *Survey* | *Analysis 1* | *Analysis 2* |
|---|---|---|---|
| QMA1 $\Delta$X (mm) | 0.1 $\pm$ 0.1 | 0.2 $\pm$ 0.1 | -0.3 $\pm$ 0.3 |
| QMA1 $\Delta$Y (mm) | 0.5 $\pm$ 0.1 | 0.5 $\pm$ 0.1 | 0.4 $\pm$ 0.1 |
| QMA2 $\Delta$X (mm) | 0.1 $\pm$ 0.1 | 0.2 $\pm$ 0.1 | 0.1 $\pm$ 0.2 |
| QMA2 $\Delta$Y (mm) | 0.5 $\pm$ 0.1 | 0.3 $\pm$ 0.1 | 0.4 $\pm$ 0.3 |
| QMA3 $\Delta$X (mm) | 0.0 $\pm$ 0.1 | 0.4 $\pm$ 0.1 | 0.1 $\pm$ 0.1 |
| QMA3 $\Delta$Y (mm) | 0.6 $\pm$ 0.1 | 0.3 $\pm$ 0.1 | 0.3 $\pm$ 0.1 |
| MMAP1/2 $\Delta$X (mm) | 0.0 $\pm$ 0.1 | 0.0 | 0.0 |
| MMAP1/2 $\Delta$Y (mm) | 0.4 $\pm$ 0.1 | 0.0 | 0.0 |
| MMAP5/6 $\Delta$X (mm) | 0.2 $\pm$ 0.1 | 0.0 | 0.0 |
| MMAP5/6 $\Delta$Y (mm) | 0.5 $\pm$ 0.1 | 0.0 | 0.0 |

It can be seen that the first basic analyses with control room tools and TRANSPORT gave results which are in fairly good agreement for QMA1 and QMA2, less so for QMA3. The initial assumption for the analysis with TRANSPORT was that the profile monitors were aligned with the beamline. However, the survey showed relevant offsets up to 0.5 mm of the profile monitors MMAP1/2 and MMAP5/6.

Great confidence lies in the measurements based on the survey points for MMAP1/2 and the quadrupoles, which truly correspond to the centers of the profile monitors and the center of the quadrupoles. However, since MMAP5/6 is in a more delicate position inside the degrader unit, it is possible that the center of the profile monitor has accidentally shifted with respect to the survey reference points since the time of its installation.

**New Measurement Protocol**

Following the advice from diagnostics expert Dr. Rudolf Dölling at PSI, the measurement protocol was once more improved. The *harfen-trace* acquisition mode, was chosen. Another specific import tool was written in Matlab: the user specifies the input file and the name of the profile monitor. The program then imports data from the text file. For each sample, the program plots the profile and the fit. This allows to discard the faulty data sets. The fit was also modified: instead of totally discarding the extremal data values from the fit, a weight factor was introduced, so that the user can choose to what extent he wishes to include the points in the analysis. This is particularly important for broader beams, where the data points corresponding to the outer broader detector strips show unrealistic values. Finally, the program outputs the mean centroid position and its standard deviation. Examples of fitted curves are shown in Fig.3.11 for a narrow beam and Fig.3.12 for a broad beam. The raw data is shown as green and blue markers, fitted by a red curve. The vertical line shows the centroid position calculated from the fit.
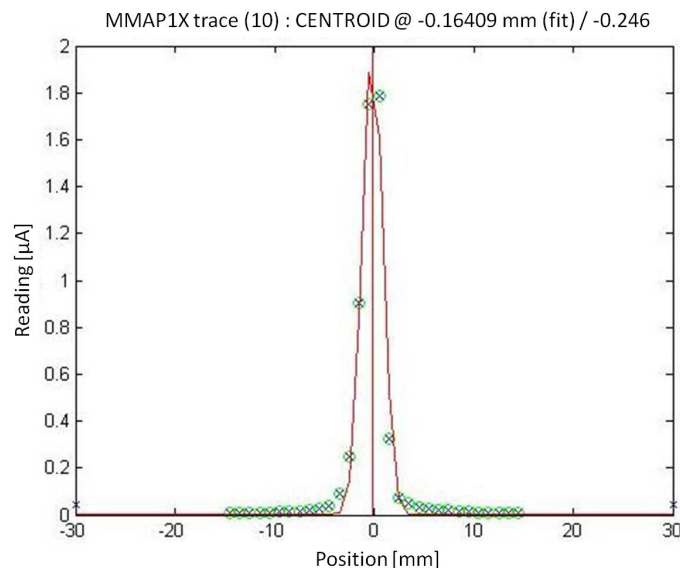


Figure 3.11: Beam profile in *harfen-trace* mode for a narrow beam

**Natural Beam Oscillations**

The increasingly complex measurement protocol for profile monitors allowed to increase the accuracy of the beam centroid determination to less than 0.05 mm for profile monitors
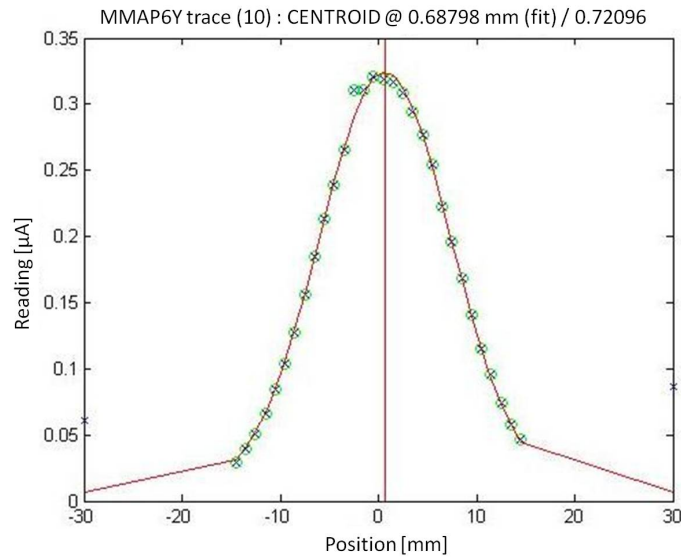
Figure 3.12: Beam profile in *harfen-trace* mode for a broad beam

MMAP1x/2y and 0.5 mm for profile monitors MMAP5x/6y (for an unfocused beam). These accuracies come from the acquisition of ten samples from each profile monitors in direct succession over a time length of a few seconds. However, when comparing identical measurements from MMAP1x/2y made a few minutes apart, their standard deviation is 0.04 mm. These deviations originate either from oscillations in the acquisition electronics of the profile monitors or from real oscillations of the beam.

**Quadrupole Alignment**

As previously, the current applied to the quadrupoles was modified and the displacements of the beam for QMA1, QMA2 and QMA3 were monitored. Results are presented in Fig.3.13, Fig.3.14 and Fig.3.15.
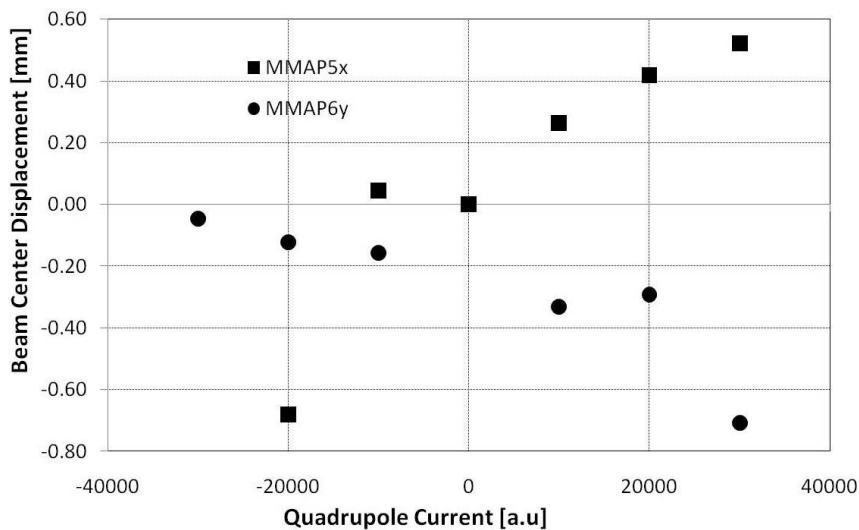


Figure 3.13: Displacements of the beam center on MMAP5x/6y when different currents are applied to quadrupole QMA1
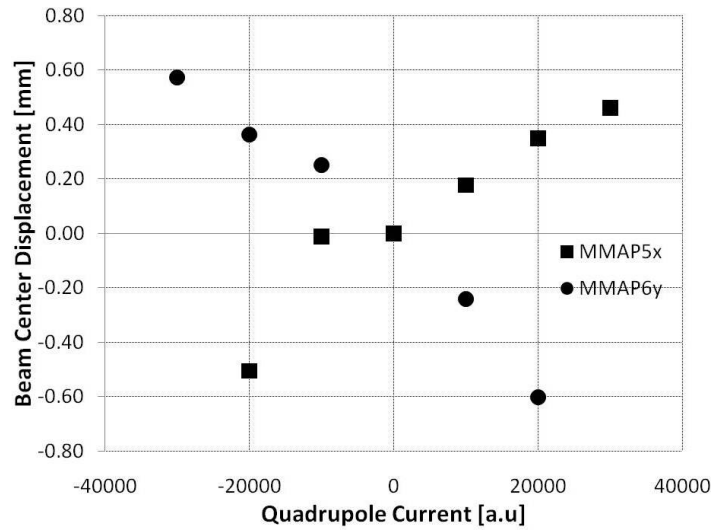
Figure 3.14: Displacements of the beam center on MMAP5x/6y when different currents are applied to quadrupole QMA2
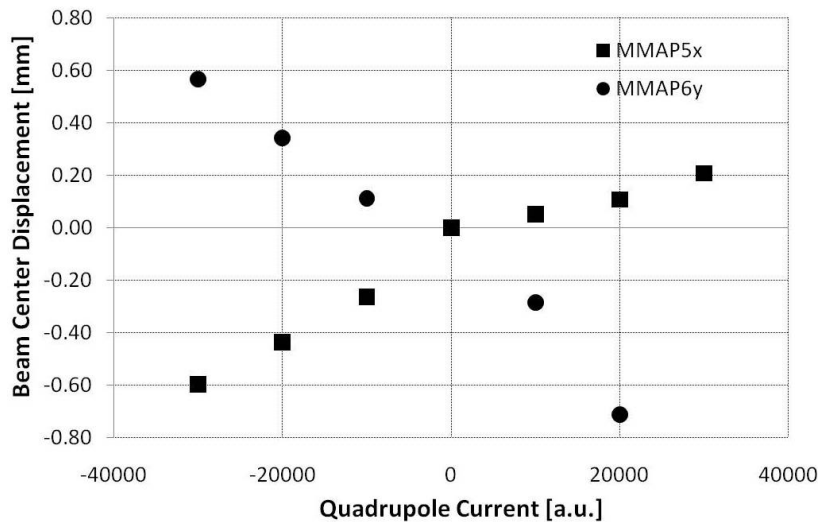


Figure 3.15: Displacements of the beam center on MMAP5x/6y when different currents are applied to quadrupole QMA3

From the simple observation of these figures and knowing that a quadrupole powered with positive current is focusing in the X direction and defocusing in the Y direction, it can be intuitively deduced that if during the measurements the beam was centered, then the quadrupoles are misaligned in both positive X and positive Y directions. This confirms the survey measurements (except for QMA3 which survey measured to be aligned in X).

To study this in more detail, the surveyed offsets of profile monitors and quadrupoles were introduced in TRANSPORT. Since the average readings of MMAP1x/2y are $(X;Y)_{mm} = (-0.09; 0.76)$ and the average readings of MMAP5x/6y (when the quadrupoles are off) are $(X;Y)_{mm} = (-0.24; -0.81)$, a beam with initial position $(X;Y)_{mm} = (-0.10; 1.18)$ and with initial divergence of $(P_X; P_Y)_{mrad} = (-0.1; -0.48)$ was introduced. Results are shown in Fig.3.16.
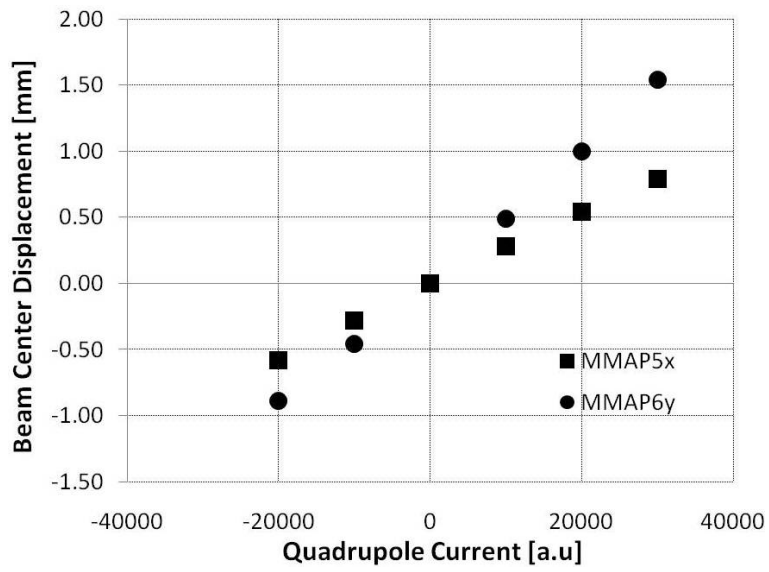
(a) QMA1
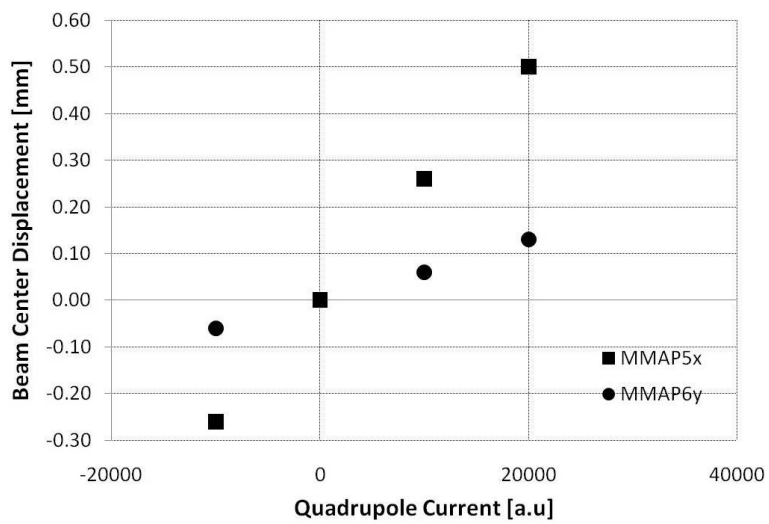


(b) QMA2
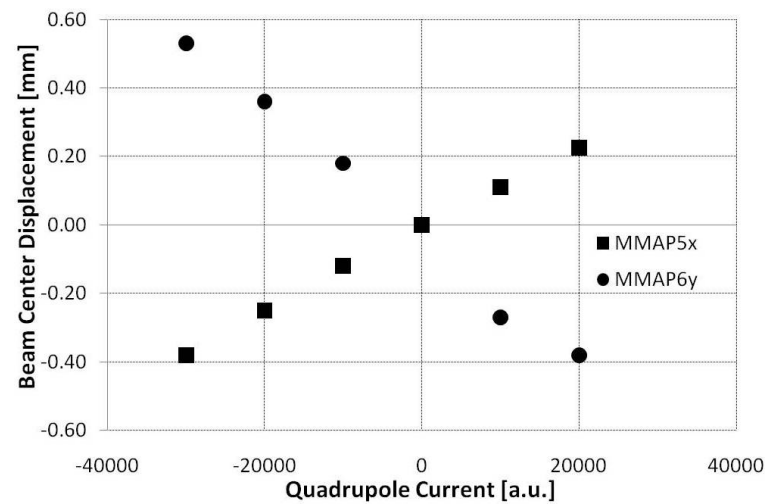


(c) QMA3

Figure 3.16: TRANSPORT-simulated displacements of the beam center on MMAP5x/6y when different currents are applied to quadrupoles QMA1-3

The comparison between these figures and the measurements shows good agreement for QMA3. However, QMA1 and QMA2 give unexpected results. Perhaps, as anticipated earlier, the position of the profile monitors MMAP5x/6y is not the one given by the survey. In this case, the exact initial beam conditions in TRANSPORT which give results similar to the measurements for QMA1 and QMA2 would have to be determined by trial and error. This would then determine the misalignment of the profile monitors.

## 3.3   Chapter Summary

The results presented offer some interesting considerations and challenges. First of all, by adopting a simple measurement and analysis protocol, it was shown that it is possible to qualitatively determine the misalignment of quadrupoles. In addition, the use of the *harfen-trace* acquisition mode from the Control Room and the special fit in Matlab allow to increase significantly the precision and consistency of the measurements of the beam centroid, especially for broad unfocused beams.

However, in order to accurately quantify the small misalignments of the elements of the beamline, an accurate study of the variations in beam position of the order of 0.1 mm would be needed. Three main challenges thus arise. Firstly, natural oscillations of the beam coming from the cyclotron induce variations in measurement conditions. Indeed, variations in the beam center of the order of 0.5 mm were recorded. Secondly, the determination of the beam centroid is very delicate since the profile of the unfocused beam is very broad and its peak very flat. A very little variation in the currents measured by the detector strips of profile monitors will induce large variations in the fitted center of the profile. Thirdly, it is important to know what the real position of the beam is, to simulate it correctly in TRANSPORT. Although information on the real position of the profile monitors at PROSCAN is not crucial in the everyday handling of the beam for medical therapy, it is essential to study the misalignments of the other elements.

Based on the results found, the following recommendations were made:

- correction of the vertical position for the beamline mechanical support for the quadrupole triplet QMA1/2/3 (by 0.5 mm downwards, following the survey measurements);

- correction of the vertical position of the profile monitor MMAP1x/2y (by 0.4 mm downwards, following the survey measurements);

- inspection of the exact position of the center of profile monitors MMAP5x/6y (by opening the degrader unit).

In the months following this study, the above recommendations were implemented. Since then, the modification of quadrupole settings do not significantly alter the beam position and the beam alignment procedure is much easier and more consistent. It was therefore concluded that the the changes were successful[5].

---

[5]private communication, M. Schippers (PSI)

# Chapter 4

# Ion Sources for CABOTO

This chapter investigates the ion source requirements of cyclinacs and reviews both the ion sources currently used for hadrontherapy and the potential newcomers. The complexities linked to ion source technology are also briefly introduced but the interested reader may find more detailed information in the bibliography[Hill, 1994; Wolf, 1995].

## 4.1 Cyclinac Beam Requirements

The beam accelerated by CABOTO has specific time characteristics, as shown in Fig.4.1.
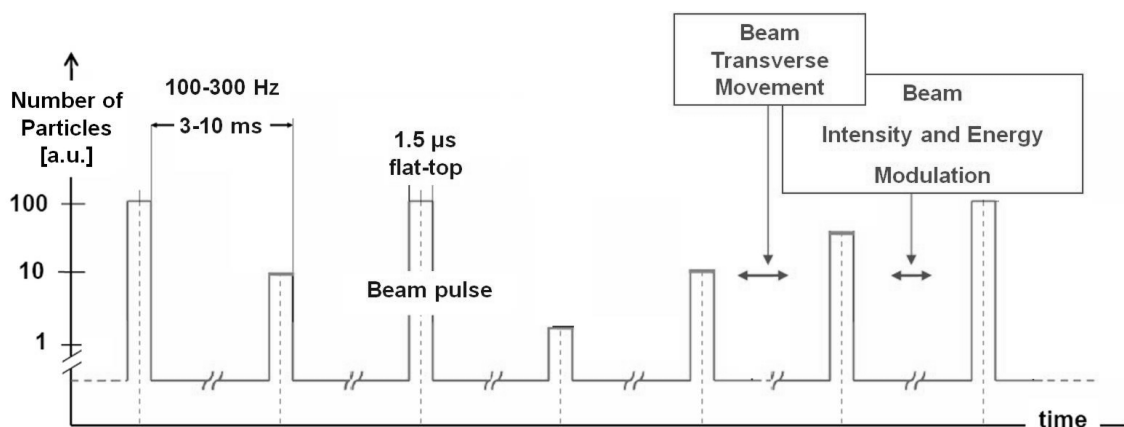


Figure 4.1: CABOTO beam characteristics

The high repetition rate takes full advantage of the linac fast energy variation and is required for an advanced 4D multipainting beam delivery system, in which the fourth dimension (the time) expresses the capability of the system to follow on-line the movements of the tumor. The pulse length is determined by the linac RF cavity filling time and the RF pulse flat-top, which is kept to a minimum to reduce the RF power consumption.

### 4.1.1 Dose Calculation

Previous studies of TERA investigated the needed particle fluence from a linac for beams of protons and carbon ions. They modeled a multipainting dose delivery system[Amaldi et al., 2009; Amaldi and Team, 2006] irradiating, from a single direction, a 1 L spherical

tumor centered at a depth of 20 cm in water. The number of visits per voxel ranged from 1 to 16. The transversal FWHM of the spots were 13.5 mm for protons and 5.9 mm for carbon ions and the interspot distance was 75 % of the spot FWHM. Similar beam sizes in the longitudinal direction were obtained using the unique property of the linac: by slightly varying the beam energy, when visiting multiple times the same voxel, the Bragg peak can be widened as needed. Finally, the biological dose in the SOBP for carbon ions was obtained from the physical dose by determining average values of the RBE[1] based on the residual ranges of the particles[ICRU, 2005].

The result was that, to achieve a clinical dose rate of 2 GyE/min[2] on the patient, with dose errors from a missing visit under 3 % of the total local dose, the maximum particle flux delivered to the spots has to be $4 \ 10^9$ protons per second (maximum current of 0.7 nA) and $6 \ 10^7$ carbon ions per second (maximum current of 0.06 enA[3]).

### 4.1.2 Particle Losses

To compute the ion output needed from the source, beam losses are estimated for each section of the cyclinac, as shown in Tab.4.1.

Table 4.1: Estimates of beam transmission in each section of the cyclinac

| | |
|---|---|
| Cyclotron Injection | 50 % |
| Cyclotron RF Longitudinal Capture | 40 % (with buncher) |
| Cyclotron Acceleration | 100 % |
| Cyclotron Ejection | 50 % |
| Linac Transverse Transmittance | 30 % |
| Linac RF Longitudinal Capture | 10 % |
| Linac Acceleration | 100 % |
| High and Low Energy Beam Lines | 70 % |
| **Total Transmission** | $\mathbf{2 \ 10^{-3}}$ |

The losses are supposed equal for both ion species. Conservative beam losses have been taken for the injection and ejection of the cyclotron[Calabretta et al., 2006]. The typical cyclotron longitudinal capture of 10 % is increased by a factor 4 with the use of a buncher[Calabretta et al., 2001]. The linac values were computed from calculations of Alberto Degiovanni, a PhD student working at the TERA Foundation. For this calculation, the fact that the beam ejected from the cyclotron has a microstructure of 30-100 MHz is irrelevant since it is seen as continuous by the 3-6 GHz linac. Other beam losses have been estimated based on the literature[Amaldi et al., 2010a]. Overall, the transmission is around 0.2 %.

---

[1] for definitions of SOBP and RBE, see Chap.1

[2] *GyE* stands for *Gray Equivalent*: 1 Gray corresponds to 1 J/kg and the term *Equivalent* specifies that it is a biological dose, as opposed to a physical dose (see Chap.1)

[3] the *e* symbol in the unit stands for *electrical* current. This means that the value stated represents the total electrical charge per unit charge and avoids any ambiguity for ions carrying multiple elementary electrical charges

### 4.1.3   Final Numbers

The aim is to deliver to the patient a particle flux of $4 \ 10^9 \ s^{-1}$ protons and $6 \ 10^7 \ s^{-1}$ carbon ions, as detailed earlier. The overall beam transmission of 0.2 % and the beam characteristics of Fig.4.1 give the source parameters listed in Tab.4.2. Note that the source ion pulse has to be longer than 1.5 $\mu s$ and can have any shape (provided it is stable in time).

Table 4.2: Ion source requirements for cyclinacs (N is the integral particle number in 1.5 $\mu s$)

| Species | $C^{6+}$ | $H_2^+$ |
|---|---|---|
| **Average Particle Intensity** $[s^{-1}] = N$ | $3 \ 10^{10}$ | $1 \ 10^{12}$ |
| **Corresponding Current** [eA] | $3 \ 10^{-8}$ | $2 \ 10^{-7}$ |
| **Repetition Rate** [Hz] = R | 300 | 100 |
| **Used Pulse Length** [$\mu s$] | 1.5 | 1.5 |
| **Particles per Pulse in 1.5** $\mu s$ = N / R | $1 \ 10^8$ | $1 \ 10^{10}$ |
| **Average Current in the Pulse** [eA] | $6 \ 10^{-5}$ | $1 \ 10^{-3}$ |

## 4.2   Ion Sources for Hadrontherapy

Ion sources operating in clinical environments have to be reliable, consume low power and require little maintenance. The requirements set in Tab.4.2 are achievable for $H_2^+$ ions with existing sources. On the contrary, the production of fully stripped (6+) carbon ions at the right levels of current, purity and energy spread remains a challenge.

### 4.2.1   Multicusp Ion Sources

Simple filament multicusp ion sources are able to produce large currents of low charge state ions. A scheme of the ion source is shown in Fig.4.2.
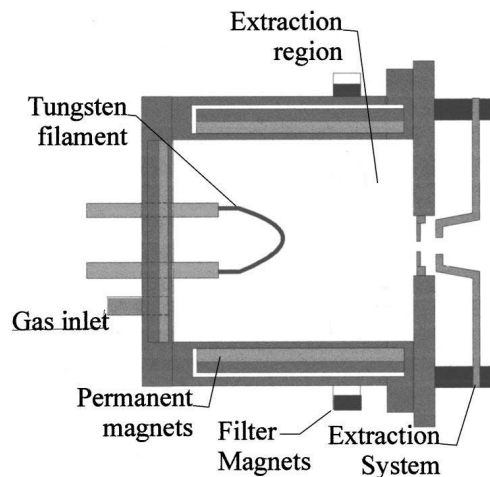


Figure 4.2: Schematic of a filament-driven multicusp ion source (modified from literature[Lee et al., 2000])

In this type of source, the filament emits electrons of a few keV to the outer walls of the source. These ionize the gas and produce a plasma confined by permanent magnets, with strong fields at the walls, and only weak fields in the central plasma volume. The ions are ejected by an electrostatic potential of a few kV. Longer lifetimes can be achieved by replacing the filament with an RF antenna[Wutte et al., 1998]. The emittance of the ejected beam is typically around 0.2 $\pi$ mm mrad (normalized, 4-rms)[4]. A source optimized for $H_2^+$ was developed at LBNL and currents of up to 8 mA were measured[Leung, 1994]. After ejection from the source, the continuous beam can be chopped to produce the required pulsed beam.

These ion sources are therefore a good candidate for use in a CABOTO cyclinac, since a single source is able to satisfy the requirements for $H_2^+$.

### 4.2.2   Electron Cyclotron Resonance Sources

Electron Cyclotron Resonance Ion Sources (ECRIS) are the workhorse ion sources for hadrontherapy centers, offering reliability, commercial availability and low power consumption.

**Operational Principle**

The operational principle of an ECRIS is schematically shown in Fig.4.3.
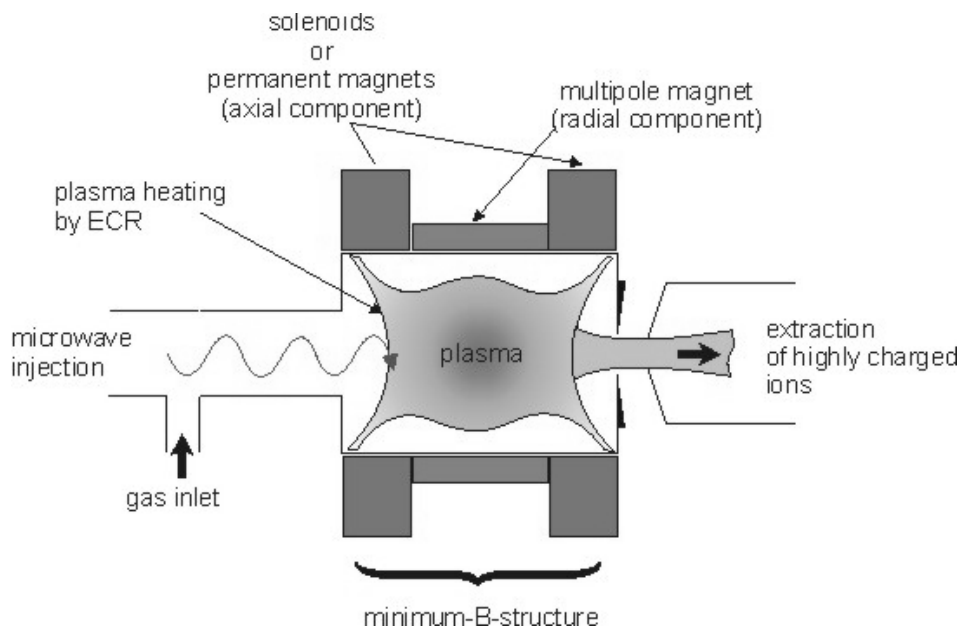


Figure 4.3:   Operation principle of an ECRIS. Figure taken from: `http://www.strz.uni-giessen.de/~ezr`

It makes use of the fact that energetic electrons rotate around magnetic field lines at a defined frequency, known as the cyclotron frequency. If an RF wave of the same frequency is present, the electron motion couples resonantly to the RF power and the electron acquires enough energy to ionize surrounding particles. This is achieved in a source where the plasma is confined longitudinally by coils in Helmholtz position, set to give a *minimum B* field configuration, shown in Fig.4.4.

---

[4]see Chap.5
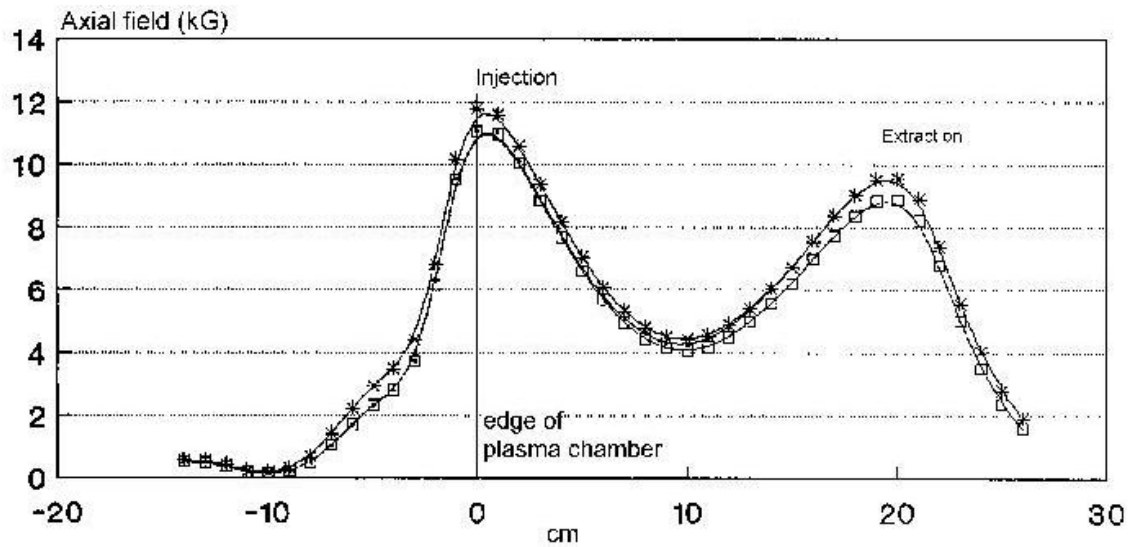
Figure 4.4: Typical longitudinal field in an ECRIS[Hill, 1994]

The radial confinement of the particles is ensured by powerful permanent magnet multi-poles. This also produces distorted beam emittances at the exit of the source. The RF frequencies used are typically in the range 1-100 GHz and ions are ejected in continuous current mode. However, there is a phenomenon that produces higher currents of highly-charged ions in short pulses. Indeed, it is possible to adjust the source in such a way that when the RF heating power is turned off, a large peak of highly charged ions appears. This effect is known as *afterglow*[Melin et al., 1990].

**Multi-turn injection in synchrotrons**

At present, all existing and under construction carbon ion therapy centers use synchrotrons with continuous current ECRIS[Kitagawa et al., 2010]. These sources produce carbon ions at low charge states (most often 4+) at 20-40 kV ejection voltage. The 200-400 e$\mu$A average current is captured in the synchrotron in a few milliseconds at the typical 0.5 Hz repetition rate (*multi-turn* injection). The ions are accelerated in a Radio Frequency Quadrupole and then a Drift-Tube Linac to 4-7 MeV/u, after which they are stripped to the 6+ charge state with close to 100 % efficiency. The reasons behind the production of $C^{4+}$ from the source are three-fold:

1) the source can produce larger ion numbers for lower charge states

2) higher $\frac{q}{A}$ allows to reduce the dimensions of the linac injector

3) the 4+ charge state allows to filter contaminant ions from Nitrogen and Oxygen, since these do not appear with $\frac{q}{A} = \frac{1}{3}$

However, this injection line is a very expensive part of the whole synchrotron complex and modern accelerator designs aim at using sources directly producing fully stripped carbon ions, as will be detailed in the next sections.

**Currently used sources for hadrontherapy**

The Japanese centers[5] use sources coming from the research and experience developed over the years at NIRS and more precisely, on its NIRS-ECRIS permanent magnet 10 GHz source. At HIBMC, two identical sources ECR1 and ECR2 are used, for fast switching between proton and carbon ion treatments[Sawada et al., 2000]. GHMC uses the Kei-GM, a 10 GHz permanent magnet source similar to the NIRS-Kei2 prototype[Muramatsu et al., 2005].

The institute hosting the Chinese hadrontherapy center developed many ECRIS and currently uses the LECR3, initially designed for atomic physics[Zhao et al., 2004].

At HIT and CNAO, the proton and carbon sources are permanent magnet commercial ECRIS called Supernanogans (Pantechnik S.A., France). The parameters requested by CNAO at the source are the following:

- Kinetic energy of 8 keV/u

- $H_2^+$ beam current of at least 0.66 mA

- $^{12}C^{4+}$ beam current of at least 0.2 emA

- Normalized emittance of at most 0.6 $\pi$ mm mrad (95 %)

The length of the source is 60 cm, the weight is 200 kg, the RF is 14,5 GHz and the source is equipped with permanent magnets (two solenoids and one sextupole). The source produces continuous beams of $H^+$, $H_2^+$, $^{12}C^{4+}$ and $^{12}C^{6+}$ with emittances in the range 0,37-0,62 $\pi$ mm mrad (95 %, normalized) and guarantees currents of respectively: 2.0 mA, 1.0 mA, 0.2 emA and 3 e$\mu$A[6]. According to the manufacturer, it is the largest and most powerful full permanent magnet ECRIS in the world.

Unfortunately, the production of bare carbon ions is a factor of 20 lower than the cyclinacs requirements set in Tab.4.2.

## 4.2.3   Electron Beam Ion Sources

Alternative sources for carbon ions have been proposed as better candidates. The most promising one is the pulsed EBIS, aiming to deliver enough current in very short pulses to achieve single-turn injection in the synchrotron. This type of injection allows the synchrotron magnets' aperture to be smaller, reducing the complexity and cost of the synchrotron[Becker, 2006].

**Operational Principle**

The electron gun has a highly emissive cathode producing the electron beam. In the ionization region, where the drift tube is segmented, the electron beam is compressed by a strong magnetic field. The gas atoms are ionized by electron collision and the resulting ions are confined in the source by an electrostatic axial trap. The radial trap is formed by the Coulomb potential of the electron beam. The ions are ejected by changing the axial trap potential. The electrons are separated from the ion beam and dumped in a water cooled electron collector. This operational principle is schematized in Fig.4.5.

---

[5]see Chap.1 and Chap.2

[6]from http://www.pantechnik.fr/, March 2011
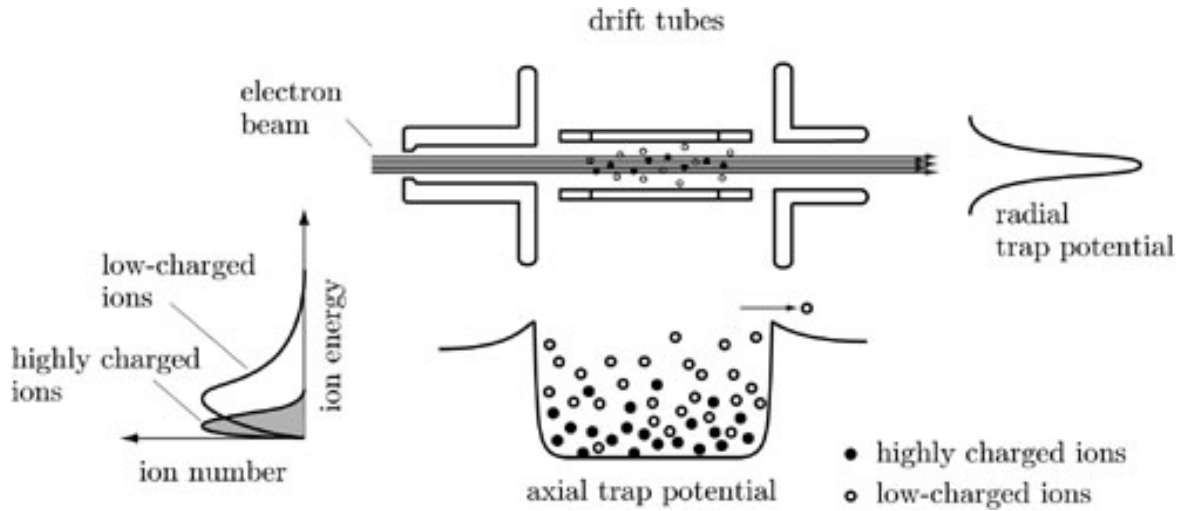
Figure 4.5: Scheme of the ionization and ion trapping mechanisms in an EBIS (courtesy of Dr. Günther Zschornack, Dreebit Gmbh)

The electrical trap capacity $C_e$ of the ion trap can be calculated[Zschornack et al., 2010] according to Eq.4.1, where $l_{trap}$, $I_e$ and $E_e$ are respectively the length of the ion trap, the electron beam current and the electron beam energy.

$$C_e = \frac{l_{trap}\, I_e}{\sqrt{E_e}} \qquad (4.1)$$

This quantity constitutes an upper limit to the ejectable ion number. Operational experience has shown that at most about 50 % of the trap capacity can be achieved.

**Sources for Ion Beam Therapy**

A dedicated prototype source for ion beam therapy was designed and constructed in Frankfurt, the MEDEBIS[Kester et al., 1996]. It aimed at the production of fully stripped carbon ions to be injected into a Radio Frequency Quadrupole with much lower duty cycle ($10^{-5}$ instead of $10^{-3}$) and injected in the synchrotron without stripping. It used a normal conducting solenoid of 0.8 T and a short trap length of 0.25 m. Tests showed that at a repetition rate of 5 Hz, up to 6 $10^8$ positive charges could be extracted in pulses of 2 $\mu$s FWHM, but the spectrum peaked for bare oxygen ions $O^{8+}$ instead of carbon ions.

More recently, the KRION2 source in operation at JINR has been proposed for use at HIMAC[Donets et al., 2004]. It has a superconducting solenoid of 3 T, a total drift tube length of 1.2 m and operates in the *electron string* mode[Donets, 2004], which enhances the electron density and ion production without increasing the power consumption. The source was also tested for a potential use with cyclinacs[Donets et al., 2010].

With experimental conditions equivalent to 400 Hz repetition rate, the ionization time was found to be suboptimal and the proportion of $C^{6+}$ in the pulse was only 7 %. Nevertheless, the ejected pulse contained 8 $10^7$ $C^{6+}$ ions with a FWHM of 2 $\mu$s, which is 25 % lower than the requirements set in Tab.4.2. However, operating the source continuously at this repetition rate would require to install additional cooling for the anode.

Operation at a repetition rate of 20 Hz showed that the proportion of $C^{6+}$ rises to 55 %

and the 2 $\mu$s FWHM ejected pulse contains 7 $10^8$ $C^{6+}$ per pulse. The current in the pulse is thus increased by a factor 8 but the average current is lower. A new source, called Krion-6T, is currently under construction with the following project parameters: 6 T superconducting solenoid of 1.2 m length and electron injection energy up to 25 keV. Two to eight times increased ion yields are expected in comparison to Krion-2.

A picture of the source is shown in Fig.4.6.



Figure 4.6: Picture of the Krion2 (courtesy of Evgeny E. Donets, JINR)

The particular features of EBIS make them very attractive for use in cyclinacs. In this perspective, a collaboration was set up by TERA with a commercial producer, Dreebit Gmbh (Germany). Measurements were made with their most powerful existing source, the EBIS-A. However, the main interest lies in the newly designed and built, EBIS-SC[Zschornack et al., 2007]. These aspects are further detailed in Sec.4.3 and Sec.4.4.

### 4.2.4 Laser Ion Sources

The recent development of high-power laser systems opened up the possibility to use them for pulsed ion sources. The laser is focused on a target to produce the required ions at repetition rates of a few Hz. For example, interesting results were found[Fournier et al., 2000] by using a small $CO_2$ laser (available in the market at repetition rates up to a few 100 Hz) focused onto a polyethylene target to produce $C^{4+}$ ions for PIMMS[7]. Although research is still at an initial stage, this could become a strong candidate source for hadrontherapy in the future.

---

[7]see Chap.1

# 4.3 Experimental Measurements on EBIS-A

This section describes the measurements on the ion source EBIS-A from Dreebit Gmbh, performed at the Rossendorf Research Center in Dresden from July $21^{st}$ to July $24^{th}$ 2009, under the supervision of Dr. Falk Ulmann. The aim of these measurements was to gather knowledge on the operation of EBIS sources, in order to estimate the performance and study the use of the new EBIS-SC as a source of bare carbon ions for cyclinacs.

## 4.3.1 EBIS-A Characteristics

The main parameters of EBIS-A are given in Tab.4.3.

Table 4.3: Technical parameters of the EBIS-A, taken from `http://www.dreebit.com` and private communication with G. Zschornack (Dreebit Gmbh)

| | |
|---|---|
| **Axial Trap Length** | 60 mm |
| **Max. Electron Current** | 200 mA |
| **Max. Electron Energy** | 20 keV |
| **Magnet** | Permanent (NdFeB) |
| **Magnetic Induction on Axis** | 0.6 T |
| **Beam Emittance** | 0.05 $\pi$ mm mrad (normalized, 4-rms) |
| **Pulse Band** | 20 ns to 0.1 ms (gaussian to flat top) |
| **Energy Spread** | $\sim$ eV/u |
| **Vaccum Conditions** | Ultra High Vacuum ($10^{-9}$-$10^{-10}$ mbar) |
| $C^{6+}$ **Production in Pulsed Mode** | 1.5 $10^9$ s$^{-1}$ |
| $H_2^+$ **Production in Pulsed Mode** | 3.1 $10^{10}$ s$^{-1}$ |

The whole source is placed on a high voltage (10-20 kV) platform, fixing the extraction potential $U_{extr}$, so that the beamline is at ground potential. The beam extracted from the source is focused with an Einzel lens, filtered with a dipole magnet and the beam current is measured with a Faraday Cup. The number of ions per pulse is computed by integrating the curve over 5 $\mu$s (all pulses had a time length lower than 5 $\mu$s). The number of ions per second can then be infered by multiplying with the repetition rate.

The capabilities of the EBIS-A were tested in terms of $C^{6+}$ and $H_2^+$ production. The influence on the source output of various parameters were investigated. A scheme of the electrical potentials that can be varied inside the EBIS-A is shown in Fig.4.7.
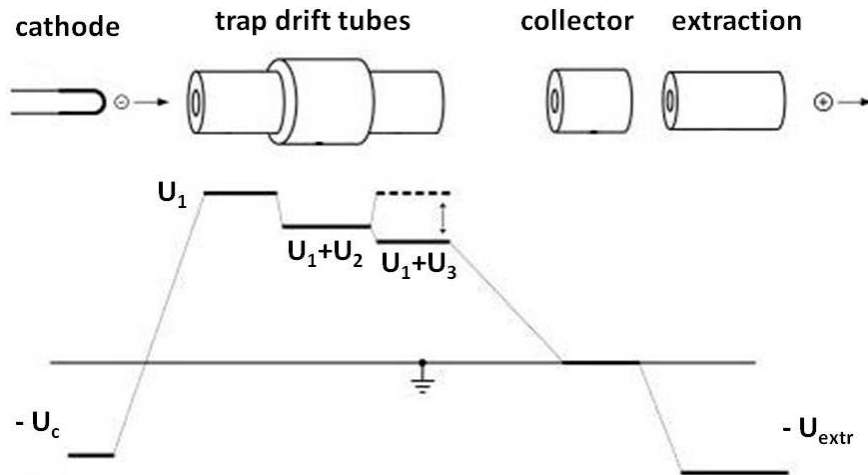
Figure 4.7: Scheme of the cathode, drift tube and extraction potentials (courtesy G. Zschornack, Dreebit Gmbh). $U_c$ is the electron gun cathode potential, $U_1$ is the potential of the first drift tube (towards electron gun), $U_2$ is the potential of the central drift tube, $U_3$ is the potential of the third drift tube (towards ion ejection) and $U_{extr}$ is the extraction potential

## 4.3.2 Influence of Gas Pressure

Vacuum inside the EBIS-A is very high and pressure lies at $10^{-10}$ mbar. Increasing this value triggers gas inflow from gas bottles connected to the source. The nature of the gas depends on what ions one wishes to produce. For carbon ions, propane ($C_3H_8$) is used, whereas for $H_2^+$, dihydrogen is obviously used. The measurements for carbon ions and ionized dihydrogen are shown in Fig.4.8.
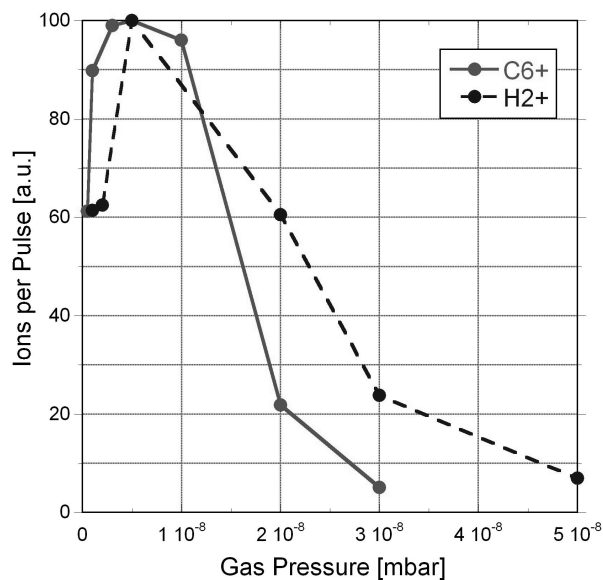


Figure 4.8: $C^{6+}$ (solid line) and $H_2^+$ (dashed line) production as a function of input gas pressure

The effects are comparable for both ion species. For carbon ions, the optimal conditions are met at a pressure of $3 \cdot 10^{-9}$ mbar. Lower pressures do not provide enough carbon ions to be ionized in the trap, whereas higher pressures induce important charge losses due to charge exchange collisions between charged carbon ions and neutral gas atoms.

### 4.3.3 Influence of Ionization Time

The ionization time determines the repetition rate of the ion beam exiting the source. The source output for different repetition rates was measured and the results are presented in Fig.4.9 for $C^{6+}$ and Fig.4.10 for $H_2^+$.
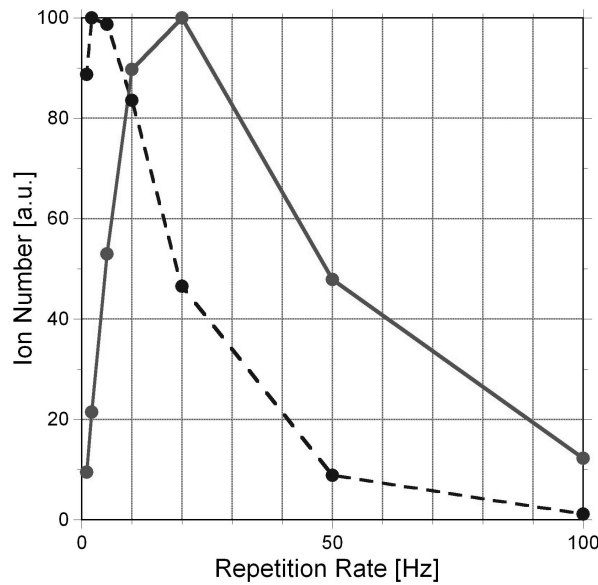
Figure 4.9: $C^{6+}$ production per pulse (dashed line) and per second (solid line) as a function of repetition rate
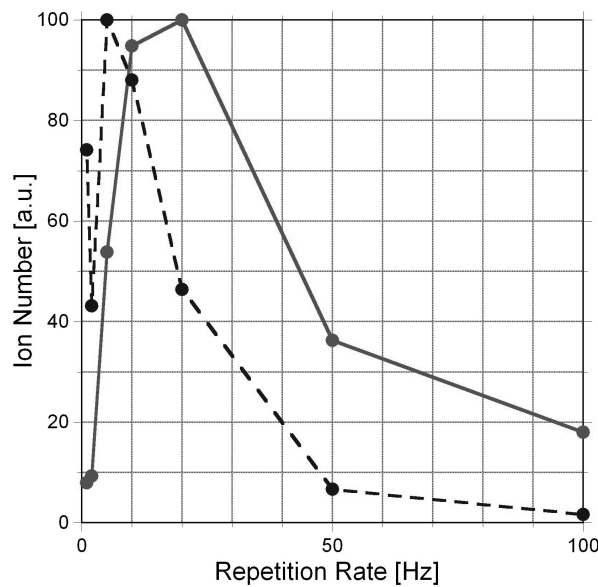
Figure 4.10: $H_2^+$ production per pulse (solid line) and per second (continuous line) as a function of repetition rate

It is clear that the optimal ionization time (in terms of ion production per pulse) for $C^{6+}$ lies at around 200 ms. For $H_2^+$, the optimal output is also found at 5 Hz repetition rate. This last value was expected to be higher since the charge state is lower than for fully

stripped carbon ions. Another interesting phenomenon is the decrease in ion output for longer ionization times (1 s and 500 ms). This could be explained by the fact that $H_2^+$ are lighter ions. Once ionized, they quickly acquire enough kinetic energy to leak out from the axial potential trap.

In terms of ion production per second, the optimum lies at 20 Hz repetition rate for both ion species.

### 4.3.4   Influence of the Electron Beam Current

The electron beam current is an essential parameter in ion production. It is proportional to the trap capacity (see Eq.4.1) and is determined by the cathode potential (typically around -3 kV) and the trap potential $U_1$ (typically around 6 kV). An increase in ion production is observed as the current is increased from 50 mA to 100 mA, as shown by the measurements for carbon ions presented in Fig.4.11.
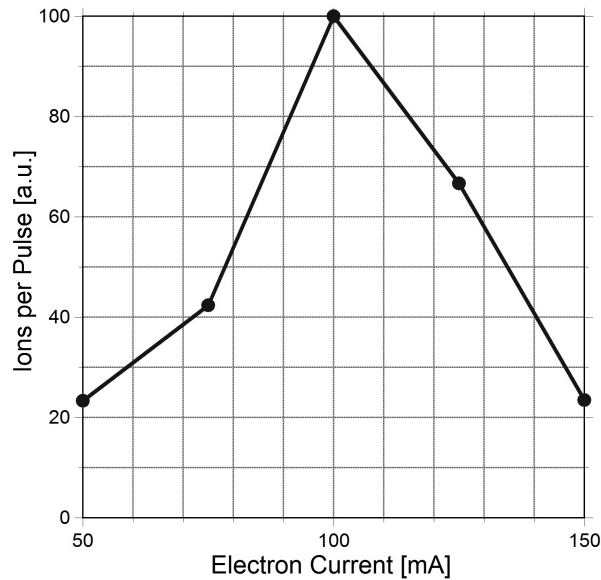


Figure 4.11: $C^{6+}$ production as a function of electron beam current

However, at higher current values, ion output decreases dramatically. This is probably due to the fact that the electron beam is compressed by the magnetic field and when the number of electrons increases, space charge forces inside the electron beam provide a counterforce to the magnetic field compression. The electron beam broadens and this reduces the trap capacity.

### 4.3.5   Influence of Trap Potential $U_1$

The potential $U_1$ determines the kinetic energy of the electron beam and the trap capacity is inversely proportional to the square root of the electron energy (see Eq.4.1). However, because of the design of the source, high electron energy ensures adequate focusing of the electron beam which increases the trap capacity. This is indeed observed in the measurements, shown in Fig.4.12. Increasing $U_1$ up to 9 kV has a positive effect on ion production, whereas higher values of $U_1$ lead to lower ion output.
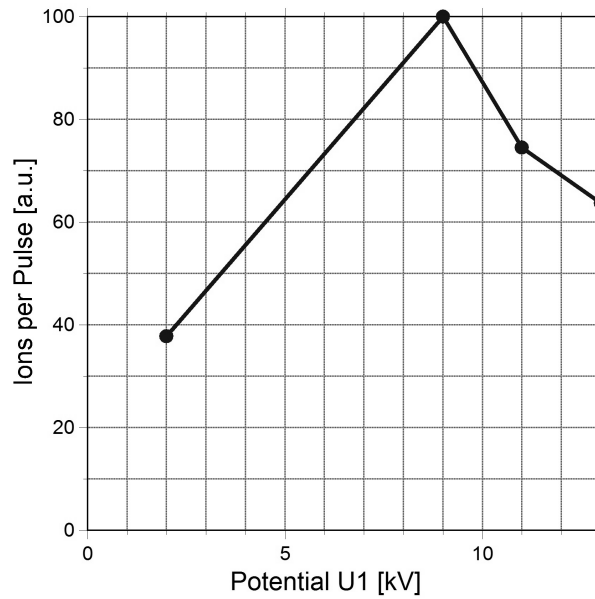
Figure 4.12: $C^{6+}$ production as a function of source potential $U_1$

## 4.3.6   Influence of Trap Potential $U_2$

The $U_2$ potential determines the depth of the potential barrier of the axial trap that confines the ions. Its value is defined relative to the potential $U_1$. Interesting effects arise when varying this parameter, as shown in Fig.4.13.
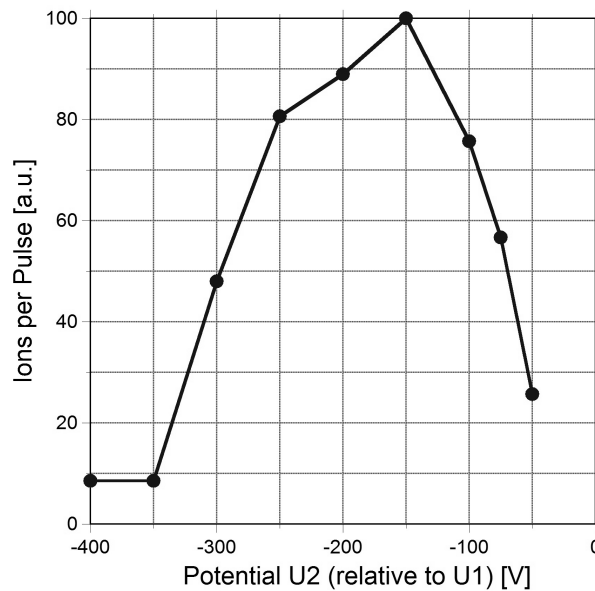


Figure 4.13: $C^{6+}$ production as a function of potential $U_2$

Ion output is clearly suboptimal for potentials higher than -100 V and lower than -250 V. Indeed, the radial trap potential (created by space charge forces from the dense electron beam) lies at values around 100 V. It can thus be assumed that axial trap potentials higher than -100 V are not sufficient to provide axial confinement to the ions and that ions with enough kinetic energy leak out of the trap. On the other hand, measurements

show that setting the potential too low determines less ejected ions. The most realistic explanation is that ion focusing effects inside the source determine ion losses when the value of $U_2$ is too low.

### 4.3.7   Influence of Trap Potential $U_3$

The potential $U_3$ is a constant operational value which defines the potential of the last trap electrode when the trap is open, relative to potential $U_1$. In this measurement, the central trap potential and the slew rate are held constant at respectively -175 V and 50 ns. The *slew rate* is the time of the switch between a closed trap (last electrode set at potential $U_1$) and an open trap (last electrode set at $(U_1 + U_3)$). This means that as $U_3$ is decreased, the voltage gap between closed and open trap is increased and the voltage change per unit time is increased. The measurements are shown in Fig.4.14.
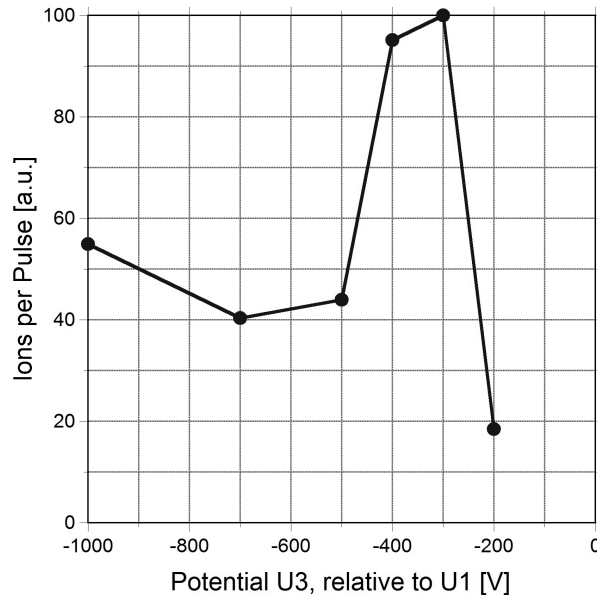


Figure 4.14: $C^{6+}$ production as a function of potential $U_3$ ($U_2$ is set at -175 V)

When $U_3$ is too high, the first ions to come out of the trap have higher energy than those leaving later. This results in an energy spread of the beam and in loss of particles in the beam line after the analyzing magnet. For lower values of $U_3$, most probably, the optics of the source determine the presence of an optimum at voltages around -300 V.

### 4.3.8   Influence of Slew Rate

With the use of a custom program, any given trap opening sequence can be chosen. More precisely, the operator can regulate how at trap opening, the voltage of the last electrode will vary from $U_1$ to $(U_1 + U_3)$. Thus, the pulse shape can be modified according to the user needs. An example of this capability is shown in Fig.4.15, where an artificial flat-top is created.

In addition, setting different trap opening times (but maintaining the same sequence) provides interesting insights into ion ejection mechanisms. Indeed, as shown in Fig.4.16, as the slew rate increases, the ion pulse becomes narrower. For the fastest slew rate (50
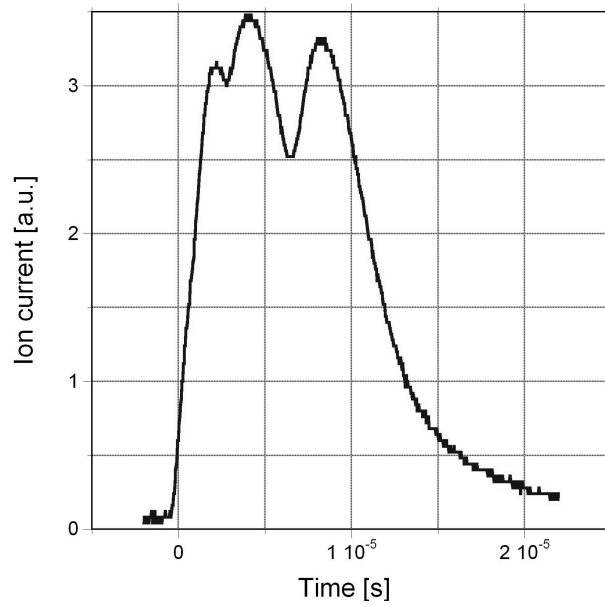
Figure 4.15: Particular carbon ion pulse produced by adjusting the slew rate

ns), all information from the opening sequence is lost, and the pulse assumes a typical Gaussian shape.
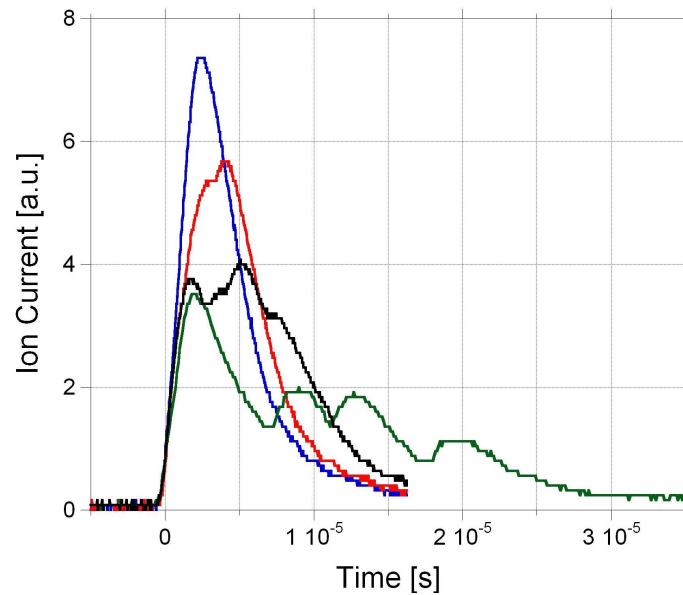


Figure 4.16: Carbon ion pulses with slew rates of 50 ns (in blue), 100 ns (in red), 500 ns (in green) and 20 $\mu$s (in black). $U_3$ is fixed at -100 V

## 4.3.9   Discussion

The EBIS-A was tested to determine its operational characteristics and the various parameters affecting its output. It was observed that the ion output from the source is very sensitive to the source settings. The optimized parameters for $C^{6+}$ production are summarized in Tab.4.4.

Table 4.4: EBIS-A optimal parameters for $C^{6+}$ production

| | |
|---|---|
| **Repetition Rate** | 20 Hz |
| **Electron Current** | 100 mA |
| **Propane Pressure** | $5\ 10^{-9}$ mbar |
| $U_1$ **Potential** | 9 kV |
| $U_2$ **Potential** | $U_1$ - 150 V |
| $U_3$ **Potential** | $U_1$ - 300 V |
| **Slew Rate** | 50 ns |
| **Maximum Output in Pulsed Operation** | $2\ 10^8$ s$^{-1}$ |

The final particle number per second is ten times lower than the value stated on the company website. However, the repetition rate used for the value of the website is not known and the performance in terms of ion production was not the aim of this particular study. In the next section, some conclusions based on the presented measurements will be drawn, regarding the expected performance of the EBIS-SC and the ability of source intensity modulation from pulse to pulse at high repetition rate.

## 4.4 EBIS-SC

A simplified scheme of the EBIS-SC hardware is shown in Fig.4.17 and the main parameters are presented in Tab.4.5.

Table 4.5: Technical parameters of the EBIS-SC, taken from `http://www.dreebit.com` and Sec.4.4.2

| | |
|---|---|
| **Axial Trap Length** | 20 cm |
| **Max. Electron Current** | 1 A |
| **Max. Electron Energy** | 30 keV |
| **Magnet** | Superconducting (liquid He free) |
| **Magnetic Induction on Axis** | 6 T |
| $C^{6+}$ **Production in Pulsed Mode** | $3.5\ 10^{11}$ s$^{-1}$ |
| $H_2^+$ **Production in Pulsed Mode** | $1.1\ 10^{11}$ s$^{-1}$ |

The mounted source is around 1 m long, 60 cm large and 84 cm high. A picture of the source is shown in Fig.4.18. It is thus very compact, compared to the Krion2 source discussed earlier (the axial trap is six times smaller).

It is optimized to produce very high charge states. Indeed, a lower electron energy would increase the ionization cross-section for lower charge elements, like carbon. Nonetheless, the expected performance (in terms of bare carbon ion production) based on the technical improvements with respect to EBIS-A and on the simulations is very promising, as detailed in the next subsections.
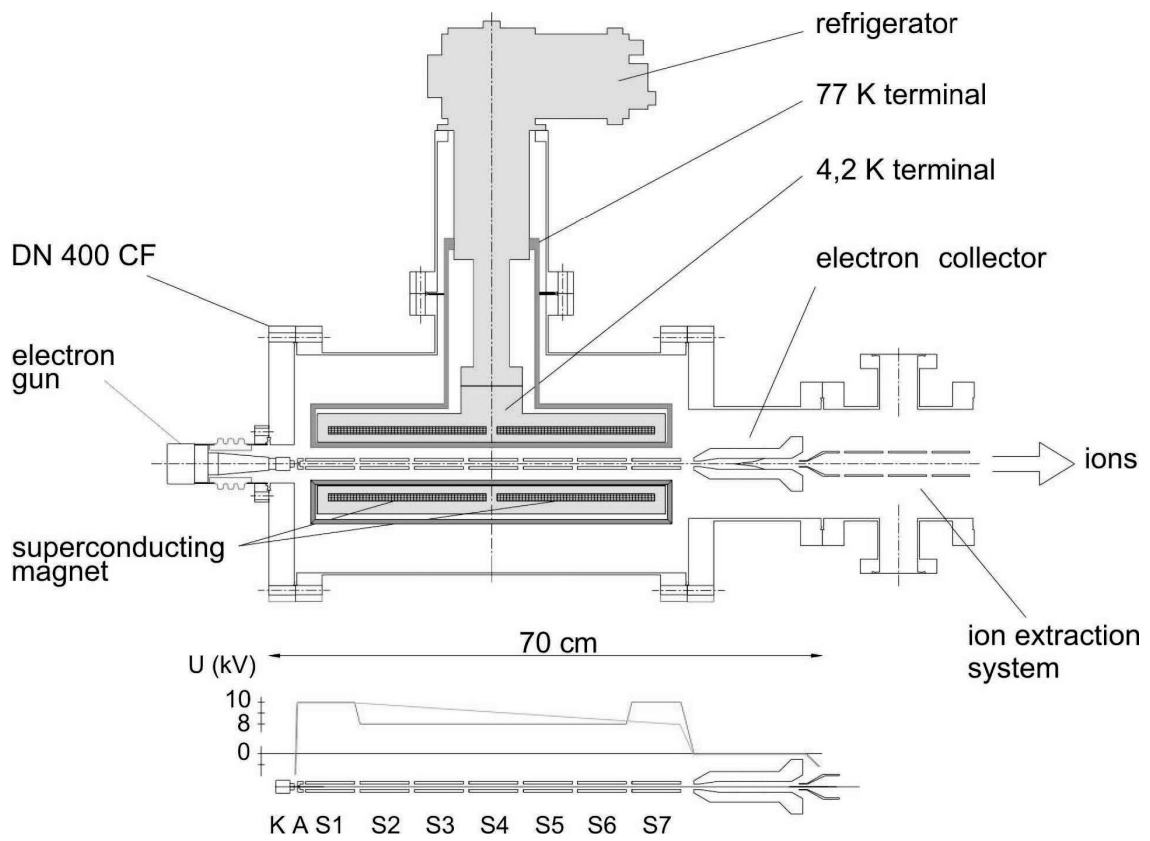
Figure 4.17: Basic structure of the EBIS-SC[Zschornack et al., 2010]



Figure 4.18: Photograph of the EBIS-SC during its first installation (courtesy of G. Zschornack, Dreebit Gmbh)

## 4.4.1   Projection of EBIS-SC future performance

**Ionization time**

EBIS-SC will feature an electron beam with current densities from 7 to 10 times higher than EBIS-A. This will accelerate the ionization process and allow the source to produce ions at higher repetition rates.

**Ion Number**

In terms of trap capacity, the EBIS-SC axial trap is more than three times longer, thus providing a wider volume where particles can be ionized and trapped. Furthermore, the maximum electron current is five times higher in EBIS-SC. Taking into account the difference in maximum electron energy between the two sources, the EBIS-SC trap capacity can be estimated to be four times higher than in EBIS-A. However, as the measurements with EBIS-A showed, the maximum electron current does not automatically correspond to the highest ion production.

**Pulse Width**

Another important aspect is the pulse width. Based on the measurements, the minimal pulse width achievable with the EBIS-A is 2 $\mu$s. This results from the time-of-flight of ions in the source before ejection. Considering that the EBIS-SC is equipped with independent fast switching devices for each of the 8 trap electrodes (compared to 3 electrodes in EBIS-A) and that the electrode axial length is smaller than in EBIS-A, the EBIS-SC could operate the trap electrode potentials in such a way as to squeeze the axial width of the trap during the ionization time so as to achieve short pulse lengths of 1 $\mu$s.

**Intensity Modulation**

Ideally, the intensity of the beam from the accelerator needs to be modulated from one pulse to the next. The simplest option would be to achieve this modulation already at the source level without affecting the accelerator parameters. Preliminary tests made on the EBIS-A showed that the variation of the central electrode trap potential can change the number of ejected ions without modifying the pulse length, shape or ion energy. With the normal switching device used at Dreebit laboratory, the time needed to vary the electrode potential is under 1 ms, which is already fast enough for cyclinacs.

Alternative ways to achieve modulation at the source include varying the ionization time, the trap potential and the trap opening time with fast (order of ns) Behlke switches[8].

**Beam purity**

Based on the working experience with the EBIS-A, impurities from $N^{7+}$ and $O^{8+}$ are expected to be present in proportions lower than 1 %[G.Zschornack et al., 2009]. This value seems acceptable in terms of therapeutic dose error. However, careful consideration has to be put to take this information into account in the treatment planning software.

**Stability**

The stability of the source output is of great importance in particle therapy. Tests with EBIS-A[9] running continuously for 24 hours showed that the maximum deviations from

---

[8] private communication, Dr. Fredrik Wenander (CERN)
[9] private communication, G. Zschornack (Dreebit Gmbh)

the mean measured ion current are of about 4 %, a factor of two lower and less frequent than for ECR ion sources. It is expected that the EBIS-SC in air conditioned environment will deliver an ion current stability of ± 1 %.

The measurements on the EBIS-A revealed however the sensibility of the ion output to the setup parameters. This will have to be carefully checked with the EBIS-SC, especially since the source will have to operate at repetition rates which could be higher than the values giving saturation of fully-stripped ions.

### 4.4.2 Simulation Results

Numerical simulations were performed by Dreebit Gmbh under the assumption of an electron beam energy of 5 keV, an electron beam current of 0.99 A, and a working gas pressure of $5 \cdot 10^{-8}$ mbar. For bare carbon ion production, the results showed that the ion density inside the source increased with ionization time and saturated for ionization times over 10 ms. At this 100 Hz repetition rate, the proportion of $C^{6+}$ in the beam is just over 50 %. The source output as a function of repetition rate is shown in Fig.4.19.
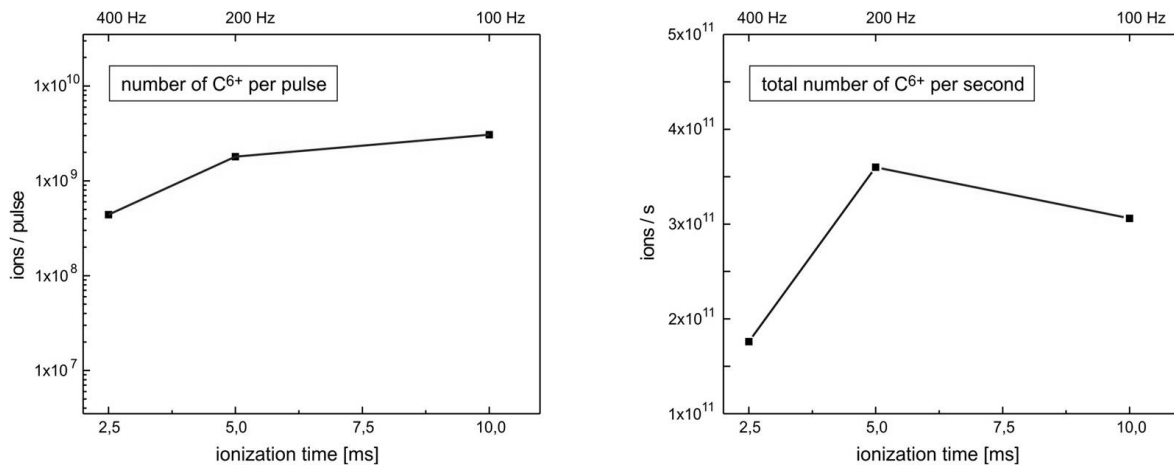


Figure 4.19: Calculated maximum number of $C^{6+}$ ions per pulse (left side) and per second (right side) for ionisation times of 2.5 ms, 5 ms and 10 ms (from private communication with G. Zschornack (Dreebit Gmbh))

The FWHM of the ion pulses can be expected to be 3 $\mu s$[10]. At 300 Hz repetition rate, the source could produce roughly $5 \cdot 10^8$ $C^{6+}$ ions in 1.5 $\mu s$. This corresponds to a factor 5 higher output than requested from the cyclinacs requirements of Tab.4.2.

### 4.4.3 First investigations

The EBIS-SC was first put in operation in January 2010 and is presently still under testing. Measurements with the EBIS-A and Krion-2 showed that the major challenge lies in the ability to produce enough carbon ions in such short ionization times (3.3 ms).

First results with the source[Zschornack et al., 2010] have recently been published. For technical reasons, these were produced with a subnominal electron current of 300 mA. According to the trap capacity expression (see Eq.4.1), the output was expected to be one

---

[10]private communication, G. Zschornack (Dreebit Gmbh)

order of magnitude higher than for EBIS-A and this was confirmed in terms of average particle flux (particles per second). For carbon ions, the optimal ionization time for 6+ charge state production was found to be 100 ms. At this 10 Hz repetition rate, the output was $1.4 \cdot 10^8$ in a pulse of 6 $\mu$s FWHM. The ejected spectrum and pulse are shown in Fig.4.20 and Fig.4.21.
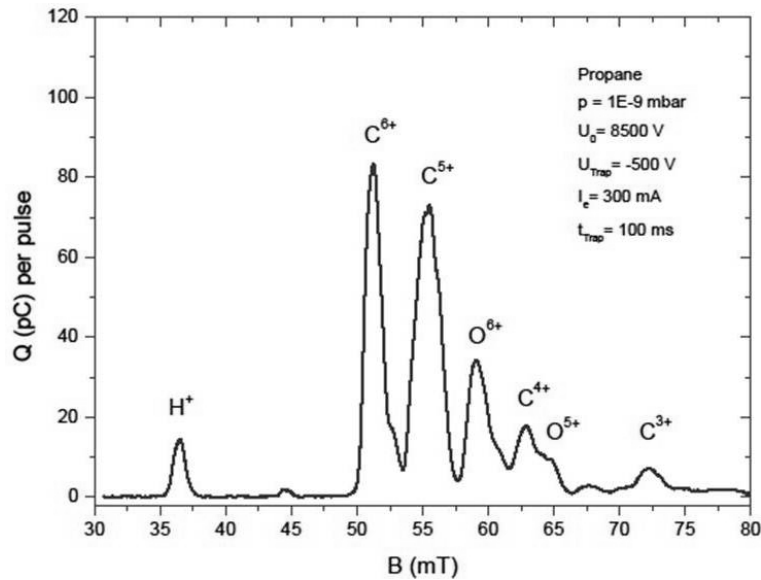


Figure 4.20: Ejection spectrum measured at an electron beam energy of 8.5 keV, an electron beam current of 300 mA and an ionization time of 100 ms[Zschornack et al., 2010]
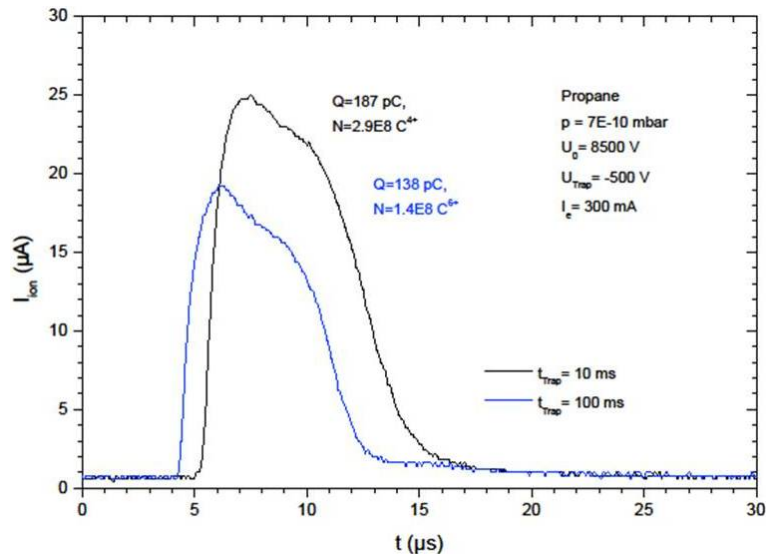


Figure 4.21: $C^{4+}$ (in black) and $C^{6+}$ (in blue) pulses at an electron beam energy of 9.2 keV, an ion start potential of 8.5 keV and at ionization times of 10 ms for $C^{4+}$ and 100 ms for $C^{6+}$, respectively[Zschornack et al., 2010]

These numbers still correspond to a factor 90 lower than the cyclinacs requirements set in Tab.4.2. The final performance of the EBIS-SC will determine the optimal repetition rate maximizing the $C^{6+}$ particle intensity. Stability, reliability and ease of use should be tested in parallel to performance, as these are crucial parameters for a medical machine.

# 4.5   Chapter Summary

The requirements on the ion sources are set by the beam losses in the cyclinac and the required clinical dose rate of 2 GyE min$^{-1}$ L$^{-1}$ at the patient. The production of $H_2^+$ is within the capabilities of a single multicusp ion source, with an appropriate system chopping the continuous beam at the required repetition rate and pulse length. The situation for carbon ions is more delicate. The beam characteristics of cyclinacs of intense pulses of bare carbon ions with short pulse lengths at fast repetition rates are not compatible with the performance of commercial ECRIS.

On the other hand, pulsed ion sources and in particular, EBIS, present many features, which match the cyclinacs requirements. Measurements on the EBIS-A source from Dreebit Gmbh showed the potential of EBIS for production of intense short ion pulses and revealed possible ways to achieve beam intensity modulation at the source level. However, tests with the Krion-2 source revealed the difficulty of producing considerable amounts of the fully stripped charge state for ionization times lower than 50 ms.

Considering the simulations and first measurements with the new EBIS-SC from Dreebit Gmbh, it is chosen to use three of these sources for CABOTO. These sources could operate at 100 Hz repetition rate in alternating mode, with a fast-switching system, connecting (and disconnecting) each source to (from) the cyclotron injection line. This choice is driven by the fact that operating the sources at lower repetition rate increases the output in terms of ions per pulse.

Chap.5 presents the design methods used to study two different cyclotrons delivering 230 MeV/u beams to be injected in CABOTO: the superconducting SC and the superconducting IC. The design methods used have the particularity of adressing all the most critical challenges related to high magnetic field cyclotrons using nearly only analytical and two-dimensional modeling. They are therefore much faster than precise three-dimensional modeling and particularly adapted for this comparative study. Applying the same design methods and constraints allows a unique quantitative comparison of these two advanced cyclotron designs.

# Chapter 5

# Cyclotron Design Methods

This chapter describes the theory and computational tools used for the designs of the SC and the IC presented in the next chapters. The designs of both cyclotrons aim at providing the machine, which is best suited to medical therapy. The underlying philosophy is, when possible, to use analytical and two-dimensional models, in order to avoid the complex and time-consuming process of three-dimensional modeling. The designs were done under the supervision of Phys. Eng. André Laisné, who shared the computational tools he developed over the years and most importantly, his solid expertise on ICs design[Laisné, 2010a] and SCs. The same constraints were applied to the two cyclotron designs, thus allowing the reliable comparison of the SC and IC designs, presented in Chap.8.

Finally, it has to be noted that these are very advanced cyclotrons designs, since the existing compact superconducting cyclotrons only reach energies up to 200 MeV/u (K1200 at Michigan State University).

## 5.1 Beam Focusing

This section describes the basic principles of the beam transverse motion in cyclotrons. The focus is on the differences between SCs and ICs. These differences have very important implications on the designs of the magnets.

### 5.1.1 Theory

A beam of particles is characterized by the parameters of its central reference particle, which defines the center of the cylindrical coordinate system used in cyclotrons. The other particles are described in terms of their deviations in transverse (radius $r$ and height $z$) and longitudinal (azimuth $\theta$) position and momentum ($p_r$, $p_z$, $p_\theta$) from this reference particle. In order to maintain these deviations in transverse motion small enough throughout acceleration, a sinusoidal periodic oscillation is induced around the reference trajectory. This is called the *betraton* motion.

The betatron tunes are the ratio of the frequency of these betatron oscillations with respect to the revolution frequency of the reference particle around the center of the cyclotron. They express the stability of the beam motion during the acceleration in

the cyclotron. The main terms of the radial and vertical betatron tunes ($\nu_r$ and $\nu_z$, respectively) are given as a function of radius $r$ in Eq.5.1. For a full derivation of these expressions, the interested reader can consult the bibliography[Scharf and Cole, 1986].

$$\begin{cases} \nu_z^2\left(r\right) = n\left(r\right) + \frac{N^2}{N^2-1}\,F\left(r\right)\left(1 + 2\tan^2\xi\left(r\right)\right) + ... \\ \\ \nu_r^2\left(r\right) = 1 - n\left(r\right) + ... \end{cases} \tag{5.1}$$

The first term in the betatron tunes equations is related to the so-called magnetic *field index n*.

$$n\left(r\right) = -\,\frac{r}{B}\,\frac{\mathrm{d}B}{\mathrm{d}r}$$

The second term in the vertical tune equation introduces the concepts of sectors (and their number $N$), spiral angle $\xi$ and *flutter F*. These parameters will be explained in the next sections.

The transverse dimension of the beam in phase space is described in terms of the beam projection in the $(r, r' = \frac{\mathrm{d}r}{\mathrm{d}\theta})$ and $(z, z' = \frac{\mathrm{d}z}{\mathrm{d}\theta})$ planes. The area occupied by the beam in these so-called *trace-spaces* is the beam emittance $\epsilon$. In the accelerator community, this quantity has different definitions and even units and this is often a source of confusion[1]. In the cyclotron designs presented in this thesis, emittances are stated in units of $\pi$ m rad, *normalized* and at *4-rms*. Using this convention, the emittance is conserved throughout acceleration as long as there is no coupling between the various two-dimensional projections of the six-dimensional phase space and the electromagnetic effects can be described by linear transformations (Gaussian optics). The rms definition of the emittance is based on the concept of an imaginary beam which has a uniform distribution within a hard-edged elliptical contour and which has the same second moments and total intensity as the real beam. The derived beam widths correspond to 2-rms of the distribution. For a Gaussian distribution, this contour contains 86.5 % of the particles.

### 5.1.2 Synchrocyclotron Case

SCs are weak-focusing accelerators where betatron focusing is achieved simply by the appropriate choice of the field index, the second term in Eq.5.1 being nought. Stable motion in both transverse planes is achieved when $n$ lies between 0 and 1. In practical terms, this means that the magnetic field is axially symmetric and that its value is slowly decreasing from the center of the magnet to the end of the pole. Since the tunes are fixed during acceleration and there is phase stability (this will be explained in the section on beam acceleration), the required precision in the magnetic field is of the order of $10^{-3}$, which is easy to realize in practice.

### 5.1.3 Isochronous Cyclotron Case

The situation for ICs is very different: by definition, particle revolution times are constant throughout acceleration. As the usual cyclotron motion equation states, the particle

---

[1]Further details on this topic can be found in the bibliography[Reiser, 2008]

angular frequency $\omega$ is proportional to its electric charge $q$ and the vertical magnetic field strength $B_z$ and inversely proportional to its relativistic mass $m_0\,\gamma$. Thus, to make the orbits isochronous, the magnetic field has to increase along the radius proportionally to the particle relativistic mass ($\langle B_z\,(r)\rangle_\theta = B_z\,(0)\,\gamma\,(r)$), as shown in Eq.5.2.

$$\omega = \frac{q\,B_z}{m_0\,\gamma} = \frac{q\,B_z\,(r=0)}{m_0} \tag{5.2}$$

The radial increase of the magnetic field corresponds to a negative magnetic field index ($n = 1-\gamma^2$) and thus results in vertical defocusing. The negative field index can however be compensated by the other terms in the expression of Eq.5.1 corresponding to two kinds of focusing: the *Thomas* focusing and the *spiral* focusing.

**Thomas Focusing**

Thomas focusing arises from an azimuthal modulation of the vertical magnetic field. The circular surface of the pole is divided in sectors, where magnet gaps have different sizes: wider magnet gap regions are called *valleys* and narrower gap regions are called *hills*, as shown in Fig.5.1.
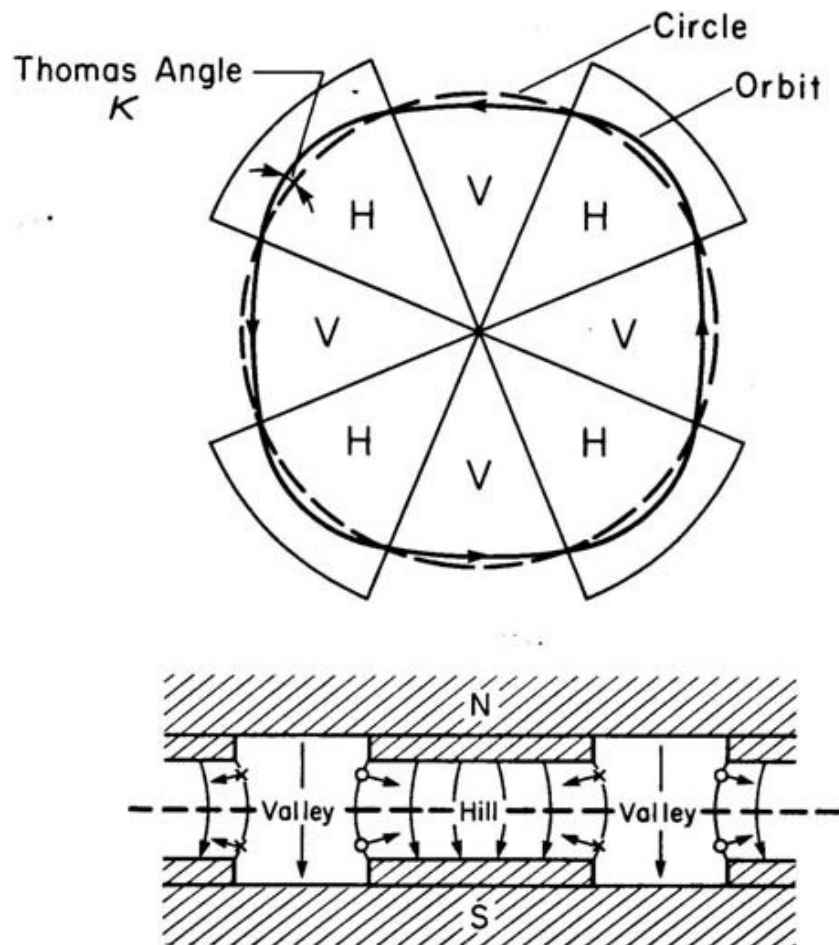


Figure 5.1: A radial-sector cyclotron pole, showing how the Thomas contribution to axial focusing arises[Craddock and Symon, 2008]

A unit of this periodic structure (one hill and one valley) is called a sector. Hills and valleys introduce an azimuthal component to the magnetic field and a radial component to the particle speed. Indeed, the magnetic field is not anymore axially symmetric and particle trajectories are not perfect circles. This orbit radius oscillation is called *scalloping*. The particle crosses the sector edges at a small angle (the Thomas angle) and a Lorentz vertical restoring force is created around the median plane at the crossing from the hill to the valley and at the crossing from the valley to the hill. This axial focusing is quantified by the flutter, which is defined as the fractional mean squared deviation of the magnetic field, as given on Eq.5.3.

$$F^2 = \left\langle \left( \frac{B(\theta)}{\langle B \rangle_\theta} - 1 \right)^2 \right\rangle \tag{5.3}$$

The number of sectors is limited by the uncrossable stopband of the intrinsic resonance $\nu_r = \frac{N}{2}$. Since the radial tune is 1 at low energy, this imposes that the number of sectors cannot be smaller than three[2].

However, the flutter is limited by the magnetic permeability of the iron and the vertical space for the beam, which limits how narrow the magnet gaps can be. Thomas focusing becomes thus insufficient at high energies, when the field index is strongly negative and/or for high central magnetic fields.

**Spiral Focusing**

When Thomas focusing is insufficient, spiral focusing is used to provide additional focusing: hills are shaped as spirals and thus, particles cross the edges of the valley/hill at modified angles, as shown in Fig.5.2.
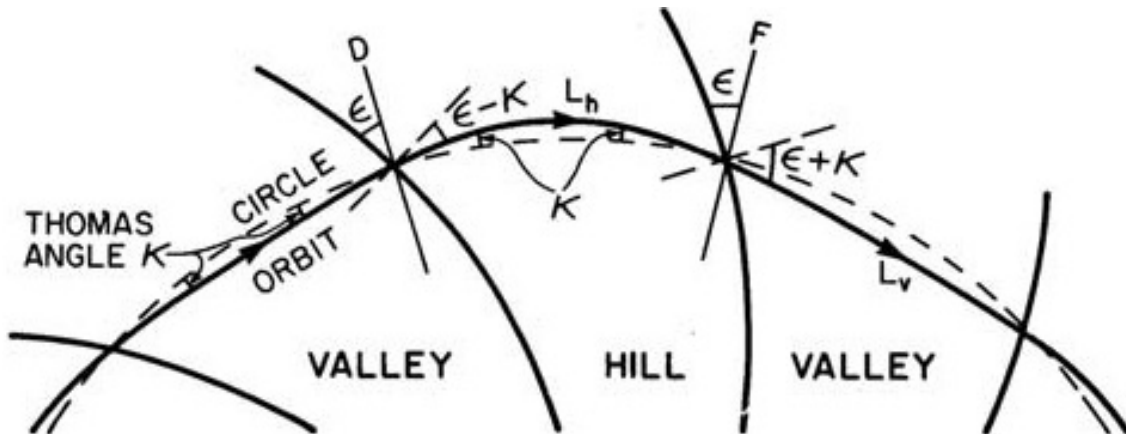


Figure 5.2: Geometry of scalloped orbits in a spiral-sector cyclotron[Craddock and Symon, 2008]

Two different parameters are used to describe this spiral shape for each radius: the spiraling angle $\xi$ and the angle $\phi$ of rotation of the hill central axis (with respect to the same axis at the machine center). They are linked by the geometric relation: $\tan \xi (r) = r \frac{\mathrm{d}\phi}{\mathrm{d}r} (r)$. An illustration is shown in Fig.5.3.

---

[2]The isochronous cyclotrons of Chap.7 and Chap.8 use four sectors. This choice will be justified in
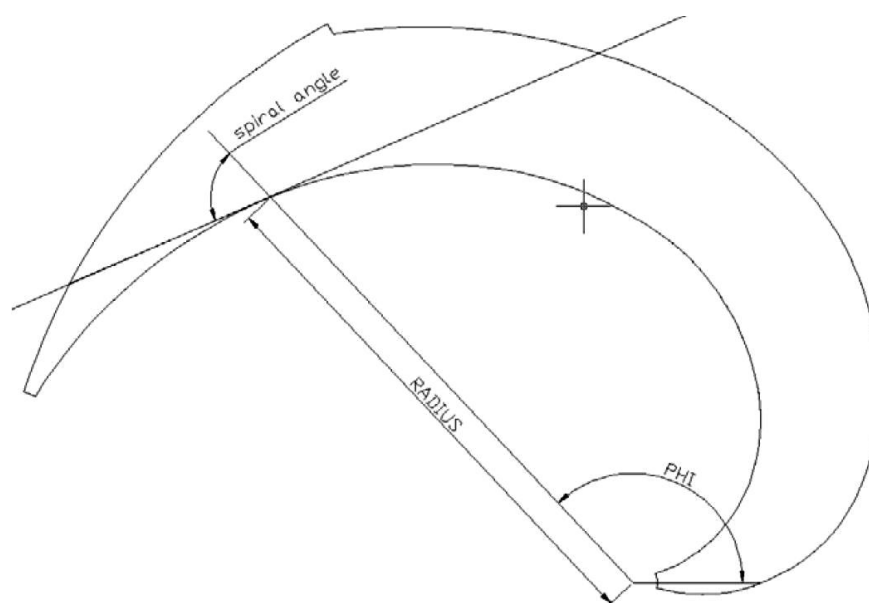
Figure 5.3: Parameters used for describing the spiraled pole sector[Calabretta et al., 2006]

Thus, one sector edge crossing will be focusing and the other defocusing but the net effect will be axially focusing: as Eq.5.1 shows, the effect of the flutter is thus doubled for a spiral angle of 35°. This comes at the expense of the complexity of the pole (whose magnetic field must be accurate to $10^{-5}$ precision) and of the RF cavity (which must fit in the free space left by the wide magnet gap of the spiraled valley).

The final magnetic field in the median plane of the cyclotron must follow the isochronous curve and can be subdivided in three contributions:

1) the magnetic field produced by the magnetized iron of the pole (whose azimuthal average remains unchanged by spiraling),

2) the magnetic field produced by the coils,

3) the magnetic field produced by the magnetized iron of the yoke.

### Universal Compact Isochronous Superconducting Cyclotron Archetype

Any cyclotron accelerating one defined ion species up to one defined energy can be considered to be derived from a *universal* cyclotron accelerating beams with $0.1 \leq \frac{q}{A} \leq 1$ up to different energies. This universal cyclotron is called the *Universal Compact Isochronous Superconducting Cyclotron Archetype*[Laisné, 1998], since it achieves many optima.

Firstly, focusing is maximized by the use of elliptical pole gaps. Secondly, isochronism is ensured by the two sets of superconducting coils: one pair of coils provides the correct radial gradient of the magnetic field, while the second pair provides the correct central magnetic field. Thirdly, magnetic flux from the iron of the pole is minimized outside of the beam acceleration region by the use of elliptical pole gaps, which reduce to a minimum the magnetic flux needed from the coils and thus minimize the size of the coils.

These concepts will be further developed in Sec.5.5 and Chap.7. A scheme of the structure of the magnet for the archetype is shown in Fig.5.4.
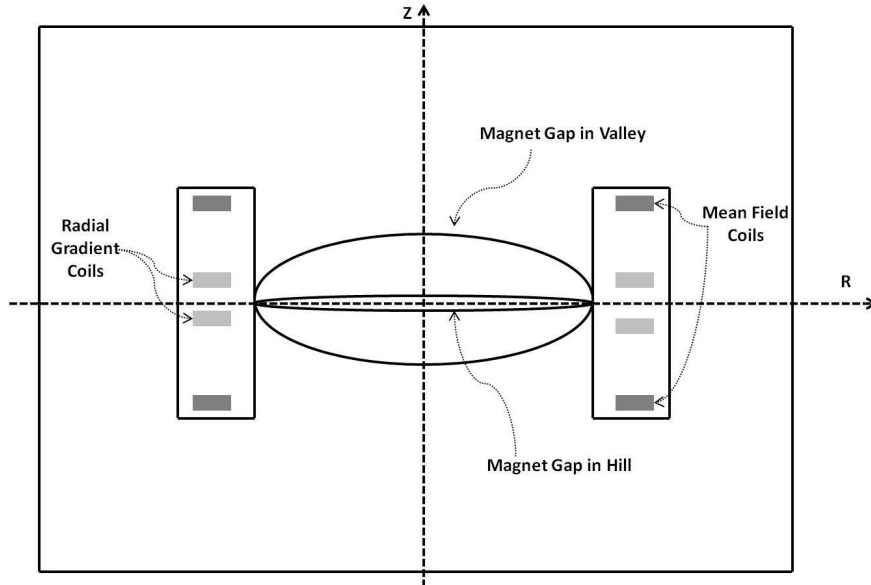


Figure 5.4: Scheme of the structure of the magnet for the archetype: the hills and valleys have elliptical pole gaps, one pair of coils provides the mean magnetic field and the second pair of coils provides the radial gradient

## 5.2   Beam Acceleration

This section describes the basic principles behind the beam longitudinal motion in ICs and SCs. As was the case for the transverse motion, the IC and the SC have very different characteristics.

### 5.2.1   Beam Acceleration in Isochronous Cyclotrons

In an IC, there is no phase stability and, in a perfectly isochronous magnetic field, a particle crosses the acceleration gaps always with the same phase of the RF sine wave. The RF cavities are located in the empty space provided by the wide magnet gap of the valleys. To obtain acceleration, the RF voltage should change sign while the particle travels in the cavity from the first gap to the second. Thus, the RF should be an even multiple of the particle revolution frequency; this multiple is called the harmonic ($h$). The kinetic energy gained after crossing one acceleration gap is given by Eq.5.4.

$$\Delta E = q\,V_{max}\,\sin\frac{h\,\alpha}{2} \tag{5.4}$$

A high acceleration voltage is essential to limit the high energy losses at ejection (as described in the next sections) and to accelerate the beam in the least possible number of turns, reducing the risk of particle losses when crossing resonances. Isochronous cyclotrons thus typically have more than one accelerating cavity and the RF system is highly power efficient (high quality factor Q). This means that high acceleration voltages can be produced (of the order of 100-200 kV peak).

Schemes of a simplified RF cavity and of the particle position with respect to the RF sine wave are shown in Fig.5.5.
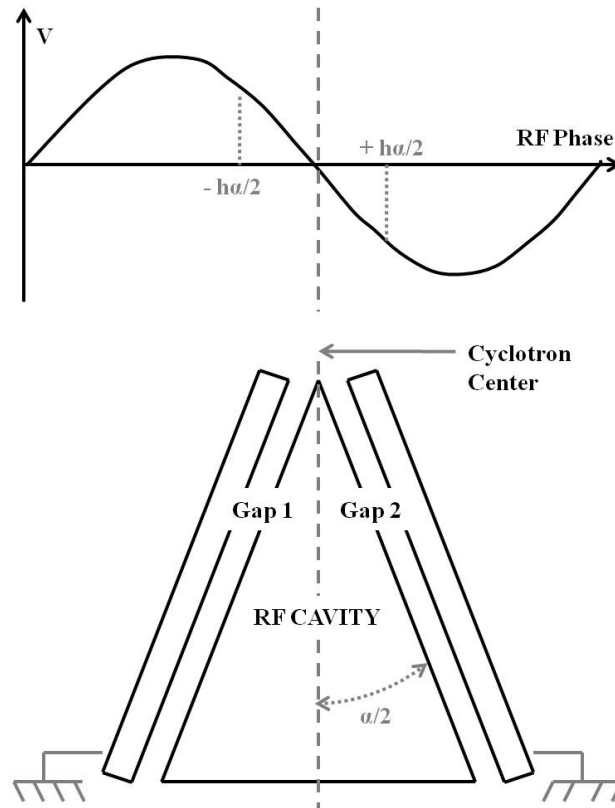


Figure 5.5: Particle crossing the sine RF wave (top) and scheme of an RF cavity in a valley (bottom)

The phase acceptance is usually $\pm$ 20° (corresponding to 11 % longitudinal acceptance). To achieve this, a phase selection is performed on the first turns at injection[Snyder, 1995], by using radial collimators called phase slits.

## 5.2.2 Beam Acceleration in Synchrocyclotrons

As explained earlier, the betatron tunes are nearly constant in SCs. Therefore, contrary to ICs, no resonances are crossed during acceleration and the number of acceleration turns is dictated by the speed of the RF modulation system.

As its name indicates, in SCs, the particle angular frequency changes during acceleration according to the particle revolution mass increase, according to the cyclotron frequency equation $\omega = \frac{q\,B_z}{m_0\,\gamma}$. The beam acceleration and the RF variation are synchronized. Indeed, the acceleration is slow enough that the RF frequency temporal variation determines the beam energy temporal variation. This defines a *synchronous* particle crossing the acceleration gaps at the synchronous phase. Other particles of the beam crossing at different phases will have slightly different revolution periods. If the phase offset is within a given interval called *bucket*, particles oscillate in phase around the synchronous particle, in the so-called *synchrotron* motion. These oscillations are very slow and synchrotron motion tunes are typically two orders of magnitude smaller than betatron motion tunes.

Particles with phases not included in the bucket will eventually be decelerated and lost in the accelerator. The RF bucket width therefore defines the phase acceptance.

Considering the special dependence of revolution frequency on radius and energy, RF buckets exist for synchronous phases between 90° and 180°[3]. A synchronous phase of 90° corresponds to the maximum beam energy gain but also to an empty bucket (nought longitudinal acceptance). On the other hand, a synchronous phase of 180° corresponds to no average beam energy gain and a longitudinal acceptance of 100 %. A popular choice in past SCs was 150°. It gave reasonable acceleration and bucket area and optimized the beam capture from the internal ion source. For illustration, the calculated RF buckets for different synchronous phases are shown in Fig.5.6. The interested reader will find a more rigorous description in the bibliography[Brück, 1966].
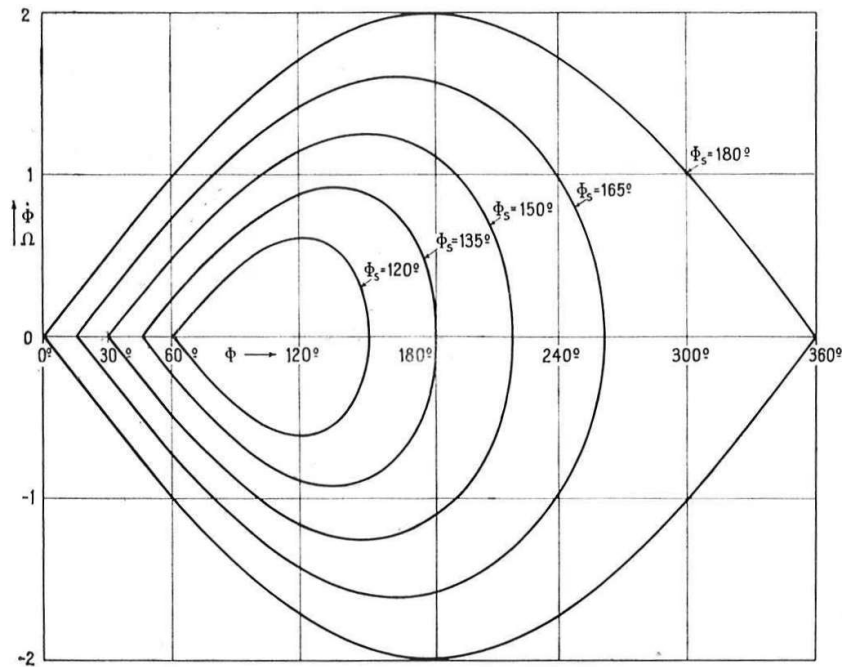


Figure 5.6: RF buckets for different synchronous phases[Brück, 1966]

## 5.3   Injection

The injection beam line consists of a dipole magnet filtering $\frac{q}{A} = \frac{1}{2}$ particles, focusing elements and a buncher tuned to the cyclotron injection RF. The buncher can increase by a factor 4 the beam longitudinal capture in the cyclotron[Calabretta and Migneco, 1984; Heikkinen, 1994]. The beam is then axially injected into the cyclotron. Its path direction needs to rotate from an axial direction to the median plane of the cyclotron. This is achieved by means of an electrostatic field provided by an inflector, as schematized in Fig.5.7.

---

[3]in the convention used, the 0° phase corresponds to the zero-crossing of the rising sine curve
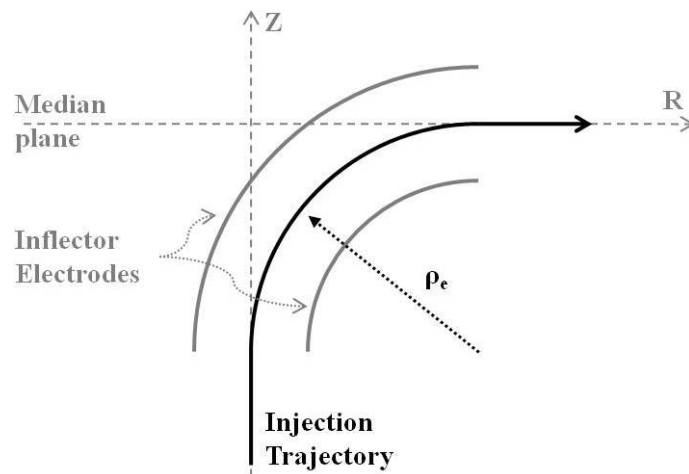
Figure 5.7: Bending of an ion beam at injection into the cyclotron (without magnetic field). $\rho_e$ is the injection electric radius

The central region of a cyclotron consists of all the elements and the conditions that allow driving the beam to the acceleration orbits. Taking aside the inflector, the main requirements to this part of the machine are the centering of the beam path curvature with respect to the cyclotron center and the beam vertical focusing.

Although various geometries for the charged electrodes of the inflector have been proposed throughout the years, the spiral inflector has proved to be the best and most popular choice, as it allows to inject the beam on axis and provides beams with good optical characteristics[Clark, 1969].

The spiral inflector is a kind of cylindrical capacitor, where the two parallel electrodes are twisted to follow the spiraled trajectory of the beam induced by the vertical magnetic field[Belmont and Pabot, 1966]. An example of these electrodes is shown in Fig.5.8.



Figure 5.8: Photograph of the K800 (LNS) spiral inflector electrodes and housing[Rifuggiato and Calabretta, 2000]. Note that $\rho_m \simeq 1.123$ cm, $\rho_e \simeq 2.7$ cm and $K \simeq 1.2$

The main parameters to describe an inflector are the electric radius (or inflector height) $\rho_e$ and the magnetic radius $\rho_m$, whose expressions are given in Eq.5.5, where $p$, $q$, $T$ are the particle's momentum, charge and kinetic energy, $B$ is the magnetic field and $E$ the electric field.

$$\begin{cases} \rho_e = \frac{2\,T}{q\,E} \\[2ex] \rho_m = \frac{p}{q\,B} \end{cases} \tag{5.5}$$

The ratio of these two radii indicates the amount of spiraling of the geometry and is called the $K$-value: $K = \frac{\rho_e}{2\,\rho_m}$. In addition, the *tilt* angle describes the rotation of the electrodes with the beam direction as axis. This is used to correct errors in the beam centering.

Another important parameter in the inflector design is the ratio between the electrode width and the gap between the two electrodes (see Fig.5.9), known as the *aspect ratio*.
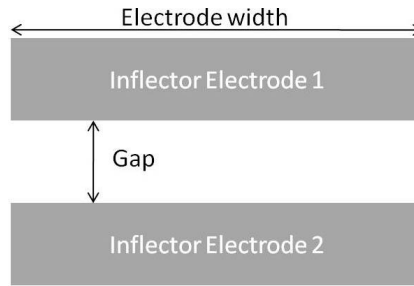


Figure 5.9: Scheme of the inflector electrodes

Spiral inflectors of superconducting machines like the K800, SCENT, C400, are designed with an aspect ratio of around 2, in order to produce a uniform electric field along the width of the electrodes, where the beam travels[Calabretta et al., 2006].

The detailed description of the beam trajectories inside the spiral inflector is complex[Toprek, 2000] and experience has shown that the spiral inflector introduces an energy spread and coupling between the transverse phase spaces. However, a careful design allows to obtain a device with a beam transmission close to 100 %.

## 5.4 Ejection

The ejection of the beam from the cyclotron is a crucial element in the design and often becomes the limiting factor in the choice of the strength of the central magnetic field or in the maximum output energy of the beam, as will be shown in Chap.6 and Chap.7. The simplicity of the ejection system is directly linked to the radial gain per turn $\frac{\mathrm{d}r}{\mathrm{d}N_t}$ of the beam at the edge of the magnet pole. As shown by Eq.5.6, this quantity depends on the radius $r$, the kinetic energy per unit mass $T$ and $\nu_r$ the radial betatron tune ($N_t$ is the number of turns).

$$\left\langle \frac{\mathrm{d}r}{\mathrm{d}N_t} \right\rangle_\theta = \left\langle \frac{\gamma}{\gamma+1}\,\frac{r}{T}\,\frac{1}{\nu_r^2}\,\frac{\mathrm{d}T}{\mathrm{d}N_t} \right\rangle_\theta \tag{5.6}$$

As introduced before, the high acceleration voltage and multiple cavities result in high beam energy gains per turn in ICs.

Many different ejection schemes have been used for ICs. The two standard methods are the use of *electrostatic deflectors* and the so-called *stripping* method.

In the former, a strong radial electric field is produced by electrostatic deflectors. This pushes the particles towards the *marginal* pole field, i.e. the region where the magnetic field radially decreases. The septum of the deflector is placed at a radius slightly larger than the one of the last acceleration orbit. A sufficient radial gain per turn avoids that particles from the next (ejection) turn hit the septum. Septa can be as thin as 0.1 mm and electric fields as high as 17 MV/m have been used[Botman and Hagedoorn, 1994; Karamysheva et al., 2010].

In the stripping method, a thin stripper foil is placed inside the cyclotron, at the position of the last acceleration orbit, to remove one or more electrons from the ions of the beam. In the case of negative ions, stripping transforms them into positive ions, whose trajectory will automatically bend out of the pole. In the case of positive ions, stripping changes their $\frac{q}{A}$ and their orbit curvature radius. By carefully adjusting stripper position and incidence angle, ions can be ejected from the cyclotron.

Upon exiting the pole, the beam passes through a series of magnetic channels. A magnetic channel is a passive magnetic device composed of iron bars which become magnetized by the magnetic field of the cyclotron and produce dipolar and quadrupolar magnetic fields which respectively, decrease locally the magnetic field to guide the particles out of the cyclotron and focus the particles to counteract the vertical defocusing arising from the strong magnetic field drop experienced by the beam at the exit from the pole. In the present designs, only quadrupolar fields are needed.

SCs have a variable RF, which most often restricts the number of cavities to one because of the problem of correctly synchronizing multiple cavities. In addition, the acceleration voltages are often limited to about 30 kV peak, because of the maximum speed of modulation of the RF frequency, the voltage limits on the RF modulator and to limit the overall RF power consumption (see Sec.6.2.3). This implies that the radial gain per turn is very small at high magnetic fields, which excludes the possibility of using the methods described earlier, as all particles would be lost on the deflector septum. Small static perturbations of the magnetic field are instead used to enhance the turn separation in the ejection region[Heikkinen, 1994; Joho, 1969; Kleeven, 2005]. Particles are forced to oscillate around their equilibrium orbit with a bump in the magnetic field where there is a resonance.

Three different schemes of resonant ejection can be distinguished. In the *brute force* ejection, the beam is ejected during the build-up of the $\nu_r = 1$ resonance by applying a first harmonic dipole bump, which determines an increase of the amplitude of coherent oscillations. In the *precessional* ejection, the process is similar but after passing this resonance, the beam is further accelerated into the fringe field of the cyclotron. Here the value of $\nu_r = 1$ drops below one. The betatron phase advance between the last two turns is substantially different from 360 degrees and a turn separation is obtained. Finally, the *regenerative* ejection is even more subtle and uses the $\nu_r = \frac{2}{2}$ resonance. This resonance is driven by a second harmonic gradient bump. This means that the perturbation should

show as a function of radius a quadrupole-like dependence (linear increase with radius). The shape of the perturbation is more critical than for the previous two methods. If the gradient is large enough, then the resonance will lock the real part of $\nu_r$ to one. The imaginary part of $\nu_r$ causes exponential growth of the betatron oscillations. When the radial gain per turn is artificially increased to the order of centimeters, magnetic channels can be introduced to guide the beam out of the pole.

## 5.5 Computational Tools

The various computational tools used for the cyclotron designs are presented in this section. The data was recorded in text files, analyzed and presented graphically with Kaleidagraph[4], Matlab or MS Office Excel. Note that the FORTRAN77 programs (OR-BLA, ANJO, NAJO, ALANEW, FIDER, Gene_a_dat, GEOPOL) detailed in this section were kindly provided by A. Laisné.

### 5.5.1 Orbit and Tracking Codes

The orbit and tracking codes used for the designs are called ORBLA and ANJO/NAJO.

ORBLA was originally written by E. Martin at the Orsay Institute for Nuclear Physics (IPNO[5]) in 1970 and later modified by A. Laisné. It is a General Orbit Code, which calculates the closed orbits on any periodic median plane magnetic field map.

ANJO and NAJO were originally developed at GANIL. ANJO tracks the median plane projection of the trajectory of a particle on any given field map, whereas NAJO extrapolates by Taylor expansion the magnetic field values in the vertical surrounding of the median plane and can thus track a beam with a given transverse emittance (by taking up to 50 particles on the contour of the trace space ellipse). Both codes allow to model the effect on the beam of electrostatic deflectors and magnetic field bumps (with libraries of tunable radial and azimuthal field shapes).

### 5.5.2 Isochronous Cyclotron Pole Design

The first and most important part of the design phase of ICs involves designing the pole of the magnet. This is done using the programs ALANEW and FIDER. The goal is to provide good focusing conditions for orbits up to the maximum energy. The programs Gene_a_dat and GEOPOL were used as tools to generate appropriate ALANEW input files and visualize the pole geometry.

A scheme of the design process steps and relative programs used is shown in Fig.5.10.

---

[4]Synergy Software, version 4.03, `http://www.synergy.com/`

[5]in French, *Institut de Physique Nucléaire de Orsay*
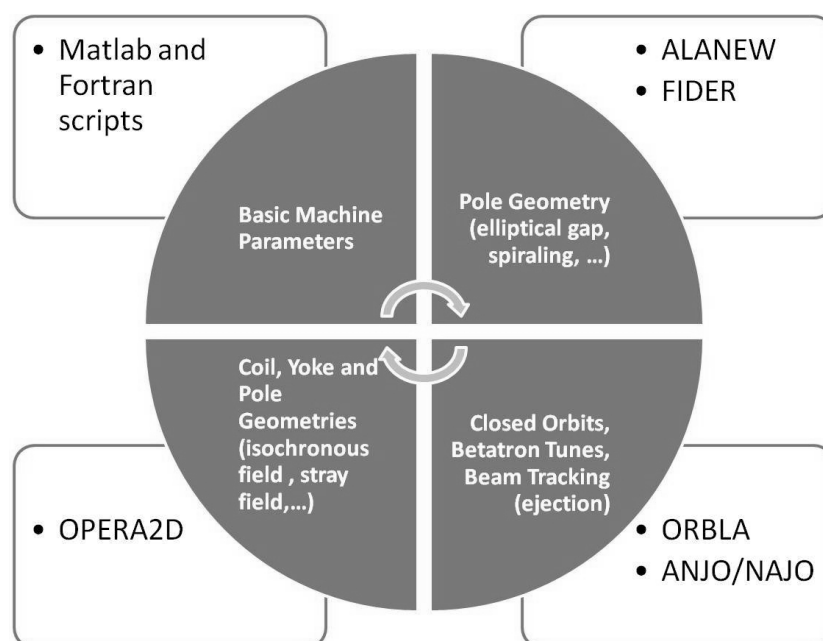
Figure 5.10: IC pole design steps and programs

**Program ALANEW**

ALANEW is written in FORTRAN77 and calculates the vertical component of the magnetostatic induction created in the median plan by a 3D distribution of horizontal magnetized surfaces. It was written by Prof. Emilio Acerbi (University of Milan), who passed it to the IPNO in 1980. Through many modifications by A. Laisné, it served as the basis for the universal compact isochronous superconducting cyclotron archetype[6][Laisné, 1998] and for the designs of the AGOR[Brandenburg and AGOR-Construction-Group, 1987; Laisné, 1981], C235 and PK210[Bieth and Laisné, 1998] cyclotrons.

The working hypothesis of the program is that the vertical component of the magnetization is known everywhere on the pole surfaces. This is where Gene_a_dat comes into play. This program creates input files for ALANEW based on the estimation of the magnetization vectors on the hill and valley. The behavior of the magnetization for many types of pole gap geometries at different central magnetic field values were carefully studied and introduced in the program.

The input file to ALANEW generated by Gene_a_dat includes information on the radial profiles of the hill and valley, divided in discrete radial steps[7] of constant magnet gap where the magnitude of the vertical magnetization vector is specified.

The program gives as output the value of the vertical magnetic field on the median plane produced by these magnetized surfaces. It allows to determine separately what are the contributions to the magnetic field, coming from the hill or from the valley. Vertical cylindrical holes through the yoke can be added to the geometry. These are used in the valleys to obtain the desired magnetic field shape and to provide an opening for the RF power, the cooling pipes and the vacuum pumping. A field map is created in polar

---

[6]see the previous section dedicated to beam focusing

[7]see Chap.7

coordinates. This *magnetic modulation* field map corresponds to the contribution of the magnetization of the iron of the pole to the total magnetic field.

The program neglects the important contributions from the iron of the yoke and the coils. However, since these contributions are azimuthally symmetric, they do not affect the pole focusing properties and can therefore be studied in a second phase of the cyclotron design.

**Program FIDER**

The knowledge of the magnetic modulation field produced by ALANEW, the central magnetic field value and the $\frac{q}{A}$ of the particles is enough to calculate the isochronous field map, following the routine of Dr. M. M. Gordon[Gordon, 1983; Gordon and Welton, 1959]. This magnetic field map is obtained without knowing if the coils and yoke can be realized but it can be used to simulate the behavior of the beam during acceleration and ejection. More precisely, it is possible to extract from the field map the values of the flutter and the betatron tunes. All of this is done by the program called *FIDER*, which reads the field map and the user-defined betatron vertical tunes as a function of radius.

When the flutter is not sufficient to produce the specified vertical focusing, a spiral angle is introduced. Thus, the final spiraled field map and hill profiles are obtained.

Finally, the program GEOPOL gives a graphical representation of the spiral shape of the hills and valleys and generates a new ALANEW input file containing the information on the spiraling of the pole, for further optimization.

## 5.5.3 Two-dimensional Magnet Design

**OPERA2D Magnetostatic Module**

The magnetostatic module of the program OPERA2D[8] is used to model in two-dimensions the magnet pole, coil and yoke. This program was chosen as it is often used for cyclotron designs and after some initial work with similar programs: POISSON[Holsinger and Halbach, 2003] and ROXIE[Russenschuck and Auchmann, 2009]. The model introduced in OPERA represents one quarter of a section of the magnet, taking advantage of the symmetries of the problem. On the median plane (planar symmetry), a *normal field* boundary condition is imposed while on the vertical axis at the center of the magnet (axial symmetry), the boundary condition is of *tangential field*.

In the case of the IC magnet, the hill and valley are introduced by defining an area whose magnetic properties reflect the fact that the structure is not azimuthally symmetric. More precisely, the region has a so-called *stacking* (or *packing*) *factor*[Zaremba, 2005] between 0 and 1, corresponding to the ratio of the hill angular width over the sector angular width and at the same time, to the ratio of the magnetization of the hill over the magnetization of a full cylinder of iron.

A screenshot of the geometry in OPERA and the magnetic field lines is shown in Fig.5.11.

---
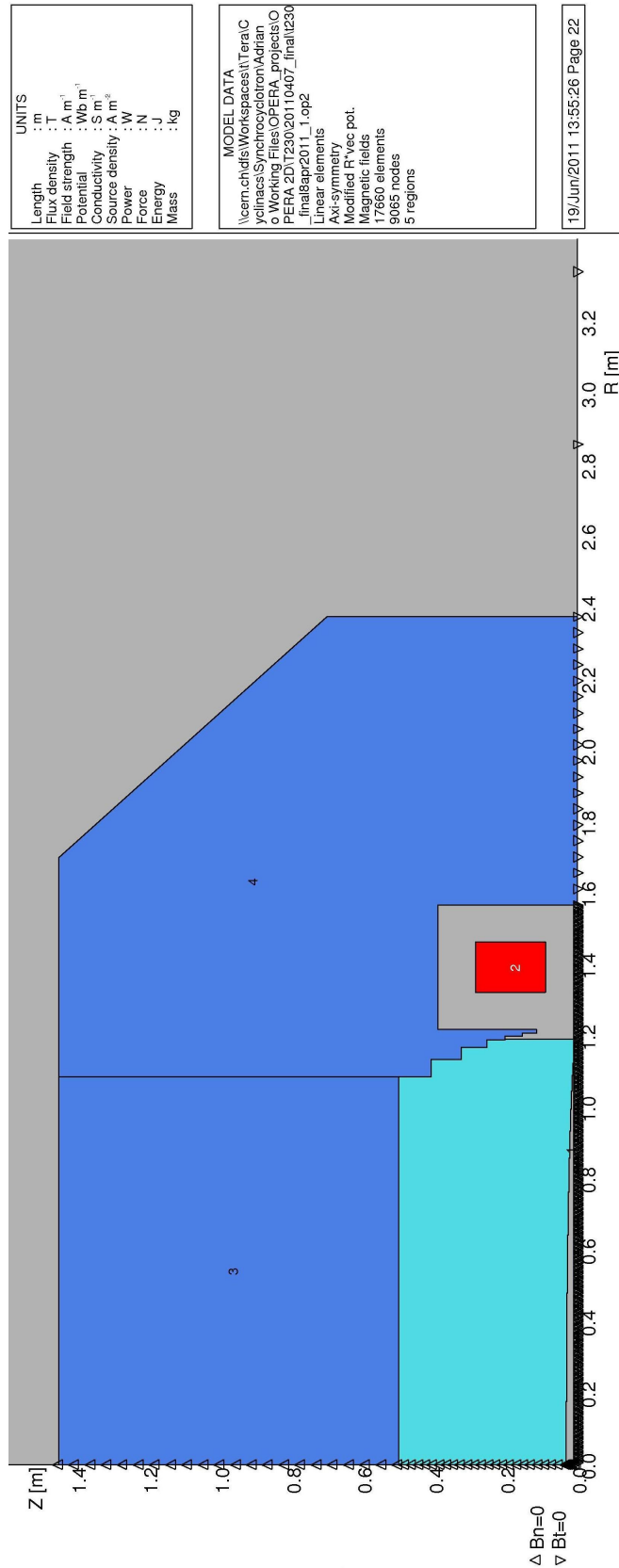
Figure 5.11: Screenshot of the geometry in OPERA. The different colors indicate materials with different magnetic properties: Armco iron (*blue*), Armco iron with reduced stacking factor (*light blue*), coil (*red*) and background (*grey*).

The iron characteristics are that of *Armco*, which is chosen because it is a low carbon content iron produced industrially in the United States, easy to manufacture and to machine. Iron choice is a compromise between purity, which ensures the best magnetic properties (maximal value of magnetization is achieved for pure iron at 2.162 T), and ease of production/machining (pure iron is very soft). The magnetization values for *Armco* are given in Tab.5.1.

Table 5.1: Magnetization values for *Armco* iron

| Magnetic Induction in Tesla | Magnetization in Tesla |
|---|---|
| 0.0000 | 0.00000 |
| 0.80000 | 0.79980 |
| 1.2000 | 1.19963 |
| 1.4000 | 1.39937 |
| 1.5000 | 1.49900 |
| 1.5500 | 1.54855 |
| 1.6000 | 1.59774 |
| 1.6500 | 1.64640 |
| 1.7000 | 1.69449 |
| 1.7500 | 1.74240 |
| 1.8000 | 1.78979 |
| 1.8500 | 1.83669 |
| 1.9000 | 1.88290 |
| 1.9500 | 1.92836 |
| 2.0000 | 1.97340 |
| 2.0500 | 2.01638 |
| 2.1000 | 2.05758 |
| 2.1500 | 2.09496 |
| 2.1750 | 2.10910 |
| 2.2000 | 2.11706 |
| 2.2500 | 2.12500 |
| 2.2800 | 2.12800 |
| 2.3060 | 2.12855 |
| 2.3443 | 2.13209 |
| 2.3996 | 2.13294 |
| 2.4905 | 2.13430 |
| 2.5627 | 2.13534 |
| 2.6706 | 2.13626 |
| 2.8498 | 2.13723 |
| 3.2074 | 2.13807 |
| 3.5644 | 2.13854 |
| 4.2782 | 2.13900 |
| 4.8134 | 2.13916 |
| 5.7052 | 2.13938 |
| 6.4186 | 2.13947 |
| 7.4887 | 2.13963 |

**Superconducting Coil**

Because of its wide-spread use, the brittle nature of $Nb_3Sn$ and the high-cost of the high critical temperature materials, NbTi is the most common choice as superconducting material for magnet coils. The choice of superconducting material dictates the critical current density inside the coil for a given maximum magnetic field. Choosing reasonable protection margins from quenches and conductor layout and materials, the maximum coil current density (including insulation) is limited to 40 $A/mm^2$. This is slightly lower than the values used for SCENT[Calabretta et al., 2006] and COMET[Negrazus et al., 2003].

A minimal physical gap of 10 cm is kept between the pole outer radius and coil inner radius, between the coil outer radius and the yoke and between the coil upper boundary and the yoke. This ensures that there is enough space to house the cryostat and the mechanical support structure for the coil. Indeed, the superconducting coil will generate high magnetic fields and strong radial and axial forces will need to be contained in order to keep the coil position stable. A study of all these forces is beyond the scope of these preliminary designs.

However, the inner mechanical stability of the coil under such strong magnetic fields has been investigated using the theory of Dr. Martin N. Wilson[Wilson, 1987]. The risk is that forces on the coil edges do not compensate each other. They can then induce tensile stress and result in inner parts of the coil to move, provoking a quench and damage. The coil shape $\alpha$ and field ratio $\beta$ of Fig.5.12 can be calculated to ensure that a situation of all-compressive inner forces is present.
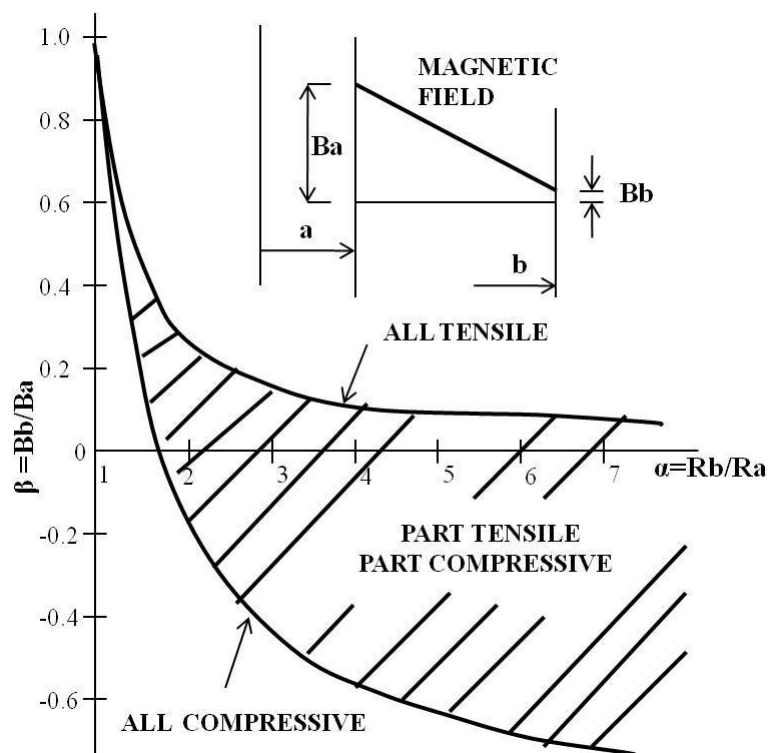


Figure 5.12: The occurence of tensile and compressive radial stress in short solenoids, as a function of coil shape $\alpha$ and field ratio $\beta$[Middleton and Trowbridge, 1968]

**Yoke**

The final dimensions (and weight) of the cyclotron depend on the limits imposed on the stray magnetic field of the magnet. There is no standard on the maximum magnetic field that can leak in the area surrounding the magnet of a cyclotron. In the designs of Chap.6-8, the magnetic field modulus is limited to 2.0 T in the inner edge of the yoke. Given the magnetization values of the iron (see Tab.5.1), the 2.0 T limit corresponds to an excitation field at the yoke edge lower than 30 mT and to a stray field just outside of the yoke lower than 50 mT. This ensures the reliable operation of the turbopumps, cryocoolers (typically limited to 50 mT[Calabretta et al., 2006]), ejection beam lines and all other hardware placed in close proximity to the cyclotron. This is a crucial point since the cyclotron will operate in a hospital environment. Note that the limit chosen on the stray field is more conservative than those chosen by SCENT[Calabretta et al., 2006] (50 mT at 1 m from the yoke) and C400[Jongen et al., 2010] (2.2 T in the inner edge of the yoke).

Finally, a practical constraint linked to transportation imposes that the length of each iron piece of the magnet does not exceed 5 m.

## 5.5.4 Magnetic Channel Modeling

The magnetic channel used for the beam ejection is modeled with a program called CANAL, written by S. Gustafsson for the design of AGOR and later modified by A. Laisné. The channel is modeled as a set of rectangular fully-saturated iron bars.

## 5.5.5 Radiofrequency Cavity Modelling

The RF cavity designs for the IC and the SC share the same methodology. The Dee[9] is the part of the cavity sitting in the magnet gap, with the magnet median plane in its middle. It is modeled as sections of coaxial transmission lines made of copper with rectangular (inner and outer conductor) cross-section. Each section is defined by four parameters ($a$, $b$, $A$ and $B$) giving the dimensions of the rectangular sides of the inner and outer conductors, as shown in Fig.5.13.
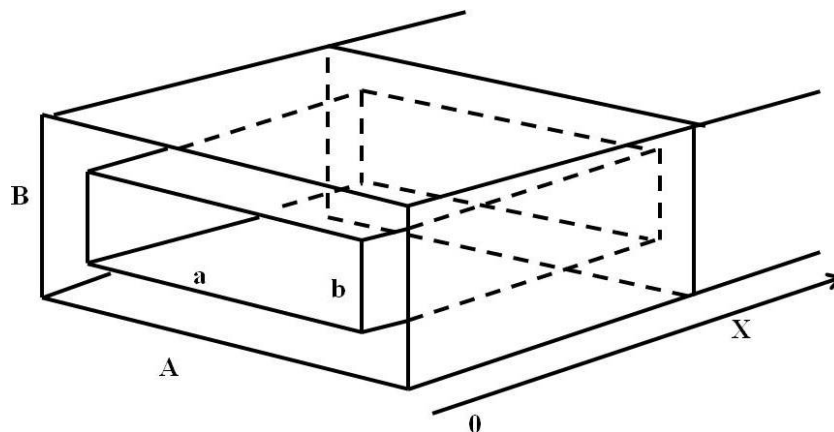


Figure 5.13: Coaxial rectangular transmission line cross-section

---

[9]The name Dee has an historical origin and relates to the shape of the first cyclotron cavities occupying half of the median plan and looking like the letter D, when seen from the top

For the characteristic impedances of rectangular coaxial transmission lines, only approximate derivations with limited validity exist[Chen, 1960; Lau, 1988] and a particular method of calculation was developed. It is explained in the next sections.

From the characteristic impedances and the length of each section, one determines the distribution of voltages, currents and impedances along the Dee. This is done using the tranformation equations for lossless lines given in Eq.5.7 for the impedance $Z$ along an electrical length $\beta\, l$.

$$
\begin{cases}
V_{i+1} = V_i \left( \cos \beta\, l + j\, \frac{Z_c}{Z_i} \sin \beta\, l \right) \\[2mm]
Z_{i+1} = Z_c \, \frac{Z_i + j\, Z_c \tan \beta\, l}{Z_c + j\, Z_i \tan \beta\, l} \\[2mm]
I_{i+1} = I_i \left( \cos \beta\, l + j\, \frac{Z_i}{Z_c} \sin \beta\, l \right)
\end{cases}
\qquad (5.7)
$$

### Isochronous Cyclotron

The RF cavity is composed of a sector electrode (Dee) and two *stems* on either side of the median plane. These form a $\lambda/2$ resonator in the vertical direction: the upper edge of the upper stem and lower edge of the lower stem are short-circuited and the maximum voltage is on the Dee at the median plane. The cavity sits in the space left free by the wide magnetic gap of the valley. It is therefore often spiraled to follow the radial shape of the valley. An illustration of this structure is shown in Fig.5.14, for a non-spiraled cavity.
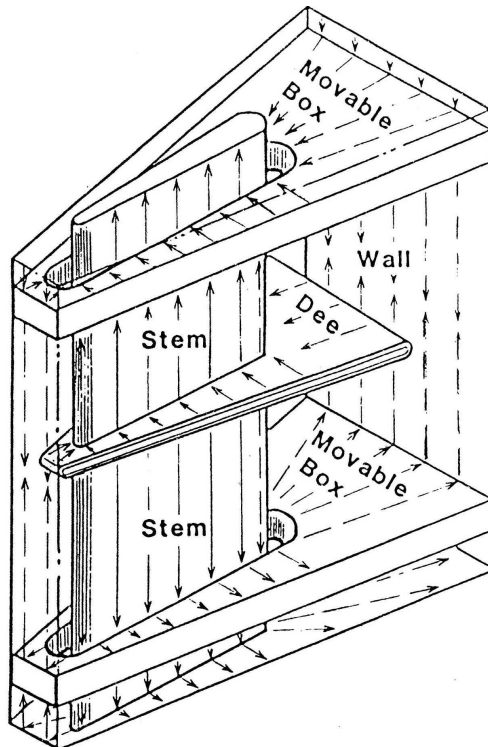


Figure 5.14: A cyclotron double gap cavity with variable frequency variation (moveable shorts), courtesy of RIKEN

Each stem is modeled as a cylindrical coaxial transmission line. The characteristic impedance $Z_c$ of the stem is then easily calculated by the exact analytical formula of Eq.5.8, where $d$ and $D$ are the inner and outer conductor diameters, $\epsilon_r$ is the relative permittivity of the space between the conductors and $\eta_0$ is the characteristic impedance of free space (equal to $120\,\pi$)[Wadell, 1991].

$$Z_c = \frac{\eta_0}{2\pi\,\sqrt{\epsilon_r}}\,\ln\frac{D}{d} \qquad (5.8)$$

The *right* extremity of the Dee (maximum radius) has a defined terminal capacitance and terminal voltage. From there, the voltages, currents and impedances at the end of each section are computed using Eq.5.7, up to the stem. The *left* extremity (innermost radius) is considered as an open circuit. The voltages, currents and impedances are calculated at the end of each section and put in parallel to the impedance of the *right* sections. The stem length required for resonance is then computed by imposing a short-circuit at its end. This model for the RF cavity is schematized in Fig.5.15. As indicated, spiraling is neglected and the stem is modeled as a single transmission line section.
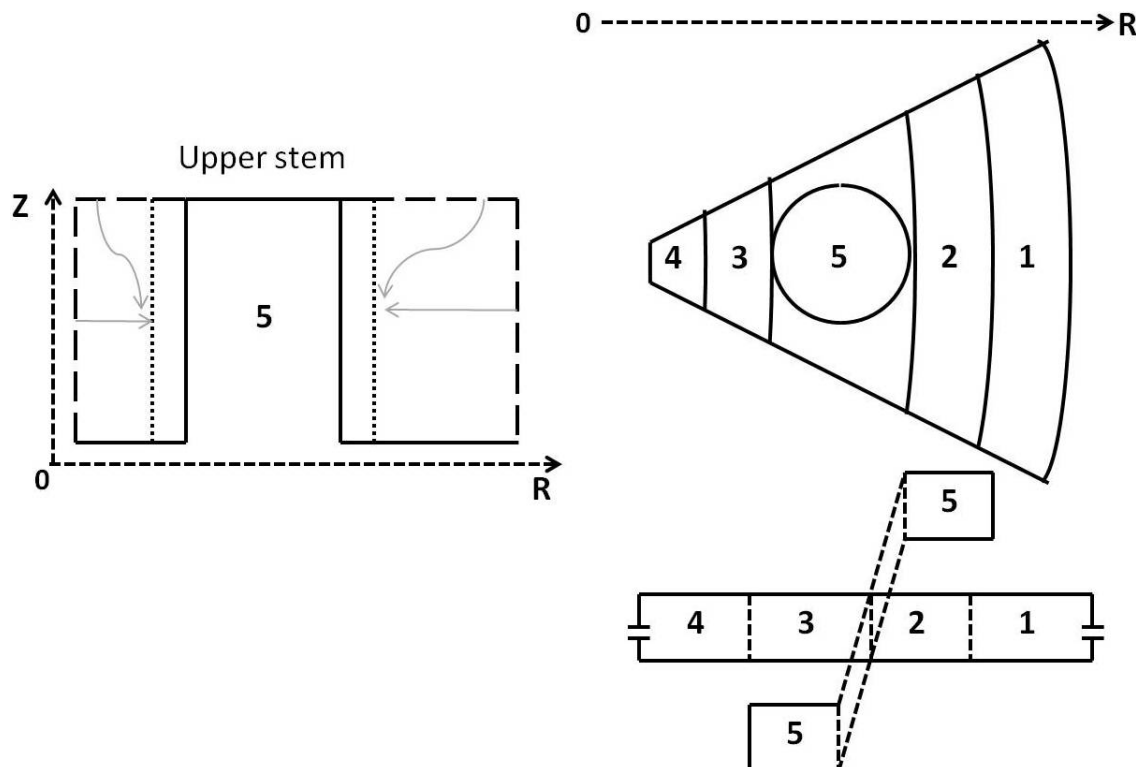


Figure 5.15: Isochronous cyclotron cavity modeled as sections of transmission lines: sections 1-4 are coaxial rectangular transmission lines (Dee) and the two sections 5 are coaxial cylindrical transmission lines (stems). The number of sections in the figure was chosen arbitrarily

**Synchrocyclotron**

The RF system is composed of a 180° Dee in the magnet gap, a rectangular coaxial transmission line through the magnet yoke and a mechanical rotating capacitor (*RotCo*). The voltage extrema are at the Dee tip, where beam acceleration occurs and at the Rotco, with a voltage node in between the two. The system thus constitutes a $\frac{\lambda}{2}$ resonator. A similar scheme used for the Orsay SC is shown in Fig.5.16.
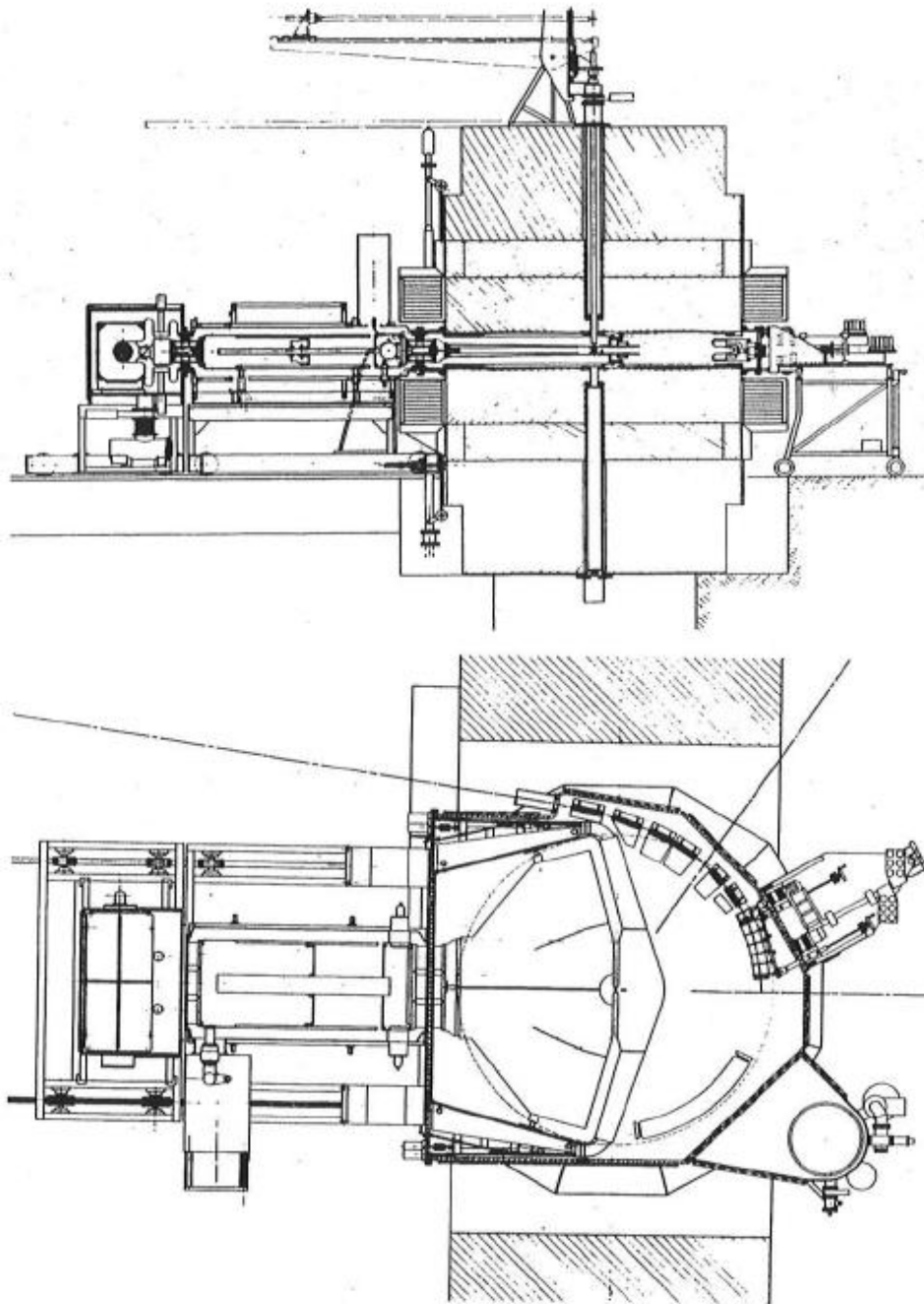
Figure 5.16: Side (shown at the top) and top (shown at the bottom) views of the RF system of the Orsay SC[Laisné, 1975]

The Dee is modeled as rectangular coaxial line segments of different characteristic impedances, connected in series, as shown in Fig.5.17.
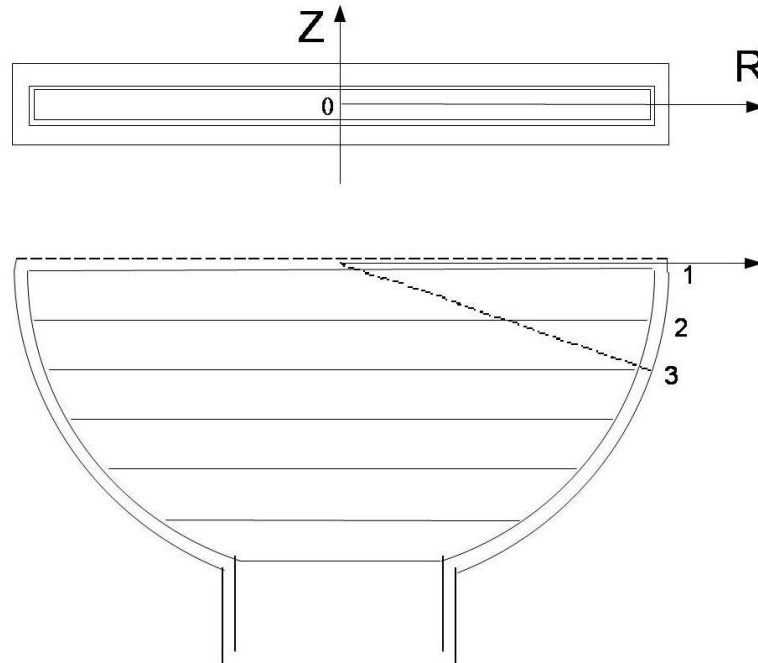


Figure 5.17: Front and top view of the 180° synchrocyclotron Dee model. Note that the aperture on the median plane is ± 1 cm

Starting from a given Dee gap capacitance, by the formula on Eq.5.7, one can compute the transformation of the impedance $Z$ along the Dee. The line length is then adjusted based on the minimum capacitance imposed on the Rotco in order to achieve resonance at the highest frequency required. Once the line length is fixed, the Rotco capacitance is increased to change the RF: the maximum capacitance corresponding to the minimal RF value.

**Analytical Derivation of the Characteristic Impedance and the Equivalent Resistance**

The following methodology was developed by A. Laisné, in collaboration with the author. The aim is to analytically assess the characteristic impedance of coaxial transmission lines, whose inner and outer conductors have rectangular cross-sections. In addition, this serves as the basis for the calculation of the power dissipation in each transmission line. For simplicity, only explanations and a few examples are given in the next section. The interested reader will find the complete derivations and expressions in the bibliography[Laisné, 2010b].

The characteristic impedance $Z_c$ of a lossless transmission line[Wadell, 1991] can be derived from the capacitance per unit length $\Gamma$ and the inductance per unit length $L$ through Eq.5.9, where $\epsilon_m$ is the medium permittivity.

$$Z_c = \sqrt{\frac{L}{\Gamma}} = \frac{120\pi \; \epsilon_m}{\Gamma} \qquad (5.9)$$

In a typical parallel plate capacitor, the capacitance is given by $\Gamma = \epsilon_m \frac{S}{g}$, where $S$ is the area of a plate and $g$ is the gap between the plates. This formula assumes that the electric field between the two plates is uniform and the fringe field is negligible. This is a valid assumption, as long as the gap between the conductors is small compared to their transverse dimension. In the case of the rectangular coaxial conductors of cyclotron cavities, the problem of determining the capacitance cannot be solved by considering four independent parallel plates because: firstly, the gap between inner and outer conductors is comparable to their transverse dimension and the inner and outer conductors have dimensions which differ by as much as a factor 20. Therefore, the capacitance coming from the corners must be somehow included.

A close-up view of the particular geometry for cyclotron cavities is shown in Fig.5.18.
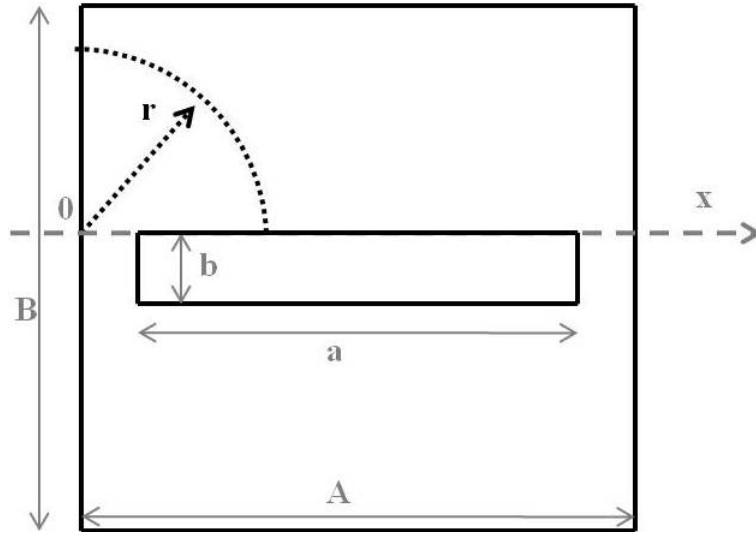


Figure 5.18: Cross-sectional geometry of a cyclotron Dee

Only geometries where $(A - a) < (B - b)$ are here considered. From the figure, it can be assumed that the capacitance arising from the electric charges on side $b$ does not depend on the size of side $B$. On the contrary, the capacitance arising from the charges on side $a$ is strongly influenced by the outer edges of side $B$. To compute the additional capacitance $\mathrm{d}\Gamma_{aB}$, the field lines between the outer edges of side $B$ and side $a$ are supposed to be circles centered on $O$. As an example, the expressions for the additional capacitance $\mathrm{d}\Gamma_{aB}$ and the capacitance on the sides $b$ are given in Eq.5.10 and Eq.5.11, respectively.

$$\mathrm{d}\Gamma_{aB} = \epsilon_m \frac{2\,\mathrm{d}r}{\pi\,r} \tag{5.10}$$

$$\Gamma_{2b} = 4\,\epsilon_m \frac{b}{A - a} \tag{5.11}$$

To evaluate the capacitance on side $a$, a distinction is introduced between three different sets of values of the geometrical parameters $a$, $b$, $B$ and $A$. These are shown in Fig.5.19.
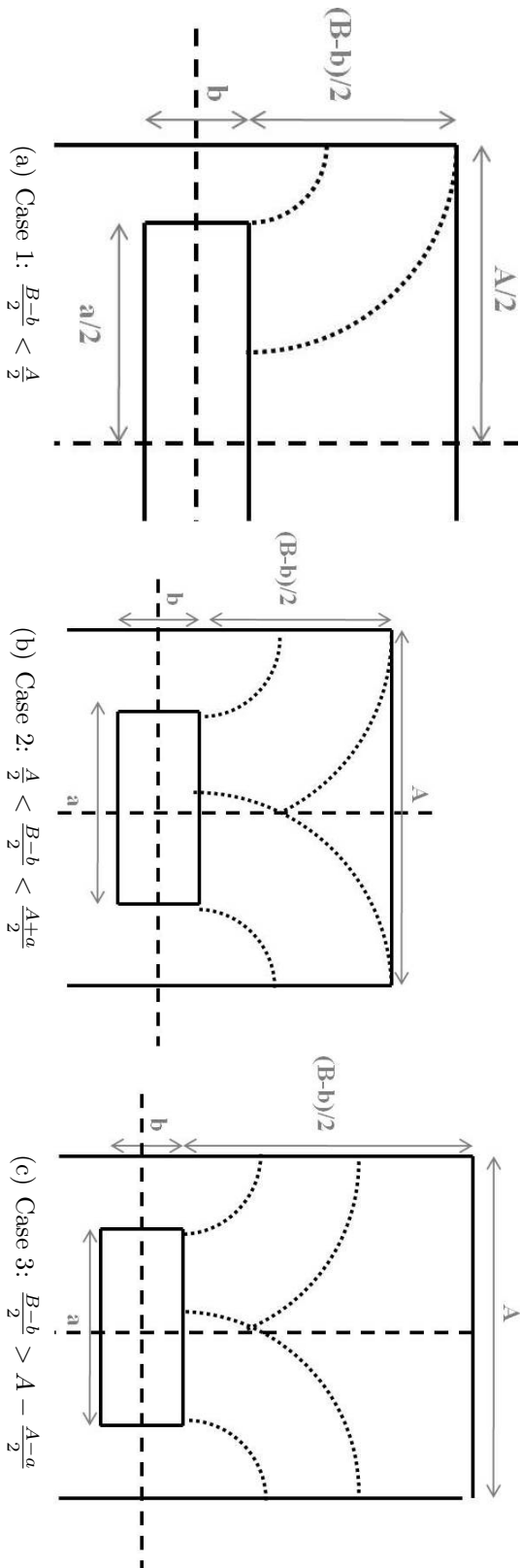
Figure 5.19: Transmission line geometries

(a) Case 1: $\frac{B-b}{2} < \frac{A}{2}$

(b) Case 2: $\frac{A}{2} < \frac{B-b}{2} < \frac{A+a}{2}$

(c) Case 3: $\frac{B-b}{2} > A - \frac{A-a}{2}$

The determination of the local capacitances $\Gamma(x)$ allows the calculation of the local current densities $J(x)$ and the local power dissipation $\mathrm{d}P$ along the width $dx$ of conductor where current $I$ is flowing, as shown in Eq.5.12.

$$\mathrm{d}P = \int R_s \, J^2 \, \mathrm{d}x = \int R_s \left(\frac{\mathrm{d}I(x)}{\mathrm{d}x}\right)^2 \mathrm{d}x = \int R_s \left(\frac{\mathrm{d}\Gamma}{\Gamma \, I}\right)^2 \mathrm{d}x \qquad (5.12)$$

Thus, as an example, the expression for the power dissipated on the sides $b$ is given by Eq.5.13.

$$\mathrm{d}P_{2b} = \frac{R_s \, I^2}{\Gamma^2} \frac{4\,b}{(A-a)^2} \qquad (5.13)$$

**Analytical Calculation of the Dissipated Power**

The computation of the power dissipated in each section of the Dee takes into account the fact that, at high frequency, the electromagnetic field penetrates only a thin layer of a conductor. This is called the *skin* effect. This layer has a depth $\delta$ given by $\delta = \sqrt{\frac{1}{\pi f \sigma \mu}}$, where $\mu$ is the permeability, $f$ the frequency of the wave and $\sigma$ the conductivity. A copper conductor at 100 MHz has a skin depth of 12 $\mu$m. Therefore, in the present case, the conductor widths are wider than the skin depth and one considers the *sheet* resistance $R_s = \frac{1}{\sigma \delta}$.

Each infinitesimal piece of conductor of the transmission line of length $\mathrm{d}x$ dissipates by Joule effect a power of $\mathrm{d}P_a = R_s \, J_{rms}^2(x) \, \mathrm{d}x$, where $J_{rms}$ is the rms current density on that section of conductor. Summing the $\mathrm{d}Pa$ for all the conductor cross-section and integrating the total section current over its length, the active power is calculated for each section. In the case of the coaxial cylindrical conductors (stem), the current distributes homogeneously and the current density is inversely proportional to the conductor radius $r$. The expression for the active power is then simply given by Eq.5.14.

$$\mathrm{d}P_a = \frac{R_s}{2\pi} \left(\frac{1}{r_{int}} + \frac{1}{r_{ext}}\right) I_{rms}^2 \, \mathrm{d}x \qquad (5.14)$$

For the dee sections, the determination of the current density is complicated by the rectangular geometry which induces strongly non-uniform current densities within the cross-section. The current density must be deduced from the local capacitances.

Finally, the infinitesimal reactive power $\mathrm{d}P_r$ is calculated from the electromagnetic energy stored in the section. The derivation is given in Eq.5.15, where $L$ is the line inductance per unit length.

$$\mathrm{d}P_r = \frac{\mathrm{d}}{\mathrm{d}t}\left(\frac{1}{2}L \, I_{rms}^2(x) \, \mathrm{d}x\right) = L \, \omega \, I_{rms}^2(x) \, \mathrm{d}x = \beta \, Z_c \, I_{rms}^2(x) \, \mathrm{d}x \qquad (5.15)$$

In the designs, the conductor material is assumed to be copper with an electrical conductivity equal to 5.8 $10^7$ S/m.

**Analytical Equations Validation**

A cross-check of the validity of the equations derived for the characteristic impedances is provided by simulations on OPERA2D Electrostatic Module. For the rectangular trans-

mission line sections, only a fourth of the geometry is modeled because of the symmetry of the problem.

Appropriate boundary conditions are introduced: the inner conductor is set at a fixed positive electrostatic potential $V$, the outer conductor is set at ground potential and tangential electric fields are imposed on the two symmetry axes. The program computes the electrostatic energy $E$ stored in the space between the conductors. From this information, the capacitance $C$ of the total cross-section is simply calculated with the expression $C = 8\,E\,V^2$ and the characteristic impedance is found.

The deviations between the characteristic impedances calculated with OPERA and those used for the designs of the IC and SC are in the range $\pm$ 8 %.

The stem geometry has also been studied. The stem is composed of a cylindrical inner conductor and a coaxial triangular shaped outer conductor, corresponding to the outer wall of the cavity. This geometry is parametrized and entered into OPERA. The parameters are the angular aperture of the cavity, the radial extent of the cavity, the inner conductor center radius and the ratio between its diameter and the azimuthal width of the cavity at this radius. Boundary conditions are used to define the inner and outer conductor potentials and the calculation of the stored electrical energy is used to compute the capacitance per unit length and the characteristic impedance, as done before for rectangular sections. A view of the geometry and the electrostatic potential lines is shown in Fig.5.20.
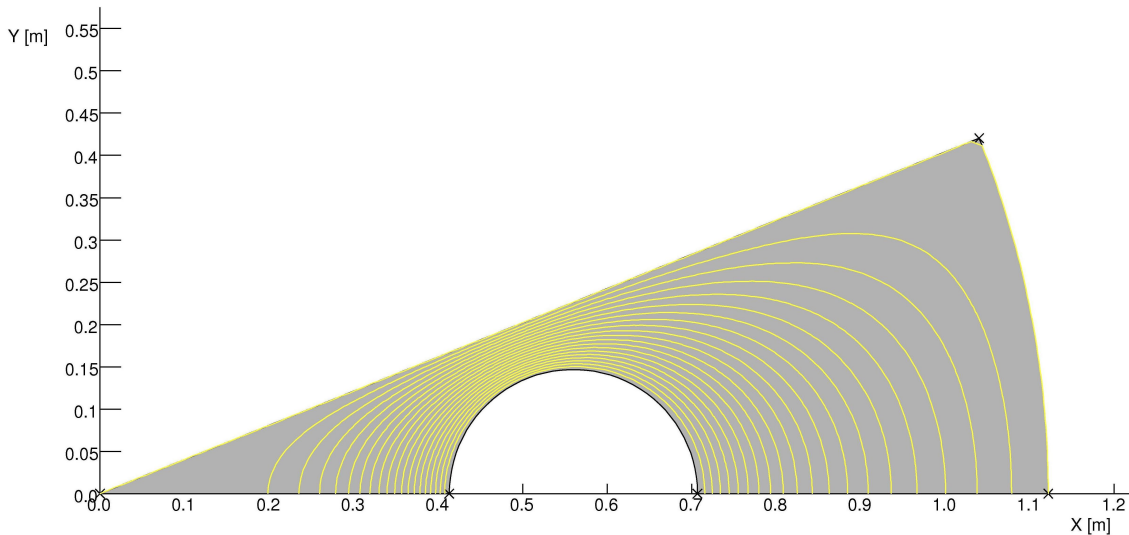


Figure 5.20: Stem cross-section, as modeled in OPERA, with electric field lines (in yellow) and space between the inner and outer conductors (in grey)

In this case, OPERA gives characteristic impedances, which differ by more than a factor two from the values used in the programs for the RF cavity design. This was expected since in the IC RF cavity design, the stem outer conductor is simplified to a cylinder, whose dimension is not related to the real geometry of the cavity outer conductor (see Chap.7).

Equivalent simulations were run with the program HFSS[10]. These confirmed the results

---

[10]Ansoft, version 11.1, `http://www.ansoft.com/products/hf/hfss/`

obtained with OPERA and gave the uncertainty of these simulations: $\pm$ 0.1 $\Omega$ (for the Dee sections) and $\pm$ 0.8 $\Omega$ (for the stem).

Since, as detailed earlier, the active power in a line section is proportional to the square of the characteristic impedance, any uncertainty on the characteristic impedance is doubled in the uncertainty of the electrical power. Thus, the uncertainty on the power calculations of the Dee sections is in the range $\pm$ 16 %.

The error on the calculation of the power dissipated in the stem is hard to estimate as the stem outer conductor geometry is over-simplified in the analytical calculation.

## 5.6   Chapter Summary

The magnets of the SC and IC are modeled in two dimensions using the magnetostatic program OPERA. This involves introducing stacking factors for the IC and an axi-symmetric pole for the SC. The IC pole design is achieved using the programs ALANEW and FIDER, allowing the introduction of elliptical pole gaps and the calculation of the sector spiraling needed to achieve adequate beam focusing. Taking into consideration the safety from quenches and mechanical viability, a limit of 40 A/mm$^2$ is chosen for the current density of the superconducting coil and adequate free space is left around the coil. Finally, to avoid problems linked to the operation of devices and the injection/ejection lines, the stray magnetic field outside the cyclotron was limited to 50 mT by imposing the maximum of the magnetic field modulus at the edge of the iron yoke to be 2.0 T. These are important considerations since the cyclotrons need to operate in hospital environments.

The RF design involves the modeling of the resonators of the IC and SC as coaxial transmission lines composed of discrete sections of rectangular or cylindrical cross-section with constant characteristic impedance. Analytical calculations used to quantify the impedance for rectangular transmission lines were developed and validated with OPERA and HFSS. The RF design method gives more accurate estimations for the SC than for the IC, as the geometry of the stem in the IC is over-simplified in the model used.

Therefore, the design method chosen cannot compete in terms of precision and realism with respect to three-dimensional simulations. However, it constitutes a powerful tool for an estimation of the RF parameters, as part of a preliminary appraisal of the problems and is therefore well adapted for the present study. Appropriate scripts were therefore implemented in Matlab and used for the design of the SC, presented in Chap.6 and the design of the IC, presented in Chap.7.

# Chapter 6

# 230 MeV/u Synchrocyclotron Design

The SC is a weak-focusing accelerator and the absence of azimuthal field variation means that there is no limitation linked to iron saturation: as far as beam focusing is concerned, very high central magnetic fields can be used, thus reducing the dimensions of the cyclotron. Although this kind of accelerator dates back to the early cyclotron research at Berkeley, it has recently regained interest for its potential application to protontherapy[Antaya, 2009; Wu, 1990]. The same reasons that led to their replacement by ICs as nuclear physics research accelerators make them suitable for hadrontherapy. Indeed, a fast-cycled beam is ideal to implement a multipainting spot-scanning dose delivery (see Chap.1). Given all these favorable characteristics, the preliminary design of a SC delivering 230 MeV/u beams of $C^{6+}$ and $H_2^+$ was made. The design is presented in this chapter.

To illustrate the typical characteristics of a SC, the technical parameters of the Orsay SC are presented in Tab.6.1. This accelerator has been in operation for nearly 20 years at the Orsay Protontherapy Center (CPO[1]) and was only recently replaced by a more modern cyclotron.

---

[1]in French, *Centre de Protonthérapie d'Orsay*

Table 6.1: Parameters of the Orsay SC. Note that these values were compiled from various sources and should be taken as indicative

| Accelerated Particle | Proton ($H^+$, $\frac{q}{A} = 1$) |
|---|---|
| Central Magnetic Field | 1.6 T |
| Number of Sectors | none |
| Pole Radius | 1.6 m |
| Central Vertical Gap | $\pm$ 20 cm |
| Betatron Radial Tune | 0.96 |
| Betatron Vertical Tune | 0.2 |
| Yoke Diameter | 7.5 m |
| Yoke Height | 4 m |
| Iron Weight | 1000 tons |
| Number of RF cavities | 1 |
| RF Harmonic Mode | 1 |
| Peak Voltage at Injection | 28 kV |
| Peak Voltage at Ejection | 28 kV |
| RF Modulation | 19-26 MHz |
| RotCo Capacity Range | 90-520 pF |
| Max. Voltage on the Rotco | 40 kV |
| Repetition Rate | 430 Hz |
| Installed RF Power Supply | 25 kW |
| Ion source | Internal |
| Ejection Method and Efficiency | Resonant , 75 % (Magnetic Bump and Electrostatic Deflector) |
| Magnetic Bump Amplitude and Azimuthal Width | 0.4 T and 5° |
| Total Beam Transmission | 75 % |
| Output Kinetic Energy | 200 MeV |

# 6.1   Magnet Design

## 6.1.1   Design parameters

As stated in Chap.5, vertical and radial betatron tunes $\nu_z$ and $\nu_r$ are fixed by the magnetic field index, which has to be between 0 and 1. No sectors are needed for focusing and the magnet can therefore be axisymmetric. This makes magnet modeling and construction

much simpler than for ICs.

The central magnetic field value is empirically chosen to be 5 T. The aim is to reduce the magnet dimensions (the ejection radius is then around 1 m, similar to the one of C235), while keeping injection and ejection feasible[Wu, 1990].

The stability of $H_2^+$ under such a high magnetic field has been studied: an electromagnetic dissociation of the electron can indeed occur due to the transformation of the magnetic field into an electric field in the rest frame of the ion at relativistic energies. The binding energy for the last electron is around 3 eV for dihydrogen and the dissociation probability is estimated to be within the limits set by existing $H^-$ accelerators[Calabretta et al., 2011; Calabretta and Rifuggiato, 1998]. An additional phenomenon is the beam loss at low energy due to the molecular vibrational states produced in the ion source. These are all current research topics as no experimental data is yet available.

The vertical betatron tune is set to an average value of 0.14. The magnet is designed using the magnetostatic module of OPERA2D (see Chap.5), with an axial hole of 2.5 cm radius for the beam injection. Each component of the model is detailed in the next subsections.

### 6.1.2 Pole Design

The final magnetic field and the relative magnetic field index are shown in Fig.6.1.
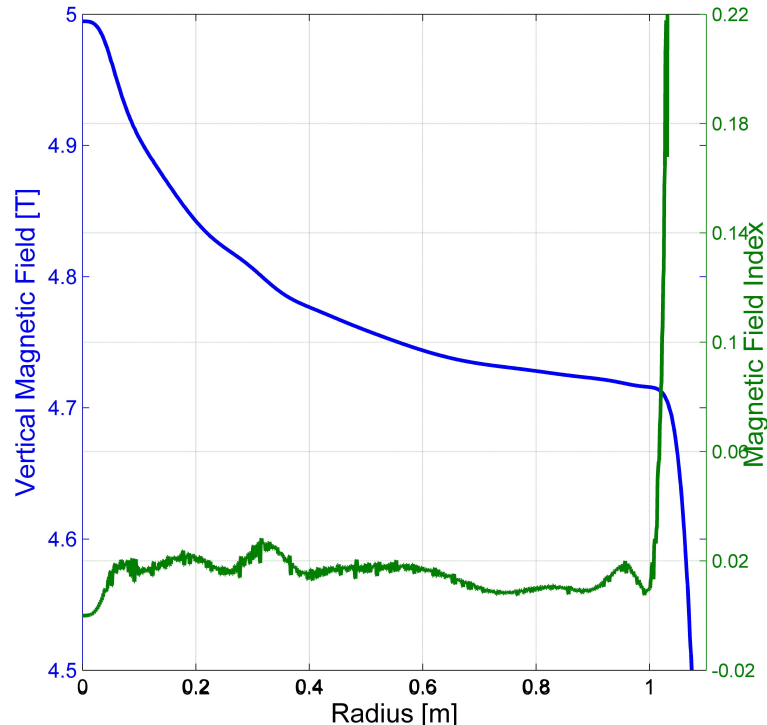


Figure 6.1: Median plane vertical magnetic field profile and relative field index. Note that the fluctuations in the field index curve are due to the modelization of the pole profile as discrete points connected with straight lines and the discrete calculation of the radial derivative of the magnetic field

It has to be noted that at 5 T central field value, the magnetic field contributions from the coil and from the pole have equal magnitude. This makes the magnet pole gap design quite delicate and the shape of the pole has to be adjusted with submillimeter precision. The geometry can only be defined by trial-and-error and this process was very time-consuming.

The field index is kept as constant as possible at the value 0.02, to satisfy the vertical betatron constraint. A safe margin from the Walkinshaw coupling resonance ($\nu_r = 2\,\nu_z$, corresponding to a field index of 0.2) is taken at the pole edge, as this constitutes a practical acceleration limit for SCs. Indeed, the equilibrium orbit at 230 MeV/u lies at a radius of 0.992 m but the pole radius is 1.075 m.

Finally, the magnet gap has been chosen to be at least $\pm$ 5 cm, to leave space for the accelerating cavity.

### 6.1.3 Coil

The coil starting shape has a similar rectangular aspect ratio as other superconducting SC designs[Antaya, 2009; Wu, 1990]. The coil current is determined by iteration until reaching 5.0 T at the center of the magnet. All these parameters are then varied to find the best compromise between a radially flat coil contribution (to obtain a flat magnetic field on the median plane) and a coil placed not too far from the pole and the median plane (to limit the total current needed in the coil and the yoke dimensions). This was done in parallel to the pole optimization.

In the final configuration, the coil centroid lies at a radius of 1.23 m and a height of 0.25 m from the median plane. With a coil radial width of 14 cm and vertical width of 34 cm, a total of 1.9 Million Ampere turns per coil are required to produce the correct central magnetic field. In addition, the maximum magnetic field in the coil is 4 T, which is safely lower than the critical field of 10 T at 4.5 K.

The pattern of the magnetic field lines in the coil region is shown in Fig.6.2. The inner radial edge $R_a$ is subject to an average magnetic field $B_a$ of -3.8 T, whereas the outer radial edge $R_b$ experiences an average field $B_b$ of 0.06 T. Computing the coil shape $\alpha = \frac{R_b}{R_a} \simeq 1.1$ and $\beta = \frac{B_b}{B_a} \simeq -0.016$ and using Fig.5.12, it has been assured that the inner forces due to the strong magnetic field on the coil are radially compressive, and thus, that the inner mechanical structure of the coil is stable.

### 6.1.4 Yoke

As detailed in Chap.5, the maximum magnetic field modulus in the yoke edge is 2.0 T and the stray magnetic field is lower than 50 mT. The yoke diameter is 4.6 m and the yoke height is 3.3 m. The iron pieces of the magnet are therefore within the practical limit for transportation of 5 m.

The main parameters of the magnet geometry introduced in OPERA2D are summarized in Fig.6.3. Using an iron density of 7.87 tons/m$^3$, the cyclotron iron weight is 335 tons. The different stacking factors linked to the holes for the RF line, the vacuum pumps, the instrumentation and the beam ejection pipe have been omitted. The iron volume calculated can thus be considered as an upper boundary to the real final iron volume of the cyclotron.
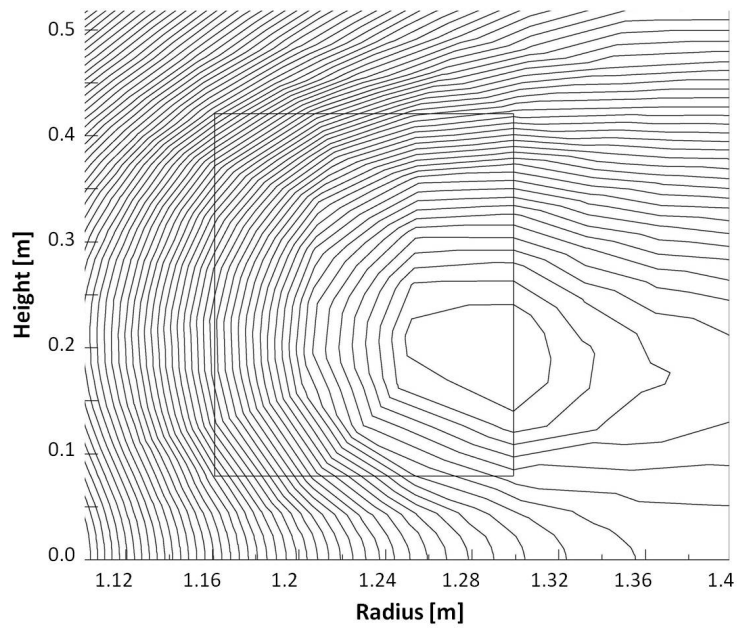
Figure 6.2: Magnetic field lines in the region around the coil
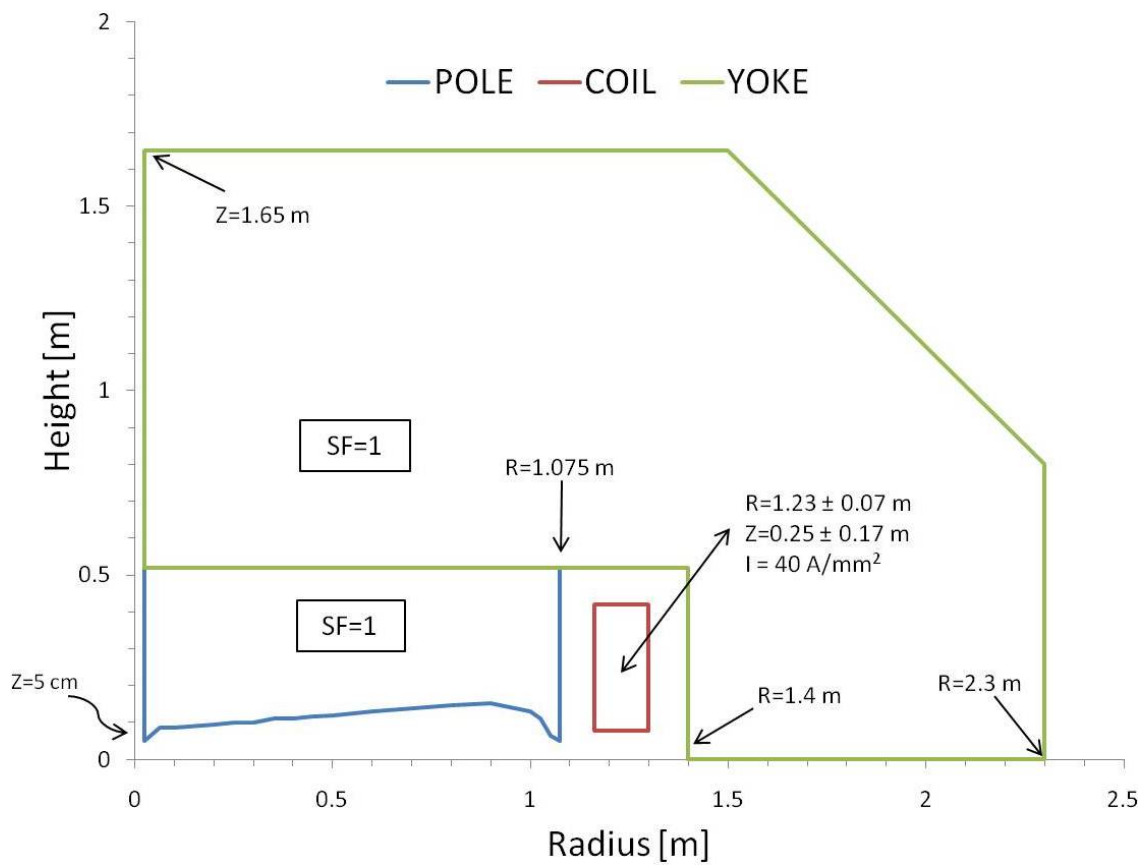


Figure 6.3: Scheme of the SC magnet geometry (SF stands for stacking factor)

## 6.2   Radiofrequency Design

The SC operates in first harmonic at a repetition rate of 300-500 Hz. The RF system is composed of: the Dee, the transmission line(s) and the RotCo. The last element provides a mechanical modulation of the line terminal capacitance and thus changes the resonant RF (see Sec.6.2.3). Indeed, as the revolution frequency decreases inversely proportional to the relativistic mass of the particle, the RF has to be modulated by 20 % from injection to ejection.

As detailed in Chap.5, the 180° Dee is modeled as sections of coaxial transmission lines, with rectangular inner and outer conductors, connected in series, as shown in Fig.6.4 and Fig.6.5.
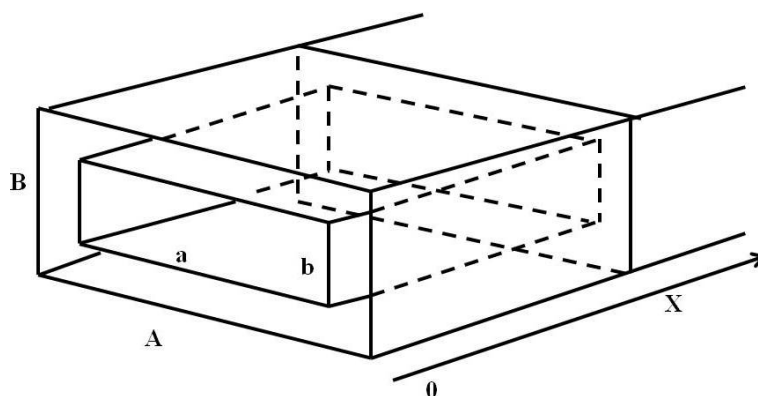


Figure 6.4: Transmission line cross-section
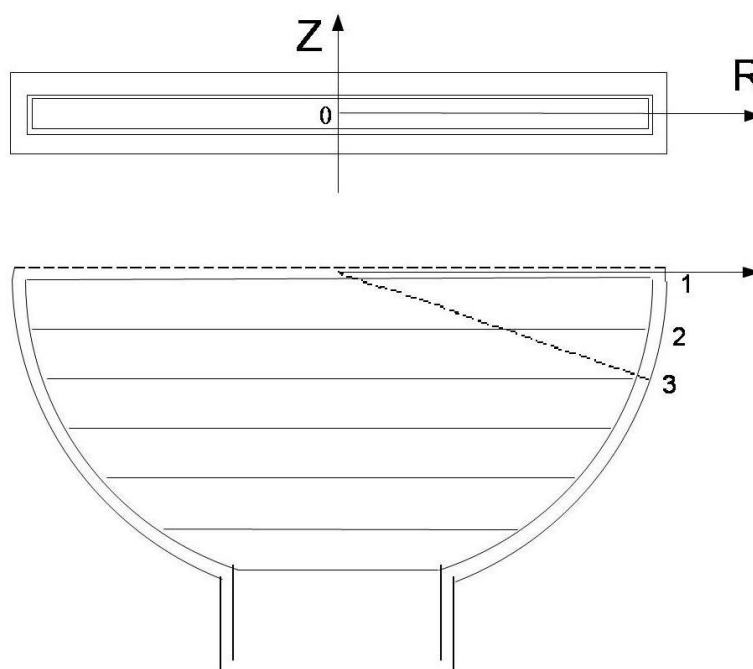


Figure 6.5: Front and top view of Dee model. Note that the aperture on the median plane is ± 1 cm

## 6.2.1 Constraints on the Parameters

The parameters for the RF system are iteratively adjusted with the following constraints:

- the RF system must resonate at frequencies ranging from 38.4 MHz (injection) to 30.2 MHz (ejection).

- the Dee should provide 20 kV rms voltage on the accelerating gaps.

- the Dee electrodes have a thickness of 6 mm. They are vertically separated by 2 cm to leave space for the beam. This corresponds to setting $b = 3.2$ cm.

- the minimum vertical distance between the Dee outer conductor and the iron of the poles is 3 mm. The minimum magnet gap is $\pm$ 5 cm. This corresponds to setting $B = 9.4$ cm.

- The Dee accelerating gap capacitance is set to 60 pF, corresponding to an accelerating gap of 5 mm. This remains 25 % lower than the Kilpatrick limit.

- the accelerating gaps extend radially up to 1.04 m and the radial distance between the inner and outer conductors is 4 cm. This value is set constant for all the Dee.

- the vertical space between the two coils is 16 cm. Taking into account the space for the cryostat, the vertical space for the RF line is limited to $\pm$ 5 cm.

- the yoke starts at a radius of 1.4 m. After this radius, there are no physical obstacles limiting the size of the RF line.

## 6.2.2 Optimized Design

The parameters for the transmission line from the Dee to the Rotco are given in Tab.6.2. The line is split in two: the first part joins the last section of the Dee to the second (and longest) part of the transmission line, which is optimized to provide the best capacity range (and peak voltages) on the Rotco. Special attention is taken to limit as much as possible the vertical space occupied by the line as it must fit in the vertical space between the two coils.

Table 6.2: Transmission line sections parameters

|   | Center Position [cm] | Length [cm] | a [cm] | b [cm] | A [cm] | B [cm] | $Z_c$ [Ω] |
|---|---|---|---|---|---|---|---|
| 11 | 140.0 | 35.0 | 51.8 | 3.5 | 65.3 | 7.7 | 8.0 |
| 12 | 313.0 | 173.0 | 40.0 | 3.8 | 65.0 | 6.0 | 5.7 |

The parameters of the 10 Dee sections are given in Tab.6.3. The first section is connected to the Dee gap where the acceleration takes place. The last section is close to the end of the pole and connected to the RF line that goes between the coils.

Table 6.3: Dee sections parameters

| | Center Position [cm] | Length [cm] | a [cm] | b [cm] | A [cm] | B [cm] | $Z_c$ [$\Omega$] |
|---|---|---|---|---|---|---|---|
| 1 | 10.5 | 10.5 | 207.7 | 3.2 | 209.7 | 9.4 | 2.6 |
| 2 | 21.0 | 10.5 | 205.6 | 3.2 | 207.6 | 9.4 | 2.7 |
| 3 | 31.5 | 10.5 | 201.3 | 3.2 | 203.3 | 9.4 | 2.7 |
| 4 | 42.0 | 10.5 | 194.7 | 3.2 | 196.7 | 9.4 | 2.8 |
| 5 | 52.5 | 10.5 | 185.5 | 3.2 | 187.5 | 9.4 | 2.9 |
| 6 | 63.0 | 10.5 | 173.4 | 3.2 | 175.4 | 9.4 | 3.1 |
| 7 | 73.5 | 10.5 | 157.6 | 3.2 | 159.6 | 9.4 | 3.4 |
| 8 | 84.0 | 10.5 | 136.9 | 3.2 | 138.9 | 9.4 | 3.9 |
| 9 | 94.5 | 10.5 | 108.6 | 3.2 | 110.6 | 9.4 | 4.8 |
| 10 | 105.0 | 10.5 | 63.6 | 3.2 | 65.6 | 9.4 | 7.5 |

The voltages along the line are shown in Fig.6.6 and the final parameters computed for the whole RF system are shown in Tab.6.4.
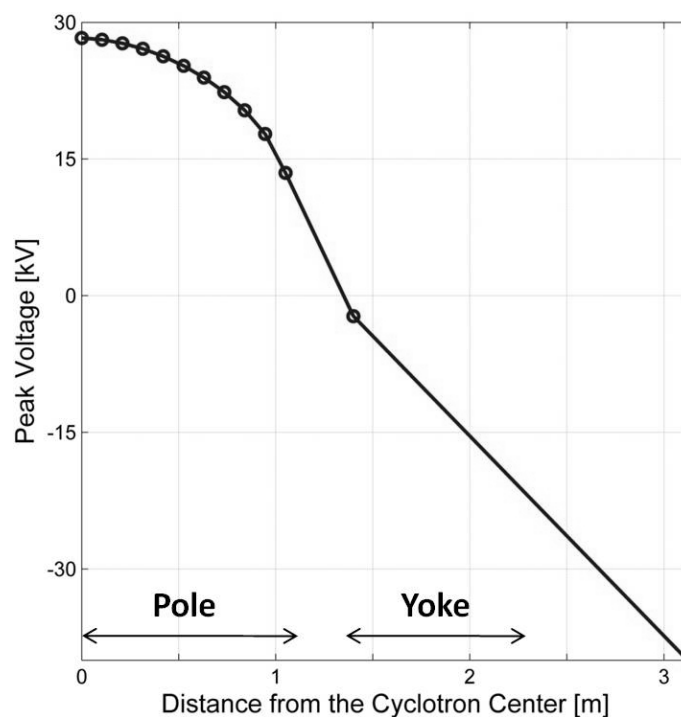


Figure 6.6: Peak voltages along the RF line for the highest (injection) RF

Table 6.4: RF system parameters

| Resonant Frequency | 38.4 MHz | 30.2 MHz |
|---|---|---|
| Peak Voltage on the RotCo | -40 kV | -27 kV |
| Capacity on the RotCo | 90 pF | 800 pF |
| Quality Factor | 2600 | 2300 |
| Dissipated Power | 37 kW | 23 kW |

As expected, the power consumption is very low. Taking into account the different power consumption for each resonant frequency, a power supply of only 30 kW is required.

### 6.2.3 Frequency Modulation

**Principle**

The cavity RF needs to be modulated by 20 %, from 38.4 MHz at injection to 30.2 MHz at ejection. This variation of frequency corresponds to a variation of stored energy in the cavity, which can be changed either capacitively or inductively. Capacitive tuning can only be achieved by mechanical means since no static components are known to vary capacitance at high power. An example of these are Rotcos. A picture of the RotCo used for many years for the Orsay SC[Laisné et al., 1979] is shown in Fig.6.7.



Figure 6.7: Picture of the Orsay RotCo (courtesy of Marco Di Giacomo, GANIL)

RotCos are large and delicate rotating mechanical structures. Indeed, electrical sparks between capacitor plates and movable electric connections have often been the source of shutdowns.

The calculated parameters for the capacity modulation of Tab.6.4 can be compared to the specifications of the Orsay RotCo. The range of capacitance modulation is wider in the present design and this would correspond to enlarging the surface of the rotor and

stator plates by 54 %. Alternatively, the gap between rotor and stator could be reduced by 35 %, combined with higher vacuum pumping to decrease the risk of sparks.

As an alternative, inductive tuning can be achieved electronically with the use of ferrites. This is typically done in RF cavities of synchrotrons and FFAGs[2][Schnase, 2000]. The end of the line is loaded with ferrites, providing a variable terminal inductance to the line and changing its resonant frequency. Indeed, as shown in Fig.6.8, the incremental permeability $\mu_r = \frac{B_{ac}}{\mu_0 H_{ac}}$ (linked to a small rapidly varying RF magnetic field $H_{ac}$) varies when the operating point on the hysteresis curve is moved.
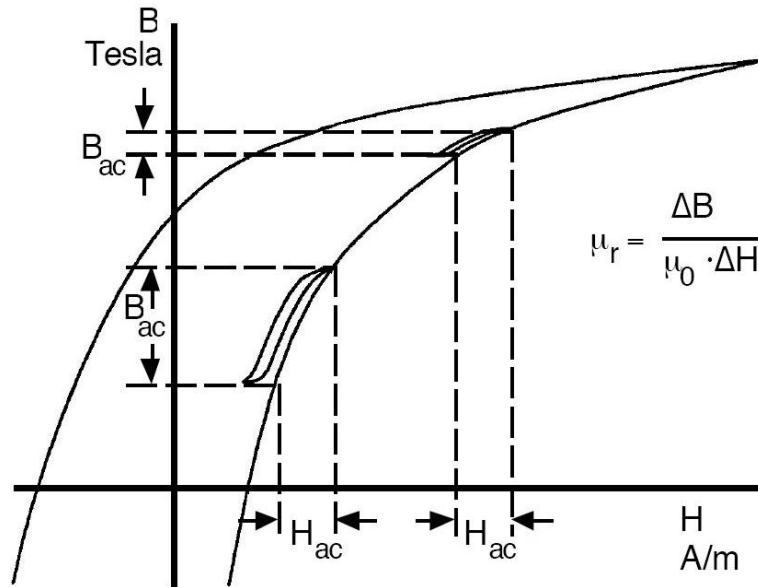


Figure 6.8: Ferrite magnetization loop with added AC field $H_{ac}$ at two different working points[Schnase, 2000]

Thus, an inductor made with a ferrite core will have a different value of inductance depending on the magnetic biasing field. However, the energy storage capability is rather limited and the active volume for an inductive tuner is therefore about 100 times larger than that of their capacitive counterpart[Pirkl, 2000]. Finally, this modulation goes at the expense of power efficiency, because of eddy current losses in the ferrites. In both cases of RF modulation, careful shielding should be studied to limit the influence of the superconducting cyclotron stray field.

**Calculations**

A synchronous phase of 110° has been chosen to maximize the beam energy gain per acceleration gap. Assuming a constant synchronous phase and the radial variation of the magnetic field given by OPERA, a Matlab script was written to estimate the beam parameters in the SC[Brück, 1966]. In reality, the synchronous phase will slightly vary during acceleration and will depend on the RF, which is defined by the speed of rotation of the Rotco rotor and the shape of the metal capacitive plates on the Rotco rotor and stator.

---

[2]more details on these accelerators can be found in Chap.2

The temporal variation of the Rotco capacitance for a constant synchronous phase is shown in Fig.6.9. The relationship is quasi-linear and this simplifies the design of the shapes of the capacitive plates of the Rotco. Some 60 RF bunches are accelerated during 0.3 ms, corresponding to 8700 beam turns in the SC pole. The bunching in the injection line can produce bunch lengths lower than $\pm 5°$[Calabretta and Migneco, 1984]. Particles will slowly oscillate longitudinally around the synchronous phase with a synchrotron tune of $1.4\ 10^{-3}$. This will result in a momentum spread at ejection of $2.7\ 10^{-4}$.
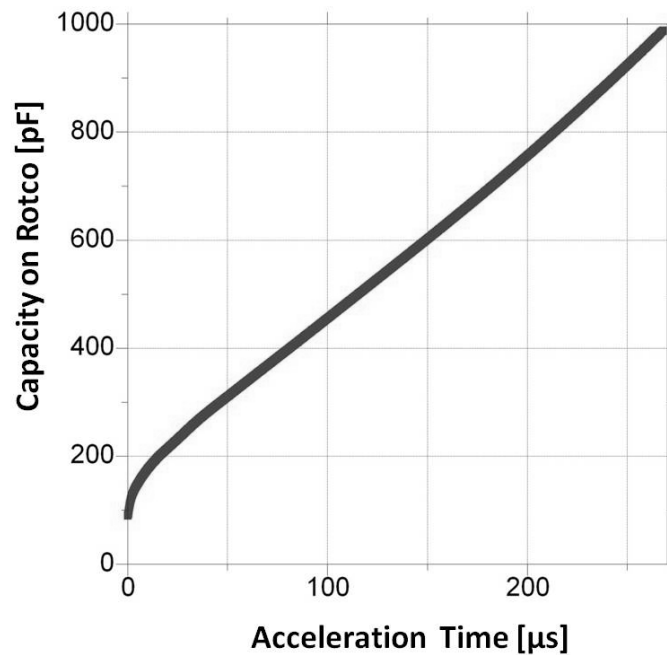


Figure 6.9: RotCo capacity modulation during beam acceleration for a constant synchronous phase

## 6.3   Injection and Ejection Designs

### 6.3.1   Inflector and Central Region Design

In this design, the magnetic radius of the beam at injection is very small because of the strong magnetic field in the cyclotron center and the geometry of the inflector is thus strongly spiraled. In addition, the high central magnetic field and the low acceleration voltage produce small orbit separations, which, as shown in the next subsection, bring about challenges linked to the computational modeling and the mechanical realization of the central region and inflector.

The study of the inflector and central region was carried out by Dr. D. Campo, in collaboration with the author, just after completing her PhD on the central region of SCENT[Campo, 2010b]. The interested reader will find details of all the computational, physical and mechanical details related to this study in the bibliography[Campo, 2010a]. An overview of the main challenges and results is presented in the following section. All the figures of this section are taken from the same reference.

Inflector parameters are adjusted to obtain a particle velocity at the exit from the inflector

with no vertical component and a nought beam vertical position. With this inflector, the reference particle in the beam exits the inflector at 8.9 mm from the cyclotron center and its orbit center is 3.2 mm from the cyclotron center (this distance is called the beam *off-center*). It has to be underlined that the low injection energy was chosen to increase the beam radial gain on the first turn. The final parameters chosen for the design are summarized in Tab.6.5.

Table 6.5: Spiral inflector parameters. Note that $K \simeq 1.4$

| | |
|---|---|
| **Injection Energy** | 10 keV/u |
| **Magnetic Radius** | 5.75 mm |
| **Electric Radius (Inflector Height)** | 16.0 mm |
| **Tilt Angle** | 0.0° |
| **Electrode Gap** | 4.0 mm |
| **Electrode Width** | 5.0 mm |
| **Applied Voltage** | ± 5000 V |

The designed inflector in OPERA3D is shown in Fig.6.10.

The most innovative aspect of this spiral inflector is the aspect ratio of its structure. A minimum gap of 4 mm between the electrodes is chosen, in order to guarantee the beam transmission and to minimize the sensitivity to errors linked to the misplacing of the device. The maximum electrode width of 5 mm is a limit imposed by the beam trajectory on the median plane. Therefore, the aspect ratio is only 1.25.

Different strategies were proposed to make the electric field uniform between the electrodes and to limit the electric stray field in the region near the electrodes. These include joining the electrode extremities with a thin layer of controlled resistivity glass or of insulator covered with a thin conducting layer, and the use of conducting wires parallel to the inflector electrodes, set at specific electric potentials.

The latter solution was chosen and added to the inflector design in OPERA3D. The inflector geometry is introduced as a discrete model of 25 sections of the electrode. This was due to the computational limitations of such a twisted geometry. The achieved uniformity of the electric field was around 2.5 % for a system of 9 wires.

In order to assess the beam losses in the inflector and the beam optical characteristics at its exit, multi-particle tracking was performed in OPERA3D starting at 5 cm from the median plane with a circular beam of 10.79 $\pi$ mm mrad geometric emittance (corresponding to the 0.05 $\pi$ mm mrad normalized emittance delivered by the EBIS-SC[3]). The beam losses are negligible. However, coupling between the two transverse motion directions results in a clear emittance increase. At the output, the emittances are 1 $\pi$ mm mrad (radially) and 20 $\pi$ mm mrad (vertically). The results are shown in Fig.6.11, Fig.6.12 and Fig.6.13.

---

[3]see Chap.4
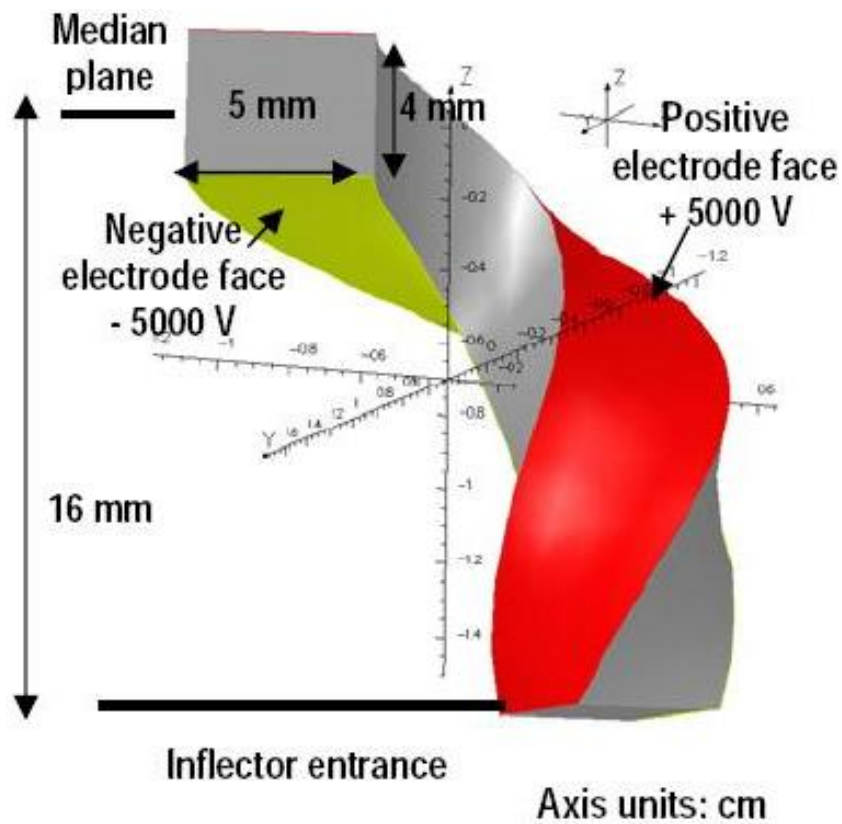
Figure 6.10: Schematic view of the spiral inflector. Note that the beam is injected from below
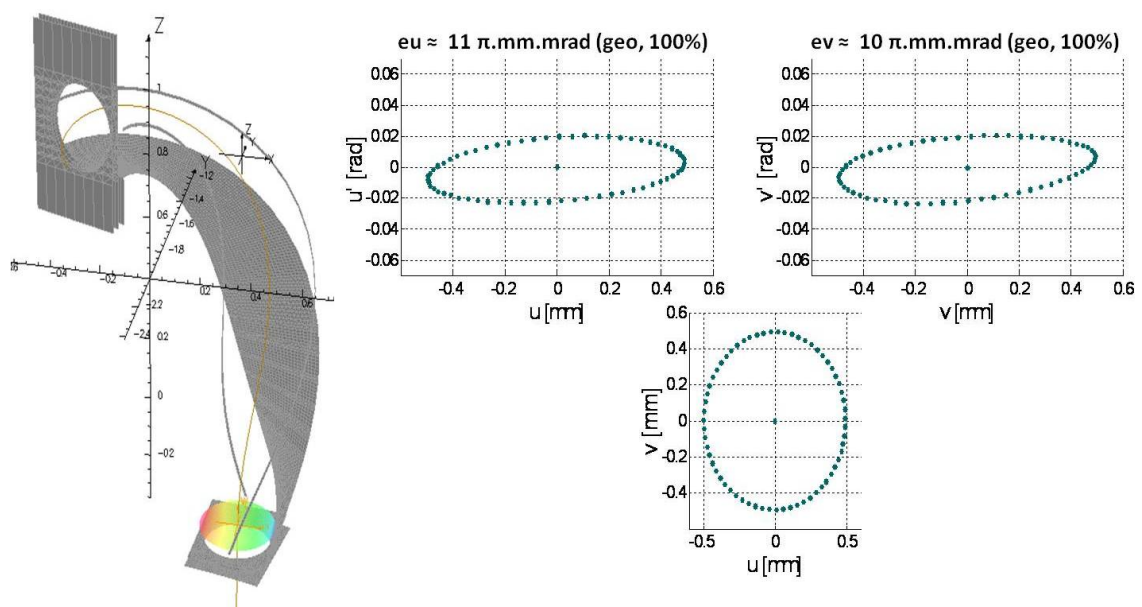


Figure 6.11: Beam transverse trace spaces and profile at the entrance of the inflector
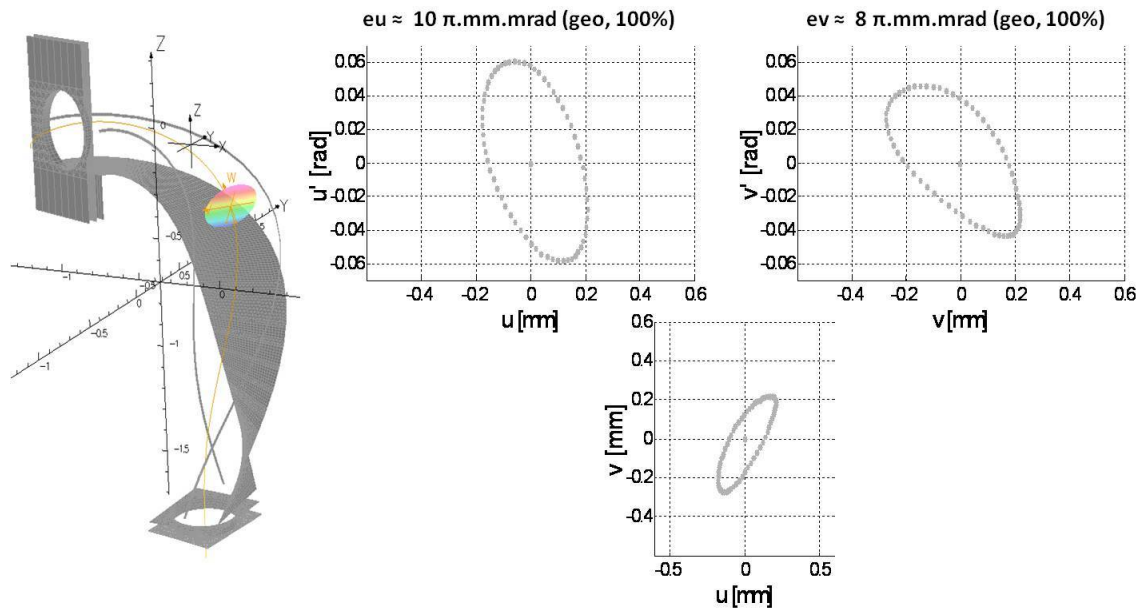
Figure 6.12: Beam transverse trace spaces and profile in the middle of the inflector
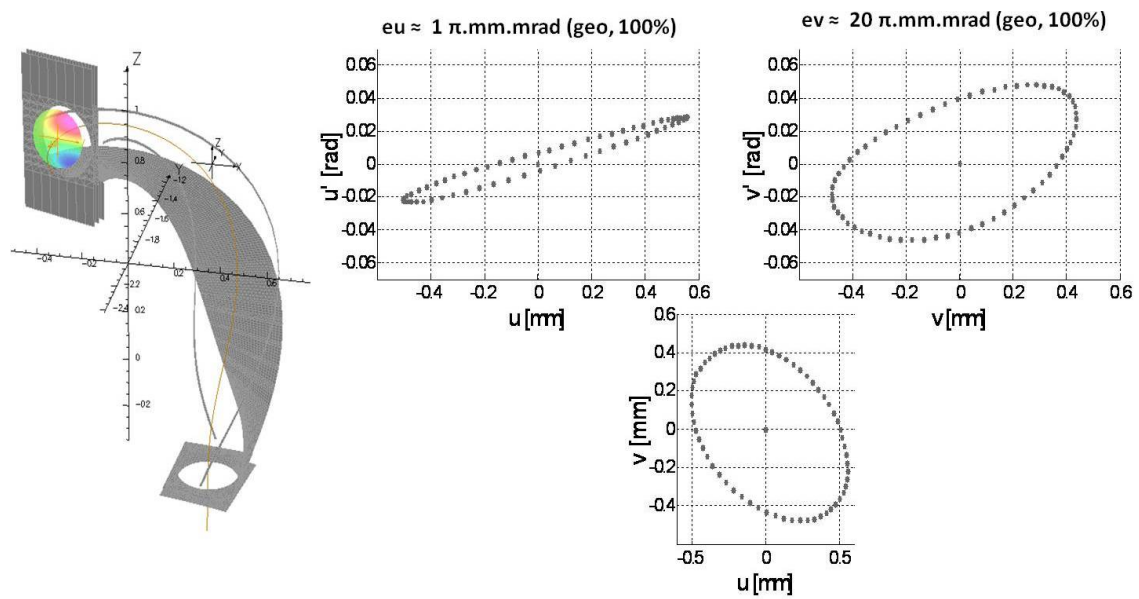


Figure 6.13: Beam transverse trace spaces and profile at the exit of the inflector

**Central Region**

The inflector model was completed with the 180° Dee with a RF voltage of 20 kV rms and the anti-Dee (at ground potential) connected to a housing, which shields the inflector electric field and provides mechanical support to the inflector electrodes (see Fig.6.14).
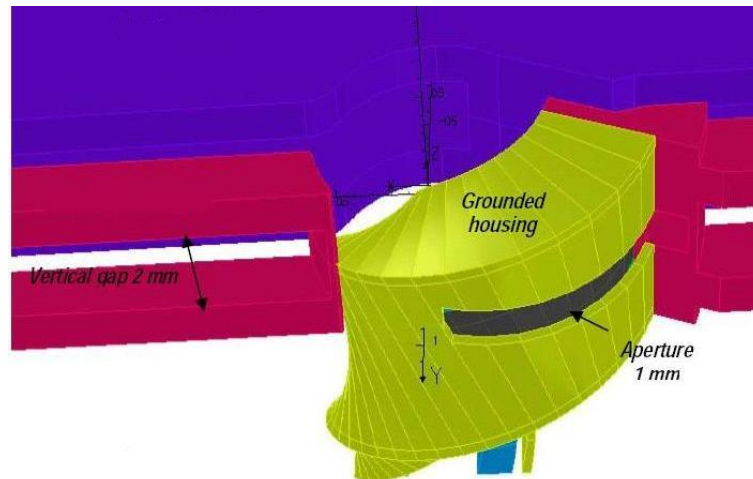


Figure 6.14: Central region model: Dee (purple), anti-Dee (magenta), housing (green)

It can be noticed that the housing has an aperture in a section near the median plane. This is done to avoid the beam hitting the housing at the end of the first turn. In addition, the correction wires used in the model of the inflector were here neglected to reduce the complexity of the model. This opening in the grounded housing however allows the electric field from the inflector to leak out. This results in a vertical kick to the beam at the end of its first turn. To avoid this, a possible solution is the optimization of the inflector electrode voltages, while keeping the electric field constant. Indeed, if the inflector is powered with the upper electrode at ground potential and the lower electrode at -10 kV, all dimensions of the inflectors remain the same but the vertical kick is corrected and the deviation of the beam vertical center from the median plane is of only 0.1 mm after two turns, as shown in Fig.6.15.
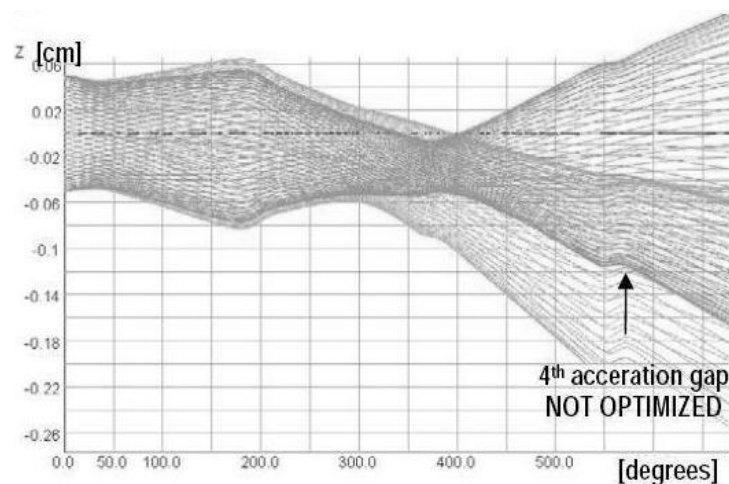


Figure 6.15: Beam vertical coordinate before (light grey) and after (dark grey) correction

**Considerations on Betatron and Synchrotron Motion**

The field index is very small in the cyclotron center (see Fig.6.1). This means that the vertical betatron tune is very small in the first turns and particles could be lost because of the wide vertical betatron oscillations. Analytical formulas[Craddock, 2010] implemented in Matlab showed that as in all cyclotrons, vertical focusing can be provided by the electric field in the acceleration gap. By correctly tuning the RF phase at which the beam crosses the gaps on the first turns, the vertical betatron oscillations can easily be contained within ± 1 mm of the median plane.

The small field index at injection could also have consequences on the longitudinal motion. Indeed, since the injection time is very short (1.5 μs), the RF remains practically constant. However, by the time the last bunch of the beam pulse is captured in an RF bucket, the first bunch of the beam pulse has done about $N_t = 60$ turns in the machine and its revolution frequency has consequently varied. Assuming a constant magnetic field and a constant RF, the dephasing $\Delta\phi$ between the first and the last bunch can be estimated based on the energy increase per turn $\Delta\gamma_{turn}$ by the expression of Eq.6.1.

$$\Delta\phi \simeq N_t\,360°\,\Delta\gamma_{turn} \leq 1° \tag{6.1}$$

This effect is therefore very small and can safely be neglected.

**Discussion**

This preliminary design of the inflector provides a realistic solution to inject the beam into the cyclotron median plane and accelerate it in the first two turns. The distorsions of the emittances by the inflector could however cause beam losses on the first turns. This effect should be quantified in a more detailed design. Furthermore, a correction electrode could be placed to correct the beam off-centering of 3 mm at the exit of the inflector. This off-centering should not be problematic during acceleration but could result in losses during the resonant ejection.

As opposed to the design of the pole and of the magnet, the inflector design involved complex simulations. The strongly spiraled geometry of the inflector put to test the capabilities of OPERA3D and constant debugging and discussions with software experts were needed.

## 6.3.2 Ejection

A high-field SC brings about challenges linked to the high central magnetic field and to the low acceleration voltage which induce a small orbit radius and a small increase of energy per turn. Indeed, using Eq.5.6, the natural radial gain per turn at the final energies is calculated to be less than 0.1 mm.

**Simulation method**

The last orbit turns of the reference particle are simulated with the tracking code ANJO. The RF cavity is centered at 180° and occupies ± 90°.

The rms voltage on the Dees is set to 20 kV. For simplicity, the RF synchronous phase is set to 90° (corresponding to an empty bucket and maximal acceleration), producing around 28 keV/u kinetic energy gain per turn.

Following the trajectory for one turn gives a mean radial gain per turn of 0.07 mm which is consistent with the previously computed value.

**Initial Conditions for the Simulation**

First of all, the stable orbit for the particle at 230 MeV/u is determined by iteration with the use of the programs ANJO and ORBLA. All relevant parameters are summarized in Tab.6.6.

Table 6.6: Ejection parameters used for the simulation. Note that the closed orbit parameters were obtained with ORBLA, the tracking parameters were obtained by iteration with NAJO, the mean radial gain per turn was calculated from Eq.5.6 and the beam emittance used does not take into account any emittance growth at injection

| | |
|---|---|
| **Kinetic Energy** | 230 MeV/u |
| **Closed Orbit Mean Radius** | 0.9812 m |
| **Closed Orbit Average Magnetic Field** | 4.7172 T |
| **Closed Orbit Radial Betatron Tune** | 0.993 |
| **Closed Orbit Vertical Betatron Tune** | 0.120 |
| **Mean Radial Gain per Turn** | 70 $\mu$m |
| **Geometric Emittance** | 0.067 $\pi$ mm mrad (4-rms) |
| **Radial Beam Half-Width** | 0.26 mm (2-rms) |
| **Vertical Beam Half-Width** | 0.74 mm (2-rms) |
| **Pole Edge Radius** | 1.075 m |
| **Minimal Radius of the Marginal Field** | 1.0 m |
| **Tracking Initial Azimuth** | 0° |
| **Tracking Initial Radius** | 0.9811 m |
| **Tracking Initial Radial Divergence** | 0.0 mrad |

**Results**

The multi-particle tracking code NAJO was used to simulate the particle orbits. A first harmonic positive magnetic perturbation of about 0.1 T and 5° azimuthal width was artifically introduced in the magnetic field map from the OPERA model.

The perturbation radial and azimuthal shapes are shown in Fig.6.16 and Fig.6.17.
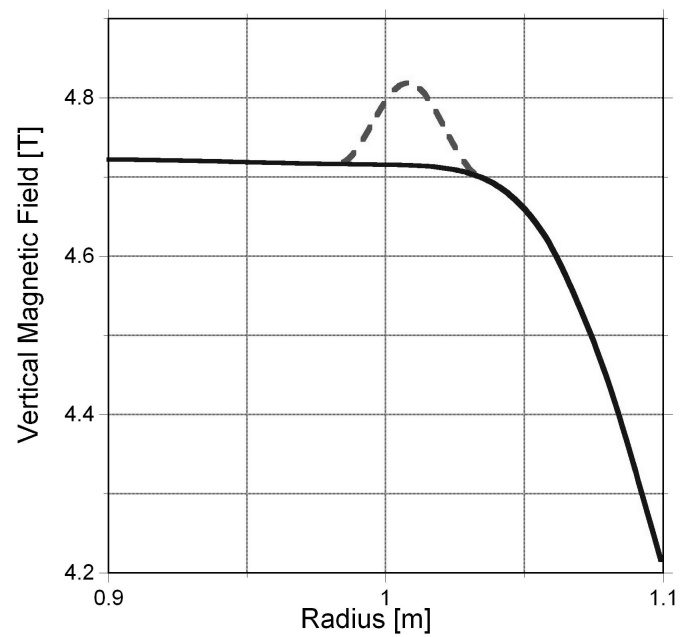
Figure 6.16: Radial profile of the magnetic field at the end of the pole with (red) and without (blue) the magnetic perturbation
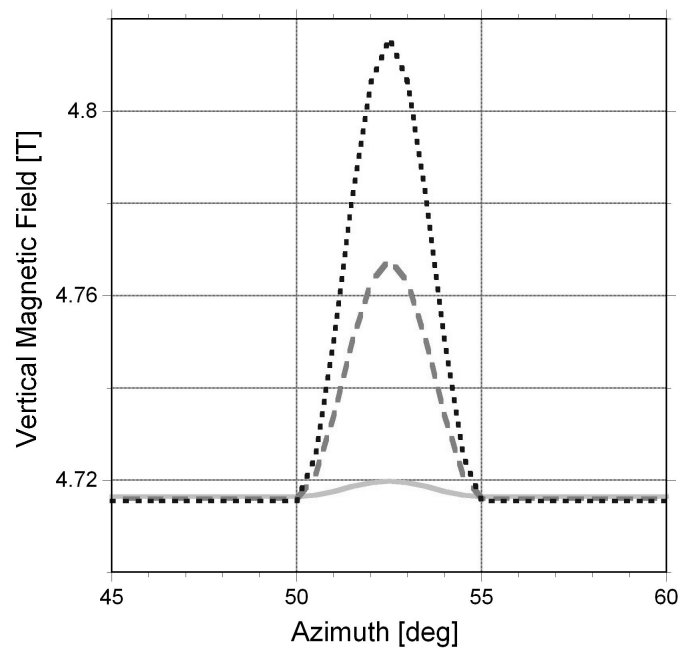


Figure 6.17: Azimuthal profile of the magnetic perturbation at radii 0.98 m (light blue), 0.99 m (blue) and 1.0 m (dark blue)

The action of the magnetic perturbation is to lock the radial tune to 1 and induce a slow displacement of the center of the orbits. The radial gain per turn slowly oscillates and increases in amplitude, as shown in Fig.6.18.
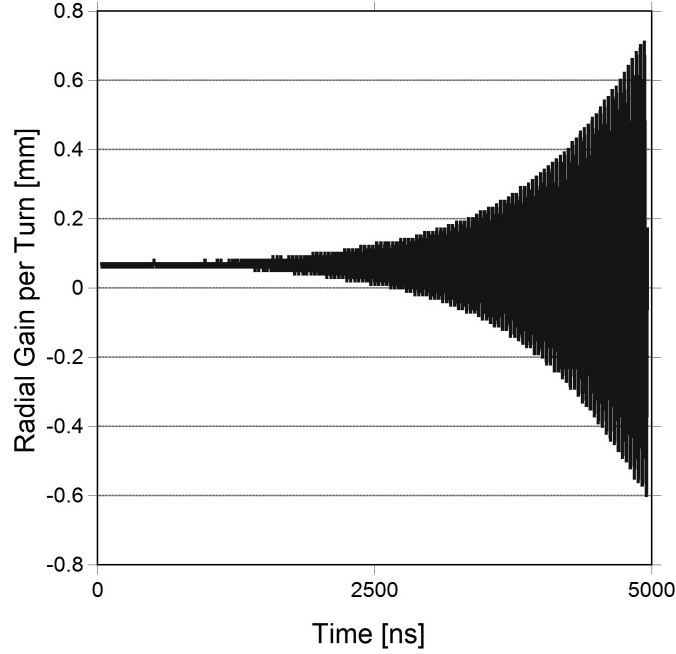


Figure 6.18: Radial gain per turn along the beam trajectory at ejection

Careful adjustment of the perturbation allows to limit the vertical betatron oscillations amplitude to $\pm$ 3.5 mm[4], as shown in Fig.6.19, and to avoid any increase in transverse emittance.

After 138 turns (energy of 233.9 MeV/u), at 0.996 m radius and 290° azimuth, the beam has a radial width $\delta_r$ of 0.05 mm and a vertical width of 0.44 mm. At that point, the radial gain per turn $\frac{\mathrm{d}r}{\mathrm{d}N_t}$ is 0.17 mm and an electrostatic deflector with a septum width $\delta_{septum}$ of 0.1 mm can be introduced with beam losses under 30 %.

The transmittance $\tau$ is estimated by the back-of-the-envelope formula of Eq.6.2.

$$\tau = \frac{\frac{\mathrm{d}r}{\mathrm{d}N_t} + \delta_r|_{turn(j)} - \delta_{septum} - \delta_r|_{turn(j-1)}}{2\,\delta_r|_{turn(j)}} \tag{6.2}$$

As can be observed on the beam trajectories for the last two turns, shown in Fig.6.20, already after 70° of deflection, there is more than 1 cm radial orbit separation, which allows to introduce another electrostatic deflector and/or a magnetic channel to locally reduce the magnetic field and focus the particles.

---

[4]as a reminder, the physical aperture corresponds to the vertical aperture of the Dee gaps: it is of $\pm$ 1 cm
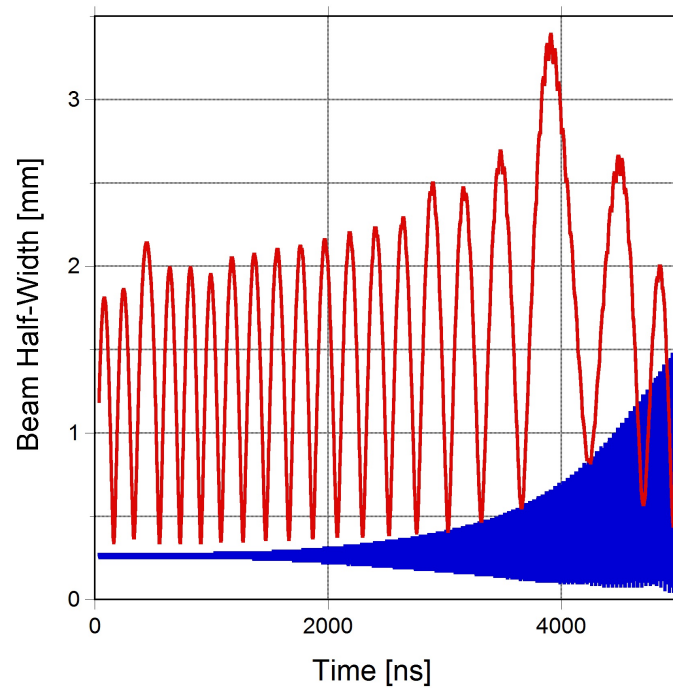
Figure 6.19: Vertical (in red) and radial (in blue) beam size growth induced by the magnetic perturbation
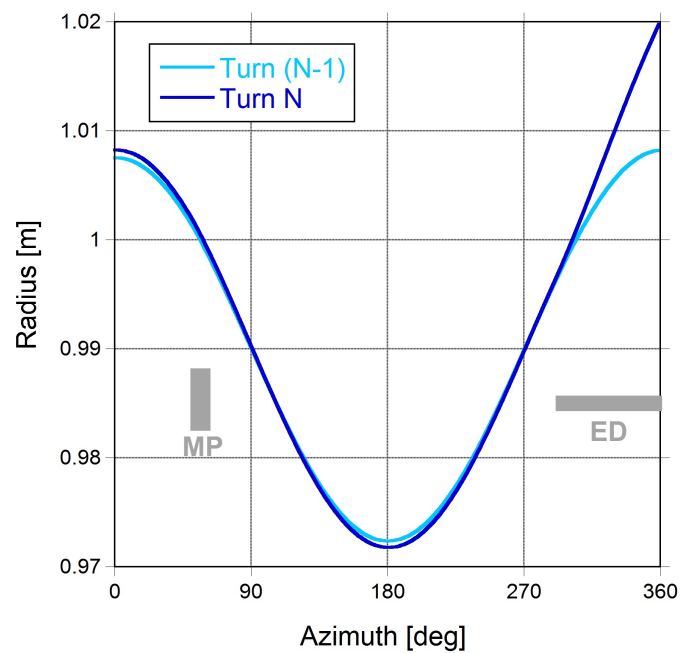


Figure 6.20: Last two orbit turns, with the magnetic perturbation (MP) and electrostatic deflector (ED)

The influence of the amount of electrostatic deflection on the radial distance between successive turns is shown in Fig.6.21. The beam ellipses after 70° of deflection are shown in Fig.6.22.
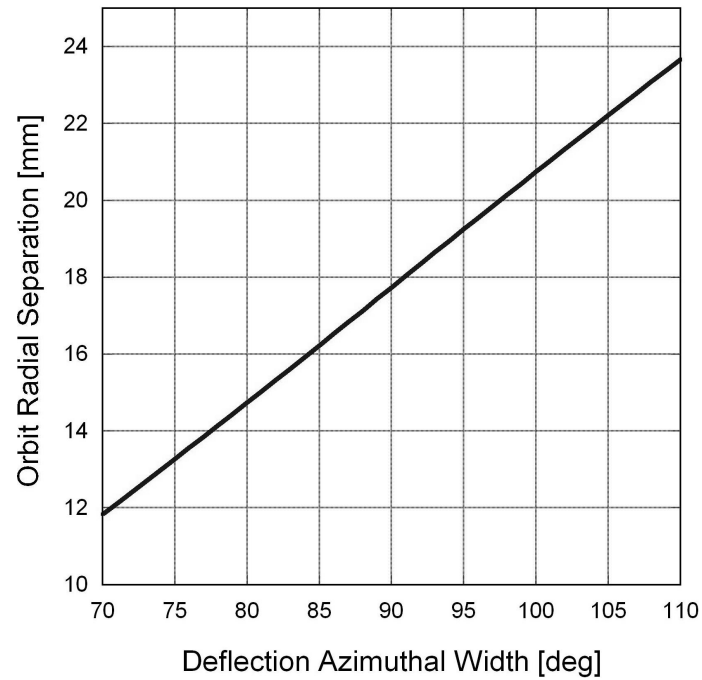


Figure 6.21: Radial separation between the last two turns as a function of deflection azimuthal width
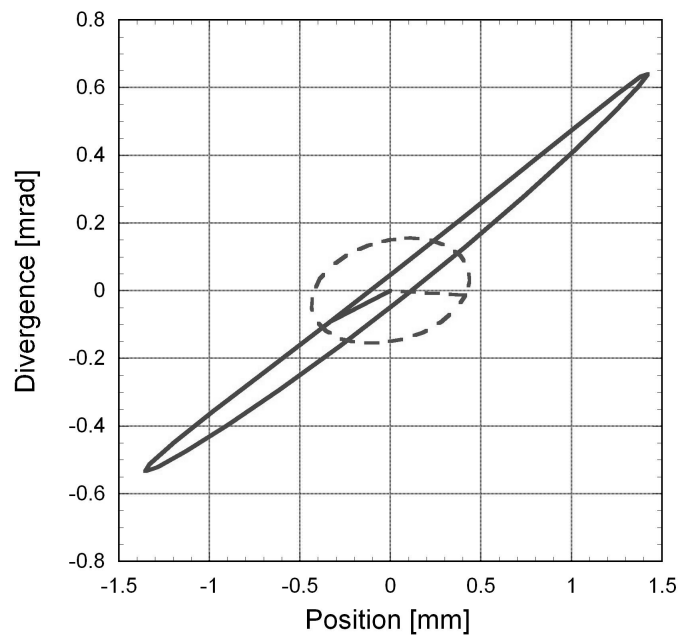


Figure 6.22: Beam in the horizontal (red) and vertical (green) phase spaces after 70° of deflection

**Discussion**

This initial study of the ejection takes full use of the subroutines of NAJO to create realistic perturbations. With this first approximation, it was proved that sufficient radial gain per turn can be induced and losses at the deflector can be limited to under 30 %, with no emittance degradation and limited beam size. However, this was achieved only after many different trials, as very small changes in the position, amplitude and shape of the magnetic perturbation have direct effects on the beam trajectory and optics.

The ejection takes place over more than 100 turns and should be very precisely tuned in terms of magnetic field and of RF synchronism. An accurate study of the ejection would require the definition of a precise radial variation of the magnetic perturbation and a simulation to assess how to achieve this perturbation with an appropriate iron geometry. Dedicated codes would also be required to carefully analyze the higher order terms in the vertical expansion of the magnetic field of the perturbation on the median plane. This is however outside the scope of this study.

## 6.4   Chapter Summary

The design of the SC presented in this chapter achieved 2D magnetostatic modeling in OPERA2D to provide a constant magnetic field index of 0.02 in the acceleration region (producing a constant vertical betatron tune of 0.14) with realistic geometries for the pole, the superconducting coil and the yoke. The very high central magnetic field of 5 T allows to limit the pole radius to a value similar to the one of the C235 protontherapy cyclotron (see Chap.2), with a total iron weight around 300 tons.

Using the model presented in Chap.5, the RF system was studied. An acceleration voltage of 28 kV peak was achieved for a RotCo with realistic voltage constraints and capacity range. As expected, the RF requirements are very small for SCs and the power supply needed is only 30 kW.

A unique design of a spiral inflector was studied with an accurate 3D model in OPERA3D, enabling beam axial injection at 10 keV/u with no beam losses, despite the difficulties linked to the strong magnetic field and low acceleration voltage. Finally, beam ejection with 30 % losses was achieved by exciting the first radial integer betatron resonance with a realistic magnetic perturbation. This enables to increase the orbit radial gain per turn and to introduce an electrostatic deflector.

The design proved the feasibility of a 230 MeV/u superconducting SC with a 5 T central magnetic field and confirmed the potential advantages of the SC: compact magnet, small RF power supply and fast pulsed operation. However, the reliability of the cyclotron is put to question by the need of a large and fragile RotCo and from the complexity of the injection and ejection systems. Therefore, a more reliable solution is studied for injection in CABOTO: a superconducting IC at 230 MeV/u, whose design is presented in the next chapter.

# Chapter 7

# 230 MeV/u Isochronous Cyclotron Design

This chapter describes the preliminary design of a superconducting IC for $H_2^+$ and $C^{6+}$ at 230 MeV/u. ICs are the most widely used cyclotron and their technology is well-known and reliable. However, this design aims at using the highest possible central magnetic field to reduce the magnet dimensions. It should make sure that such a high magnetic field does not introduce any complications in the magnet system, RF system, injection and ejection, that could affect the machine reliability. The most important design characteristic is the use of elliptical pole gaps, which have the potential to limit the sector spiraling and simplify the beam ejection, with respect to the typical constant pole gaps of superconducting ICs.

## 7.1 Magnet Design

The chosen design philosophy is to maximize the flutter provided by the iron of the pole geometry (see Chap.5), as this reduces the amount of spiraling of the sectors needed to achieve adequate beam focusing. Strongly spiraled sectors result in complex RF cavity design. This increases the time and cost of designing, manufacturing and testing of the RF system and could result in a reduced reliability. It should therefore be avoided in a medical industry perspective.

This was achieved by both:

1. using elliptical pole gaps,

2. setting $\frac{\text{Hill Azimuthal Width}}{\text{Sector Azimuthal Width}} = \frac{1}{2}$

These choices influence the number of sectors. Having an elliptical hill gap excludes using three sectors. Indeed, in this case, for symmetry, all valleys would house accelerating cavities, leaving only the hill gaps free for ejection elements. However, this conflicts with the reduced hill gap at the outer radii of the elliptical profiles chosen. Therefore, the choice goes to adopting four sectors, where two opposite valleys house accelerating cavities and the two others are free for ejection elements (only one electrostatic deflector, if possible) and beam diagnostic devices (radial probe).

### 7.1.1   Choice of Central Magnetic Field

To choose the central magnetic field, two criteria are used: feasibility of ejection and feasibility of injection. Of course, the goal is to use the highest possible magnetic field in order to reduce the machine dimensions.

Existing and designed cyclotrons are used as benchmarks to assess the feasibility of ejection. A simplified model of ejection assuming an electrostatic deflector in a free valley of a 4-sector machine is here considered. Taking the electrostatic deflection as a small perturbation of the stable motion and integrating Newton's equation (with electric field $E$ and particle charge $q$) over the path length $l$ of deflection (half a sector), the radial kick $\Delta p_r$ produced by the deflector is simply determined by Eq. 7.1.

$$q\,E\,l \simeq m\,v^2\,\Delta p_r \Rightarrow \Delta p_r \simeq \frac{E\,\frac{\pi}{4}}{B_0\,\gamma\,\beta\,c} \tag{7.1}$$

Based on the available literature, the parameters used for the cyclotrons C235, C400, COMET and SCENT (see Chap.2) are introduced in the formula. Radial kicks of respectively 19 mrad, 15 mrad, 19 mrad and 16 mrad are thus calculated. To obtain the same average kick at 230 MeV/u, the central magnetic field should be 4 T.

However, injection also constrains the choice of magnetic fields since high magnetic fields result in complicated central regions, where the geometries of the inflector, the central region electrodes and collimators are squeezed. The potential limit is set by the SCENT cyclotron with a central magnetic field of 3.2 T. This represents therefore the limiting factor.

All things considered, the central magnetic field is chosen to be 3.2 T. It has to be noted that this is the first IC design with elliptical pole profiles at such a high central magnetic field.

### 7.1.2   Hill Design

The studies that led to the design of the C235 showed that[Laisné, 1981, 1994, 1998] giving an elliptical shape to the hill gap allows to produce a magnetic field contribution (from the iron of the hill on the median plane), which : is (maximal and) constant with radius and abruptly decays just before the radius of the generating ellipse. The former maximizes the flutter at all radii (and thus minimizes the spiral angle needed to achieve adequate focusing), while the latter reduces to the strict minimum the radius of the pole compared to a constant gap hill solution and allows a simplified ejection, which requires only one electrostatic deflector, placed inside one of the valleys without RF cavity.

More precisely, the iron of the hill is shaped to have a distance $h$ from the median plane (or hill gap) which changes along the radius $R$ according to Eq.7.2.

$$h\left(r\right) = h_{max}\,\sqrt{1 - \left(\frac{r}{r_{ellipse}}\right)^2} \tag{7.2}$$

The parameter $h_{max}$ is big enough to allow comfortable positioning of the central region elements and small enough to provide magnetic focusing on the first orbits, as will be

further detailed in Sec.7.3.1. In the present design, the value is set to 3 cm. This is larger than in SCENT and allows to obtain vertical focusing already at 5 cm radius, corresponding to the end of the central region, after 1 turn (kinetic energy around 320 keV/u).

The parameter $R_{ellipse}$ is determined from the equilibrium orbit radius at 230 MeV/u and the expected scalloping on the hill. It is then optimized according to the real scalloping value, given by orbit tracking. In the present case, the equilibrium orbit radius lies at 1.160 m and scalloping makes the orbit radius oscillate between 1.136 m and 1.180 m. The ellipse radius is then set to 1.193 m.

Ideally, the hill gap $h$ goes down to zero and the upper and lower poles are in contact at the median plane. This provides a constant magnetic field up to the ellipse radius. However, for practical reasons, a minimum half-gap of 3 mm is maintained. The radial width of this constant gap part is adjusted to make the magnetic field on the median plan constant up to the maximum radius of the last orbit (1.18 m). The ALANEW input files for the hill and valley profiles were generated with Gene_a_dat, which, at this central magnetic field, assumes that the hill and valley are fully-saturated and that the magnetization on the pole is vertical. A close-up view of this part of the hill is shown in Fig.7.1.
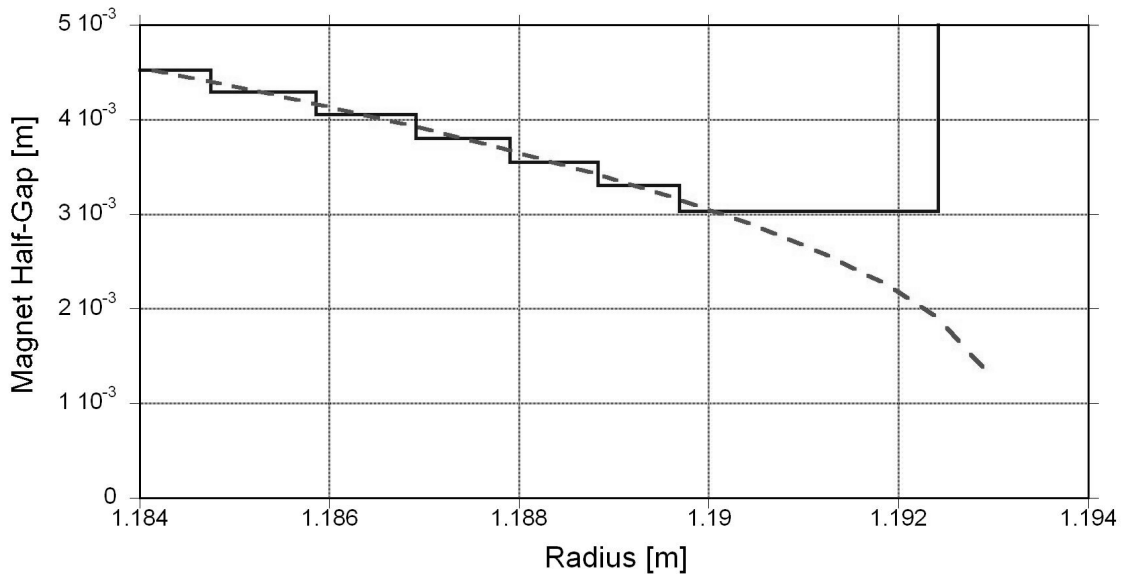


Figure 7.1: Hill profile modelization at the end of the pole (solid line) and corresponding elliptical curve (dashed line)

As mentioned before, to achieve the goal of producing the highest possible flutter, the hill angular width is set to the maximum value of 45 °. The hill profile and its (azimuthally averaged) magnetic field contribution on the median plane are shown in Fig.7.2.
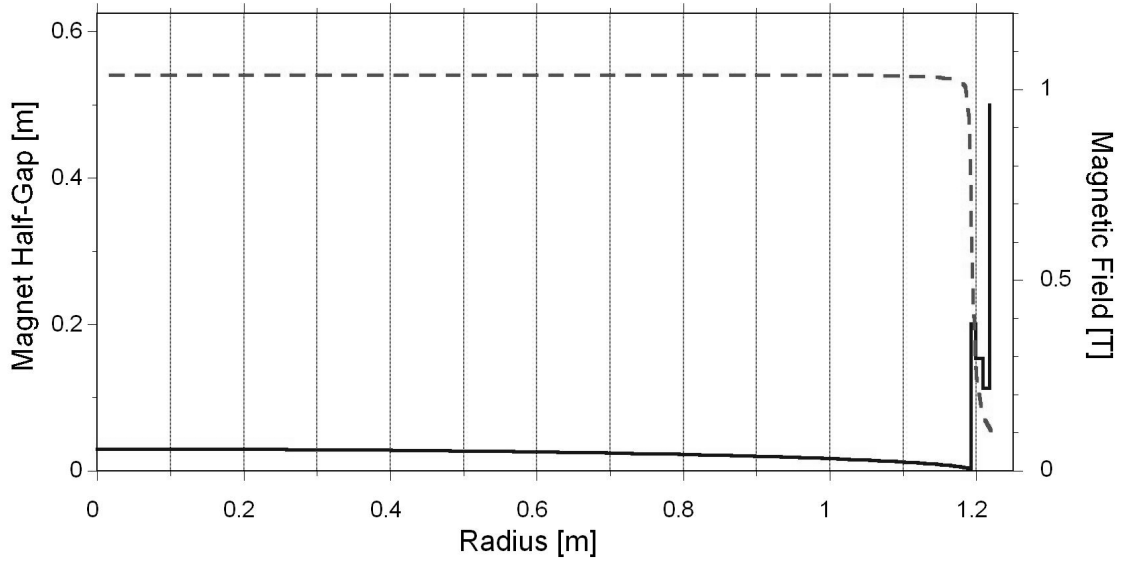
Figure 7.2: Hill profile (solid line) and mean magnetic field on the median plane, produced by the magnetized iron of the hill (dashed line)

### 7.1.3  Valley Design

The valley is designed following a similar procedure as for the hill. This time though, the gap at the center of the machine is set to the same value as the ellipse radius, which is slightly larger than before (1.219 m). This geometry creates a spherical valley structure which results in a low and radially constant magnetic field of around $\frac{2.14}{6} = 0.35$ T.

For practical reasons, the pure elliptical profile is cut and a constant gap of 0.5 m is introduced from the machine center up to a radius of 1.087 m. The gap then decreases following the elliptical curve. This simplifies the practical realization of the valley, since a constant gap valley is easily produced and an iron block can be subsequently assembled on it. No vertical holes were introduced, as these resulted in a positive radial gradient of the magnetic field produced by the iron of the pole and forced the coil position to be far (radially) from the pole edge. The valley profile and its (azimuthally averaged) magnetic field contribution on the median plan are shown in Fig.7.3.

The valley profile extending radially further than the end of the hill is applied to the whole sector. These last few centimeters of the pole have azimuthal symmetry and constitute the so-called *skirt*. This is shown in Fig.7.4.

The radial width of the last section at the end of the skirt is adjusted to obtain a sharp drop of the magnetic field beyond the last orbit radius. At the same time, the skirt is shaped to produce the correct isochronous magnetic field at the pole edge. Finally, the skirt focuses the magnetic flux of the valley towards the beam acceleration region (the *useful* flux) and minimizes the flux which is lost in other areas (the *marginal* flux). Since the sum of the useful and marginal fluxes is constant and related to the magnetization of the iron of the valley, the absence of the skirt would result in an increase of the magnetic flux needed from the coils and thus, in an increased volume of iron around the coils to contain this flux.
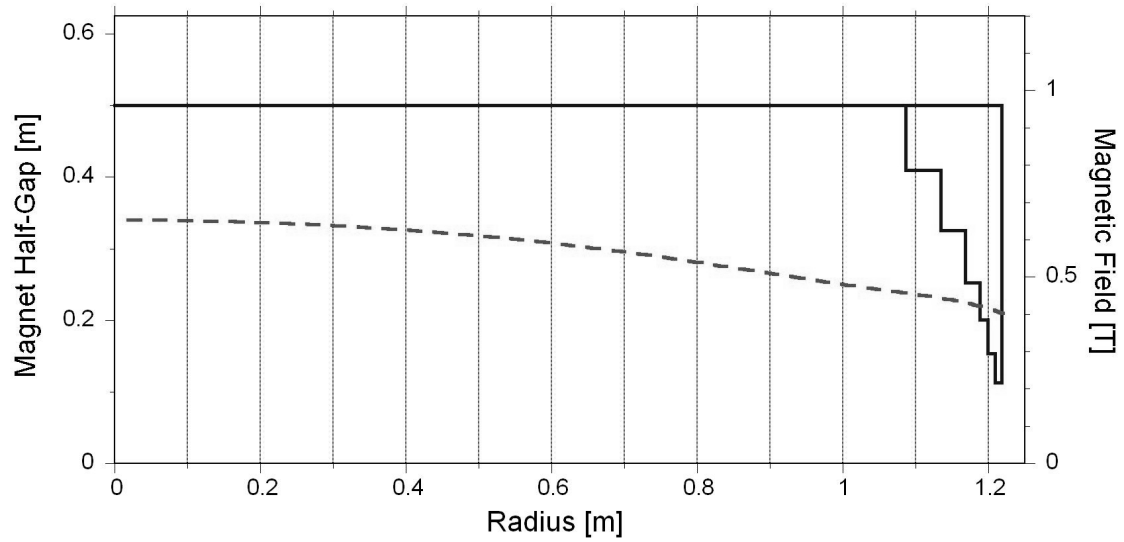
Figure 7.3: Valley profile (solid line) and mean magnetic field on the median plane (dashed line), produced by the magnetized iron of the valley (dashed line)
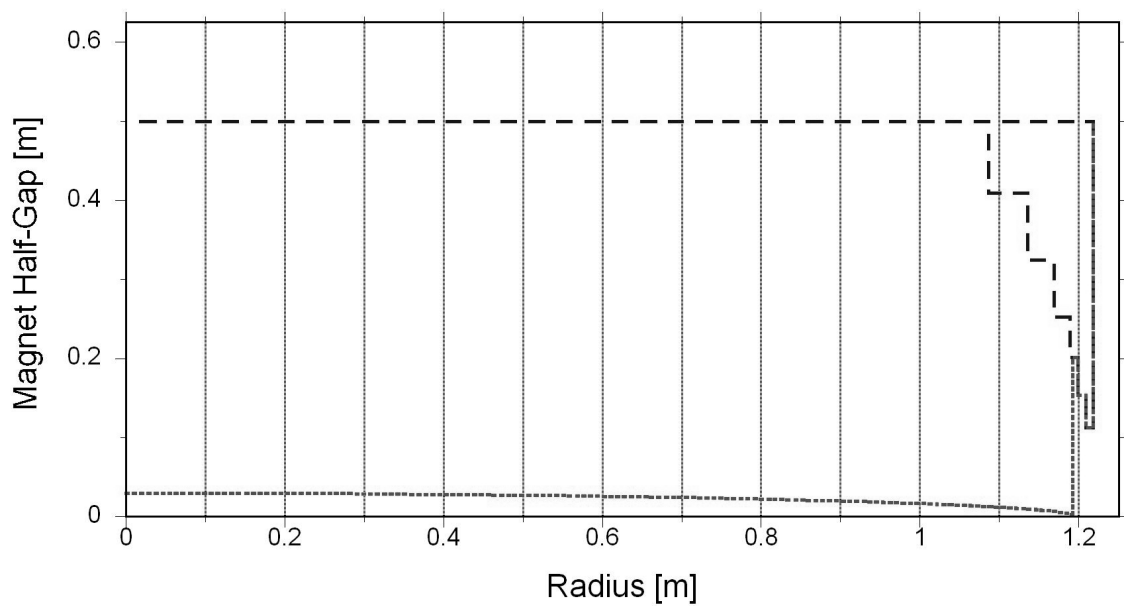


Figure 7.4: Hill (dotted line) and valley (dashed line) profiles: the common geometry at the end of the pole is the skirt

### 7.1.4 Spiraling

Spiraling is introduced to ensure good vertical focusing conditions at high energy. Having good focusing conditions means that no destructive (low-order) resonance is crossed and that the vertical betatron tune lies between 0.2 and 0.5[1]. This determines a start of spiraling from the radius 0.4 m, with a maximum spiral angle of 68°. It is important to note that in this design, the hill axis rotation at the end of the pole reaches 85°. This corresponds to a very mild spiraling compared to the values of SCENT[Calabretta et al., 2006] and C400[Jongen et al., 2010], which greatly simplifies the pole and RF cavity geometries. A top view of the spiraled sectors is shown in Fig.7.5.
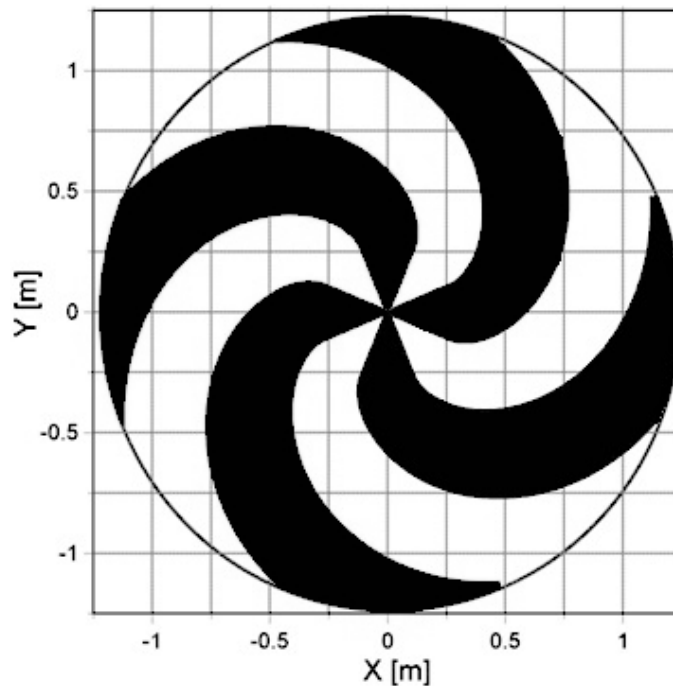


Figure 7.5: Top view of the spiraled pole

### 7.1.5 Working Diagram

The evolution of the betatron tunes during acceleration is shown in Fig.7.6. During acceleration, the beam crosses only fourth-order resonances, as shown in the working diagram of Fig.7.7.

These are intrinsic resonances and the beam betatron oscillations may be driven into resonance by the fourth harmonic component of the magnetic field $(3\nu_r + \nu_z = 4)$, or the average magnetic field $(\nu_r - 3\nu_z = 0)$. A detailed study of all the resonance crossings and their effect on the beam is beyond the scope of this preliminary design. Once the final 3D model of the magnet is performed, the precise magnetic field map can be used to study the resonance crossings and determine the tolerances on the magnetic field imperfections, the maximal beam oscillation widths, the magnetic field corrections and the minimum acceleration voltages on the Dees, as was done for C400[Jongen et al., 2007, 2006] and COMET[Schippers et al., 2004].

---

[1]for comparison, values used in other cyclotron designs are presented in Chap.2
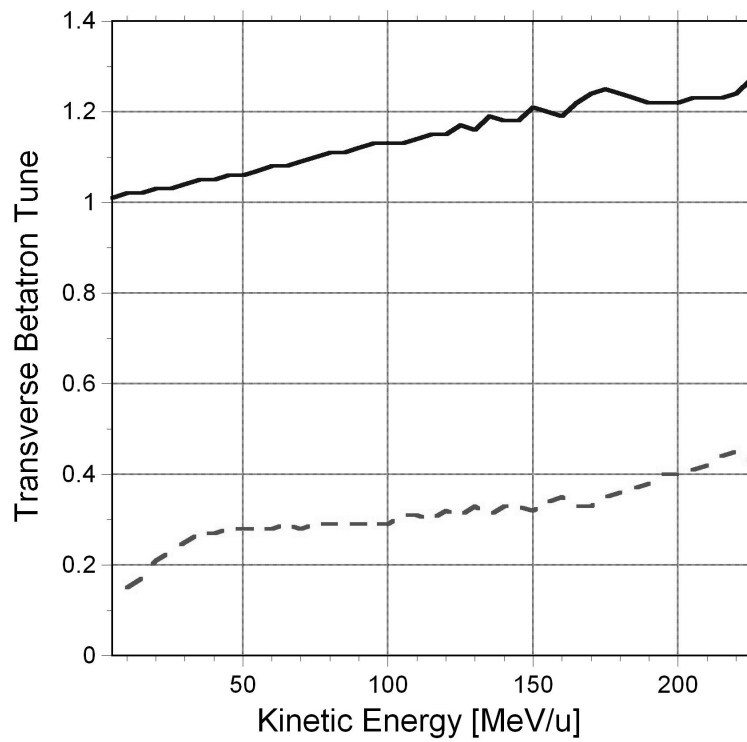
Figure 7.6: Radial (solid line) and vertical (dashed line) betatron tunes
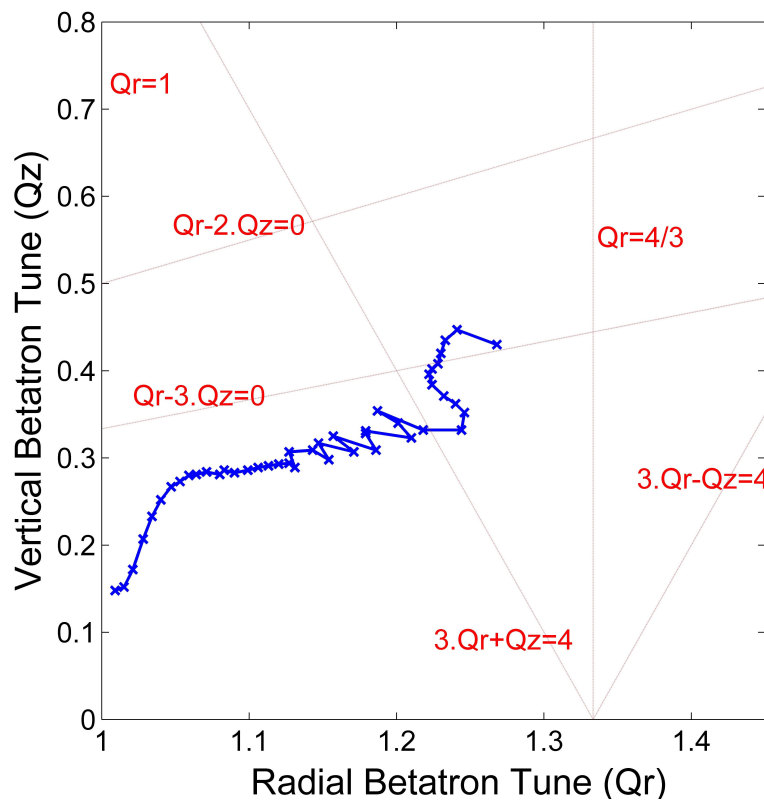


Figure 7.7: Working diagram with crossed resonances

At this stage of design, it can be assumed that the acceleration is fast enough for the beam to pass the resonances without beam loss or emittance growth. This is an optimistic but reasonable working hypothesis since the total beam loss calculated for C400 is around 13 %[Jongen et al., 2010], which corresponds to the initial beam loss estimate of Chap.4. In addition, the same assumption was made for SCENT[Calabretta et al., 2006], which however operates with higher energy gains per turn. A more realistic estimation of the beam output emittance from the cyclotron is discussed in Chap.8.

### 7.1.6   Superconducting Coil

The geometry studied in the previous sections focused on the azimuthal variation of the magnetic field to provide focusing. The next step concerns the radial variation of the mean magnetic field so as to ensure that it follows the isochronous curve.

The coil starting shape has a similar rectangular aspect ratio as the coils of the cyclotrons SCENT[Calabretta et al., 2006] and COMET[Negrazus et al., 2003]. The coil current is determined by iteration until reaching 3.2 T at the center of the magnet. All these parameters are then varied to find the best match between the vertical magnetic field produced on the median plane and the ideal isochronous curve. This is done in parallel to the pole iron optimization. Indeed, the skirt is shaped to allow the coil to be positioned as close as possible: radially, to the pole edge and vertically, to the median plane. This ensures that the total current in the coil needed to produce the isochronous field is as small as possible.

In the final configuration, the coil centroid lies at a radius of 1.393 m and a height of 0.185 m from the median plane. With a coil radial width of 14 cm and vertical width of 20 cm, a total of 1.1 Million Ampere turns per coil are required to produce the isochronous magnetic field. In addition, the maximum magnetic field in the coil is 4 T, which is safely lower than the critical field of 10 T at 4.5 K.

In terms of mechanical stability, the inner radial edge of the coil $R_a$ is subject to an average magnetic field $B_a$ of -3.27 T, whereas the outer radial edge $R_b$ experiences an average field $B_b$ of 0.23 T. Computing the coil shape $\alpha = \frac{R_b}{R_a} \simeq 1.1$ and $\beta = \frac{B_b}{B_a} \simeq -0.069$ and using Fig.5.12, it has been assured that the inner forces due to the strong magnetic field on the coil are radially compressive, and thus, that the inner mechanical structure of the coil is stable.

The pattern of the field lines in the coil is shown in Fig.7.8.
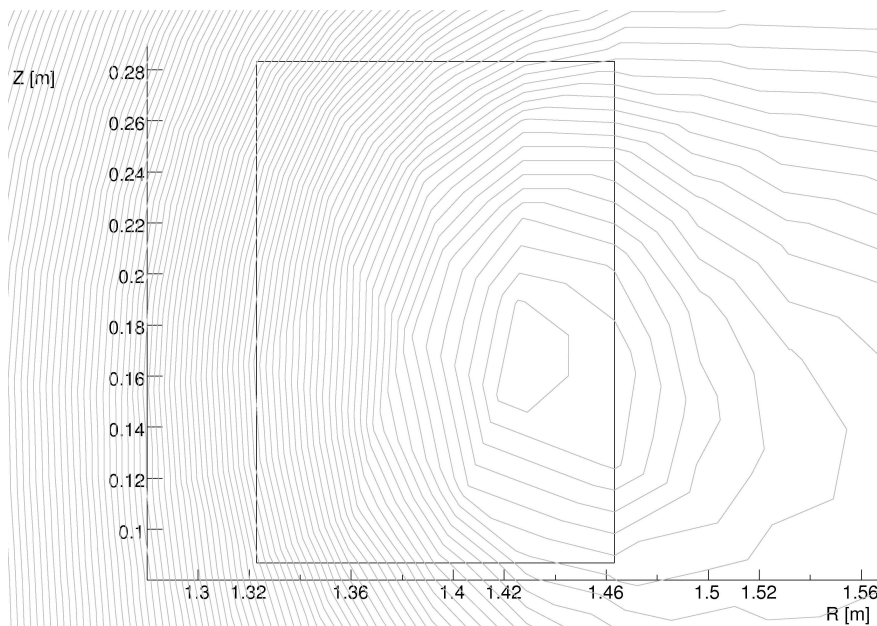
Figure 7.8: Magnetic field lines in the coil region

## 7.1.7 Yoke

As detailed in Chap.5, the maximum magnetic field modulus in the yoke edge is 2.0 T and the stray magnetic field is lower than 50 mT. The yoke diameter is 4.75 m and the yoke height is 2.9 m. The iron pieces of the magnet are therefore within the practical limit for transportation of 5 m.

For the present design, using an iron density of 7.87 tons/m$^3$, a cyclotron iron weigth of 314 tons is obtained. In computing the volume, the different stacking factors linked to the injection hole, the holes for the RF power feed, the vacuum, the instrumentation and the beam ejection line, are omitted. The iron volume calculated from this geometry can thus be considered as an upper boundary to the real final iron volume of the cyclotron.

## 7.1.8 Isochronism

A custom-written MATLAB script allows to automatically convert the geometry of the poles contained in the ALANEW input file into a command file readable in OPERA2D. The script also takes into account the user-defined parameters of the coil, yoke and background, as well as the magnetization values of Armco. The generated OPERA command file automatically creates the geometry, launches the magnetostatic simulation and exports the values of the vertical magnetic field on the median plane in a text file.

This magnet model produces an average vertical magnetic field on the median plan, whose deviations from the isochronous curve are lower than 0.8 %. This is an acceptable value for a preliminary cyclotron design. A detailed design study will need to accurately compute the tridimensional shape of the magnet and ensure the isochronicity of the magnetic field to a precision of $10^{-5}$, by using shimming techniques and trim rods for the fine tuning.

The main parameters of the magnet geometry are summarized in Fig.7.9.
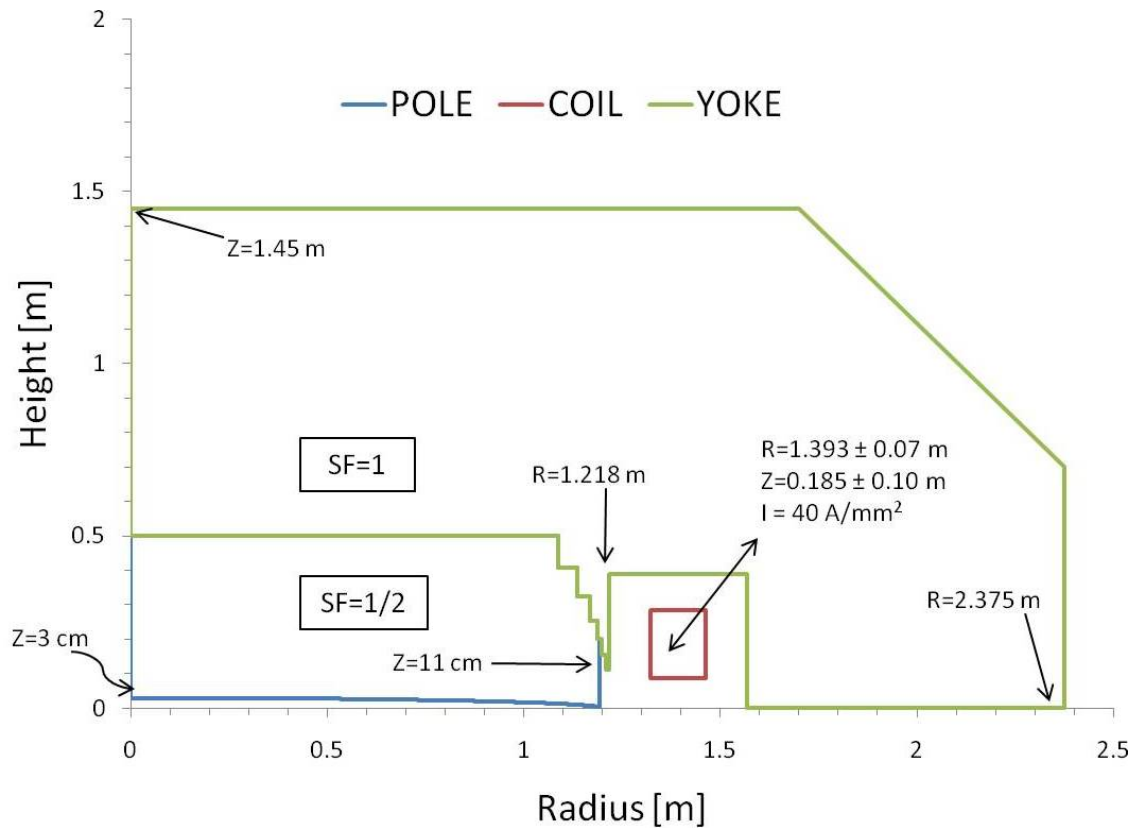
Figure 7.9: Scheme of the IC magnet geometry modeled in OPERA2D(SF stands for stacking factor)

## 7.2  Radiofrequency Design

As detailed in Chap.5, the double gap RF cavity sits in the empty space of a valley. It is divided into the Dee which lies on the median plane and the two Dee stems placed on either side of the median plane and connecting the Dee to the outer wall of the cavity. This is schematized in Fig.7.10.

The Dee is modeled as sections of coaxial rectangular transmission lines with an inner conductor of height $b$ and width $a$ and an outer conductor of height $B$ and width $A$, as shown in Fig.7.11. The stems are modeled as coaxial cylindrical transmission lines with an inner conductor of diameter $d_{stem}$ and an outer conductor of diameter $D_{stem}$.
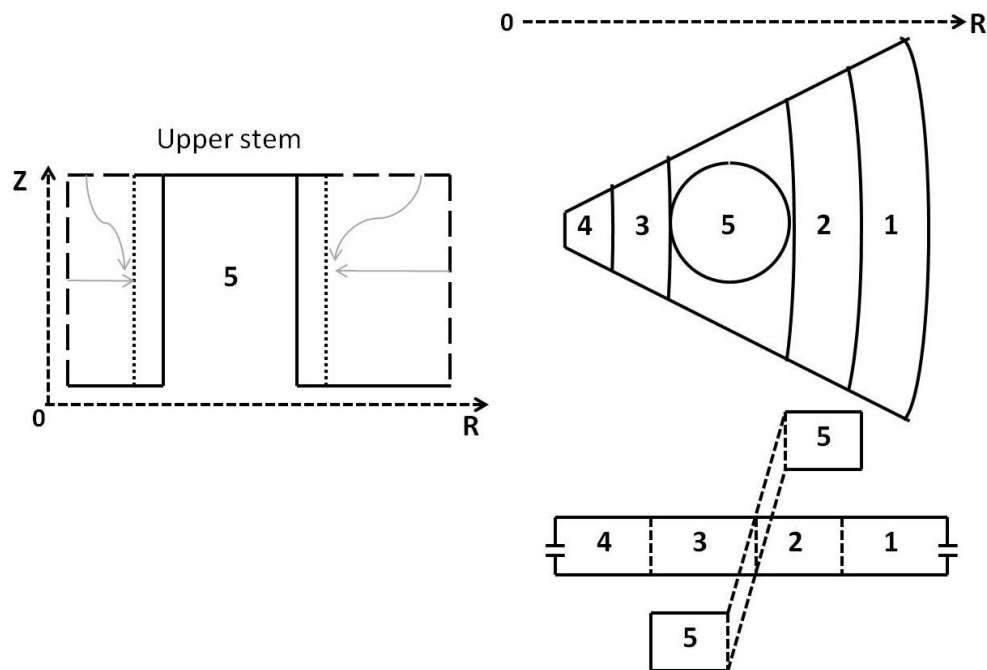
Figure 7.10: IC cavity modeled as sections of transmission lines: sections 1-4 are coaxial rectangular transmission lines (Dee) and the two sections 5 are coaxial cylindrical transmission lines (stem). Note that the number of sections in the figure is arbitrary
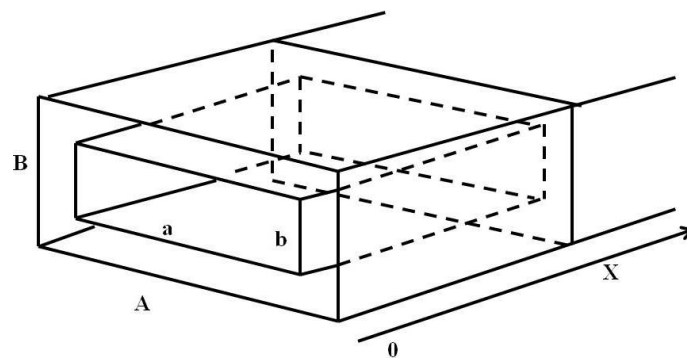


Figure 7.11: Rectangular coaxial transmission line cross-section

## 7.2.1 Constraints on the Parameters

The parameters for the Dee and stems are iteratively adjusted with the constraints detailed as follows:

- the RF cavities are working in fourth harmonic with a resonant frequency of 98.3 MHz. The fourth harmonic is chosen to increase the energy gain compared to lower harmonics and to power both cavities with the same power supply, without needing phase synchronization or phase shifts.

- the cavity should provides at least 70 kV peak voltage at injection and 120 kV peak voltage at ejection.

- the cavity lies between the two radii: 5 cm (injection) and 1.18 m (ejection).

- the maximum valley height is $\pm$ 50 cm.

- the Dee outer conductor stays close to the radial edges of the valley and its azimuthal width is set to $\theta_c = 44°$. This 1° margin (compared to the valley total azimuthal width) leaves place for the water pipes to cool the cavity outer conductor and facilitates the physical introduction of the cavity in the valley. More concretely, the Dee outer width $A$ satisfies: $A(r) = r\,\theta_c$.

- the Dee inner electrode consists of two metal sheets of 1 cm thickness each, separated by 2 cm of vertical space for the beam in the median plane. This geometry is approximated by a rectangular conductor having $b = 4$ cm (the median plane opening is neglected and the two lateral capacities are overestimated).

- the accelerating gap widths, given by $\frac{A-a}{2}$, are an important factor affecting the impedance of the line and determining the transit time factor. At the machine center, the objective is to maximize acceleration on the first turns. The Kilpatrick limit sets the minimum gap to 6 mm (for 70 kV). The gap is then increased linearly along the radius up to a maximum of 4 cm in order to increase the characteristic impedance (and lower the losses) of the line.

- a margin of 3 cm separates vertically the outer electrode from the valley floor. The cavity height $B$ takes different values corresponding to the valley magnetic gap at different radii. In this case, these are: 2 x (50-3) cm, 2 x (40.9-3) cm and 2 x (25.3-3) cm.

- the stem inner conductor is centered on a radius $R_{stem}$ in order to provide the correct voltage variation along the radius in the Dee. Its diameter $d_{stem}$ and that of the outer conductor are adjusted so that the stem has the appropriate length required for the short-circuit at its end.

- The terminal capacity at the outermost radius of the cavity is estimated to 8 pF.

Table 7.1: Dee section parameters

| | Center Position [cm] | Length [cm] | a [cm] | b [cm] | A [cm] | B [cm] | $Z_c$ [Ω] |
|---|---|---|---|---|---|---|---|
| 1 | 113.3 | 9.5 | 79.3 | 4.0 | 87.0 | 44.6 | 27 |
| 2 | 103.8 | 9.5 | 72.6 | 4.0 | 79.7 | 94.0 | 32 |
| 3 | 94.3 | 9.5 | 65.9 | 4.0 | 72.5 | 94.0 | 31 |
| 4 | 84.9 | 9.5 | 59.2 | 4.0 | 65.2 | 94.0 | 31 |
| 5 | 75.4 | 9.5 | 52.5 | 4.0 | 57.9 | 94.0 | 30 |
| 6 | 37.7 | 7.3 | 25.8 | 4.0 | 28.9 | 94.0 | 28 |
| 7 | 30.4 | 7.3 | 20.6 | 4.0 | 23.4 | 94.0 | 27 |
| 8 | 23.2 | 7.3 | 15.5 | 4.0 | 17.8 | 94.0 | 26 |
| 9 | 15.9 | 7.3 | 10.4 | 4.0 | 12.2 | 94.0 | 24 |
| 10 | 8.6 | 7.3 | 5.2 | 4.0 | 6.6 | 94.0 | 22 |

## 7.2.2   Optimized Design

**Dee and Stem**

For the calculation, the Dee is composed of 10 sections. The optimized parameters for the Dee sections and the relative characteristic impedances $Z_c$ are listed in Tab.7.1.

As shown, the Dee sections 5 and 6 are tangent to the stem inner conductor. The radial gap between these two sections corresponds to the space left for the stem inner conductor. The optimized parameters for the stem are given in Tab.7.2. The stem outer conductor dimensions are fictional and are determined to obtain reasonable stem length and power dissipation.

Table 7.2: Stem parameters

| | |
|---|---|
| **Radial Center** | 56.0 cm |
| **Outer Conductor Diameter** | 36.7 cm |
| **Inner Conductor Diameter** | 29.4 cm |
| **Ratio of inner conductor diameter and cavity azimuthal width** | 70 % |
| **Length** | 45.3 cm |
| **Characteristic Impedance** | 13.4 Ω |

The voltage distribution is also evaluated and used to optimize the stem position and impedance. The optimized voltage distribution is shown in Fig.7.12.
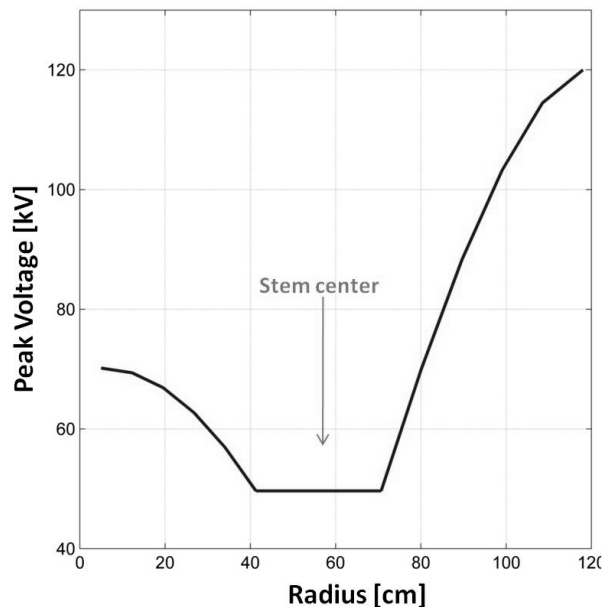


Figure 7.12: Dee voltage distribution along the pole radius

It ensures high peak acceleration voltages at injection and ejection, where the radial gains per turn are very important. In between, the voltage should also be sufficiently large to make the beam cross resonances in the least number of turns.

Finally, the reactive and active power losses are estimated. The detailed results are shown in Tab.7.3.

Table 7.3: RF power calculations

| Section | Active Power [kW] | Reactive Power [MV A] |
|---|---|---|
| Dee | 11.6 | 154 |
| Single Stem (including short-circuit) | 19.3 | 101 |
| Total Stems | 38.5 | 202 |
| Total | 50 | 360 |

The cavity dissipates around 50 kW and $Q \simeq 7100$. The whole RF system thus requires a single 100 kW power amplifier, which is a typical solution for this type of cyclotron.

# 7.3   Injection and Ejection Designs

## 7.3.1   Injection

The central magnetic field corresponds to that used in the design of SCENT. A detailed study of the injection would therefore be redundant. The design of the spiral inflector and central region for SCENT can be found in the bibliography[Campo, 2010b]. The main parameters of the SCENT inflector are given in Tab.7.4.

Table 7.4: Inflector parameters of SCENT. Note that $K \simeq 1.5$

| | |
|---|---|
| **Injection Energy** | 25 keV/u |
| **Magnetic Radius** | 14 mm |
| **Electric Radius** | 43 mm |
| **Tilt angle** | 0.0° |
| **Electrode Gap** | 6 mm |
| **Electrode Width** | 12 mm |
| **Applied Voltage** | ± 6 kV |

This inflector can also be used for this cyclotron. However, a difference which has to be taken into account, is the fact that the present cyclotron design has two RF Dees, while the SCENT cyclotron has four. Indeed, the hills have an elliptical shape and do not leave enough vertical space for electrostatic deflectors. These must therefore be placed in the valleys. The radial gain per turn in the central region will therefore be reduced with respect to SCENT and the shape of the central region electrodes for acceleration and orbit centering will, in a detailed design, have to be modified accordingly.

## 7.3.2   Ejection

**Principle**

In the present design, electrostatic deflectors are for ejection of fully-stripped carbon ions. This is detailed in the following sections. On the contrary, the stripping method is used for ejection of $H_2^+$ (by stripping it to two $H^+$), as in SCENT[Calabretta et al., 2006] and C400[Jongen et al., 2010]. The ejection of $H_2^+$ is however not detailed in this preliminary study.

**Simulation method**

The last orbit turns of the reference particle are simulated with the tracking code ANJO. As shown previously in Fig.7.5, the hills are spiraled and the 0° aximuth which corresponded to the centre of a hill in the (non-spiraled) first radii near the machine center is shifted by some 80° relative to the hill at the outer radii. At the ejection radius, the hills are centered at the azimuths 83°, 173°, 263° and 353°, whereas the valleys are centered at the azimuths 38°, 128°, 218° and 308°. The RF cavities are placed on the valleys centered at 38° and 218°.

The peak voltage on the Dees is set to 120 kV, a typical value for cyclotrons at the ejection radii. The RF phase is adjusted to ensure maximum acceleration of the particles,

producing little less than 240 keV/u kinetic energy gain per turn (due to the transit time factor). Following the trajectory for one turn gives a mean radial gain per turn of 0.6 mm which is consistent with the 0.5 mm computed from Eq.5.6.

The deflector occupies an entire valley (one of the two without RF cavity). The one centered on 128° is chosen because it features the highest radial gain per turn. At the entrance of the valley, the orbit radial separation is 0.8 mm. The beam losses are therefore expected to be very low on the deflector since the radial gain per turn is higher than the sum of the beam radial width and the septum width, which is chosen to be 0.1 mm. The maximal electric field that can be applied with confidence on the deflector is 14 MV/m and this is the value that is used in the simulation.

### Initial Conditions for the Simulation

First of all, the stable orbit for the particle at 230 MeV/u is determined by iteration with the use of the programs ORBLA and ANJO/NAJO. All relevant parameters are summarized in Tab.7.5.

Table 7.5: Ejection parameters used for the simulation. Note that the closed orbit parameters were obtained with ORBLA, the tracking parameters were obtained by iteration with NAJO, the mean radial gain per turn was calculated from Eq.5.6 and the beam emittance used does not take into account any emittance growth at injection or at resonance crossing (a more realistic estimation of the beam emittance is given in Chap.8)

| | |
|---|---|
| **Kinetic Energy** | 230 MeV/u |
| **Closed Orbit Mean Radius** | 1.1596 m |
| **Closed Orbit Maximum Radius** | 1.1798 m |
| **Closed Orbit Minimum Radius** | 1.1358 m |
| **Average Magnetic Field** | 3.9917 T |
| **Mean Radial Gain per Turn** | 0.5 mm |
| **Geometric Emittance** | 0.067 $\pi$ mm mrad (4-rms) |
| **Radial Beam Half-Width** | 0.26 mm (2-rms) |
| **Vertical Beam Half-Width** | 0.33 mm (2-rms) |
| **Vertical Physical Aperture at Hill Edge** | 3 mm |
| **Hill Edge Radius** | 1.192 m |
| **Pole Edge (Skirt) Radius** | 1.218 m |
| **Minimal Radius of the Marginal Field** | 1.18 m |
| **Tracking Initial Azimuth** | 0° |
| **Tracking Initial Radius** | 1.1772 m |
| **Tracking Initial Radial Divergence** | -31.35 mrad |

### Results

Particles trajectories are tracked with ANJO. The radial trajectories of the last two orbit turns are shown in Fig.7.13.
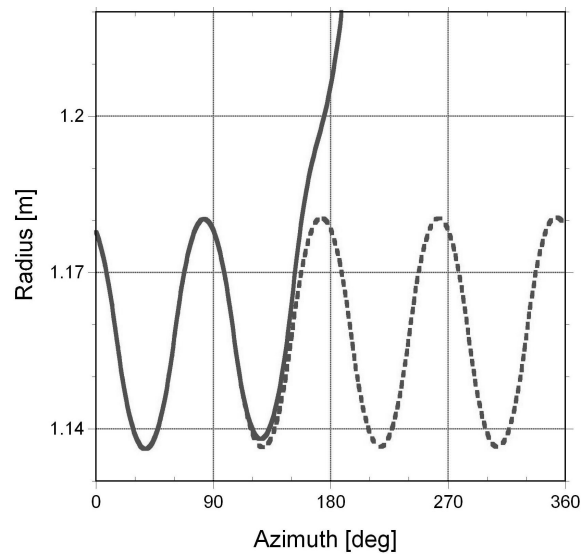
Figure 7.13: Trajectories of the last two turns, the last turn (solid line) is affected by an electrostatic deflector between 106° and 151°

The deflector acting between 105.5° and 150.5° produces an outer radial kick, which displaces the orbit from its stable position towards the marginal field of the hill, at radii higher than 1.18 m. The radial kick is 18.4 mrad at the end of the deflector. This is consistent with the initial estimation of Sec.7.1.1.

The particle exits the hill at azimuth 166.5° with a radial angle of 48 mrad (or 3°). At this point, the so-called skirt starts, the magnet gap widens and the vertical magnetic field drops radially. This has a strong radially defocusing effect on the beam. The field drop and its radial defocusing effect are shown in Fig.7.14 and Fig.7.15.
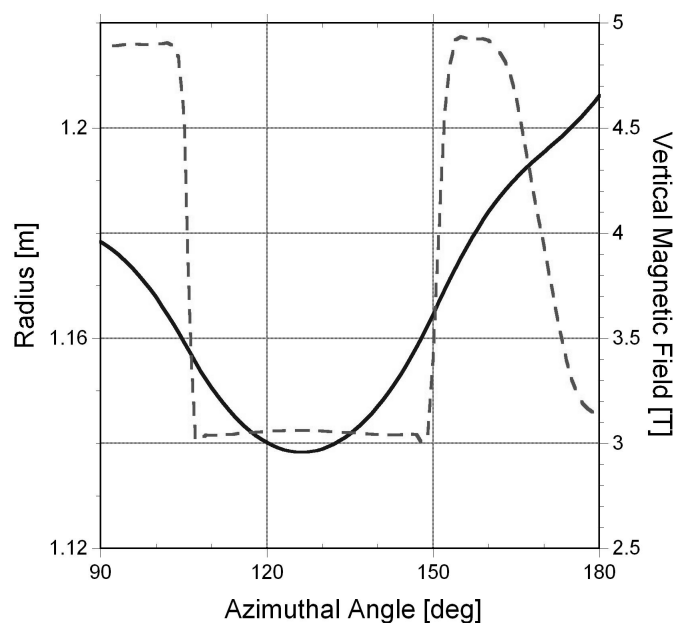


Figure 7.14: Radial path (solid line) and vertical magnetic field (dashed line) encountered by the particle exiting the pole
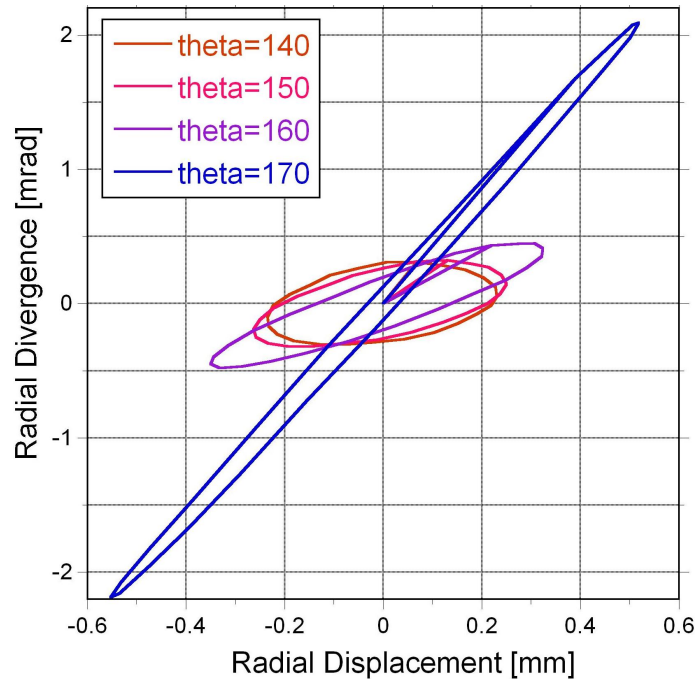
Figure 7.15: Beam ellipses in the radial phase space. Note that the emittance remains constant

Since this is an inherent characteristic of this IC design, it is crucial to prove the feasibility of a correction scheme avoiding the beam blow-up at ejection. The correction is performed before the beam exits the pole, by the introduction of a magnetic channel. Iron bars are placed on either side of the trajectory and a radial separation of a few mm between the trajectory and the hill edge is therefore needed. A reasonable radial separation between the orbit and the end of the hill of 5.5 mm is chosen and the magnetic channel starts at 173° azimuth. The magnetic field radial gradient between the 1.198 m radius and the 1.218 m pole edge radius (between azimuths 173° and 187°) is on average -26 T/m (the maximum is -132 T/m).

The magnetic channel is introduced between the azimuths 173° and 187° and between the radii 1.198 m and 1.217 m. Since only straight sections can be modeled with CANAL, the optimal curved shape which follows the beam path is replaced by three straight sections, each having the same structure and composed of nine rectangular iron bars. A sketch of this geometry as seen by the particle entering the first channel is shown in Fig.7.16.

This particular shape of the iron bars produces a strong quadrupolar field on the axis of the magnetic channel. The magnetic field and relative radial gradient produced are shown in Fig.7.17. The radial gradient on the central axis is around 180 T/m.

The magnetic fields produced by the magnetic channels are superimposed on the cyclotron magnetic field map, in such a way that the central axis of the magnetic channel is within $\pm$ 1 mm of the reference ejection trajectory. Thus, the beam path is not modified by the magnetic field produced by the magnetic channels. The beam trajectory is studied using the program NAJO, with the parameters given previously in Tab.7.5.
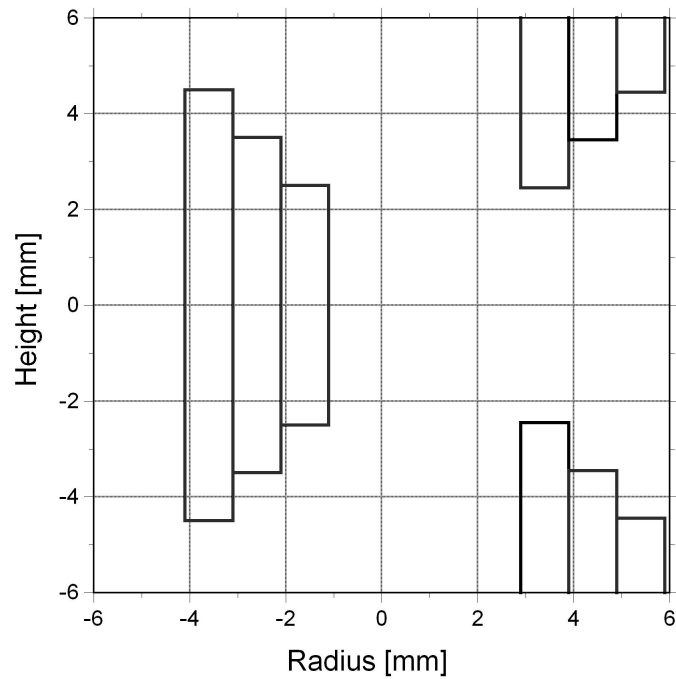
Figure 7.16: Front view of the entrance of the first channel: the origin of the ordinate axis corresponds to the median plane of the cyclotron
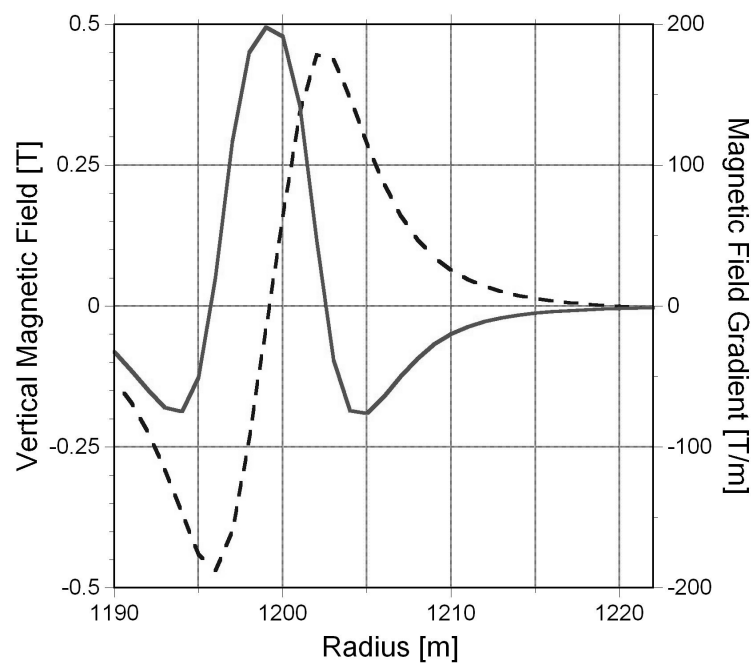


Figure 7.17: Vertical magnetic field (dashed line) and relative radial gradient (solid line) produced by the magnetic channel at its entrance at azimuth 174°

The magnetic field on the median plane and the path of the beam are shown in Fig.7.18.
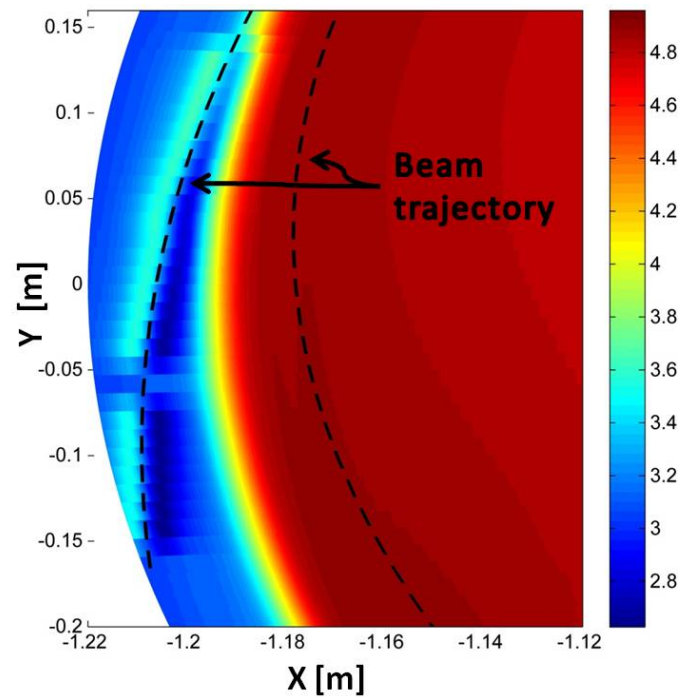


Figure 7.18: Vertical magnetic field (in color) and beam path (in black dashed line) over the last two turns, on a section of the pole. The field distortions introduced by the magnetic channels are clearly visible on the left

A beam with arbitrary focusing conditions and of the correct emittance is tracked for the last two turns. The beam envelopes at ejection are shown in Fig.7.19.
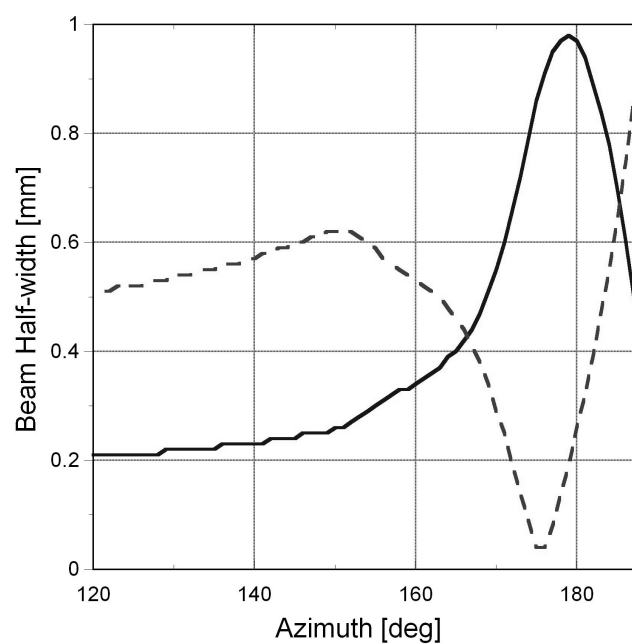


Figure 7.19: Radial (solid line) and vertical (dashed line) beam half-widths at ejection

The initial and final phase spaces for the radial and vertical motions are shown in Fig.7.20 and Fig.7.21, respectively. The 30 % increase of the radial emittance is due to the misalignment of the magnetic channels with respect to the trajectory. This arises from our basic model of the magnetic channel with rectangular iron bars. A more detailed curved geometry which would need a tri-dimensional study would correct this effect, but this is beyond the scope of the present study.
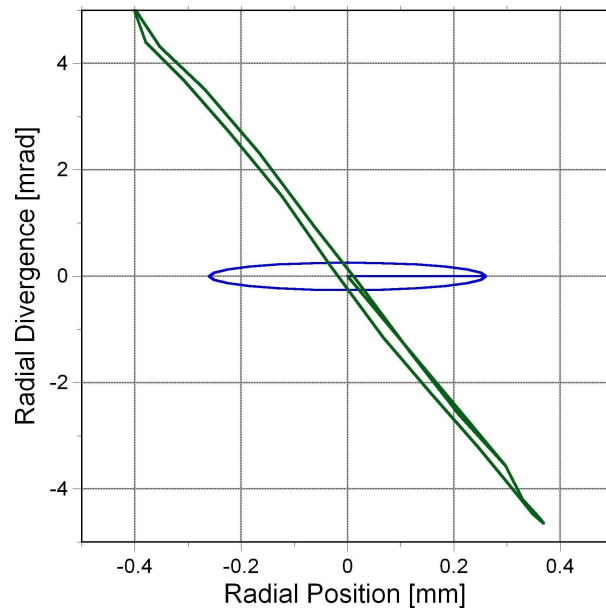


Figure 7.20: Initial (blue) and final (green) beam radial phase spaces at ejection. Note that the emittance grows from 0.07 $\pi$ mm mrad to 0.09 $\pi$ mm mrad
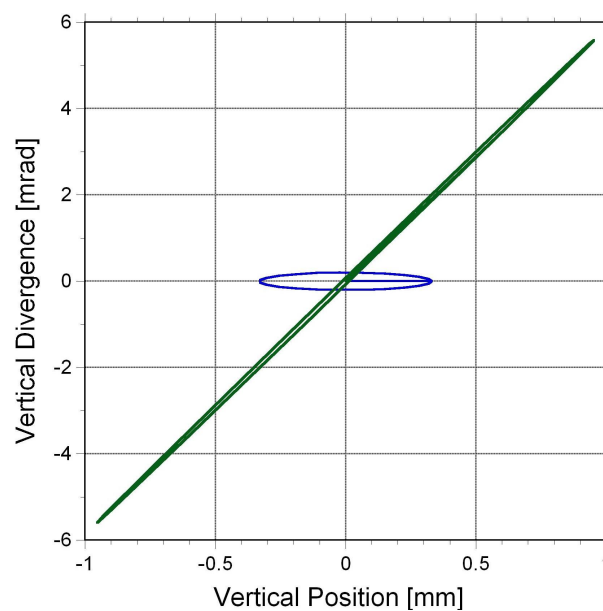


Figure 7.21: Initial (blue) and final (green) beam vertical phase spaces at ejection. Note that the emittance remains constant at 0.07 $\pi$ mm mrad

## 7.4   Discussion concerning $H_2^+$

As stated earlier, the cyclotron is intended for both carbon ion and proton therapies. However, the charge over mass ratio of $C^{6+}$ and $H_2^+$ are slightly different. Indeed, taking into account the charge state of the particles, $\frac{q}{A}(^{12}C^{6+}) \simeq 0.500137$ and $\frac{q}{A}(^{1}H_2^+) \simeq 0.496253$. This 0.78 % difference results in a different isochronous magnetic curve in the cyclotron pole. Various strategies have been proposed to apply these corrections in other ICs: SCENT uses a set of 26 Trim rods[Calabretta et al., 2006] and/or two normal conducting correction coils in the yoke[Campo, 2010b], AGOR uses an addition coil[Brandenburg and AGOR-Construction-Group, 1987] and K800 and C400 split the main coil in 2-3 independently powered subcoils[Jongen et al., 2010; Resmini et al., 1981].

In addition, the RF needed for $H_2^+$ acceleration differs by 763 kHz. This difference must be provided by a mechanical tuning system[Jongen et al., 2010].

## 7.5   Chapter Summary

The design proves the feasibility of an IC with a central magnetic field of 3.2 T and elliptical pole gaps. The elliptical pole gaps allow to limit the total hill axis rotation angle to only 85°. This very moderate spiraling simplifies the geometry of the RF cavity, with respect to superconducting IC designs with the typical constant polar gap. The total iron weight of the magnet is 310 tons, which is even lower than the value for the SC design presented in the previous chapter.

A simplified ejection with a single electrostatic deflector in a valley with no RF cavity is achieved with negligible beam losses. A magnetic channel is placed on the beam path at the exit of the hill, to compensate the strong negative radial gradient of the magnetic field (characteristic of elliptical pole gaps) and provides vertical focusing. The RF system produces an acceleration voltage of 70 kV at injection and 120 kV at ejection, with $Q \simeq 7100$. The two RF cavities can be powered by a single 100 kW power supply. Finally, the inflector design is the same as the one of SCENT.

The IC and SC at 230 MeV/u can thus be accurately compared as injectors for CABOTO, based on designs using the highest possible central magnetic fields and having the same constraints. This is done in the next chapter. The comparison shows that the IC is a better solution compared to the SC, because it is as compact and more reliable. To quantitatively determine the industrial and clinical optimum for the CABOTO injection energy, three complementary ICs of 70, 120 and 170 MeV/u are also studied, based on the 230 MeV/u design and a first optimization of the overall cyclotron-linac system is presented.

# Chapter 8

# Cyclotron Optimization

The designs of Chap.6 and Chap.7 represent two valid and very advanced *compact* cyclotron injectors for CABOTO. Both designs share methodologies and constraints and can thus be compared on an equal footing. The comparison is presented in this chapter. The aim is to determine the best cyclotron in terms of reliability, magnet weight and RF power consumption.

The chosen cyclotron design is then complemented by similar cyclotron designs at output energies of 70, 120 and 170 MeV/u to study the technical, industrial and medical implications linked to the choice of the linac injection energy in a cyclinac hadrontherapy center. It will be shown that the final choice is strongly linked to the clinical aims of the therapy center.

## 8.1 Comparison of Isochronous and (Synchro-) cyclotrons

Two different technologies have been investigated and described in the previous chapters: the superconducting SC[Garonna, 2010] and the superconducting IC. Both designs can be considered as very advanced since they use the highest possible magnetic field.

A careful analysis of the designs and their limitations is done hereafter, in order to compare the two solutions and select the accelerator system that guarantees the highest performance considering the present technology. The conclusion of this comparison is that the IC is the most appropriate solution.

The final design parameters for the SC and IC designs are summarized in Tab.8.1.

Table 8.1: Comparison of the design parameters of the isochronous cyclotron and the synchrocyclotron

| | Isochronous Cyclotron | Synchrocyclotron |
|---|---|---|
| **Accelerated Particles** | $^{12}C^{6+}$ and $H_2^+$ | |
| **Output Kinetic Energy** | 230 MeV/u | |
| **Central Magnetic Field** | 3.2 T | 5.0 T |
| **Pole Type** | 4 Sectors | Axi-symmetric |
| **Pole Radius** | 1.2 m | 1.1 m |
| **Total Current per Coil** | 1.1 $10^6$ A turns | 1.9 $10^6$ A turns |
| **Ion sources** | at least 2 (external) | |
| **Number of RF cavities** | 2 | 1 |
| **RF Harmonic Mode** | 4 | 1 |
| **RF** | 98 MHz | 38-30 MHz |
| **Peak Voltage at Injection** | 70 kV | 28 kV |
| **Peak Voltage at Ejection** | 120 kV | 28 kV |
| **RF Power Supply** | 100 kW | 30 kW |
| **Ion Ejection Method** | Electrostatic Deflector | Magnetic Bump and Electrostatic Deflector |
| **Yoke Diameter** | 4.75 m | 4.6 m |
| **Yoke Height** | 2.9 m | 3.3 m |
| **Iron Weight** | 310 tons | 330 tons |

## 8.1.1   Magnet Size

The initial assumption that the SC would constitute a more compact solution, because of its higher central magnetic field, proves to be incorrect: both designs show very similar magnet weights and yoke dimensions. As explained in Sec.5.5.3, the size of the cyclotron magnet is strongly influenced by the limit imposed on the stray magnetic field outside of the cyclotron. The same criterium was applied to the SC and the IC designs. In addition, the same coil current density and space around the coil (for the cryostat and coil support) were applied in both designs. Therefore, the differences between the two designs can only originate from the position and the cross-section of the coil.

The IC, even though it has a lower central magnetic field, manages to reach the same compactness as that of the higher central magnetic field SC because of two main reasons. Both characteristics of the IC design contribute to minimize the magnetic flux in the return yoke.

These are:

a) the elliptical hill and valley gaps allow to reduce the fringing polar magnetic flux to its minimum. The pole radius is minimized. This maximizes the useful part of the pole flux and reduces the additional magnetic flux needed from the coil.

b) the coil position is closer to the median plane and the pole edge, thus providing the needed radial increase of the magnetic field in the median plane.

Instead, in the SC design, the magnet gap is larger due to the presence of the Dee and this increases considerably the fringing part of the polar flux because of the increased pole radius. Furthermore, the condition of having a radially decreasing field translates into a coil position far from the pole edge (radially) and/or far from the median plane (vertically). This also increases the fringing flux contribution from the coil and the total magnetic flux to be stored in the return yoke.

## 8.1.2 Magnet Complexity

Because of the elliptical pole gaps, the spiraled sectors and the high precision required in the magnetic field, the IC magnet is certainly more complex than the SC magnet, which has an axisymmetric pole and loose requirements on the magnetic field precision. This means that both the three-dimensional design and the manufacturing of the magnet disfavor the IC design.

## 8.1.3 RF Power

Although the low accelerating voltage of the SC RF system implies many challenges in the design of the injection and ejection systems, it allows to reduce by more than three the RF power requirements compared with the IC. As in the case of the SC, the RF power consumption could be reduced in the IC by pulsing the power sent to the RF cavities, a procedure which is under investigation in collaboration with L. Calabretta and the K800 team at LNS. This has never been tested before because ICs normally operate in continuous mode. The RF switch on time is about 50 $\mu$s. Instead of a complete switch off, the cavity voltage could be reduced by a factor 4, in order to maintain thermal and electrical stability. This would result in an electrical power reduction of a factor 16.

In terms of magnet power consumption, there is no substantial difference between the two cyclotron designs and about 40 kW should be added to the RF power consumption to account for the cryogenic cooling. Therefore, the total installed electrical power is 140 kW for the IC and 70 kW for the SC, which goes in favor of the SC. However, both of these power requirements are very minor compared to those of the CABOTO linac (see Tab.8.4). The choice between the SC and the IC should therefore not be based on the RF power.

## 8.1.4 RF System Complexity

The pole with elliptical gaps of the IC allows to introduce very moderate spiraling (similar to that of the COMET cyclotron, having a lower central magnetic field and lower output energy) and thus, the design and manufacturing of the RF cavities are within the current

industrial capabilities. On the contrary, the RF system for the SC has the disadvantage of requiring a frequency modulation system, bringing its burden of complexity and reduced reliability, as detailed in Sec.6.2.3, and represents therefore the worse solution.

### 8.1.5 Injection and Ejection

Both designs use spiral inflectors with similar K-values. However, the SC requires to use a narrow electrode width because of the smaller orbit radial gain on the first turn. This involves also mechanisms to contain the fringing field effects of the electric field (see Chap.6). However, a more significant difference in the IC and SC designs comes from the ejection system. Here also, the small orbit radial gain per turn of the SC creates complications, whereas in the IC, the natural radial gain per turn coming from the acceleration is enough to eject the particles with a single electrostatic deflector placed inside a free valley. Therefore, the complexity of both injection and ejection systems disfavors the choice of the SC.

### 8.1.6 Dual Acceleration

The difference in $\frac{q}{A}$ between $H_2^+$ and $C^{6+}$ is critical for the IC. Various solutions have been proposed to correct the magnetic field and the RF (see Chap.7) but none are simple because of the small phase acceptance and high precision needed for the magnetic field. This situation does not occur in SCs where the tolerances on the magnetic field precision are more relaxed.

All things considered, the IC is a better solution for the two most crucial parameters: the overall reliability and magnet size.

## 8.2 Designs of Cyclotron/Linac at Different Energies

The main feature of cyclinacs is the possibility to vary the energy of the hadron beam electronically, by switching off a certain number of klystrons and changing the amplitude and/or phase of the drive signal sent to the last active klystron. To take advantage of the linac modularity, the cyclotron injector should have an output energy between 70 MeV/u and 230 MeV/u. The maximal energy of the cyclotron of 230 MeV/u allows to install a separate beam line for protons ($H_2^+$ ejection by stripping) at 230 MeV for protontherapy using standard passive energy modulation techniques. At the other extremum, the minimal energy of the cyclotron of 70 MeV/u allows to install a separate beamline for protons ($H_2^+$ ejection by stripping) at 70 MeV for protontherapy of ocular tumors.

### 8.2.1 Isochronous Cyclotron Designs

IC designs at 70, 120, 170 MeV/u have been studied based on the same methods and constraints as the IC design at 230 MeV/u. The designs are limited to the magnetic and the RF systems: the injection system is exactly the same as that of the 230 MeV/u design and the ejection is naturally simpler for lower beam magnetic rigidities. However, the major difference compared to the 230 MeV/u design lies in the fact that the ejection of $H_2^+$ ions by stripping is not possible, because $H^+$ would not be accelerated by the linac, which is designed to accelerate $C^{6+}$. The ejection of the $H_2^+$ beam should be designed to use the

same electrostatic deflector and magnetic channels as for the $C^{6+}$ beam. In the simplest configuration (maintaining the same central magnetic field and changing both the RF and the radial variation of the mean magnetic field to make the field isochronous), the difference in $\frac{q}{A}$ between the two ion species would result in a difference of kinetic energy at ejection. For example, the ejection system for the $C^{6+}$ beam at 230 MeV/u would only be able to extract the $H_2^+$ beam at around 226 MeV/u. The 0.9 % difference in momentum at the entrance of the linac would however need to be corrected by designing the linac with a lower input energy of 226 MeV/u and when using carbon ions (at 230 MeV/u), either switch off the first accelerating cells or introduce a small absorber before the injection in the linac. These modifications to the linac would not be needed with a fine tuning of the central magnetic field, RF frequency and magnetic field profile, which can make the orbit of the two ion species coincide at the extraction radius with the same kinetic energy[1].

An advantage linked to the post-acceleration of an $H_2^+$ beam in the linac is that it opens the way to the proton radiography of patients (see Chap.1).

As already pointed out in Chap.7, the model for the design of the RF cavities of the IC has a rather simplistic approach and the values stated for the power consumption are thus to be taken as qualitative. However, the following sections will demonstrate that the RF power consumption has a very small impact on the outcome of this optimization study.

The results of the three cyclotron designs are summarized and compared to the 230 MeV/u design, in Tab.8.2.

---

[1]private communication, L. Calabretta (LNS)

Table 8.2: Parameters of IC designs for various output energies

| | | | | |
|---|---|---|---|---|
| Magnetic Rigidity [T m] | 2.45 | 3.25 | 3.92 | 4.63 |
| **Output Kinetic Energy [MeV/u]** | **70** | **120** | **170** | **230** |
| Number of Sectors | 4 , Elliptical | | | |
| Central Hill Half-gap [cm] | 3.0 | | | |
| Central Magnetic Field [T] | 3.2 | | | |
| **Pole Radius [m]** | **0.761** | **0.955** | **1.092** | **1.218** |
| Elliptical Hill Profile Radius [m] | 0.735 | 0.923 | 1.067 | 1.193 |
| Central Valley Half-gap [cm] | 45 | 50 | 52 | 50 |
| Max. Spiral Angle [°] | 49 | 57 | 63 | 68 |
| **Max. Sector Azimuthal Rotation [°]** | **34** | **54** | **69** | **85** |
| Max. Coil Current Density [A/mm$^2$] | 40 | | | |
| Coil Centroid Radius [m] | 0.946 | 1.135 | 1.268 | 1.393 |
| Coil Centroid Height [m] | 0.235 | 0.235 | 0.205 | 0.185 |
| Max. Magnetic Field Modulus in Yoke inner edge [T] | 2.0 | | | |
| Yoke Diameter [m] | 3.18 | 3.8 | 4.3 | 4.75 |
| Yoke Height [m] | 2.2 | 2.5 | 2.7 | 2.9 |
| **Iron Weight [tons]** | **100** | **170** | **240** | **310** |
| Number of RF Cavities | 2 | | | |
| RF (harmonic) [MHz] | 98 (4) | | | |
| Peak Voltage at Injection-Ejection [kV] | 70-120 | | | |
| **RF Power Supply [kW]** | **90** | **94** | **110** | **100** |

In order to benchmark the cyclotron designs, a bibliographic research of all superconducting compact cyclotrons and designs by experienced research groups was made. Their magnet weights and RF power consumptions are listed in Tab.8.3.

As shown in Fig.8.1, the iron weights calculated in this study are consistent with the values of similar existing cyclotrons and designs.

Table 8.3: Parameters for various existing and designed superconducting cyclotrons. Note that the values were compiled from various sources[Craddock and Symon, 2008; Walter, 2001] and should be taken as indicative (in particular the RF power, which is not clearly defined in the literature)

|  | Pole Radius [m] | Iron Weight [tons] | RF Power Installed [kW] | RF Cavities |
|---|---|---|---|---|
| K500 | 0.7 | 100 | 240 | 3 |
| Harper Hospital | 0.3 | 25 | 25 | 3 |
| K1200 | 1.1 | 270 | 920 | 3 |
| AGOR | 1.0 | 330 | 200 | 3 |
| COMET | 0.8 | 90 | 110 | 4 |
| C400 | 1.9 | 700 | 100 | 2 |
| SCENT | 1.3 | 350 | 200 | 4 |
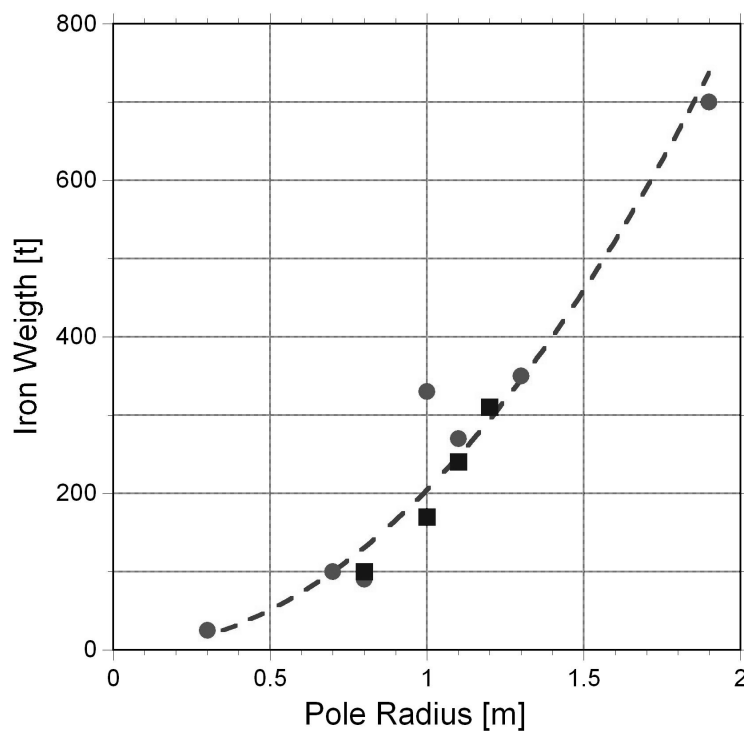


Figure 8.1: Plot of the iron magnet weights in relation to the pole radius, compiled from the data of Tab.8.3 (in circles) and Tab.8.2 (in squares). The fit (dashed line) indicates a second-order polynomial trend (coefficient of determination $R^2 = 0.94$)

## 8.2.2   Linac Designs

In parallel, a comparative study for the linac at various injection energies was performed by A. Degiovanni (TERA). The critical parameters for each design were the length of the linac and the RF power consumption. The results are summarized in Tab.8.4.

Table 8.4: Parameters for CABOTO injected at various energies

| Input Kinetic Energy [MeV/u] | 70 | 120 | 170 | 230 |
|---|---|---|---|---|
| Klystron and Line Power Loss | 33 % | | | |
| RF duty cycle | 0.1 % | | | |
| Repetition Rate | 300 Hz | | | |
| RF | 5.7 Ghz (C-band) | | | |
| Klystron Power | 12 MW | | | |
| Number of Klystron Modules | 20 | 16 | 13 | 9 |
| Linac Length [m] | 32 | 27 | 22 | 16 |
| Average RF Power Consumption [kW] | 720 | 580 | 470 | 320 |

# 8.3   Industrial Comparison

## 8.3.1   Accelerator Building Size

In terms of industrial cost of an accelerator, an important factor is the size of the building hosting the accelerator. This area has to accomodate cranes for lifting heavy material, high power cabling and thick walls for radiation shielding. Thus, its cost is a very important quantity to minimize. After an analysis of the layout of the existing clinical protontherapy centers (cyclotron bunkers and beam transport lines, among others) and various designs of linac-based therapy centers, the following assumptions are made to estimate the accelerator building size:

- the cyclotron bunker area is approximately 4 times the area occupied by the cyclotron magnet

- the average width of the linac corridor is of 4 m

For the cyclotron, the space needed for the cryogenic unit, the RF amplifiers and the ion sources (typically placed in a room under the cyclotron and injected from below) need to be accounted for. It was therefore chosen to make the cyclotron bunker area proportional to 9 times the area occupied by the cyclotron magnet. This corresponds to adding a ring around the cyclotron with a radial width of twice the cyclotron outer radius.

For the linac, space for the klystrons is counted by adding 15 m$^2$ of bunker surface for each klystron used.

The final results are shown in Tab.8.5.

Table 8.5: Accelerator building area for various cyclinac configurations

| Input Kinetic Energy [MeV/u] | 70 | 120 | 170 | 230 |
|---|---|---|---|---|
| Cyclotron Bunker Area [m$^2$] | 70 | 100 | 130 | 160 |
| Linac Bunker Area [m$^2$] | 430 | 350 | 280 | 200 |
| Total Accelerator Bunker Area [m$^2$] | 500 | 450 | 410 | 360 |

For the cyclotron output energies studied, the cyclotron building would have an area ranging from 70 to 160 m$^2$ and the linac building would have an area ranging from 200 to 430 m$^2$. Clearly, the linac building is the driving term in the overall accelerator building size. Minimizing the surface of the accelerator building corresponds to maximizing the cyclotron output energy. It has to be pointed out that other elements of a therapy center (such as the beam lines and the gantries) occupy considerable space. Therefore, the space occupied by the cyclotron and linac discussed here should not be the only parameter determining the optimal cyclotron energy.

## 8.3.2  Electrical Power Consumption

In terms of RF power consumption, even taking the pessimistic assumption that the RF power needed is the same for all cyclotron output energies and the RF system is not pulsed but always powered, the linac power consumption is the driving term in the overall RF power consumption. This is shown in Tab.8.6.

Table 8.6: Accelerator power consumption for various cyclinac configurations

| Input Kinetic Energy [MeV/u] | 70 | 120 | 170 | 230 |
|---|---|---|---|---|
| Cyclotron RF Power [kW] | | 100 | | |
| Cyclotron Magnet Power [kW] | | 40 | | |
| Linac RF Power [kW] | 720 | 580 | 470 | 320 |
| Total Power Consumption [kW] | 860 | 720 | 610 | 460 |

In this analysis, only the RF power of the linac, the RF power of the cyclotron and the cryogenic power linked to the cyclotron magnet operation are taken into account.

Given the present comparisons, in order to minimize the overall accelerator building size and overall power consumption, the cyclotron energy has to be maximized: the initial choice of an output energy of 230 MeV/u looks therefore optimal. Naturally, in a more complete industrial optimization of a therapy center, many other parameters should be taken into account. For example, the considerable building space needed for the beam lines and the gantries will put into perspective the importance of the accelerator building size.

## 8.4   Comparison in Terms of Clinical Capability

The previous sections showed how the configuration with the highest cyclotron output energy (and linac injection energy) is the most industrially effective solution, both in terms of the space occupied by the accelerator and in terms of power consumption. However, the clinical implications for the energy modulation of the linac have also to be taken into account.

Indeed, the fast energy modulation of the linac is the main specificity of cyclinacs and one of its best features. In order to take full advantage of this, the range covered by the modulation should correspond to the range of energies needed to treat most tumors. The ranges in water for 70 MeV/u, 120 MeV/u, 170 MeV/u and 230 MeV/u carbon ions are respectively[Ziegler et al., 2008] 1 cm, 4 cm, 6 cm and 11 cm.

The survey of clinical treatments with carbon ions at HIMAC[Noda et al., 2007] over a period of more than ten years is presented in Fig.8.2. The most common tumor indications are prostate, lung and head and neck (indicated as *H&N* in the figure). The maximum ranges used for these cases vary between 5 and 25 cm. Having optimal beam conditions for lung tumor treatment is crucial to demonstrate the capabilities of the fast energy modulation of linacs for the treatment of moving organs.

This data therefore favors having a minimal energy of carbon ions at the exit of the linac of 150 MeV/u (corresponding to a 5 cm range in water), to cover the whole spectrum of tumor indications, with a linac-based active beam energy modulation system. Whether ion beams from the cyclotron of energies higher than 150 MeV/u could be safely decelerated and transported in the linac is currently under investigation at TERA. This information is important for $H_2^+$ beams, as the proton energies needed for the treatment of ocular tumors are as low as 70 MeV (4 cm range in water). In the worst case scenario, where beam deceleration is not possible in the linac, the $H_2^+$ beam coming out of the linac is stripped to a 150 MeV proton beam (16 cm range in water) and a small energy degrader is then used to produce beam energies down to 70 MeV.
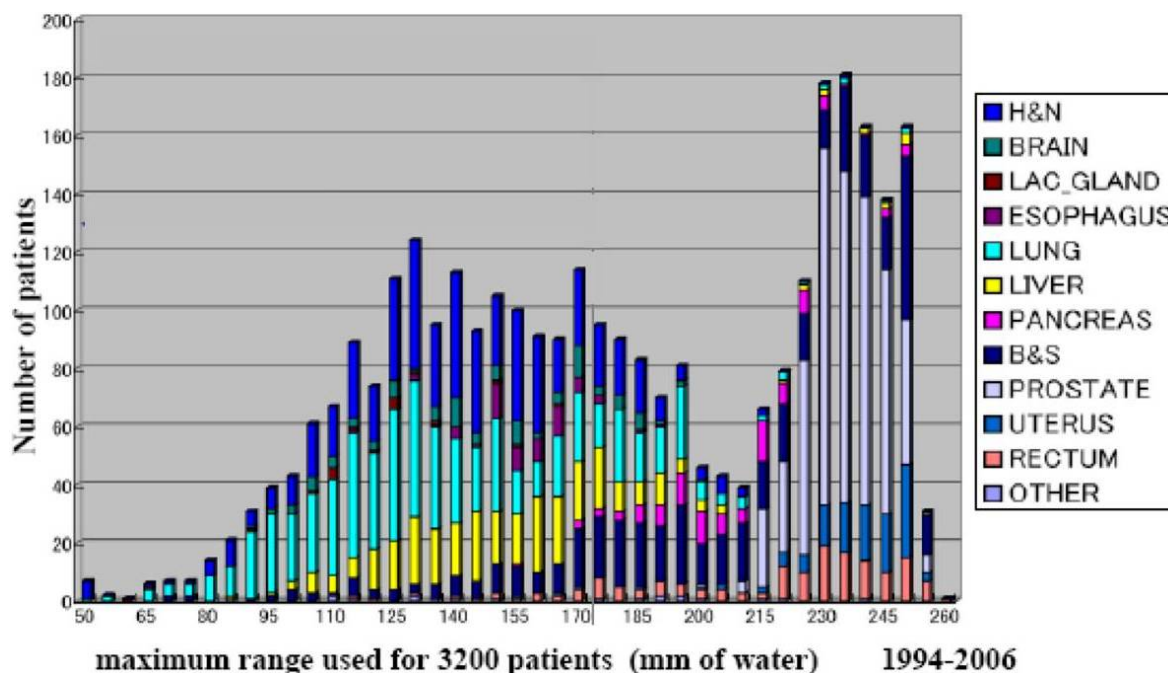
Figure 8.2: Number of patients as a function of the water equivalent depth of the maximum range used for each patient. The 3200 HIMAC patients from 1994-2006 had the tumors indicated in the inset (courtesy of Dr. Hirohiko Tsujii)

## 8.5 Final Cyclotron-Linac Configuration

On one hand, accelerating particles up to 230 MeV/u in the cyclotron represents the most industrially effective solution for a dual therapy center. However, it implies using passive energy degraders for the proton beam (70-250 MeV) and for the carbon ion beam[2] (150-400 MeV/u). This solution would suit centers wishing to first treat patients with protons and allow an upgrade to carbon ions in a second phase.

On the other hand, accelerating particles up to 70 MeV/u in the cyclotron enables the use of a linac-based active energy modulation system for both ion species. This solution is therefore suited for centers conceived as dual proton and carbon ion clinical research facilities using the same beam delivery system and treatment protocols. However, it represents a very costly solution, as it implies a very long and power consuming linac.

The analysis presented in this chapter reveals that a 150 MeV/u cyclotron energy represents the best compromise when considering overall accelerator size and power consumption and the possibility of beam delivery with fast cycling beams. In this case, the carbon ion beam would span the needed energy range (150 - 400 MeV/u) while the protons would be directly produced by the linac in the energy range 150 - 250 MeV. To treat shallow tumors, the 150 MeV/u $H_2^+$ beam would be decelerated in the first units of the linac, a possibility which is presently under study by TERA. Any further energy decrease of the output proton beam would be obtained with a standard, but simpler, ESS.

Therefore, the final decision strongly depends on the clinical aims of the therapy center.

---

[2]possibly, part of the carbon ion energy reduction could be made by decelerating the beam with the first units of the linac; this possibility is under study by TERA

In the next sub-section, the 150 MeV/u cyclotron solution is further detailed.

### 8.5.1 Beam Parameters along the Cyclinac

The output emittance of the cyclotron is estimated based on the studies carried out for SCENT, C400 and COMET. This is a delicate task since everything depends on the final magnetic field of the cyclotron. The beam dynamics studies carried out for the C400[Jongen et al., 2010] showed that, without any sextupole correction, the beam emittance can grow by factors between 6 and 40 due to the non-linearities of the magnetic field in the beam path from the end of the pole to the exit of the cyclotron. In addition, the emittance growth linked to the beam injection through the SCENT spiral inflector is roughly a factor 4[3]. Finally, the emittance growth during resonance crossings depends strongly on the amplitude of the betatron oscillations[Jongen et al., 2007, 2006; Schippers et al., 2004]. Considering the smaller output energy of the cyclotron compared to the design of Chap.7 and the small emittance of the EBIS-SC compared to the standard ECRIS (see Chap.4), the emittance growth during acceleration should be less important than for the ejection and injection.

All things considered, the total emittance growth factor is estimated to be 24 from the source to the injection in the linac. This corresponds to a beam emittance at the output of the cyclotron of 1.2 $\pi$ mm mrad (normalized, 4-rms). The Fig.8.3 summarizes the carbon ion kinetic energies, average currents and transverse geometric emittances along the cyclinac.
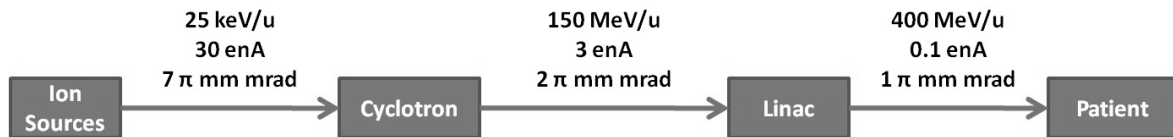


Figure 8.3: Carbon ion average currents and transverse geometric emittances (4-rms) along the cyclinac

### 8.5.2 General Considerations

Based on the cyclotron designs of Tab.8.2 and the linac designs of Tab.8.4, the weight of the 150 MeV/u cyclotron can be estimated to be 200 tons, the length of the linac 24 m and the total power consumption of the cyclinac 600 kW. It is interesting to note that the cyclotron has a weight and spiraling which are similar to that of the most widely used cyclotron for protontherapy, the normal conducting C235 (see Chap.2). This shows the industrial viability of the advanced design of this 150 MeV/u cyclotron.

A comparison between the dimensions of different carbon ion accelerators is shown in Fig.8.4.

---

[3]private communication, L. Calabretta (LNS)
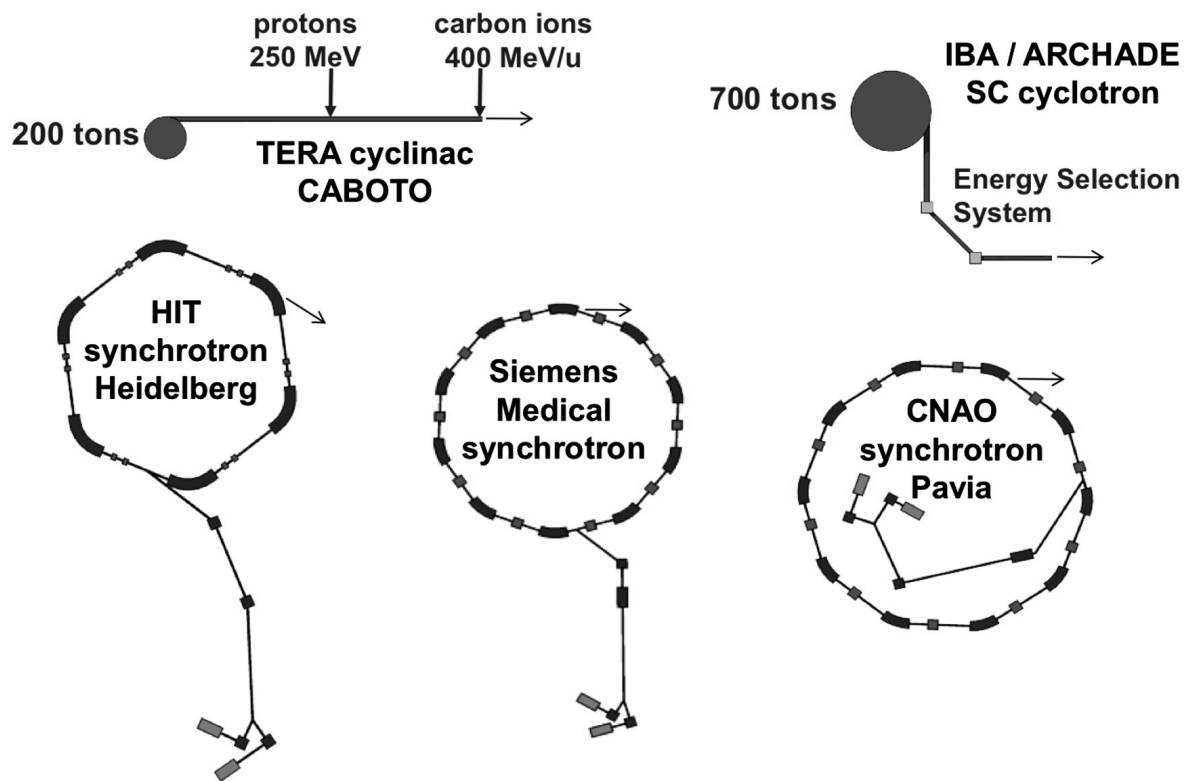
Figure 8.4: Dimensional comparison of the cyclinac solution with the European carbon ion accelerators (courtesy of M. Garlasché, TERA)

When judging the length of the linac, the natural yardsticks are:

1) the diameter of a synchrotron of equal energy (6–8 m for protons and 18–25 m for carbon ions), with its injector linac (15–20 m long),

2) the length of the ESS needed for reducing the energy of the proton and carbon ion beams coming from a cyclotron, which is 15–20 m long.

Three considerations play in favor of the cyclinac. Firstly, the two solutions using cyclotrons are more compact with respect to the synchrotron ones. Secondly, the C400 cyclotron is 3.5 times heavier than the CABOTO cyclotron. Moreover, the transverse emittances of the linac beam are smaller than the ones of the other accelerators of Fig.8.4. This entails smaller and lighter beam transport magnets.

This final cyclinac configuration is presented in Fig.8.5.
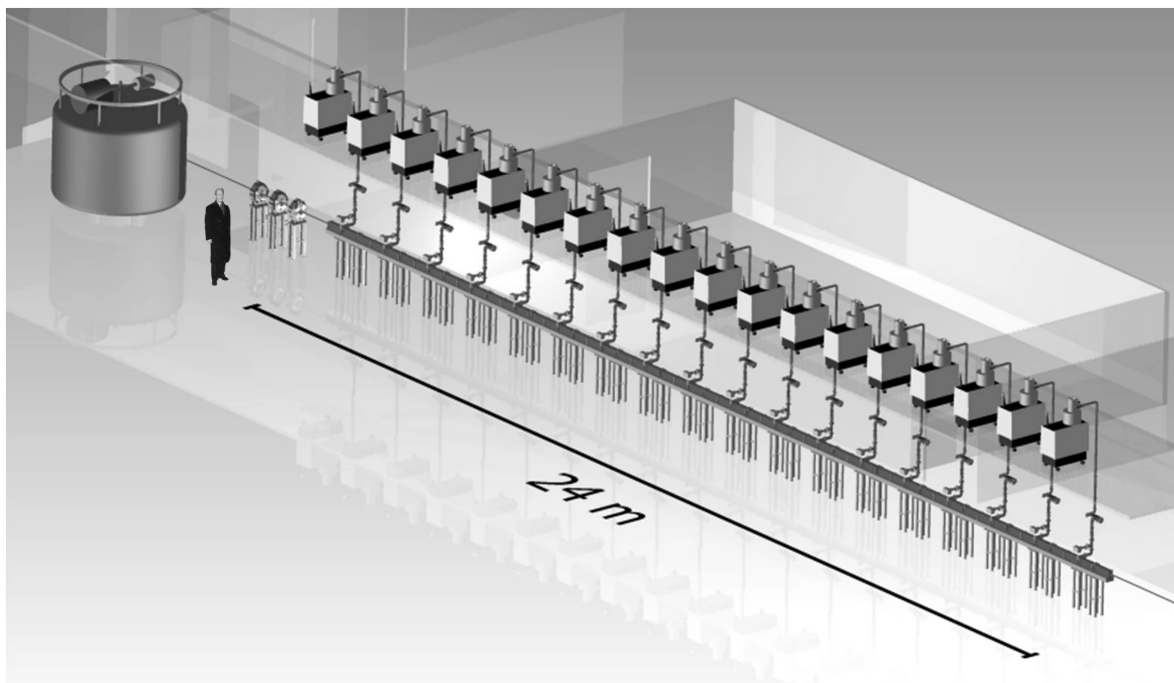
Figure 8.5: Model view of the cyclotron (150 MeV/u) and the linac (150–400 MeV/u), courtesy of M. Garlasché (TERA)

# Conclusion

Ion beam therapy offers attractive radiobiological, physical and clinical advantages. This explains its recent development, with many new clinical centers opening every year. However, the spread of advanced beam delivery systems (like the spot-scanning technique and the methods for irradiating a moving tumor) reveal the performance limitations of current accelerators. The cyclotrons used for protontherapy have the disadvantage of requiring a passive energy degradation system which leads to neutron activation. The synchrotrons suffer from the fluctuations of the extracted beam current and the low repetition rate at which the energy of the beam can be changed. In this perspective, the fast electronic energy variation of the RF linacs is a very important property for ion beam treatment. Their association with a fixed energy *compact* (as opposed to separated-sector) cyclotron is called *cyclinac* and is a long term development of the TERA Foundation. The focus of this PhD thesis is the quantitative assessment of the optimal injector to CABOTO: a 400 MeV/u high-gradient high RF linac delivering $C^{6+}/H_2^+$ beams with short pulse length (1.5 $\mu$s) and fast repetition rates (100-300 Hz).

Ideally, the specific time characteristics of the CABOTO beam should be met already at the source level. All dual proton/carbon ion centers use ECRIS in continuous current operation. Based on the maximum number of ions needed to deliver a clinical dose rate of 2 Gy/min to a 1 L tumor centered at 20 cm depth in water with a multipainting spot-scanning delivery method and the estimated 0.2 % cyclinac total beam transmission, the needed average currents in the pulse from the source are 60 e$\mu$A for $C^{6+}$ at 300 Hz and 1 mA for $H_2^+$ at 100 Hz. These requirements are not compatible with the sources presently used in therapy centers, but are met for $H_2^+$ by standard multicusp ion sources. The continuous current beam produced can be chopped at low energy to produce the required repetition rate and pulse length.

For carbon ions, the high repetition rates and short pulse lengths required by cyclinacs are very well-suited to the characteristics of EBIS. After measurements with the commercial source EBIS-A (Dreebit Gmbh), the tests on the Krion2 (JINR) and based on the simulated performance of the new superconducting EBIS-SC (Dreebit Gmbh), the use of three EBIS-SC at 100 Hz repetition rate in alternating mode was chosen. The EBIS-SC is characterized by a very small transversal beam emittance: only 0.05 $\pi$ mm mrad (normalized, 4-rms).

The injector to CABOTO should provide fixed energy beams of $C^{6+}/H_2^+$ in the most compact, energy-efficient and reliable way. The cyclotron energy should lie between 70 MeV/u (for protontherapy of ocular tumors) and 230 MeV/u (for protontherapy of deep-seated tumors with passive degraders). However, the existing *compact* cyclotrons can

only reach up to 200 MeV/u (K1200 of Michigan State University). Therefore, new designs have been produced. Once the optimal cyclotron at 230 MeV/u is determined, lower energy cyclotrons can easily be designed.

The design methods used have the particularity of adressing all the most critical challenges related to high magnetic field cyclotrons using nearly only analytical and two-dimensional modeling. They are therefore much faster than precise three-dimensional modeling and particularly adapted for this comparative study. Similar constraints for the two designs are imposed on the superconducting coil, the magnetic stray field outside of the cyclotron and the RF cavity parameters, so that the two designs can be quantitatively compared on an equal footing. This is the first time that such a comparison has been produced.

A 230 MeV/u superconducting SC is first investigated as a possible injector for CABOTO. This type of cyclotron is a good candidate because: it can be designed at very high magnetic field and can be pulsed at the same repetition rate as the linac.

The SC central magnetic field is 5 T. The design features an axially symmetric pole of 1.1 m radius. The coil and pole are designed in order to obtain a constant magnetic field index of 0.02. The OPERA2D model gives a total iron weight of 330 tons. The RF system is composed of a 180° Dee in the aperture of the magnet providing a peak acceleration voltage of 28 kV, a transmission line and a mechanical capacity modulation system, outside of the cyclotron magnet. The Dee is modeled as sections of coaxial rectangular transmission lines with a constant characteristic impedance. The RF is modulated from 38 MHz at injection to 30 MHz at ejection. This corresponds to a capacity variation between 90 pF to 900 pF. The RF system has a Q-value of 2500 and requires a 30 kW power supply. The axial injection system is complicated by the small magnetic radius of 6 mm and a radial gain on the first turn of a few millimeters. The spiral inflector has a special geometry to allow beam transmission with negligible losses. The radial gain per turn of only 70 $\mu$m at the ejection radii is boosted to 0.2 mm by a static magnetic perturbation (of 0.1 T maximum amplitude and 5° azimuthal width) exciting the first integer radial resonance. This radial orbit separation obtained without any emittance growth is sufficient to place an electrostatic deflector pushing the beam trajectory out of the pole with 30 % beam losses. Overall, the design proved the feasibility of a 230 MeV/u synchrocyclotron working at 5 T magnetic field.

The SC's best features are the simple and compact magnet and the low RF power consumption. However, its reliability is brought to question by the need of a rotative capacitor and by the complexity of the injection and ejection systems. Therefore, a more reliable solution is studied for injection in CABOTO: a superconducting IC at 230 MeV/u. The isochronous cyclotron design features a central magnetic field of 3.2 T, four sectors, two RF cavities and elliptical pole gaps. It has to be noted that isochronous cyclotrons with elliptical pole gaps have never been designed at such high magnetic fields. Adequate focusing is achieved with a total hill axis rotation angle of only 85°. This very moderate spiraling simplifies the geometry of the pole and of the RF cavity, with respect to superconducting IC designs with the typical constant polar gap. The two-dimensional OPERA model, including the superconducting coils and the yoke, produces a magnetic field in the beam acceleration region with deviations from the isochronous curve under 1 %. The total iron weight of the magnet is 310 tons. The two RF cavities are placed in

the magnet gaps of two valleys. The Dee is modeled as sections of coaxial transmission lines. The acceleration voltage is 70 kV at injection and 120 kV at ejection, for a power consumption of the cavity of 50 kW and a Q-value of 7100. The inflector is the same as the one studied for SCENT (LNS). The ejection is achieved with a single electrostatic deflector placed in a free valley. A magnetic channel on the beam path at the exit of the hill is studied to compensate the strong negative radial gradient of the magnetic field (characteristic of elliptical pole gaps) and provides vertical focusing.

The comparison between the two designs shows that the superconducting IC with elliptical pole gaps can be as light as a SC with higher central magnetic field. Although the installed RF power requirement of the SC is more than three times lower than that of the IC and the magnet requires a lower precision, the technical difficulties linked to the injection, ejection and the RF modulation raise concerns over the reliability of SC operation. Since this is a very important aspect for a medical treatment machine, the IC is chosen as the optimal injector to CABOTO. In a final design, special care will have to be taken in the study of the RF and magnetic field corrections needed for the acceleration and ejection of $H_2^+$ because of the 0.7 % $\frac{q}{A}$ difference with $C^{6+}$.

To quantitatively determine the industrial and clinical optimum for the CABOTO injection energy, three complementary IC designs of 70, 120 and 170 MeV/u have been investigated. An industrial comparison based on the area of the accelerator building and the RF power consumption shows that the optimum corresponds to the highest cyclotron energy. In terms of clinical capability, statistical patient data shows that the minimum beam energy needed for treatment is around 150 MeV/u for carbon ions. This corresponds to a range of 5 cm in water, which is needed to treat shallow tumors. In the case of protons, the minimum required energy is about 70 MeV for the treatment of ocular tumors. When designing a facility, these low energy limits have to be taken into account. The optimal cyclotron energy depends on the clinical aim of the facility. For centers wishing to first treat patients with standard protontherapy with degraders and allow in a second phase an upgrade to carbon ions, the optimal cyclotron energy is 230 MeV/u. For centers wishing to treat patients with both ion species without passive degraders, the optimal cyclotron energy is 70 MeV/u.

For a dual proton and carbon ion centre, the best compromise between clinical flexibility, accelerator size and power consumption is to have a CABOTO injection energy of 150 MeV/u. To put this into perspective, the 150 MeV/u cyclotron has similar weight and spiraling as the most widely used cyclotron for protontherapy (C235 by IBA S.A.), the linac is 24 m long and the power consumption of the cyclinac is 650 kW. Adding to these characteristics, the unique property of fast energy variation of the linac makes this cyclinac a strongly competitive accelerator for dual proton and carbon ion therapy.

# Bibliography

Amaldi, U. (2001). The Italian Hadrontherapy Project CNAO. *Physica Medica*, 17 Suppl 1:33–37.

Amaldi, U. (2007). Cyclinacs: Novel Fast-Cycling Accelerators for Hadrontherapy. In *Proceedings of the 18th International Conference on Cyclotrons and Their Applications*, pages 166–168.

Amaldi, U., Badano, L., Brianti, G., Bourhaleb, F., Casalegno, L., Crescenti, M., Donetti, M., Gallo, S., Gerardi, F., Greco, P., Nodari, M., Primadei, G., Rossi, S., Pezzetta, M., Pullia, M., Toncelli, S., Zennaro, R., Chimenti, V., Clozza, A., Monache, G. D., Lollo, V., Pellegrino, L., Sgamma, F., Sanelli, C., Spataro, B., Zolla, A., Cirio, R., Boriano, A., Cucuzza, L., Goebel, W., Luparia, A., Marchetto, F., Peroni, C., and Freire, C. S. (2010a). *The Path to the Italian National Centre for Ion Therapy*. Ed. Mercurio.

Amaldi, U., Berra, P., Crandall, K., Toet, D., Weiss, M., Zennaro, R., Rosso, E., Szeless, B., Vretenar, M., Cicardi, C., Martinis, C. D., Giove, D., Davino, D., Masullo, M. R., and Vaccaro, V. (2004). LIBO-a Linac-Booster for Protontherapy: Construction and Tests of a Prototype. *Nuclear Instruments and Methods in Physics Research Section A*, 521(2-3):512 – 529.

Amaldi, U., Bianchi, A., Chang, Y.-H., Go, A., Hajdas, W., Malakhov, N., Samarati, J., Sauli, F., and Watts, D. (2011). Construction, Test and Operation of a Proton Range Radiography System. *Nuclear Instruments and Methods in Physics Research Section A*, 629(1):337 – 344.

Amaldi, U., Bonomi, R., Braccini, S., Crescenti, M., Degiovanni, A., Garlasché, M., Garonna, A., Magrin, G., Mellace, C., Pearce, P., Pittà, G., Puggioni, P., Rosso, E., Andrés, S. V., Wegner, R., Weiss, M., and Zennaro, R. (2010b). Accelerators for Hadrontherapy: from Lawrence Cyclotrons to Linacs. *Nuclear Instruments and Methods in Physics Research Section A*, 620(2-3):563 – 577.

Amaldi, U., Braccini, S., and Puggioni, P. (2009). High Frequency Linacs for Hadrontherapy. *Reviews of Accelerator Science and Technology*, 2:111–131.

Amaldi, U. and Larsson, B. (1994). *Hadrontherapy in Oncology*. Elsevier.

Amaldi, U. and Team (2006). Institute for Diagnostics and Radiotherapy - IDRA: First Application of the Cyclinac Concept. Technical report, TERA Foundation.

Andrés, S. V. (2011). Comparison between RF Linacs and FFAGs for Hadrontherapy. *PARTNER Work Package 25 "Novel Accelerator Concepts for Hadrontherapy"*.

Andrés, S. V., Amaldi, U., Bonomi, R., Degiovanni, A., Garlasché, M., Garonna, A.,

Wegner, R., Mellace, C., and Pearce, P. (2010). High-Gradient Test of a 3 GHz Single-Cell Cavity (THP037). In *Proceedings of 25th International Linear Accelerator Conference.*

Antaya, T. A. (2009). High-Field Superconducting Synchrocyclotron (International Patent 7541905).

Baron, M. H., Pommier, P., Favrel, V., Truc, G., Balosso, J., and Rochat, J. (2004). A "One-Day Survey": as a Reliable Estimation of the Potential Recruitment for Proton- and Carbon-Ion Therapy in France. *Radiotherapy and Oncology*, 73 Suppl. 2:S15–17.

Bazzano, G. and CNAO-Collaboration (2010). Status of the Commissioning of the Centro Nazionale di Adroterapia Oncologica (CNAO). In *Proceedings of the 1st International Particle Accelerator Conference*, pages 283–285.

Becker, R. (2006). Modern Options for Hadron Therapy of Tumors. *Review of Scientific Instruments*, 77(3):03A903.

Belmont, J. L. and Pabot, J. L. (1966). Study of Axial Injection for the Grenoble Cyclotron. *IEEE Transactions on Nuclear Science*, 13(4):191 –193.

Bieth, C. and Laisné, A. (1998). A Very Compact Protontherapy Facility Based on an Extensive Use of High Temperature Superconductors (HTS). In *Proceedings of the 15th International Conference on Cyclotrons and their Applications*, pages 669–672.

Blosser, H. and Team (1993). Proposal for a Manufacturing Prototype Superconducting Cyclotron for Advanced Cancer Therapy. Technical Report MSUCL-874, National Superconducting Cyclotron Laboratory - Michigan State University.

Bortfeld, T. and Schlegel, W. (1996). An Analytical Approximation of Depth - Dose Distributions for Therapeutic Proton Beams. *Physics in Medicine and Biology*, 41(8):1331.

Botman, J. I. M. and Hagedoorn, H. L. (1994). Extraction from Cyclotrons. In *CERN Accelerator School*, pages 169–185.

Braccini, S., Ereditato, A., Kreslo, I., Moser, U., Pistillo, C., Studer, S., Scampoli, P., Coray, A., and Pedroni, E. (2010). First Results on Proton Radiography with Nuclear Emulsion Detectors. *Journal of Instrumentation*, 5(09):P09001.

Brandenburg, S. and AGOR-Construction-Group (1987). The Superconducting Cyclotron AGOR: Acceleration for Light and Heavy Ions. In *Proceedings of the Particle Accelerator Conference*, pages 376–378.

Brück, H. (1966). *Accélérateurs Circulaires de Particules: Introduction à la Théorie.* Bibliothèque des sciences et techniques nucléaires. PUF, Paris.

Bryant, P., Badano, L., Benedikt, M., Bryant, P., Crescent, M., Holy, P., Maier, A., Pullia, M., Rossi, S., and Knaus, P. (1999). Progress of the Proton-Ion Medical Machine Study (PIMMS). *Strahlentherapie und Onkologie*, 175:1–4. 10.1007/BF03038873.

Calabretta, L., Caruso, A., Spartà, A., Zappalà, E., Zhe, X., and Zhao, J. (2001). The radio frequency pulsing system at INFN-LNS. *AIP Conference Proceedings*, 600(1):297–299. Proceedings of the 16th International Conference on Cyclotrons and Their Applications.

Calabretta, L., Celona, L., Gammino, S., Rifuggiato, D., Ciavola, G., Maggiore, M., Piazza, L., Alonso, J., Barletta, W., Calanna, A., and Conrad, J. (2011). Preliminary Design Study of High-Power H2+ Cyclotrons for the DAEdALUS Experiment. *arXiv:1107.0652v1 [physics.acc-ph]*.

Calabretta, L., Cuttone, G., Battaglia, D., Campo, D., Celona, L., Gammino, S., Garufi, D., Lojacono, P., Piazza, L., Raia, G., Re, M., Rifuggiato, D., Sabini, M. G., Fabbricatore, P., Farinon, S., Musenich, R., Maggiore, M., and Greco, C. (2006). Preliminary Study of the SCENT Project. Technical report, INFN-LNS, INFN-Genoa, Catania University, Catanzaro Magna Grecia University.

Calabretta, L. and Migneco, E. (1984). Study for a beam bunching system at LNS. *Nuclear Instruments and Methods in Physics Research*, 220(1):158 – 160.

Calabretta, L. and Rifuggiato, D. (1998). Superconducting Cyclotrons for Acceleration of H2+. In *Proceedings of the 15th International Conference on Cyclotrons and their Applications*, pages 665–668.

Campo, D. (2010a). Study of the Injection in the 230 Mev/u Synchrocyclotron. Technical report, TERA Foundation.

Campo, D. (2010b). *A Superconducting Cyclotron for Hadrontherapy: Study of the Central Region*. PhD thesis, Università degli Studi di Catania.

Caporaso, G. J., Chen, Y.-J., and Sampayan, S. E. (2009). The Dielectric Wall Accelerator. *Reviews of Accelerator Science and Technology*, 2:253–263.

Chen, T.-S. (1960). Determination of the Capacitance, Inductance and Characteristic Impedance of Rectangular Lines. *IRE Transactions on Microwave Theory and Techniques*, 8(5):510 –519.

Chu, W., Staples, J., Ludewigt, B., Renner, T., Singh, R., Nyman, M., Collier, J., Daftari, I., Petti, P., Alonso, J., Kubo, H., Verhey, L., and Castro, J. (1993). Performance Specifications for Proton Medical Facility. Technical report, Lawrence Berkeley Laboratory.

Clark, D. J. (1969). Survey of External Injection Systems for Cyclotrons. In *Proceedings of International Cyclotron Conference*, pages 583–601.

Coutrakon, G., Hubbard, J., Johanning, J., Maudsley, G., Slaton, T., and Morton, P. (1994). A Performance Study of the Loma Linda Proton Medical Accelerator. *Medical Physics*, 21(11):1691–1701.

Craddock, M. (2010). Physics and Technology of Cyclotrons and FFAGs. In *United States Particle Accelerator School*. http://trshare.triumf.ca/ craddock/USPAS/.

Craddock, M. K. and Symon, K. R. (2008). Cyclotrons and Fixed-Field Alternating-Gradient Accelerators. *Reviews of Accelerator Science and Technology*, 1:65–97.

Doelling, R. (2004). Profile, Current and Halo Monitors of the PROSCAN Beam Lines. *AIP Conference Proceedings*, 732(1):244–252.

Donets, D. E., Donets, E. D., Donets, E. E., Salnikov, V. V., and Shutov, V. B. (2010). Production of Highly Charged Ion Beams Kr 32+ , Xe 44+ , Au 54+ with Electron String Ion Source (ESIS) Krion-2 and Corresponding Basic and Applied Studies. *Jour-*

*nal of Instrumentation*, 5(09):C09001.

Donets, E. D. (2004). Electron String Phenomenon: Physics and Use. *Journal of Physics: Conference Series*, 2(1):213.

Donets, E. E., Donets, E. D., and Syresin, E. M. (2004). Heavy Ion Injection Into Synchrotrons, Based on Electron String Ion Sources. In *Proceedings of the 19th Russian Accelerator Conference*, pages 453–455. Dubna, Russian Federation.

Enghardt, W., Crespo, P., Fiedler, F., Hinz, R., Parodi, K., Pawelke, J., and Pönisch, F. (2004). Charged hadron tumour therapy monitoring by means of PET. *Nuclear Instruments and Methods in Physics Research Section A*, 525(1-2):284 – 288. Proceedings of the International Conference on Imaging Techniques in Subatomic Physics, Astrophysics, Medicine, Biology and Industry.

Fano, U. (1963). Penetration of Protons, Alpha Particles, and Mesons. *Annual Review of Nuclear Science*, 13(1):1–66.

Fournier, P., Haseroth, H., Kugler, H., Lisi, N., Scrivens, R., Rodriguez, F. V., Lazzaro, P. D., Flora, F., Duesterer, S., Sauerbrey, R., Schillinger, H., Theobald, W., Veisz, L., Tisch, J. W. G., and Smith, R. A. (2000). Novel Laser Ion Sources. *Review of Scientific Instruments*, 71(3):1405–1408.

Friesel, D. L. and Antaya, T. A. (2009). Medical Cyclotrons. *Reviews of Accelerator Science and Technology*, 2:133–156.

Garonna, A. (2010). Synchrocyclotron Preliminary Design for a Dual Hadrontherapy Center. In *Proceedings of the 1st International Particle Accelerator Conference*, pages 552–554.

Garonna, A., Amaldi, U., Bonomi, R., Campo, D., Degiovanni, A., Garlasché, M., Mondino, I., Rizzoglio, V., and Andrés, S. V. (2010). Cyclinac Medical Accelerators using Pulsed C6+ /H2+ Ion Sources. *Journal of Instrumentation*, 5(09):C09004. Proceedings of the International Symposium on Electron Beam Ion Sources and Traps.

Geisler, A., Hottenbacher, J., Klein, H.-U., Krischel, D., Röcken, H., Schillo, M., Stephani, T., Timmer, J., and Baumgarten, C. (2007). Commissioning of the Accel 250 Mev Proton Cyclotron. In *Proceedings of the 18th International Conference on Cyclotrons and Their Applications*, pages 9–14.

Goethem, M. J. V., van der Meer, R., Reist, H. W., and Schippers, J. M. (2009). Geant4 Simulations of Proton Beam Transport through a Carbon or Beryllium Degrader and following a Beam Line. *Physics in Medicine and Biology*, 54(19):5831.

Gordon, M. M. (1983). Calculation of isochronous fields for sector-focused cyclotrons. *Particle Accelerators*, 13:67–84.

Gordon, M. M. and Welton, T. A. (1959). Computation methods for AVF cyclotron design studies. Technical report, Oak Ridge National Laboratory.

Grudiev, A., Calatroni, S., and Wuensch, W. (2009). New Local Field Quantity Describing the High Gradient Limit of Accelerating Structures. *Physical Review Special Topics - Accelerators and Beams*, 12(10):102001.

G.Zschornack, F.Grossmann, V.P.Ovsyannikov, A.Schwan, F.Ullmann, E.Tanke, and

P.Urschütz (2009). Status of Electron Beam Ion Sources for Particle Therapy. Dreebit Gmbh website.

Haberer, T., Becher, W., Schardt, D., and Kraft, G. (1993). Magnetic Scanning System for Heavy Ion Therapy. *Nuclear Instruments and Methods in Physics Research Section A*, 330(1-2):296 – 305.

Hall, E. (2002). Radiobiology for the Radiologist. *Radiology*, 5th ed.(2):512.

Hanson, K. M., Bradbury, J. N., Cannon, T. M., Hutson, R. L., Laubacher, D. B., Macek, R. J., Paciotti, M. A., and Taylor, C. A. (1981). Computed Tomography using Proton Energy Loss. *Physics in Medicine and Biology*, 26(6):965.

Heikkinen, P. (1994). Injection and Extraction for Cyclotrons. In *CERN Accelerator School*, volume II, pages 819–831.

Hill, C. (1994). Ion and Electron Sources. In *CERN Accelerator School on Cyclotrons, Linacs and Their Applications*, pages 95–112.

Holsinger, R. and Halbach, K. (2003). Poisson version 7. maintained and distributed by the Los Alamos Accelerator Code Group (LAACG).

ICRU (2005). *Report 73: Stopping of Ions Heavier than Helium*, volume 5. Journal of the International Commission on Radiation Units and Measurements, Bethesda, MD.

Iwata, Y., Furukawa, T., Mizushima, K., Noda, K., Shirai, T., Takeshita, E., Takada, E., Fujimoto, T., Kadowaki, T., Sano, Y., and Uchiyama, H. (2010). Multiple-Energy Operation with Quasi-DC Extension of Flattops at HIMAC. In *Proceedings of the 1st International Particle Accelerator Conference*, pages 79–81.

Jäkel, O. (2009). Medical Physics Aspects of Particle Therapy. *Radiation Protection Dosimetry*, 137 (1-2):156–66.

Johnstone, C., Koscielniak, S., Berz, M., Makino, K., Snopok, P., and Mills, F. (2009). Nonscaling FFAG Variants for HEP and Medical Applications. In *Proceedings of Particle Accelerator Conference*.

Joho, W. (1969). Extraction from Medium and High Energy Cyclotrons. In *Proceedings of the 5th International Cyclotron Conference*, pages 159–179.

Joho, W. (1986). Modern Trends in Cyclotrons. In *CERN Accelerator School*, pages 260–290.

Jongen, Y., Abs, M., Blondin, A., Kleeven, W., Zaremba, S., Vandeplassche, D., Aleksandrov, V., Gursky, S., Karamyshev, O., Karamysheva, G., Kazarinov, N., Kostromin, S., Morozov, N., Samsonov, E., Shirkov, G., Shevtsov, V., Syresin, E., and Tuzikov, A. (2010). Compact Superconducting Cyclotron C400 for Hadron Therapy. *Nuclear Instruments and Methods in Physics Research Section A*, 624(1):47 – 53.

Jongen, Y., Beeckman, W., Kleeven, W., Vandeplassche, D., Zaremba, S., Samsonov, E., and Morozov, N. (2007). Numerical Study of the Resonances in Superconducting Cyclotron C400. In *Proceedings of the 18th International Conference On Cyclotrons And Their Applications*, pages 382–384.

Jongen, Y., Karamysheva, G., Kleeven, W., Kostromin, S., Morozov, N., and Samsonov,

E. (2006). Simulation of Ions Acceleration and Extraction in Cyclotron C400. In *Proceedings of the 10th European Particle Accelerator Conference*, pages 2113–2115.

Kanai, T., Kanematsu, N., Minohara, S., Komori, M., Torikoshi, M., Asakura, H., Ikeda, N., Uno, T., and Takei, Y. (2006). Commissioning of a Conformal Irradiation System for Heavy-Ion Radiotherapy using a Layer-Stacking Method. *Medical Physics*, 33(8):2989–2997.

Karamysheva, G., Kostromin, S., Morozov, N., Samsonov, E., Syresin, E., and Shirkov, G. (2010). Simulation of Beam Extraction from C235 Cyclotron for Proton Therapy. *Physics of Particles and Nuclei Letters*, 7:507–510. 10.1134/S1547477110070174.

Kester, O., Becker, R., and Kleinod, M. (1996). The Frankfurt MEDEBIS: a Prototype of an Injector for a Synchrotron Dedicated for Cancer Therapy. *Review of Scientific Instruments*, 67(3):1165–1167.

Kitagawa, A., Fujita, T., Muramatsu, M., Biri, S., and Drentje, A. G. (2010). Review on Heavy Ion Radiotherapy Facilities and Related Ion Sources. *Review of Scientific Instruments*, 81(2):02B909.

Kleeven, W. (2005). Injection and Extraction for Cyclotrons. In *Proceedings of the Specialised CERN Accelerator School on Small Accelerators*, pages 271–296.

Koehler, A. M., Schneider, R. J., and Sisterson, J. M. (1977). Flattening of Proton Dose Distributions for Large-Field Radiotherapy. *Medical Physics*, 4(4):297–301.

Kraft, G. (2000). Tumor Therapy with Heavy Charged Particles. *Progress in Particle and Nuclear Physics*, 45(Supplement 2):S473 – S544.

Krengli, M. and Orecchia, R. (2004). Medical Aspects of the National Centre For Oncological Hadrontherapy (CNAO-Centro Nazionale Adroterapia Oncologica) in Italy. *Radiotherapy and Oncology*, 73 Suppl 2:S21–23.

Laisné, A. (1975). The Orsay 200 Mev Synchrocyclotron Machine. In *Proceedings of the 7th International Conference on Cyclotrons and Their Applications*, pages 99–102.

Laisné, A. (1981). IPN Orsay Project - First Machine Design Studies. *Proceedings of the 9th International Conference on Cyclotrons and their Applications*, pages 203–208.

Laisné, A. (1994). Compact Isochronic Cyclotron (International Patent H05H13/00).

Laisné, A. (1998). More About a Universal Compact Isochronous Superconducting Cyclotron Archetype. In *Proceedings of the 15th International Conference on Cyclotrons and Their Applications*, pages 684–686.

Laisné, A. (2010a). Preliminary Design Method for Compact Isochronous Cyclotrons with Central Fields Higher than 1.7 Tesla. Technical report, TERA Foundation.

Laisné, A. (2010b). Puissances Dissipées dans les Lignes de Transmission à Sections Rectangulaires. Technical report, TERA Foundation.

Laisné, A., Debray, P., and SC-Conversion-Staff (1979). The Orsay 200 Mev Synchrocyclotron. *IEEE Transactions on Nuclear Science*, 26(2):1919 –1922.

Langen, K. M. and Jones, D. T. L. (2001). Organ Motion and its Management. *International Journal of Radiation Oncology*Biology*Physics*, 50(1):265 – 278.

Lau, K. (1988). Loss Calculations for Rectangular Coaxial Lines. *Microwaves, Antennas and Propagation, IEE Proceedings H*, 135(3):207 – 209.

Lee, Y., Ji, Q., Leung, K. N., and Zahir, N. (2000). Nanobeam Production with the Multicusp Ion Source. *Review of Scientific Instruments*, 71(2):722–724.

Leung, K. N. (1994). Multicusp ion sources (invited). *Review of Scientific Instruments*, 65(4):1165–1169.

Lomax, A. (1999). Intensity Modulation Methods for Proton Radiotherapy. *Physics in Medicine and Biology*, 44(1):185.

Mayer, R., Mock, U., Jäger, R., Pötter, R., Vutuc, C., Eiter, H., Krugmann, K., Hammer, J., Hirn, B., Hawliczek, R., Knocke-Abulesz, T., Lukas, P., Nechville, E., Pakisch, B., Papauschek, M., Raunik, W., Rhomberg, W., Sabitzer, H., Schratter-Sehn, A., Sedlmayer, F., Wedrich, I., and Auberger, T. (2004). Epidemiological Aspects of Hadron Therapy: a Prospective Nationwide Study of the Austrian project MedAustron and the Austrian Society of Radiooncology. *Radiotherapy and Oncology*, 73 Suppl 2:S24–28.

Melin, G., Bourg, F., Briand, P., Debernardi, J., Delaunay, M., Geller, R., Jacquot, B., Ludwig, P., N'Guyen, T. K., Pin, L., Pontonnier, M., Rocco, J. C., and Zadworny, F. (1990). Some Particular Aspects of the Physics of the ECR sources for Multicharged Ions. *Review of Scientific Instruments*, 61(1):236–238.

Middleton, A. and Trowbridge, C. (1968). Mechanical Stress in Large High Field Magnet Coils. In *Proceedings of the 2nd International Conference on Magnet Technology*, pages 140–9.

Muramatsu, M., Kitagawa, A., Sakamoto, Y., Sato, S., Sato, Y., Ogawa, H., Yamada, S., Ogawa, H., Yoshida, Y., and Drentje, A. G. (2005). Development of a Compact Electron-Cyclotron-Resonance Ion Source for High-Energy Carbon-Ion Therapy. *Review of Scientific Instruments*, 76(11):113304.

Negrazus, M., Duppich, J., and Schippers, M. (2003). Cooling Down and First Powering of the Comet Superconducting Coils. Scientific and Technical Report Vol.VI, Paul Scherrer Institute.

Noda, K., Furukawa, T., Fujisawa, T., Iwata, Y., Kanai, T., Kanazawa, M., Kitagawa, A., Komori, M., Minohara, S., Murakami, T., Muramatsu, M., Sato, S., Takei, Y., Tashiro, M., Torikoshi, M., Yamada, S., and Yusa, K. (2007). New Accelerator Facility for Carbon-Ion Cancer-Therapy. *Journal of Radiation Research*, 48(Suppl.A):A43–A54.

Pedroni, E., Bacher, R., Blattmann, H., Bohringer, T., Coray, A., Lomax, A., Lin, S., Munkel, G., Scheib, S., Schneider, U., and Tourovsky, A. (1995). The 200-MeV Proton Therapy Project at the Paul Scherrer Institute: Conceptual Design and Practical Realization. *Medical Physics*, 22(1):37–53.

Pedroni, E., Bohringer, T., Coray, A., Goitein, G., Grossmann, M., Lomax, A., Lin, S., and Jermann, M. (2001). A Novel Gantry for Proton Therapy at the Paul Scherrer Institute. In Marti, F., editor, *Proceedings of the 16th International Conference on Cyclotrons and Applications*, pages 13–17. AIP.

Picardi, L. and Ronsivalle, C. (2004). Progress in the Development of the TOP Linac. In

*Proceedings of the 22nd International Linear Accelerator Conference*, pages 633–635.

Pirkl, W. (2000). Choice of RF Frequency. In Miles, J., editor, *CERN Accelerator School on Radiofrequency Engineering*, pages 336–350. CERN Accelerator School on Radiofrequency Engineering.

Reiser, M. (2008). *Theory and Design of Charged Particle Beams; 2nd ed.* Wiley.

Reist, H., Amrein, B., Atchison, F., Graf, M., Sigrist, U., Suter, D., and Zumbach, C. (2003). Concept for Handling and Service of the Proscan Degrader Unit. Technical report, Paul Scherrer Institute. Scientific and Technical Report, Vol.VI.

Resmini, F. G., Bellomo, G., Blosser, H. G., Fabrici, E., and Johnson, D. (1981). Final Design of the Magnetic Field for the K-800 Superconducting Cyclotron at MSU. *IEEE Transactions on Nuclear Science*, 28(3):2749 –2751.

Rifuggiato, D. and Calabretta, L. (2000). Axial Injection in the Superconducting Cyclotron. Technical Report INFN-TC-2000-01, INFN-LNS, Italy.

Rohrer, U. (2007a). PSI Graphic Transport Framework version 2.61c based on a CERN-SLAC-FERMILAB version by K.L. Brown et al.

Rohrer, U. (2007b). PSI Graphic Turtle Framework version 2.45b based on a CERN-SLAC-FERMILAB version by K.L. Brown et al.

Rossi, S. (2006). Developments in Proton and Light-Ion Therapy. In *Proceedings of European Particle Accelerator Conference*.

Russenschuck, S. and Auchmann, B. (2009). ROXIE. distributed by CERN.

Sawada, K., Sawada, J., Sakata, T., Uno, K., Okanishi, K., Harada, H., Itano, A., Higashi, A., Akagi, T., Yamada, S., Noda, K., Torikoshi, M., and Kitagawa, A. (2000). Performance Test of Electron Cyclotron Resonance Ion Sources for the Hyogo Ion Beam Medical Center. *Review of Scientific Instruments*, 71(2):987–989.

Schardt, D., Elsaesser, T., and Schulz-Ertner, D. (2010). Heavy-ion Tumor Therapy: Physical and Radiobiological Benefits. *Reviews of Modern Physics*, 82(1):383–425.

Scharf, W. H. and Cole, F. T. (1986). *Particle Accelerators and their Uses.* Harwood, 3 edition.

Schillo, M., Geisler, A., Hobl, A., Klein, H., Krischel, D., Meyer-Reumers, M., C.Piel, Blosser, H., Kim, J.-W., Marti, F., Vincent, J., Brandenburg, S., and Beijers, J. (2001). Compact Superconducting 250 MeV Proton Cyclotron for the PSI Proscan Proton Therapy Project. In *Proceedings of Cyclotron Conference*.

Schippers, J. (2001). Architectural Overview of the PROSCAN beam lines. Technical report, Paul Scherrer Institute. PROSCAN Review Meeting.

Schippers, J., Adelmann, A., Joho, W., Negrazus, M., Seidel, M., Stam, M., and Homeyer, H. (2009). A Novel Design of a Cyclotron Based Accelerator System for Multi-Ion Therapy. In *Proceedings of 11th International Conference on Heavy Ion Accelerator Technology*, pages 74–78 (TU–11).

Schippers, J., Dölling, R., Duppich, J., Goitein, G., Jermann, M., Mezger, A., Pedroni, E., Reist, H., and Vrankovic, V. (2007). The SC Cyclotron and Beam Lines of PSI's

New Protontherapy Facility PROSCAN. *Nuclear Instruments and Methods in Physics Research Section B*, 261(1-2):773 – 776. Proceedings of the 19th International Conference on the Application of Accelerators in Research and Industry.

Schippers, J. M., Duppich, J., Goitein, G., Jermann, M., Lomax, A., Pedroni, E., Reist, H., Timmermann, B., and Verweij, J. (2006). The Use of Protons in Cancer Therapy at PSI and Related Instrumentation. *Journal of Physics: Conference Series*, 41(1):61.

Schippers, J. M., George, D. C., and Vrankovic, V. (2004). Results of 3D Beam Dynamic Studies in Distorted Fields of a 250 MeV Superconducting Cyclotron. In *Proceedings of the 17th International Conference on Cyclotrons and Their Applications*, pages 435–438.

Schnase, A. (2000). Cavities with a Swing. In Miles, J., editor, *CERN Accelerator School on Radiofrequency Engineering*, pages 236–272.

Schulte, R., Bashkirov, V., Li, T., Liang, Z., Mueller, K., Heimann, J., Johnson, L., Keeney, B., Sadrozinski, H.-W., Seiden, A., Williams, D., Zhang, L., Li, Z., Peggs, S., Satogata, T., and Woody, C. (2004). Conceptual Design of a Proton Computed Tomography System for Applications in Proton Radiation Therapy. *IEEE Transactions on Nuclear Science*, 51(3):866 – 872.

Slater, J. M., Slater, J. D., and Wroe, A. J. (2009). Proton Radiation Therapy in the Hospital Environment: Conception, Development, and Operation of the Initial Hospital-Based Facility. *Reviews of Accelerator Science and Technology*, 2:35–62.

Snyder, S. L. (1995). *Study and Redesign of the NSCL K500 Injection, Central Region and Phase Selection Systems*. PhD thesis, Michigan State University.

Suit, H., Delaney, T. F., and Trofimov, A. (2009). Physical and Biological Basis of Proton and of Carbon Ion Radiation Therapy and Clinical Outcome Data. *Reviews of Accelerator Science and Technology*, 2:1–15.

Symon, K. R., Kerst, D. W., Jones, L. W., Laslett, L. J., and Terwilliger, K. M. (1956). Fixed-Field Alternating-Gradient Particle Accelerators. *Physical Review*, 103(6):1837–1859.

Tajima, T., Habs, D., and Yan, X. (2009). Laser Acceleration of Ions for Radiation Therapy. *Reviews of Accelerator Science and Technology*, 2:201–228.

Talamonti, C., Reggioli, V., Bruzzi, M., Bucciolini, M., Civinini, C., Marrazzo, L., Menichelli, D., Pallotta, S., Randazzo, N., Sipala, V., Cirrone, G., Petterson, M., Blumenkrantz, N., Feldt, J., Heimann, J., Lucia, D., Seiden, A., Williams, D., Sadrozinski, H.-W., Bashkirov, V., and Schulte, R. (2010). Proton Radiography for Clinical Applications. *Nuclear Instruments and Methods in Physics Research Section A*, 612(3):571 – 575. Proceedings of the 7th International Conference on Radiation Effects on Semiconductor materials, Detectors and Devices.

Toprek, D. (2000). Theory of the Central Ion Trajectory in the Spiral Inflector. *Nuclear Instruments and Methods in Physics Research Section A*, 440(2):285 – 295.

Trbojevic, D. (2009). FFAGs as Accelerators and Beam Delivery Devices for Ion Cancer Therapy. *Reviews of Accelerator Science and Technology*, 2:229–251.

Vaccaro, V. G., Buiano, R., A.D'Elia, Michele, G. D., Masullo, M. R., Alessandria, F., Giove, D., Martinis, C. D., Betta, E., M.Mauri, Rainò, A., Variale, V., Calabretta, L., and Rush, R. (2007). ACLIP: a 3 GHz Side Coupled Linac for Protontherapy to be Used as a Booster for 30 MeV Cyclotrons. In *Proceedings of the 18th International Conference on Cyclotrons and Their Applications*, pages 172–174.

Wadell, B. C. (1991). *Transmission Line Design Handbook.* Artech House.

Walter, M. (2001). List of Cyclotrons. In *Proceedings of the 16th International Conference on Cyclotrons and Their Applications.* http://accelconf.web.cern.ch/accelconf/c01/cyc2001/ListOfCyclotrons.html.

Wiedemann, H. (2007). *Particle Accelerator Physics.* Springer, 3rd edition.

Wieszczycka, W. and Schaf, W. H. (2001). *Proton Radiotherapy Accelerators.* World Scientific, Singapore.

Wilson, M. (1987). *Superconducting Magnets.* Oxford University Press.

Wilson, R. R. (1946). Radiological Use of Fast Protons. *Radiology*, 47(5):487–491.

Wolf, B. H. (1995). *Handbook of Ion Sources.* CRC Press, Boca Raton, FL.

Wu, X. (1990). *Conceptual Design and Orbit Dynamics in a 250 MeV Superconducting Synchrocyclotron.* PhD thesis, Michigan State University.

Wutte, D., Freedman, S., Gough, R., Lee, Y., Leitner, M., Leung, K. N., Lyneis, C., Pickard, D. S., Williams, M. D., and Xie, Z. Q. (1998). Development of an RF Driven Multicusp Ion Source for Nuclear Science Experiments. *Nuclear Instruments and Methods in Physics Research Section B*, 142(3):409 – 416.

Yonai, S., Kanematsu, N., Komori, M., Kanai, T., Takei, Y., Takahashi, O., Isobe, Y., Tashiro, M., Koikegami, H., and Tomita, H. (2008). Evaluation of Beam Wobbling Methods for Heavy-Ion Radiotherapy. *Medical Physics*, 35(3):927–938.

Zaremba, S. (2005). Magnets for cyclotrons. In *CERN Accelerator School (Specialised Course on Small Accelerators)*, pages 253–270.

Zhao, H. W., Zhang, Z. M., He, W., Zhang, X. Z., Guo, X. H., Cao, Y., Yuan, P., Sun, L. T., Ma, L., Song, M. T., Zhan, W. L., Wei, B. W., and Xie, D. Z. (2004). Intense Heavy Ion Beam Production from IMP LECR3 and Construction Progress of a Superconducting ECR Ion Source SECRAL. *Review of Scientific Instruments*, 75(5):1410–1413.

Ziegler, J. F., Ziegler, M., and Biersack, J. (2008). Stopping and Range of Ions in Matter (SRIM) version 2008.04. http://www.srim.org/.

Zschornack, G., Grossmann, F., Ovsyannikov, V., and Griesmayer, E. (2007). A new Generation of Powerful Ion Sources for the Medical Particle Therapy. In *Proceedings of the 18th International Conference On Cyclotrons And Their Applications*, pages 298–299.

Zschornack, G., Ovsyannikov, V. P., Grossmann, F., Schwan, A., and Ullmann, F. (2010). First Experiments with the Dresden EBIS-SC. *Journal of Instrumentation*, 5(08):C08012.

# Appendix

## A. Magnet Design

Matlab script to define the Synchrocyclotron magnet geometry

```
1   clc; format long;
2   %********* ATTENTION *********
3   % NO SPACES IN FILE/FOLDER NAMES!!!!!!!!!!!!
4   %********* ATTENTION *********
5   folder1='\\xxx'; folder2='\xxx';
6   folder3='\xxx\'; folder4='xxx\';
7   name_bhfile='XXX'; %name_alafile='xxx.txt';
8   name_comifile='xxxx'; name_graphfile=strcat(name_comifile, 'graph.dat');
9   %************pole points*****************************************
10  %injection hole
11  Rinj=xxxx; Pole_xy=[];
12  Pole_xy=[Pole_xy; [Rinj XXX]];
13  Pole_xy=[Pole_xy; [XXX  XXX]];
14  %..................
15  %********* variables for yoke and coil*************************
16  Yoke_h=XXXX; Yoke_r=XXXX; Coilspace_h=Xxx;  Coilspace_r=xxx;
17  %centroid position
18  Coil_r0=xxx; Coil_z0=XXX;
19  %full−widths
20  Coil_dr=XXX; Coil_dz=XXXX;
21  I=XXXX; %in A.m^2
22  %************variables for COMI file***********************
23  SF_hill=XXX; mesh_c=XXX; mesh_coil=XXX; mesh_yoke=XXX; BG_r=XXXX;
24  BG_h=XXX; mesh_bg=XXX;
25  %************variables for graph export********************
26  Rin=XX; Rend=XXX; dR=XXX;
27  %*****************************************************************
28  % ************PROGRAMS*****************************************
29  %**** write the comi file for OPERA import AND export****************
30  writeComiImportExportSC;
31  %*****************************************************************
```

Matlab script to create the OPERA command file for the synchrocyclotron magnet

```
1   bh_file=strcat(folder1, folder2,'\bh\', name_bhfile);
2   input_file=strcat(folder1,folder2,folder3,folder4,name_comifile, '.comi');
3   %the coil is created from input parameters in main program
4   Coil_xy=[];
5   Coil_xy=[Coil_xy; [Coil_r0−0.5*Coil_dr  Coil_z0−0.5*Coil_dz]];
6   Coil_xy=[Coil_xy; [Coil_r0+0.5*Coil_dr  Coil_z0−0.5*Coil_dz]];
7   Coil_xy=[Coil_xy; [Coil_r0+0.5*Coil_dr  Coil_z0+0.5*Coil_dz]];
8   Coil_xy=[Coil_xy; [Coil_r0−0.5*Coil_dr  Coil_z0+0.5*Coil_dz]];
9   script=strcat('/++ ',' OPERA 2D input file made on : ', datestr(now), ' \n ');
10  script=strcat(script,'/++ ',' with BH file : ', name_bhfile, ' \n ');
11  script=strcat(script,'/++ ',' Written on Matlab by : Adriano Garonna', ' \n ', ' \n ');
12  script=strcat(script,'/++ ',' ********** PARAMETERS ************', ' \n ');
13  script=strcat(script,'/++ ',' MESH size is : the background (', num2str(mesh_bg),'), the
        coil (',num2str(mesh_coil),'), the yoke (',num2str(mesh_yoke),'), the hill (',
        num2str(mesh_c),'), \n ');
14  script=strcat(script,'/++ ',' YOKE half height of ', num2str(Yoke_h),' m and radius of
        ', num2str(Yoke_r), ' m \n ');
```

```
15  script=strcat(script,'/++ ',' COIL centroid(width) is : ', num2str(Coil_r0),' (',
        num2str(Coil_dr),') m in R and ', num2str(Coil_z0),' (', num2str(Coil_dz),') m in Z
        \n ');
16  script=strcat(script,'/++ ',' COIL distance to yoke is : ', num2str(Coilspace_r),' m in
        R and ', num2str(Coilspace_h),' m in Z \n ');
17  script=strcat(script,'/++ ',' COIL current is : ', num2str(I),' A/mm^2 \n ');
18  script=strcat(script,'/++ ',' ***********POLE COORDINATES*******', ' \n ', ' \n ');
19  for j=1:length(Pole_xy)
20      script=strcat(script,'/++ ','X=',num2str(Pole_xy(j,1)),' Y=',num2str(Pole_xy(j,2)),'
            \n ') ;
21  end
22  script=strcat(script,'/++ ',' ********************************', ' \n ', ' \n ');
23  script=strcat(script,'UNITS LENGTH=METRE FLUX=TESLA FIELD=AM POTENTIAL=WBM CONDUCTIVITY=
        SM DENSITY=AM2 FORCE=NEWTON ENERGY=JOULE POWER=WATT MASS=KG');
24  script=strcat(script,' \n ','SET FIELD=MAGNETIC SYMMETRY=AXISYMMETRY AUTOMATIC=YES
        ELEMENT=LINEAR',' \n ');
25  %draw the pole*************************
26  script=strcat(script,' \n ','/++ ',' draw POLE******************', ' \n ');
27  script=strcat(script,'DRAW SHAPE=POLYGON,', ' \n ');
28  script=strcat(script,'DRAW +DEFAULTS SHAPE=POLYGON TOLERANCE=1.0E-05 MATERIAL=4 PERM=100
        DENS=0 CONDUCTIVITY=0 PHASE=0 VELOCITY=0 N=0 SYMMETRY=0 XCEN=0 YCEN=0 ANGLE=0 NX=1
        DX=0 NY=1 DY=0 ROTATIONS=1 TROTATION=0 MIRROR=NO', ' \n ');
29  script=strcat(script,'POLYGON -DATA +SIZE ESIZE=',num2str(mesh_c),' BIAS=0.5 LINESHAPE=
        STRAIGHT F=NO', ' \n ');
30  script=strcat(script,'POLYGON -DATA OPTION=PICK +NEW', ' \n ');
31  for j=1:length(Pole_xy)
32      script=strcat(script,'POLYGON X=',num2str(Pole_xy(j,1)),' Y=',num2str(Pole_xy(j,2))
            ,' -POLAR -RELATIVE',' \n ') ;
33  end
34  script=strcat(script,'POLYGON X=',num2str(Pole_xy(end,1)),' Y=',num2str(max(Coil_xy(:,2)
        )+Coilspace_h),' -POLAR -RELATIVE',' \n ') ;
35  script=strcat(script,'POLYGON X=',num2str(Rinj),' Y=',num2str(max(Coil_xy(:,2))+
        Coilspace_h),' -POLAR -RELATIVE',' \n ') ;
36  script=strcat(script,'POLYGON OPTION=CLOSE', ' \n ');
37  %********************************
38  % draw coil *************************
39  script=strcat(script,' \n ','/++ ',' draw COIL*****************', ' \n ');
40  script=strcat(script,'DRAW SHAPE=POLYGON,', ' \n ');
41  script=strcat(script,'DRAW +DEFAULTS SHAPE=POLYGON TOLERANCE=1.0E-05 MATERIAL=1 PERM=1
        DENS=',num2str(I),' CONDUCTIVITY=0 PHASE=0 VELOCITY=0 N=0 SYMMETRY=0 XCEN=0 YCEN=0
        ANGLE=0 NX=1 DX=0 NY=1 DY=0 ROTATIONS=1 TROTATION=0 MIRROR=NO', ' \n ');
42  script=strcat(script,'POLYGON -DATA +SIZE ESIZE=',num2str(mesh_coil),' BIAS=0.5
        LINESHAPE=STRAIGHT F=NO', ' \n ');
43  script=strcat(script,'POLYGON -DATA OPTION=PICK +NEW', ' \n ');
44  for j=1:length(Coil_xy)
45      script=strcat(script,'POLYGON X=',num2str(Coil_xy(j,1)),' Y=',num2str(Coil_xy(j,2))
            ,' -POLAR -RELATIVE',' \n ') ;
46  end
47  script=strcat(script,'POLYGON OPTION=CLOSE', ' \n ');
48  %***************************
49  % draw yoke (SF=1)************
50  script=strcat(script,' \n ','/++ ',' draw YOKE******************', ' \n ');
51  script=strcat(script,'DRAW SHAPE=POLYGON,', ' \n ');
52  script=strcat(script,'DRAW +DEFAULTS SHAPE=POLYGON TOLERANCE=1.0E-05 MATERIAL=4 PERM=1
        DENS=0 CONDUCTIVITY=0 PHASE=0 VELOCITY=0 N=0 SYMMETRY=0 XCEN=0 YCEN=0 ANGLE=0 NX=1
        DX=0 NY=1 DY=0 ROTATIONS=1 TROTATION=0 MIRROR=NO', ' \n ');
53  script=strcat(script,'POLYGON -DATA +SIZE ESIZE=',num2str(mesh_yoke),' BIAS=0.5
        LINESHAPE=STRAIGHT F=NO', ' \n ');
54  script=strcat(script,' \n ','/++ ',' draw YOKE******', ' \n ');
55  script=strcat(script,'POLYGON -DATA OPTION=PICK +EXIST', ' \n ');
56  script=strcat(script,'POLYGON X=',num2str(Rinj),' Y=',num2str(max(Coil_xy(:,2))+
        Coilspace_h),' -POLAR -RELATIVE',' \n ') ;
57  script=strcat(script,'POLYGON X=',num2str(Pole_xy(end,1)),' Y=',num2str(max(Coil_xy(:,2)
        )+Coilspace_h),' -POLAR -RELATIVE',' \n ') ;
58  script=strcat(script,'POLYGON -DATA OPTION=PICK +NEW', ' \n ');
59  script=strcat(script,'POLYGON X=',num2str(max(Coil_xy(:,1))+Coilspace_r),' Y=',num2str(
        max(Coil_xy(:,2))+Coilspace_h),' -POLAR -RELATIVE',' \n ') ;
60  script=strcat(script,'POLYGON X=',num2str(max(Coil_xy(:,1))+Coilspace_r),' Y=',num2str
        (0.0),' -POLAR -RELATIVE',' \n ') ;
61  script=strcat(script,'POLYGON X=',num2str(Yoke_r),' Y=',num2str(0.0),' -POLAR -RELATIVE
        ',' \n ') ;
```

```
62  script=strcat(script,'POLYGON X=',num2str(Yoke_r),' Y=',num2str(Yoke_h),' -POLAR -
       RELATIVE',' \n ') ;
63  script=strcat(script,'POLYGON X=',num2str(Rinj),' Y=',num2str(Yoke_h),' -POLAR -RELATIVE
       ',' \n ') ;
64  script=strcat(script,'POLYGON OPTION=CLOSE', ' \n ');
65  %*****************************
66  % draw background *************
67  script=strcat(script,' \n ','/++ ',' draw BACKGROUND*********************', ' \n ', '
       \n ');
68  script=strcat(script,'DRAW SHAPE=POLYGON,', ' \n ');
69  script=strcat(script,'DRAW +DEFAULTS SHAPE=BACKGROUND TOLERANCE=1.0E-05 MATERIAL=0 PERM
       =1 DENS=0 CONDUCTIVITY=0 PHASE=0 VELOCITY=0 N=0 SYMMETRY=0 XCEN=0 YCEN=0 ANGLE=0 NX
       =1 DX=0 NY=1 DY=0 ROTATIONS=1 TROTATION=0 MIRROR=NO', ' \n');
70  %tangential boundary condition: F=V V=0
71  script=strcat(script,'POLYGON -DATA +SIZE ESIZE=',num2str(mesh_c),' BIAS=0.5 LINESHAPE=
       STRAIGHT F=V V=0', ' \n ');
72  script=strcat(script,'POLYGON -DATA OPTION=PICK +NEW', ' \n ');
73  script=strcat(script,'POLYGON X=',num2str(0),' Y=',num2str(Yoke_h),' -POLAR -RELATIVE','
       \n ') ;
74  script=strcat(script,'POLYGON X=',num2str(0),' Y=',num2str(Pole_xy(1,2)),' -POLAR -
       RELATIVE',' \n ') ;
75  script=strcat(script,'POLYGON -DATA +SIZE ESIZE=',num2str(mesh_bg/100),' BIAS=0.5
       LINESHAPE=STRAIGHT F=V V=0', ' \n ');
76  script=strcat(script,'POLYGON -DATA OPTION=PICK +NEW', ' \n ');
77  script=strcat(script,'POLYGON X=',num2str(0.0),' Y=',num2str(0.0),' -POLAR -RELATIVE','
       \n ') ;
78  % normal boundary condition: F=DV DV=0
79  script=strcat(script,'POLYGON -DATA +SIZE ESIZE=',num2str(mesh_bg/100),' BIAS=0.5
       LINESHAPE=STRAIGHT F=DV DV=0', ' \n ');
80  script=strcat(script,'POLYGON -DATA OPTION=PICK +EXIST', ' \n ');
81  script=strcat(script,'POLYGON X=',num2str(max(Coil_xy(:,1))+Coilspace_r),' Y=',num2str
       (0.0),' -POLAR -RELATIVE',' \n ') ;
82  script=strcat(script,'POLYGON -DATA +SIZE ESIZE=',num2str(mesh_bg),' BIAS=0.5 LINESHAPE=
       STRAIGHT F=DV DV=0', ' \n ');
83  script=strcat(script,'POLYGON X=',num2str(Yoke_r),' Y=',num2str(0.0),' -POLAR -RELATIVE
       ',' \n ') ;
84  script=strcat(script,'POLYGON -DATA OPTION=PICK +NEW', ' \n ');
85  script=strcat(script,'POLYGON X=',num2str(BG_r),' Y=',num2str(0.0),' -POLAR -RELATIVE','
       \n ') ;
86  %no boundary condition: F=NO
87  script=strcat(script,'POLYGON -DATA +SIZE ESIZE=',num2str(mesh_bg),' BIAS=0.5 LINESHAPE=
       STRAIGHT F=NO', ' \n ');
88  script=strcat(script,'POLYGON X=',num2str(BG_r),' Y=',num2str(BG_h),' -POLAR -RELATIVE
       ',' \n ') ;
89  script=strcat(script,'POLYGON X=',num2str(0.0),' Y=',num2str(BG_h),' -POLAR -RELATIVE','
       \n ') ;
90  %tangential boundary condition: F=V V=0
91  script=strcat(script,'POLYGON -DATA +SIZE ESIZE=',num2str(mesh_bg),' BIAS=0.5 LINESHAPE=
       STRAIGHT F=V V=0', ' \n ');
92  script=strcat(script,'POLYGON OPTION=CLOSE', ' \n ');
93  %script=strcat(script,'YES', ' \n ');
94  % *************************
95  %load bh file
96  data_bh=[]; file_bh=fopen(bh_file,'r');
97  temp=fgetl(file_bh); temp=get_nos(temp);
98  if (temp.numbers(2)==0)
99      convB=1/10000;
100 else convB=1;
101 end
102 if (temp.numbers(3)==0)
103     convH=1000/(4*pi);
104 else convH=1;
105 end
106 while(feof(file_bh)==0)
107 temp=fgetl(file_bh); temp=get_nos(temp);
108 temp.numbers=[temp.numbers(1)*convB temp.numbers(2)*convH]; data_bh=[data_bh; [temp.
       numbers]];
109 end
110 fclose(file_bh);
111 %add bh curve for each material**********
112 script=strcat(script,' \n ','/++ ',' add BH CURVE for every material
```

```
113 | script=strcat(script,'/++ ',' mat. 4: yoke+pole', ' \n ');
114 | %material 4:yoke+pole
115 | script=strcat(script,'BHDATA MATERIAL=4 TYPE=ISOTROPIC MENU=SET', ' \n ');
116 | script=strcat(script,'BHDA', ' \n ');
117 | for j=1:length(data_bh)
118 | script=strcat(script,'ADD B=',num2str(data_bh(j,1)),' H=',num2str(data_bh(j,2)),' \n ');
119 | end
120 | script=strcat(script,'QUIT', ' \n ');
121 | %*****************************************
122 | script=strcat(script,' \n ','/++ ',' choose solver type magnetostatic
       ********************', ' \n ');
123 | script= strcat(script, 'SOLVE TYPE=ST', ' \n');
124 | script= strcat(script, 'DATA LINEAR=NO TOLERANCE=1.0E−03 NITERATION=21 ITTYPE=NEWTON
       LOSSYD=NO ADIT=0 ADEL=* ADAC=5 |QUIT ', ' \n');
125 | %LAUNCH THE SIMULATION****************************************************
126 | script=strcat(script,' \n ','/++ ',' save file and run the simulation
       ********************', ' \n ');
127 | script=strcat(script, 'WRITE FILE=''',regexprep(folder1, '\\', '\\\\'),regexprep(folder2
       , '\\', '\\\\'),regexprep(folder3, '\\', '\\\\'),regexprep(folder4, '\\', '\\\\'),
       name_comifile,'.op2'' +SOLVENOW',' \n ');
128 | %ANALYSE THE DATA AND EXPORT*****************************************
129 | script=strcat(script,' \n ','/++ ',' output result ********************', ' \n ');
130 | output_file=strcat(regexprep(folder4, '\\', '\\\\'),name_graphfile);
131 | script=[script '$ open 1 ' output_file ' write' ' \n'];
132 | script=[script '$ FORMAT 1 EXPONENTIAL 5' ' \n '];
133 | script=[script '$ FORMAT 2 EXPONENTIAL 7' ' \n '];
134 | script=[script '$ FORMAT 3 string string='' '' \n '];
135 | script=[script '$ ASSIGN 1 3 2' ' \n '];
136 | %median plane plot
137 | for R=Rin:dR:Rend
138 |     script=[script 'POINT METHOD=CARTESIAN XP=' num2str(R) ' YP=0 COMPONENT=−Bz
           HOMOGENEITY=NO' ' \n '];
139 |     script=[script '$ write 1 XP −Bz ' ' \n '];
140 | end
141 | script=[script '$ close 1' ' \n '];
142 | %*************************************
143 | file=fopen(input_file,'w');
144 | fprintf(file,script);
145 | fclose(file);
```

### ALANEW input file for Isochronous Cyclotron

```
   0, 0, 1, 3, 0,                       /KEY1,KEY2,KEY3,KEYN,IMPBZ
   4                                    /NSECT
0.000, 1.220, 0.005, 0.000, 45.00      /R2MIN,R2MAX,DR2,T2MIN,DT2
144, 1,  0,  0,  0,  0,                 /NSHIL,NSURF,NSSAI,NSVAL,NTROU,NSCYL
 247.50,  292.50      /TETHDd(1),TETHGd(1)
 RTEMP1, RTEMP2, AKHD , AKHG , FRACT, FRACT, ZSAI , AIMV, ZV  , AIMC, ZC1 , ZC2, ZC3
0.00000,0.03000,0.0000,0.0000,0.0000,0.0000,2.138,.40000,2.140,0.500,2.139,.03000
0.03000,0.05993,0.0000,0.0000,0.0000,0.0000,2.138,.40000,2.140,0.500,2.139,.02998
0.05993,0.08967,0.0000,0.0000,0.0000,0.0000,2.138,.40000,2.140,0.500,2.139,.02994
0.08967,0.11909,0.0000,0.0000,0.0000,0.0000,2.138,.40000,2.140,0.500,2.139,.02989
0.11909,0.14808,0.0000,0.0000,0.0000,0.0000,2.138,.40000,2.140,0.500,2.139,.02982
0.14808,0.17654,0.0000,0.0000,0.0000,0.0000,2.138,.40000,2.140,0.500,2.139,.02973
0.17654,0.20439,0.0000,0.0000,0.0000,0.0000,2.138,.40000,2.140,0.500,2.139,.02963
0.20439,0.23157,0.0000,0.0000,0.0000,0.0000,2.138,.40000,2.140,0.500,2.139,.02951
0.23157,0.25803,0.0000,0.0000,0.0000,0.0000,2.138,.40000,2.140,0.500,2.139,.02938
0.25803,0.28373,0.0000,0.0000,0.0000,0.0000,2.139,.40000,2.140,0.500,2.139,.02924
0.28373,0.30867,0.0726,0.0726,0.0000,0.0000,2.139,.40000,2.140,0.500,2.139,.02909
0.30867,0.33283,0.6735,0.6735,0.0000,0.0000,2.139,.40000,2.140,0.500,2.139,.02893
0.33283,0.35622,1.0351,1.0351,0.0000,0.0000,2.139,.40000,2.140,0.500,2.139,.02876
0.35622,0.37884,1.2324,1.2324,0.0000,0.0000,2.140,.40000,2.140,0.500,2.139,.02859
0.37884,0.40072,1.3690,1.3690,0.0000,0.0000,2.140,.40000,2.140,0.500,2.139,.02841
0.40072,0.42188,1.4699,1.4699,0.0000,0.0000,2.141,.40000,2.140,0.500,2.139,.02822
0.42188,0.44233,1.5417,1.5417,0.0000,0.0000,2.141,.40000,2.140,0.500,2.139,.02803
0.44233,0.46211,1.5949,1.5949,0.0000,0.0000,2.142,.40000,2.140,0.500,2.139,.02784
0.46211,0.48123,1.6278,1.6278,0.0000,0.0000,2.143,.40000,2.140,0.500,2.139,.02764
0.48123,0.49974,1.6606,1.6606,0.0000,0.0000,2.143,.40000,2.140,0.500,2.139,.02744
0.49974,0.51764,1.6795,1.6795,0.0000,0.0000,2.144,.40000,2.140,0.500,2.139,.02723
0.51764,0.53498,1.6916,1.6916,0.0000,0.0000,2.145,.40000,2.140,0.500,2.139,.02703
0.53498,0.55177,1.7003,1.7003,0.0000,0.0000,2.146,.40000,2.140,0.500,2.139,.02682
0.55177,0.56804,1.7053,1.7053,0.0000,0.0000,2.147,.40000,2.140,0.500,2.139,.02661
0.56804,0.58382,1.7009,1.7009,0.0000,0.0000,2.148,.40000,2.140,0.500,2.139,.02640
0.58382,0.59911,1.7000,1.7000,0.0000,0.0000,2.149,.40000,2.140,0.500,2.139,.02619
0.59911,0.61396,1.7003,1.7003,0.0000,0.0000,2.151,.40000,2.140,0.500,2.139,.02597
0.61396,0.62837,1.6935,1.6935,0.0000,0.0000,2.152,.40000,2.140,0.500,2.139,.02576
0.62837,0.64237,1.6978,1.6978,0.0000,0.0000,2.153,.40000,2.140,0.500,2.139,.02554
0.64237,0.65598,1.6942,1.6942,0.0000,0.0000,2.155,.40000,2.140,0.500,2.139,.02533
0.65598,0.66920,1.6926,1.6926,0.0000,0.0000,2.156,.40000,2.140,0.500,2.139,.02512
```

```
0.66920,0.68207,1.6998,1.6998,0.0000,0.0000,2.158,.40000,2.140,0.500,2.139,.02490
0.68207,0.69459,1.6958,1.6958,0.0000,0.0000,2.160,.40000,2.140,0.500,2.139,.02469
0.69459,0.70677,1.7015,1.7015,0.0000,0.0000,2.161,.40000,2.140,0.500,2.139,.02447
0.70677,0.71864,1.7023,1.7023,0.0000,0.0000,2.163,.40000,2.140,0.500,2.139,.02426
0.71864,0.73020,1.7092,1.7092,0.0000,0.0000,2.165,.40000,2.140,0.500,2.139,.02404
0.73020,0.74147,1.7099,1.7099,0.0000,0.0000,2.167,.40000,2.140,0.500,2.139,.02383
0.74147,0.75246,1.7115,1.7115,0.0000,0.0000,2.169,.40000,2.140,0.500,2.139,.02361
0.75246,0.76317,1.7235,1.7235,0.0000,0.0000,2.172,.40000,2.140,0.500,2.139,.02340
0.76317,0.77363,1.7268,1.7268,0.0000,0.0000,2.174,.40000,2.140,0.500,2.139,.02318
0.77363,0.78383,1.7262,1.7262,0.0000,0.0000,2.176,.40000,2.140,0.500,2.139,.02297
0.78383,0.79379,1.7415,1.7415,0.0000,0.0000,2.179,.40000,2.140,0.500,2.139,.02276
0.79379,0.80352,1.7396,1.7396,0.0000,0.0000,2.181,.40000,2.140,0.500,2.139,.02254
0.80352,0.81302,1.7428,1.7428,0.0000,0.0000,2.184,.40000,2.140,0.500,2.139,.02233
0.81302,0.82231,1.7503,1.7503,0.0000,0.0000,2.186,.40000,2.140,0.500,2.139,.02212
0.82231,0.83138,1.7525,1.7525,0.0000,0.0000,2.189,.40000,2.140,0.500,2.139,.02190
0.83138,0.84026,1.7709,1.7709,0.0000,0.0000,2.192,.40000,2.140,0.500,2.139,.02169
0.84026,0.84893,1.7590,1.7590,0.0000,0.0000,2.195,.40000,2.140,0.500,2.139,.02148
0.84893,0.85742,1.7778,1.7778,0.0000,0.0000,2.198,.40000,2.140,0.500,2.139,.02127
0.85742,0.86572,1.7798,1.7798,0.0000,0.0000,2.201,.40000,2.140,0.500,2.139,.02106
0.86572,0.87384,1.7847,1.7847,0.0000,0.0000,2.204,.40000,2.140,0.500,2.139,.02085
0.87384,0.88179,1.7906,1.7906,0.0000,0.0000,2.207,.40000,2.140,0.500,2.139,.02064
0.88179,0.88957,1.7899,1.7899,0.0000,0.0000,2.210,.40000,2.140,0.500,2.139,.02043
0.88957,0.89719,1.8087,1.8087,0.0000,0.0000,2.213,.40000,2.140,0.500,2.139,.02022
0.89719,0.90465,1.8099,1.8099,0.0000,0.0000,2.217,.40000,2.140,0.500,2.139,.02001
0.90465,0.91195,1.8124,1.8124,0.0000,0.0000,2.220,.40000,2.140,0.500,2.139,.01980
0.91195,0.91910,1.8205,1.8205,0.0000,0.0000,2.224,.40000,2.140,0.500,2.139,.01959
0.91910,0.92611,1.8276,1.8276,0.0000,0.0000,2.227,.40000,2.140,0.500,2.139,.01939
0.92611,0.93298,1.8345,1.8345,0.0000,0.0000,2.231,.40000,2.140,0.500,2.139,.01918
0.93298,0.93971,1.8414,1.8414,0.0000,0.0000,2.234,.40000,2.140,0.500,2.139,.01897
0.93971,0.94630,1.8491,1.8491,0.0000,0.0000,2.238,.40000,2.140,0.500,2.139,.01876
0.94630,0.95276,1.8499,1.8499,0.0000,0.0000,2.242,.40000,2.140,0.500,2.139,.01856
0.95276,0.95910,1.8497,1.8497,0.0000,0.0000,2.246,.40000,2.140,0.500,2.139,.01835
0.95910,0.96531,1.8654,1.8654,0.0000,0.0000,2.250,.40000,2.140,0.500,2.139,.01814
0.96531,0.97139,1.8744,1.8744,0.0000,0.0000,2.254,.40000,2.140,0.500,2.139,.01794
0.97139,0.97736,1.8804,1.8804,0.0000,0.0000,2.258,.40000,2.140,0.500,2.139,.01773
0.97736,0.98321,1.8792,1.8792,0.0000,0.0000,2.262,.40000,2.140,0.500,2.139,.01753
0.98321,0.98895,1.8798,1.8798,0.0000,0.0000,2.266,.40000,2.140,0.500,2.139,.01732
0.98895,0.99457,1.8954,1.8954,0.0000,0.0000,2.270,.40000,2.140,0.500,2.139,.01712
0.99457,1.00009,1.9024,1.9024,0.0000,0.0000,2.274,.40000,2.140,0.500,2.139,.01691
1.00009,1.00550,1.8975,1.8975,0.0000,0.0000,2.278,.40000,2.140,0.500,2.139,.01671
1.00550,1.01080,1.9043,1.9043,0.0000,0.0000,2.283,.40000,2.140,0.500,2.139,.01651
1.01080,1.01600,1.9181,1.9181,0.0000,0.0000,2.287,.40000,2.140,0.500,2.139,.01630
1.01600,1.02110,1.9245,1.9245,0.0000,0.0000,2.291,.40000,2.140,0.500,2.139,.01610
1.02110,1.02610,1.9286,1.9286,0.0000,0.0000,2.295,.40000,2.140,0.500,2.139,.01590
1.02610,1.03101,1.9336,1.9336,0.0000,0.0000,2.300,.40000,2.140,0.500,2.139,.01569
1.03101,1.03582,1.9384,1.9384,0.0000,0.0000,2.304,.40000,2.140,0.500,2.139,.01549
1.03582,1.04054,1.9431,1.9431,0.0000,0.0000,2.309,.40000,2.140,0.500,2.139,.01529
1.04054,1.04517,1.9478,1.9478,0.0000,0.0000,2.313,.40000,2.140,0.500,2.139,.01508
1.04517,1.04970,1.9525,1.9525,0.0000,0.0000,2.318,.40000,2.140,0.500,2.139,.01488
1.04970,1.05415,1.9570,1.9570,0.0000,0.0000,2.322,.40000,2.140,0.500,2.139,.01468
1.05415,1.05851,1.9613,1.9613,0.0000,0.0000,2.327,.40000,2.140,0.500,2.139,.01448
1.05851,1.06279,1.9650,1.9650,0.0000,0.0000,2.331,.40000,2.140,0.500,2.139,.01428
1.06279,1.06698,1.9688,1.9688,0.0000,0.0000,2.336,.40000,2.140,0.500,2.139,.01407
1.06698,1.07109,1.9773,1.9773,0.0000,0.0000,2.340,.40000,2.140,0.500,2.139,.01387
1.07109,1.07512,1.9877,1.9877,0.0000,0.0000,2.345,.40000,2.140,0.500,2.139,.01367
1.07512,1.07907,1.9935,1.9935,0.0000,0.0000,2.349,.40000,2.140,0.500,2.139,.01347
1.07907,1.08294,1.9961,1.9961,0.0000,0.0000,2.354,.40000,2.140,0.500,2.139,.01327
1.08294,1.08673,1.9998,1.9998,0.0000,0.0000,2.358,.40000,2.140,0.500,2.139,.01307
1.08673,1.09045,2.0037,2.0037,0.0000,0.0000,2.363,.40000,2.140,0.409,2.139,.01286
1.09045,1.09409,2.0072,2.0072,0.0000,0.0000,2.367,.40000,2.140,0.409,2.139,.01266
1.09409,1.09765,2.0108,2.0108,0.0000,0.0000,2.372,.40000,2.140,0.409,2.139,.01246
1.09765,1.10114,2.0143,2.0143,0.0000,0.0000,2.376,.40000,2.140,0.409,2.139,.01226
1.10114,1.10456,2.0179,2.0179,0.0000,0.0000,2.381,.40000,2.140,0.409,2.139,.01206
1.10456,1.10791,2.0212,2.0212,0.0000,0.0000,2.385,.40000,2.140,0.409,2.139,.01186
1.10791,1.11119,2.0244,2.0244,0.0000,0.0000,2.390,.40000,2.140,0.409,2.139,.01166
1.11119,1.11440,2.0263,2.0263,0.0000,0.0000,2.394,.40000,2.140,0.409,2.139,.01145
1.11440,1.11753,2.0305,2.0305,0.0000,0.0000,2.399,.40000,2.140,0.409,2.139,.01125
1.11753,1.12060,2.0374,2.0374,0.0000,0.0000,2.403,.40000,2.140,0.409,2.139,.01105
1.12060,1.12361,2.0456,2.0456,0.0000,0.0000,2.407,.40000,2.140,0.409,2.139,.01085
1.12361,1.12654,2.0513,2.0513,0.0000,0.0000,2.412,.40000,2.140,0.409,2.139,.01065
1.12654,1.12941,2.0543,2.0543,0.0000,0.0000,2.416,.40000,2.140,0.409,2.139,.01044
1.12941,1.13221,2.0552,2.0552,0.0000,0.0000,2.420,.40000,2.140,0.409,2.139,.01024
1.13221,1.13495,2.0570,2.0570,0.0000,0.0000,2.424,.40000,2.140,0.409,2.139,.01004
1.13495,1.13763,2.0609,2.0609,0.0000,0.0000,2.428,.40000,2.140,0.325,2.139,.00983
1.13763,1.14024,2.0672,2.0672,0.0000,0.0000,2.432,.40000,2.140,0.325,2.139,.00963
1.14024,1.14278,2.0741,2.0741,0.0000,0.0000,2.437,.40000,2.140,0.325,2.139,.00943
1.14278,1.14527,2.0795,2.0795,0.0000,0.0000,2.441,.40000,2.140,0.325,2.139,.00922
1.14527,1.14769,2.0831,2.0831,0.0000,0.0000,2.444,.40000,2.140,0.325,2.139,.00902
1.14769,1.15005,2.0848,2.0848,0.0000,0.0000,2.448,.40000,2.140,0.325,2.139,.00881
1.15005,1.15235,2.0864,2.0864,0.0000,0.0000,2.452,.40000,2.140,0.325,2.139,.00861
1.15235,1.15459,2.0882,2.0882,0.0000,0.0000,2.456,.40000,2.140,0.325,2.139,.00840
1.15459,1.15677,2.0909,2.0909,0.0000,0.0000,2.460,.40000,2.140,0.325,2.139,.00820
1.15677,1.15889,2.0927,2.0927,0.0000,0.0000,2.463,.40000,2.140,0.325,2.139,.00799
1.15889,1.16095,2.0944,2.0944,0.0000,0.0000,2.467,.40000,2.140,0.325,2.139,.00778
1.16095,1.16295,2.0930,2.0930,0.0000,0.0000,2.470,.40000,2.140,0.325,2.139,.00757
1.16295,1.16488,2.0941,2.0941,0.0000,0.0000,2.474,.40000,2.140,0.325,2.139,.00736
1.16488,1.16676,2.0987,2.0987,0.0000,0.0000,2.477,.40000,2.140,0.325,2.139,.00715
1.16676,1.16859,2.1064,2.1064,0.0000,0.0000,2.480,.40000,2.140,0.325,2.139,.00694
1.16859,1.17035,2.1162,2.1162,0.0000,0.0000,2.484,.40000,2.140,0.253,2.139,.00673
1.17035,1.17205,2.1250,2.1250,0.0000,0.0000,2.487,.40000,2.140,0.253,2.139,.00652
1.17205,1.17370,2.1313,2.1313,0.0000,0.0000,2.490,.40000,2.140,0.253,2.139,.00630
1.17370,1.17529,2.1383,2.1383,0.0000,0.0000,2.493,.40000,2.140,0.253,2.139,.00609
1.17529,1.17681,2.1441,2.1441,0.0000,0.0000,2.496,.40000,2.140,0.253,2.139,.00587
1.17681,1.17828,2.1500,2.1500,0.0000,0.0000,2.498,.40000,2.140,0.253,2.139,.00565
1.17828,1.17970,2.1561,2.1561,0.0000,0.0000,2.501,.40000,2.140,0.253,2.139,.00543
1.17970,1.18105,2.1614,2.1614,0.0000,0.0000,2.504,.40000,2.140,0.253,2.139,.00521
```

```
1.18105,1.18234,2.1667,2.1667,0.0000,0.0000,2.506,.40000,2.140,0.253,2.139,.00498
1.18234,1.18357,2.1721,2.1721,0.0000,0.0000,2.508,.40000,2.140,0.253,2.139,.00475
1.18357,1.18475,2.1766,2.1766,0.0000,0.0000,2.511,.40000,2.140,0.253,2.139,.00452
1.18475,1.18586,2.1813,2.1813,0.0000,0.0000,2.513,.40000,2.140,0.253,2.139,.00429
1.18586,1.18691,2.1853,2.1853,0.0000,0.0000,2.515,.40000,2.140,0.253,2.139,.00405
1.18691,1.18790,2.1898,2.1898,0.0000,0.0000,2.517,.40000,2.140,0.253,2.139,.00380
1.18790,1.18883,2.1933,2.1933,0.0000,0.0000,2.519,.40000,2.140,0.253,2.139,.00355
1.18883,1.18969,2.1974,2.1974,0.0000,0.0000,2.521,.40000,2.140,0.201,2.139,.00330
1.18969,1.19048,2.2001,2.2001,0.0000,0.0000,2.522,.40000,2.140,0.201,2.139,.00303
1.19048,1.19120,2.2040,2.2040,0.0000,0.0000,2.524,.40000,2.140,0.201,2.139,.00303
1.19120,1.19185,2.2054,2.2054,0.0000,0.0000,2.525,.40000,2.140,0.201,2.139,.00303
1.19185,1.19242,2.2091,2.2091,0.0000,0.0000,2.526,.40000,2.140,0.201,2.139,.00303
1.19242,1.19290,2.2106,2.2106,0.0000,0.0000,2.527,.40000,2.140,0.201,2.139,.20100
1.19290,1.19475,2.2153,2.2153,0.0000,0.0000,2.528,.40000,2.140,0.201,2.139,.20100
1.19475,1.19900,2.2275,2.2275,0.0000,0.0000,2.534,.40000,2.140,0.201,2.139,.20100
1.19900,1.20900,2.2561,2.2561,0.0000,0.0000,2.140,.40000,2.140,0.154,2.139,.15400
1.20900,1.21810,2.2943,2.2943,0.0000,0.0000,2.140,.40000,2.140,0.113,2.139,.11300
```

### Matlab script to generate OPERA command file from ALANEW input file

```matlab
1   %SI UNITS
2   clc; format long;
3   folder1='\\xxx'; folder2='\xxx';
4   folder3='\xxx\'; folder4='xxx\';
5   name_bhfile='xxx'; name_alafile='xxx';
6   name_comifile='xxx'; name_graphfile=strcat(name_comifile, 'graph.dat');
7   %********* variables for yoke and coil*****************************
8   Yoke_h=xxx; Yoke_r=xxx;
9   Coilspace_h=xxx; Coilspace_r=xxx; Coil_r0=xxx;%centroid position
10  Coil_z0=xxx; Coil_dr=xxx;%full-widths
11  Coil_dz=xxxx; I=xxxx; %in A.mm^2
12  %*************variables for COMI file***************************
13  SF_hill=xxx; mesh_c=xxx; mesh_coil=xxx; mesh_yoke=xxx;
14  BG_r=xxx; BG_h=xxx; mesh_bg=xxx;
15  %*************variables for graph export***********************
16  Rin=xxx; Rend=xxx; dR=xxxx;
17  % ************PROGRAMS****************************************
18  %**** input geometry from ALANEW file (can be commented)*************
19  readAlanew;
20  %**** make coil and yoke geometry coordinates *******************
21  makeYokeCoil;
22  %**** write the comi file for OPERA Import+Export *******************
23  writeComiImportExport;
24  %****************************************************************
```

### Matlab script to read ALANEW input file

```matlab
1   % the program reads the alanew input file and writes a vector with
2   % XY coordinates of the pole
3   % load ALANEW file ***************
4   Hill_xy=[]; Valley_xy=[]; Hole_xy=[]; hole_r=[];
5   hole_rp=[]; hole_y=[];
6   alanew_file=strcat(folder1,folder2,folder3,folder4,name_alafile);
7   file_ala=fopen(alanew_file,'r');
8   %go to fourth line
9   temp=fgetl(file_ala);temp=fgetl(file_ala);temp=fgetl(file_ala);
10  %read fourth line
11  temp=fgetl(file_ala); temp=get_nos(temp);
12  nbxyhill=temp.numbers(1); nbholes=temp.numbers(5);
13  %read xy coordinates from alanew data
14  temp=fgetl(file_ala); temp=fgetl(file_ala);
15  for i=1:nbxyhill
16  temp=fgetl(file_ala); temp=get_nos(temp);
17  Hill_xy=[Hill_xy; [temp.numbers(1) temp.numbers(12)]];
18  Hill_xy=[Hill_xy; [temp.numbers(2) temp.numbers(12)]];
19  Valley_xy=[Valley_xy; [temp.numbers(1) temp.numbers(10)]];
20  Valley_xy=[Valley_xy; [temp.numbers(2) temp.numbers(10)]];
21  end
22  %we cut the Hill at its lowest point
23  i_eh=max(find(Hill_xy(:,2)==min(Hill_xy(:,2))));
24  Hill_xy=Hill_xy(1:i_eh,:);
25  % simplify the geometry: cancel intermediate points on a line
26  i=1;
27  while(i+2<=length(Hill_xy))
```

```
28        temp=Hill_xy(i,2);
29        if (temp==Hill_xy(i+1,2)&& temp==Hill_xy(i+2,2))
30          Hill_xy=[Hill_xy(1:i,:);Hill_xy(i+2:end,:)];
31        else    i=i+1;
32          end
33    end
34    %we keep in the valley the point at same radius as end of hill
35    temp2=Valley_xy(i_eh,:);
36    i=1;
37    while(i+2<=length(Valley_xy))
38        temp=Valley_xy(i,2);
39        if (temp==Valley_xy(i+1,2)&& temp==Valley_xy(i+2,2))
40          Valley_xy=[Valley_xy(1:i,:);Valley_xy(i+2:end,:)];
41        else    i=i+1;
42          end
43    end
44    YokeR_newstart=1+max(find(Valley_xy(:,1)==Hill_xy(end,1)));
45    if (length(YokeR_newstart)==0)
46        YokeR_newstart=min(find(Valley_xy(:,1)>temp2(1)));
47        Valley_xy=[Valley_xy(1:YokeR_newstart-1,:); temp2; Valley_xy(YokeR_newstart:end, :)];
48        YokeR_newstart=YokeR_newstart+1;
49    end
50    %introduce holes
51    %read alanew file for hole info
52    %!!!!!!!!!!!!!!!!!!
53    % ATTENTION: the holes should be written in rising R order in alanew file!!
54    %!!!!!!!!!!!!!!!!!!
55    for i=1:nbholes
56    temp=fgetl(file_ala); temp=get_nos(temp);
57    hole_r=[hole_r;temp.numbers(1)];
58    hole_rp=[hole_rp; temp.numbers(3)];
59    hole_y=[hole_y; temp.numbers(4)];
60    Hole_xy=[Hole_xy [hole_r(i)-hole_rp(i) hole_y(i); hole_r(i)+hole_rp(i) hole_y(i)]];
61    Valley_xy=[Valley_xy(1:2*i-1,:);Hole_xy(:,2*i-1:2*i);Valley_xy(2*i:end,:)];
62    end
63    fclose(file_ala);
64    %we look for the index in valley corresponding to end of hill
65    YokeR_newstart=1+max(find(Valley_xy(:,1)==Hill_xy(end,1)));
66    Pole_xy=[Hill_xy(1:end,:); Valley_xy(YokeR_newstart-1:-1:1,:)];
67    %clean the vector from double inputs
68    i=1;
69    while(i+1<=length(Pole_xy))
70        if (Pole_xy(i,:)==Pole_xy(i+1,:))
71          Pole_xy=[Pole_xy(1:i-1,:);Pole_xy(i+1:end,:)];
72        else    i=i+1;
73          end
74    end
```

### Matlab script to generate the Yoke and Coil geometries

```
1    YokeL_xy=[]; YokeR_xy=[]; Coil_xy=[];
2    %the coil is created from input parameters in main program
3    Coil_xy=[Coil_xy; [Coil_r0-0.5*Coil_dr Coil_z0-0.5*Coil_dz]];
4    Coil_xy=[Coil_xy; [Coil_r0+0.5*Coil_dr Coil_z0-0.5*Coil_dz]];
5    Coil_xy=[Coil_xy; [Coil_r0+0.5*Coil_dr Coil_z0+0.5*Coil_dz]];
6    Coil_xy=[Coil_xy; [Coil_r0-0.5*Coil_dr Coil_z0+0.5*Coil_dz]];
7    %the part of the yoke over the hill is the yokeL(eft), the part of the yoke
8    %over the coil is called yokeR(ight)
9    %the yoke regions are numbered from left to right: these are regions
10   % with stacking factor 1
11   YokeL_xy=[YokeL_xy; Valley_xy(1:2,:); Valley_xy(2:-1:1,:)];
12   YokeL_xy(end-1,end)=Yoke_h; YokeL_xy(end,end)=Yoke_h;
13   if (nbholes~=0)
14   %in the case of 2 holes: this is the region between the two holes
15   Hole_xy=[Hole_xy;Hole_xy(2:-1:1,:)]; Hole_xy(3:4,2)=[Yoke_h; Yoke_h];
16   if (nbholes==2)
17       YokeL_xy=[YokeL_xy [Valley_xy(3:4,:); Valley_xy(4:-1:3,:)]];
18       YokeL_xy(end-1,end)=Yoke_h; YokeL_xy(end,end)=Yoke_h;
19   Hole_xy(3:4,4)=[Yoke_h; Yoke_h];
20   end
```

```
21  %index of last straight section of valley (after the holes)
22  j=1+find(Valley_xy(:,1)==Hole_xy(2,end-1));
23  YokeL_xy=[YokeL_xy [Valley_xy(j-1:j,:); Valley_xy(j:-1:j-1,:)]];
24  YokeL_xy(end-1,end)=Yoke_h; YokeL_xy(end,end)=Yoke_h;
25  else
26  j=2;
27  end
28  %last section of the yoke: end of valley, around the coil,...
29  YokeR_xy=[YokeR_xy;[Valley_xy(j,1) Yoke_h]];
30  YokeR_xy=[YokeR_xy;[Valley_xy(j:end,:)]];
31  %index of first new point YokeR_newstart defined in readAlanew
32      i=1;
33  while(i<=size(YokeR_xy,1))
34      if(YokeR_xy(i,1)==Valley_xy(YokeR_newstart,1))
35          if(YokeR_xy(i,2)==Valley_xy(YokeR_newstart,2))
36              YokeR_newstart=i;
37              i=size(YokeR_xy,1)+1000;
38          end
39      end
40      i=i+1;
41  end
42  if (YokeR_xy(end,2)~=max(Coil_xy(:,2))+Coilspace_h)
43      YokeR_xy=[YokeR_xy; [Valley_xy(end,1) max(Coil_xy(:,2))+Coilspace_h]];
44  end
45  %space for the coil
46  YokeR_xy=[YokeR_xy;[max(Coil_xy(:,1))+Coilspace_r max(Coil_xy(:,2))+Coilspace_h];[max(
        Coil_xy(:,1))+Coilspace_r 0]];
47  YokeR_xy=[YokeR_xy;[Yoke_r 0];[Yoke_r Yoke_h]];
```

### Matlab script to generate the OPERA command file

```
1   bh_file=strcat(folder1, folder2,'\bh\', name_bhfile);
2   input_file=strcat(folder1,folder2,folder3,folder4,name_comifile, 'import.comi');
3   script=strcat('/++ ',' OPERA 2D input file made on : ', datestr(now), ' \n ');
4   script=strcat(script,'/++ ',' from ALANEW input file : ',name_alafile, ' \n ');
5   script=strcat(script,'/++ ',' with BH file : ', name_bhfile, ' \n ');
6   script=strcat(script,'/++ ',' Written on Matlab by : Adriano Garonna', ' \n ', ' \n ');
7   script=strcat(script,'/++ ',' ********** PARAMETERS ************', ' \n ');
8   script=strcat(script,'/++ ',' MESH size is : the background (', num2str(mesh_bg),'), the
        coil (',num2str(mesh_coil),'), the yoke (',num2str(mesh_yoke),'), the hill (',
        num2str(mesh_c),'), \n ');
9   script=strcat(script,'/++ ',' YOKE half height of ', num2str(Yoke_h),'m and radius of
        ', num2str(Yoke_r), ' m \n ');
10  script=strcat(script,'/++ ',' COIL centroid(width) is : ', num2str(Coil_r0),' (',
        num2str(Coil_dr),') m in R and ', num2str(Coil_z0),' (', num2str(Coil_dz),') m in Z
        \n ');
11  script=strcat(script,'/++ ',' COIL distance to yoke is : ', num2str(Coilspace_r),' m in
        R and ', num2str(Coilspace_h),' m in Z \n ');
12  script=strcat(script,'/++ ',' COIL current is : ', num2str(I),' A/mm^2 \n ');
13  script=strcat(script,'/++ ',' ********************************', ' \n ', ' \n ');
14  script=strcat(script,'UNITS LENGTH=METRE FLUX=TESLA FIELD=AM POTENTIAL=WBM CONDUCTIVITY=
        SM DENSITY=AM2 FORCE=NEWTON ENERGY=JOULE POWER=WATT MASS=KG');
15  script=strcat(script,' \n ','SET FIELD=MAGNETIC SYMMETRY=AXISYMMETRY AUTOMATIC=YES
        ELEMENT=LINEAR',' \n ');
16  %draw the hill *************************
17  script=strcat(script,' \n ','/++ ',' draw HILL*****************', ' \n ');
18  script=strcat(script,'DRAW SHAPE=POLYGON,', ' \n ');
19  script=strcat(script,'DRAW +DEFAULTS SHAPE=POLYGON TOLERANCE=1.0E-05 MATERIAL=5 PERM=100
        DENS=0 CONDUCTIVITY=0 PHASE=0 VELOCITY=0 N=0 SYMMETRY=0 XCEN=0 YCEN=0 ANGLE=0 NX=1
        DX=0 NY=1 DY=0 ROTATIONS=1 TROTATION=0 MIRROR=NO', ' \n ');
20  script=strcat(script,'POLYGON -DATA +SIZE ESIZE=',num2str(mesh_c),' BIAS=0.5 LINESHAPE=
        STRAIGHT F=NO', ' \n ');
21  script=strcat(script,'POLYGON -DATA OPTION=PICK +NEW', ' \n ');
22  for j=1:length(Pole_xy)
23      script=strcat(script,'POLYGON X=',num2str(Pole_xy(j,1)),' Y=',num2str(Pole_xy(j,2))
            ,' -POLAR -RELATIVE',' \n ') ;
24  end
25  script=strcat(script,'POLYGON OPTION=CLOSE', ' \n ');
26  % draw coil ****************************
27  script=strcat(script,' \n ','/++ ',' draw COIL*****************', ' \n ');
```

```
28  script=strcat(script,'DRAW SHAPE=POLYGON,',' \n ');
29  script=strcat(script,'DRAW +DEFAULTS SHAPE=POLYGON TOLERANCE=1.0E−05 MATERIAL=1 PERM=1
        DENS=',num2str(I),' CONDUCTIVITY=0 PHASE=0 VELOCITY=0 N=0 SYMMETRY=0 XCEN=0 YCEN=0
        ANGLE=0 NX=1 DX=0 NY=1 DY=0 ROTATIONS=1 TROTATION=0 MIRROR=NO',' \n ');
30  script=strcat(script,'POLYGON −DATA +SIZE ESIZE=',num2str(mesh_coil),' BIAS=0.5
        LINESHAPE=STRAIGHT F=NO',' \n ');
31  script=strcat(script,'POLYGON −DATA OPTION=PICK +NEW',' \n ');
32  for j=1:length(Coil_xy)
33      script=strcat(script,'POLYGON X=',num2str(Coil_xy(j,1)),' Y=',num2str(Coil_xy(j,2))
            ,' −POLAR −RELATIVE',' \n ') ;
34  end
35  script=strcat(script,'POLYGON OPTION=CLOSE',' \n ');
36  % draw yoke  (SF=1)*************
37  script=strcat(script,' \n ','/++ ',' draw YOKE********************',' \n ');
38  script=strcat(script,'DRAW SHAPE=POLYGON,',' \n ');
39  script=strcat(script,'DRAW +DEFAULTS SHAPE=POLYGON TOLERANCE=1.0E−05 MATERIAL=4 PERM=1
        DENS=0 CONDUCTIVITY=0 PHASE=0 VELOCITY=0 N=0 SYMMETRY=0 XCEN=0 YCEN=0 ANGLE=0 NX=1
        DX=0 NY=1 DY=0 ROTATIONS=1 TROTATION=0 MIRROR=NO',' \n ');
40  script=strcat(script,'POLYGON −DATA +SIZE ESIZE=',num2str(mesh_yoke),' BIAS=0.5
        LINESHAPE=STRAIGHT F=NO',' \n ');
41  % yoke part left
42  script=strcat(script,' \n ','/++ ',' draw YOKE, LEFT part******',' \n ');
43  for i=1:2:size(YokeL_xy,2)−1
44  script=strcat(script,'POLYGON −DATA OPTION=PICK +EXIST',' \n ');
45  script=strcat(script,'POLYGON X=',num2str(YokeL_xy(1,i)),' Y=',num2str(YokeL_xy(1,i+1))
        ,' −POLAR −RELATIVE',' \n ') ;
46  script=strcat(script,'POLYGON X=',num2str(YokeL_xy(2,i)),' Y=',num2str(YokeL_xy(2,i+1))
        ,' −POLAR −RELATIVE',' \n ') ;
47  script=strcat(script,'POLYGON −DATA OPTION=PICK +NEW',' \n ');
48  script=strcat(script,'POLYGON X=',num2str(YokeL_xy(3,i)),' Y=',num2str(YokeL_xy(3,i+1))
        ,' −POLAR −RELATIVE',' \n ') ;
49  script=strcat(script,'POLYGON X=',num2str(YokeL_xy(4,i)),' Y=',num2str(YokeL_xy(4,i+1))
        ,' −POLAR −RELATIVE',' \n ') ;
50  script=strcat(script,'POLYGON OPTION=CLOSE',' \n ');
51  end
52  % yoke part right
53  script=strcat(script,' \n ','/++ ',' draw YOKE, RIGHT part*********',' \n ');
54  script=strcat(script,'POLYGON −DATA OPTION=PICK +EXIST',' \n ');
55  i=1;
56  while(i<YokeR_newstart)
57  script=strcat(script,'POLYGON X=',num2str(YokeR_xy(i,1)),' Y=',num2str(YokeR_xy(i,2)),'
        −POLAR −RELATIVE',' \n ') ;
58  i=i+1;
59  end
60  script=strcat(script,'POLYGON −DATA OPTION=PICK +NEW',' \n ');
61  while(i<=length(YokeR_xy))
62  script=strcat(script,'POLYGON X=',num2str(YokeR_xy(i,1)),' Y=',num2str(YokeR_xy(i,2)),'
        −POLAR −RELATIVE',' \n ') ;
63  i=i+1;
64  end
65  script=strcat(script,'POLYGON OPTION=CLOSE',' \n ');
66  if (nbholes>=1)
67  %new SF (material 6):hole 1
68  script=strcat(script,' \n ','/++ ',' draw RF HOLE 1******************',' \n ',' \n ')
        ;
69  script=strcat(script,'DRAW SHAPE=POLYGON,',' \n ');
70  script=strcat(script,'DRAW +DEFAULTS SHAPE=POLYGON TOLERANCE=1.0E−05 MATERIAL=6 PERM=1
        DENS=0 CONDUCTIVITY=0 PHASE=0 VELOCITY=0 N=0 SYMMETRY=0 XCEN=0 YCEN=0 ANGLE=0 NX=1
        DX=0 NY=1 DY=0 ROTATIONS=1 TROTATION=0 MIRROR=NO',' \n ');
71  script=strcat(script,'POLYGON −DATA +SIZE ESIZE=',num2str(mesh_yoke),' BIAS=0.5
        LINESHAPE=STRAIGHT F=NO',' \n ');
72  script=strcat(script,'POLYGON −DATA OPTION=PICK +EXIST',' \n ');
73  for i=1:size(Hole_xy,1)
74  script=strcat(script,'POLYGON X=',num2str(Hole_xy(i,1)),' Y=',num2str(Hole_xy(i,2)),' −
        POLAR −RELATIVE',' \n ') ;
75  end
76  script=strcat(script,'POLYGON OPTION=CLOSE',' \n ');
77  %new SF (material 7):hole 2
78  if (nbholes==2)
79  script=strcat(script,' \n ','/++ ',' draw RF HOLE 2****************',' \n ');
80  script=strcat(script,'DRAW SHAPE=POLYGON,',' \n ');
```

```
81  script=strcat(script,'DRAW +DEFAULTS SHAPE=POLYGON TOLERANCE=1.0E-05 MATERIAL=7 PERM=1
        DENS=0 CONDUCTIVITY=0 PHASE=0 VELOCITY=0 N=0 SYMMETRY=0 XCEN=0 YCEN=0 ANGLE=0 NX=1
        DX=0 NY=1 DY=0 ROTATIONS=1 TROTATION=0 MIRROR=NO', ' \n');
82  script=strcat(script,'POLYGON -DATA +SIZE ESIZE=',num2str(mesh_yoke),' BIAS=0.5
        LINESHAPE=STRAIGHT F=NO', ' \n ');
83  script=strcat(script,'POLYGON -DATA OPTION=PICK +EXIST', ' \n ');
84  for i=1:size(Hole_xy,1)
85  script=strcat(script,'POLYGON X=',num2str(Hole_xy(i,3)),' Y=',num2str(Hole_xy(i,4)),' -
        POLAR -RELATIVE',' \n ') ;
86  end
87  script=strcat(script,'POLYGON OPTION=CLOSE', ' \n ');
88  end
89  end
90  % draw background *************
91  script=strcat(script,' \n ','/++ ',' draw BACKGROUND*********************', ' \n ', '
        \n ');
92  script=strcat(script,'DRAW SHAPE=POLYGON,', ' \n ');
93  script=strcat(script,'DRAW +DEFAULTS SHAPE=BACKGROUND TOLERANCE=1.0E-05 MATERIAL=0 PERM
        =1 DENS=0 CONDUCTIVITY=0 PHASE=0 VELOCITY=0 N=0 SYMMETRY=0 XCEN=0 YCEN=0 ANGLE=0 NX
        =1 DX=0 NY=1 DY=0 ROTATIONS=1 TROTATION=0 MIRROR=NO', ' \n');
94  %tangential boundary condition: F=V V=0
95  script=strcat(script,'POLYGON -DATA +SIZE ESIZE=',num2str(mesh_bg),' BIAS=0.5 LINESHAPE=
        STRAIGHT F=V V=0', ' \n ');
96  script=strcat(script,'POLYGON -DATA OPTION=PICK +EXIST', ' \n ');
97  script=strcat(script,'POLYGON X=',num2str(0),' Y=',num2str(Pole_xy(end,2)),' -POLAR -
        RELATIVE',' \n ') ;
98  script=strcat(script,'POLYGON -DATA +SIZE ESIZE=',num2str(mesh_bg/100),' BIAS=0.5
        LINESHAPE=STRAIGHT F=V V=0', ' \n ');
99  script=strcat(script,'POLYGON -DATA OPTION=PICK +EXIST', ' \n ');
100 script=strcat(script,'POLYGON X=',num2str(0),' Y=',num2str(Pole_xy(1,2)),' -POLAR -
        RELATIVE',' \n ') ;
101 script=strcat(script,'POLYGON -DATA OPTION=PICK +NEW', ' \n ');
102 script=strcat(script,'POLYGON X=',num2str(0.0),' Y=',num2str(0.0),' -POLAR -RELATIVE','
        \n ') ;
103 % normal boundary condition: F=DV DV=0
104 script=strcat(script,'POLYGON -DATA +SIZE ESIZE=',num2str(mesh_bg/100),' BIAS=0.5
        LINESHAPE=STRAIGHT F=DV DV=0', ' \n ');
105 script=strcat(script,'POLYGON -DATA OPTION=PICK +EXIST', ' \n ');
106 script=strcat(script,'POLYGON X=',num2str(max(Coil_xy(:,1))+Coilspace_r),' Y=',num2str
        (0.0),' -POLAR -RELATIVE',' \n ') ;
107 script=strcat(script,'POLYGON -DATA +SIZE ESIZE=',num2str(mesh_bg),' BIAS=0.5 LINESHAPE=
        STRAIGHT F=DV DV=0', ' \n ');
108 script=strcat(script,'POLYGON X=',num2str(Yoke_r),' Y=',num2str(0.0),' -POLAR -RELATIVE
        ',' \n ') ;
109 script=strcat(script,'POLYGON -DATA OPTION=PICK +NEW', ' \n ');
110 script=strcat(script,'POLYGON X=',num2str(BG_r),' Y=',num2str(0.0),' -POLAR -RELATIVE','
        \n ') ;
111 %no boundary condition: F=NO
112 script=strcat(script,'POLYGON -DATA +SIZE ESIZE=',num2str(mesh_bg),' BIAS=0.5 LINESHAPE=
        STRAIGHT F=NO', ' \n ');
113 script=strcat(script,'POLYGON X=',num2str(BG_r),' Y=',num2str(BG_h),' -POLAR -RELATIVE
        ',' \n ') ;
114 script=strcat(script,'POLYGON X=',num2str(0.0),' Y=',num2str(BG_h),' -POLAR -RELATIVE','
        \n ') ;
115 %tangential boundary condition: F=V V=0
116 script=strcat(script,'POLYGON -DATA +SIZE ESIZE=',num2str(mesh_bg),' BIAS=0.5 LINESHAPE=
        STRAIGHT F=V V=0', ' \n ');
117 script=strcat(script,'POLYGON OPTION=CLOSE', ' \n ');
118 script=strcat(script,'YES', ' \n ');
119 %load bh file
120 data_bh=[];
121 file_bh=fopen(bh_file,'r');
122 temp=fgetl(file_bh);
123 temp=get_nos(temp);
124 if (temp.numbers(2)==0)
125     convB=1/10000;
126 else convB=1;
127 end
128 if (temp.numbers(3)==0)
129     convH=1000/(4*pi);
130 else convH=1;
```

```
131  end
132  while ( feof ( file_bh )==0)
133  temp=fgetl ( file_bh );
134  temp=get_nos (temp);
135  temp.numbers=[temp.numbers(1)*convB temp.numbers(2)*convH];
136  data_bh=[data_bh; [temp.numbers]];
137  end
138  fclose ( file_bh );
139  %add bh curve for each material **********
140  script=strcat(script,' \n ','/++ ',' add BH CURVE for every material
         *********************', ' \n ');
141  script=strcat(script,'/++ ',' mat. 4: yoke, mat. 5: pole, mat. 6-7: RF holes ', ' \n ');
142  %material 4:yoke
143  script=strcat(script,'BHDATA MATERIAL=4 TYPE=ISOTROPIC MENU=SET', ' \n ');
144  script=strcat(script,'BHDA', ' \n ');
145  for j=1:length(data_bh)
146  script=strcat(script,'ADD B=',num2str(data_bh(j,1)),' H=',num2str(data_bh(j,2)),' \n ');
147  end
148  script=strcat(script,'QUIT', ' \n ');
149  %material 5: pole
150  script=strcat(script,'BHDATA MATERIAL=5 TYPE=ISOTROPIC MENU=SET', ' \n ');
151  script=strcat(script,'BHDA', ' \n ');
152  for j=1:length(data_bh)
153  script=strcat(script,'ADD B=',num2str(4*pi*1e-7*data_bh(j,2)+SF_hill*(data_bh(j,1)-4*pi
         *1e-7*data_bh(j,2))),' H=',num2str(data_bh(j,2)),' \n ');
154  end
155  script=strcat(script,'QUIT', ' \n ');
156  if (nbholes>=1)
157  %material 6: rf1
158  SF_rf1=1-(hole_rp(1)/hole_r(1));
159  script=strcat(script,'BHDATA MATERIAL=6 TYPE=ISOTROPIC MENU=SET', ' \n ');
160  script=strcat(script,'BHDA', ' \n ');
161  for j=1:length(data_bh)
162  script=strcat(script,'ADD B=',num2str(4*pi*1e-7*data_bh(j,2)+SF_rf1*(data_bh(j,1)-4*pi*1
         e-7*data_bh(j,2))),' H=',num2str(data_bh(j,2)),' \n ');
163  end
164  script=strcat(script,'QUIT', ' \n ');
165  if (nbholes==2)
166  %material 7: rf2
167  SF_rf2=1-(hole_rp(2)/hole_r(2));
168  script=strcat(script,'BHDATA MATERIAL=7 TYPE=ISOTROPIC MENU=SET', ' \n ');
169  script=strcat(script,'BHDA', ' \n ');
170  for j=1:length(data_bh)
171  script=strcat(script,'ADD B=',num2str(4*pi*1e-7*data_bh(j,2)+SF_rf2*(data_bh(j,1)-4*pi*1
         e-7*data_bh(j,2))),' H=',num2str(data_bh(j,2)),' \n ');
172  end
173  script=strcat(script,'QUIT', ' \n ');
174  end
175  end
176  %*****************************************
177  script=strcat(script,' \n ','/++ ',' choose solver type magnetostatic
         ********************', ' \n ');
178  script= strcat(script, 'SOLVE TYPE=ST', ' \n');
179  script= strcat(script, 'DATA LINEAR=NO TOLERANCE=1.0E-03 NITERATION=21 ITTYPE=NEWTON
         LOSSYD=NO ADIT=0 ADEL=* ADAC=5 |QUIT ', ' \n');
180  %LAUNCH THE SIMULATION **********************************************
181  script=strcat(script,' \n ','/++ ',' save file and run the simulation
         ********************', ' \n ');
182  script=strcat(script,' \n ','MESH +ERRORCHECK TOLERANCE=1.0E-06 -DISPLAY | NO', ' \n ');
183  script=strcat(script, 'WRITE FILE='''',regexprep(folder1, '\\', '\\\\'),regexprep(folder2
         , '\\', '\\\\'),regexprep(folder3, '\\', '\\\\'),regexprep(folder4, '\\', '\\\\'),
         name_comifile,'.op2'' +SOLVENOW',' \n ');
184  %ANALYSE THE DATA AND EXPORT*****************************************
185  script=strcat(script,' \n ','/++ ',' output result *******************', ' \n ');
186  output_file=strcat(regexprep(folder4, '\\', '\\\\'),name_graphfile);
187  script=[script '$ open 1 ' output_file ' write' ' \n'];
188  script=[script '$ FORMAT 1 EXPONENTIAL 5' ' \n '];
189  script=[script '$ FORMAT 2 EXPONENTIAL 7' ' \n '];
190  script=[script '$ FORMAT 3 string string='' ' \n '];
191  script=[script '$ ASSIGN 1 3 2' ' \n '];
192  %median plane plot
```

```
193  for R=Rin:dR:Rend
194      script=[script 'POINT METHOD=CARTESIAN XP=' num2str(R) ' YP=0 COMPONENT=-Bz
             HOMOGENEITY=NO' ' \n '];
195      script=[script '$ write 1 XP -Bz ' ' \n '];
196  end
197  script=[script '$ close 1' ' \n '];
198  %**************************************
199  file=fopen(input_file,'w');
200  fprintf(file,script);
201  fclose(file);
```

# B. RF Design

Matlab script for Isochronous Cyclotron RF Cavity

```
1   %SI UNITS AND RMS VALUES
2   folder='\\xxx\'; name_file='xxx';
3   export_file=strcat(folder,name_file,'_export.txt');
4   F=XXXX; %RF frequency
5   Vf=XXXXX; %terminal voltage at extraction
6   Rmin=XXX; Rmax=XXX/100;
7   thetacav=XXX; %cavity opening angle in rad
8   Rpva=XXXX; % end of valley skirt -> outer conductor limit
9   Sc=XXX; %stem percent occupation
10  Rstem=XXXX; %center of stem
11  dstem=Sc*2*Rstem*sin(thetacav/2); Dstem=XXX*dstem;
12  Nsecd=XX; Nsecg=XX;
13  ld=(Rmax-(Rstem+0.5*dstem))/Nsecd;
14  Rd=[Rmax-0.5*ld:-ld:Rstem+0.5*dstem+0.5*ld]';
15  ld=ld*ones(Nsecd,1);
16  lg=(Rstem-0.5*dstem-Rmin)/Nsecg;
17  Rg=[Rmin+0.5*lg:lg:Rstem-0.5*dstem-0.5*lg]';
18  lg=lg*ones(Nsecg,1); Ag=Rg*thetacav;
19  Ad=Rd*thetacav; b=XX;
20  bd=b*ones(Nsecd,1); bg=b*ones(Nsecg,1);
21  Zvmax=XXX/100; %valley floor
22  Bg=2*(Zvmax-(XX/100));
23  Bd=2*(Zvmax-(XX/100))*ones(Nsecd-1,1);
24  Bd=[2*(XXX-XX)/100;Bd];
25  Bg=Bg*ones(Nsecg,1);
26  damin=XX; %at Rmin
27  damax=XXX; %at Rmax
28  dad=damin+(damax-damin)*(Rd-Rmin)/(Rmax-Rmin);
29  dag=damin+(damax-damin)*(Rg-Rmin)/(Rmax-Rmin);
30  ad=Ad-2*dad; ag=Ag-2*dag;
31  epsilon0=8.854E-12; %in F/m
32  Cterm=epsilon0*bd(end)*Rmax*thetacav/(Rpva-Rmax)%[F]
33  Zcar_cyl=@(xD,xd)138*log(xD/xd)/log(10);
34  %pure reactance: for practical reasons, we omit complex and sign convention
35  Zf=abs(-.159/(F*Cterm)); If=Vf/Zf;
36  Zcstem=Zcar_cyl(Dstem,dstem);
37  Zcd=[]; Rnewd=[];Zcg=[]; Rnewg=[];
38  for i=1:1:length(ad),
39      [temp1 temp2]=ZcReq_AL_NT2011(Ad(i),ad(i),Bd(i),bd(i));
40      Zcd=[Zcd; temp1]; Rnewd=[Rnewd; temp2];
41  end
42  for i=1:1:length(ag),
43      [temp1 temp2]=ZcReq_AL_NT2011(Ag(i),ag(i),Bg(i),bg(i));
44      Zcg=[Zcg; temp1]; Rnewg=[Rnewg; temp2];
45  end
46  Beta=2*pi*F/3e8;
47  Rs=sqrt(pi*F*4e-7*pi/5.8e7);%surface resistivity
48  Zd=zeros(length(ld),1); Vd=zeros(length(ld),1);
49  Id=zeros(length(ld),1); dPd=zeros(length(ld),1);
50  Vd(1)=Vf*(cos(Beta*ld(1))-Zcd(1)*sin(Beta*ld(1))/Zf);
51  Id(1)=If*(cos(Beta*ld(1))+Zf*sin(Beta*ld(1))/Zcd(1));
52  dPd(1)=If*If*(ld(1)*0.5*(1+(Zf./Zcd(1)).^2)+(1-(Zf./Zcd(1)).^2).*(sin(2*Beta*ld(1))./(4*
        Beta))+Zf.*(1-cos(2*Beta*ld(1)))./(2*Beta.*Zcd(1)));
```

```
53  Zd(1)=Vd(1)./Id(1);
54  for n=2:1:length(ld),
55      Vd(n)=Vd(n-1).*(cos(Beta.*ld(n))-Zcd(n)*sin(Beta.*ld(n))./Zd(n-1));
56      Id(n)=Id(n-1).*(cos(Beta.*ld(n))+Zd(n-1).*sin(Beta.*ld(n))/Zcd(n));
57      Zd(n)=Vd(n)./Id(n);
58      dPd(n)=Id(n-1)*Id(n-1)*(ld(n)*0.5*(1+(Zd(n-1)./Zcd(n)).^2)+(1-(Zd(n-1)./Zcd(n)).^2)
            .*(sin(2*Beta*ld(n))./(4*Beta))+Zd(n-1).*(1-cos(2*Beta*ld(n)))./(2*Beta.*Zcd(n))
            );
59  end
60  Zg=zeros(length(lg),1); Vg=zeros(length(lg),1);
61  Ig=zeros(length(lg),1); dPg=zeros(length(lg),1);
62  Zg(1)=Zcg(1)./tan(Beta*lg(1)); %formula for open circuit
63  Vg(end)=Vd(end); %same voltage at end of LEFT/RIGHT sections
64  for i=2:1:length(lg)
65      Zg(i)=Zcg(i)*(Zg(i-1)-tan(Beta.*lg(i))*Zcg(i))./(Zcg(i)+tan(Beta.*lg(i)).*Zg(i-1));
66  end
67  Ig(end)=Vg(end)/Zg(end);
68  for j=length(lg)-1:-1:1,
69      Vg(j)=Vg(j+1)./(cos(Beta.*lg(j+1))-Zcg(j+1)*sin(Beta.*lg(j+1))./Zg(j));
70      Ig(j)=Vg(j)/Zg(j);
71      end
72  %voltage and current at Rmin edge of the Dee
73  Vi=Vg(1)/cos(Beta*lg(1)); Ii=0;
74  %because of the different index convention in LEFT sections, (n-1)-> n in
75  for n=1:1:length(lg),
76  dPg(n)=Ig(n)*Ig(n)*(lg(n)*0.5*(1+(Zg(n)./Zcg(n)).^2)+(1-(Zg(n)./Zcg(n)).^2).*(sin(2*Beta
        *lg(n))./(4*Beta))+Zg(n).*(1-cos(2*Beta*lg(n)))./(2*Beta.*Zcg(n)));
77  end
78  Istem=0.5*(Id(end)+Ig(end));
79  Zstem=Vg(end)/Istem;
80  Lstem=atan(Zstem/Zcstem)./Beta; %length towards a short-circuit
81  dPstem=Istem*Istem*(Lstem*0.5*(1+(Zstem./Zcstem).^2)+(1-(Zstem./Zcstem).^2).*(sin(2*Beta
        *Lstem)./(4*Beta))+Zstem.*(1-cos(2*Beta*Lstem))./(2*Beta.*Zcstem));
82  Isc=Istem*cos(Beta*Lstem);
83  Radius=[Rg+0.5*lg;Rd(end:-1:1)-0.5*ld(end:-1:1)]; Vr=[Vg;Vd(end:-1:1)];
84  Ir=[Ig;Id(end:-1:1)]; Zr=[Zg;Zd(end:-1:1)];
85  Lr=[lg;ld(end:-1:1)]; ar=[ag; ad(end:-1:1)];
86  Ar=[Ag; Ad(end:-1:1)]; br=[bg; bd(end:-1:1)];
87  Br=[Bg; Bd(end:-1:1)]; dPr=[dPg; dPd(end:-1:1)];
88  Zcr=[Zcg; Zcd(end:-1:1)]; Rnewr=[Rnewg; Rnewd(end:-1:1)];
89  Pr=zeros(length(Lr),1); Pa=zeros(length(Lr),1);
90  Pa=4*Rs*Rnewr.*dPr.*(Zcr/(120*pi)).^2;
91  Pr=Zcr.*dPr*Beta;
92  Radius=[Rmin; Radius; Rmax]; Vr=[Vi; Vr; Vf];
93  Ir=[Ii; Ir; If]; Zr=[Inf; Zr; Zf];
94  Lr=[0; Lr; 0]; Pa=[0; Pa; 0];
95  Pr=[0; Pr; Zf*If*If];
96  Pastem=dPstem*Rs*((2/Dstem)+(2/dstem))/(2*pi);
97  Prstem=dPstem*Zcstem*Beta;
98  Psc=Rs*Isc*Isc*log(Dstem/dstem);
99  Papeak=sum(Pa)+2*(Pastem+Psc);
100 Prpeak=sum(Pr)+2*Prstem; Q=Prpeak./Papeak;
```

## Matlab script for Synchrocyclotron RF Cavity

```
1   % SI UNITS and RMS values
2   folder='\\xxx\'; name_file='xxx';
3   export_file=strcat(folder,name_file,'_export.txt');
4   F_max=XXX; F_min=XXX;
5   F=[F_max:-(F_max-F_min)/2:F_min]; %RF frequency
6   Cdee=XXXX; %terminal capacity
7   Crmin=XXX; %minimal capacity on the Rotco
8   Vdee=ones(1,length(F))*XXXX; %terminal voltage at extraction
9   Lambda=3e8./F; Rmax= XXX;
10  Rmargin=XXX; Zvalleymargin=XXX;
11  Zvalley=XXX; Zdee=XXXX;
12  da=Rmargin; Nsec= XX;
13  l=ones(Nsec,1)*(Rmax+Rmargin)/Nsec;
14  B=ones(Nsec,1)*2*(Zvalley-Zvalleymargin);
15  b=ones(Nsec,1)*2*Zdee;
```

```
16  A=[]; a=[]; Length=[0];
17  temp1=0.5*l(1); da=da*ones(Nsec,1);
18  for i=1:1:length(l),
19  temp2=2*sqrt(((Rmax+Rmargin)^2-(temp1)^2));
20  A=[A;temp2]; a=[a;temp2-2*da(i)];
21  Length=[Length; Length(end)+l(i)];
22  if i<length(l) temp1=temp1+0.5*l(i)+0.5*l(i+1);
23  end end
24  Aline=XXX; aline=XXXX; Bline=XXXX; bline=XXXX;
25  Ryoke=XXX; l=[l;Ryoke-(Rmax+Rmargin)];
26  A=[A; 0.5*(A(end)+Aline)];a=[a; 0.5*(a(end)+aline)];
27  b=[b; 0.5*(b(end)+bline)];B=[B; 0.5*(B(end)+Bline)];
28  Length=[Length; sum(l)];
29  %pure reactance: for practical reasons, we omit complex and sign convention
30  Zdee=abs(-.159./(F*Cdee)); Idee=Vdee./Zdee;
31  Zc=[]; Rnew=[];
32  for i=1:1:length(A),
33      [temp1 temp2]=ZcReq_AL_NT2011(A(i),a(i),B(i),b(i));
34      Zc=[Zc; temp1]; Rnew=[Rnew; temp2];
35  end
36  [temp1 temp2]=ZcReq_AL_NT2011(Aline,aline,Bline,bline);
37  Zcline= temp1; Rnewline=temp2;
38  Beta=2*pi*F/3e8; Rs=sqrt(pi*F*4e-7*pi/5.8e7);%surface resistivity
39  Z=zeros(length(l),length(F)); V=zeros(length(l),length(F));
40  I=zeros(length(l),length(F)); dP=zeros(length(l),length(F));
41  Pr=zeros(length(l),length(F)); Pa=zeros(length(l),length(F));
42  V(1,:)=Vdee.*(cos(Beta*l(1))-Zc(1)*sin(Beta*l(1))./Zdee);
43  I(1,:)=Idee.*(cos(Beta*l(1))+Zdee.*sin(Beta*l(1))/Zc(1));
44  dP(1,:)=Idee.*Idee.*(l(1)*0.5*(1+(Zdee/Zc(1)).^2)+(1-(Zdee/Zc(1)).^2.*(sin(2*Beta*l(1))
        ./(4*Beta))+Zdee.*(1-cos(2*Beta*l(1)))./(2*Beta.*Zc(1)));
45  Z(1,:)=V(1,:)./I(1,:); Pa(1,:)=4*Rs*Rnew(1).*dP(1,:)*(Zc(1)/(120*pi))^2;
46  Pr(1,:)=Zc(1)*dP(1,:).*Beta;
47  for n=2:1:length(l),
48  V(n,:)=V(n-1,:).*(cos(Beta*l(n))-Zc(n)*sin(Beta*l(n))./Z(n-1,:));
49  I(n,:)=I(n-1,:).*(cos(Beta*l(n))+Z(n-1,:).*sin(Beta*l(n))/Zc(n));
50  Z(n,:)=V(n,:)./I(n,:);
51  dP(n,:)=I(n-1,:).*I(n-1,:).*(l(n)*0.5*(1+(Z(n-1,:)./Zc(n)).^2)+(1-(Z(n-1,:)./Zc(n)).^2)
        .*(sin(2*Beta*l(n))./(4*Beta))+Z(n-1,:).*(1-cos(2*Beta*l(n)))./(2*Beta.*Zc(n)));
52  Pa(n,:)=4*Rs*Rnew(n).*dP(n,:)*(Zc(n)/(120*pi))^2;
53  Pr(n,:)=Zc(n)*dP(n,:).*Beta;
54  end
55  Zr_h=abs(.159/(F(1)*Crmin));
56  ZTEST=[];%we put all to positive for simplicity
57  Zres=Z(end,1);%final impedance : resonance condition
58  if (Zres<0) Zres=-Zres;
59  end
60  for k=0:0.1:Lambda(1)/2
61      TEST=Zcline*(Zr_h-tan(Beta(1)*k)*Zcline)./(Zcline+tan(Beta(1).*k).*Zr_h);
62  ZTEST=[ZTEST TEST];
63  if (TEST<-Zres)
64      lline=k-0.1*(-Z(end,1)-ZTEST(end))/(ZTEST(end-1)-ZTEST(end));
65      Length=[Length; Length(end)+lline];
66      break;
67  end end
68  Vrotco=V(end,:).*(cos(Beta*lline)-Zcline*sin(Beta*lline)./Z(end,:));
69  Irotco=I(end,:).*(cos(Beta*lline)+Z(end,:).*sin(Beta*lline)/Zcline);
70  Zrotco=Vrotco./Irotco;
71  dProtco=I(end,:).*I(end,:).*(lline*0.5*(1+(Z(end,:)./Zcline).^2)+(1-(Z(end,:)./Zcline)
        .^2).*(sin(2*Beta*lline)./(4*Beta))+Z(end,:).*(1-cos(2*Beta*lline))./(2*Beta.*Zcline
        ));
72  Parotco=4*Rs*Rnewline.*dProtco*(Zcline/(120*pi))^2;
73  Prrotco=Zcline*dProtco.*Beta; Crotco=abs(0.159./(F.*Zrotco));
74  Vlength=[Vdee; V; Vrotco]; Ilength=[Idee; I; Irotco];
75  Zlength=[Zdee; Z; Zrotco]; Vlength=[Vdee; V; Vrotco];
76  Zclength=[0; Zc; Zcline]; Palength=[zeros(1,length(F));
77  Pa; zeros(1,length(F))]; Prlength=[zeros(1,length(F));
78  Pr; zeros(1,length(F))]; Papeak=sum(Palength);
79  Prpeak=sum(Prlength); Q=Prpeak./Papeak;
```

Matlab script to calculate the Characteristic Impedance and Active Power of Rectangular Transmission Lines

```
1  function [zzcc RReq]=ZcReq_AL_NT2011(AA,aa,BB,bb)
2  xxaa=0.5*(BB-bb);
3  xxbb=0.5*(AA-aa);
4  if (xxbb+0.5*aa<AA-xxaa) %'case 1'
5      zzcc=120*pi./((4*bb./(AA-aa))+(4*aa./(BB-bb))+(8*log((BB-bb)./(AA-aa))/pi));
6      RReq=(aa/(2*xxaa^2))+(((2/pi)^2)*((1/xxbb)-(1/xxaa)))+((4/(pi*xxaa))*log(xxaa/xxbb))
        ;
7      RReq=RReq+(((1/xxbb)-(1/xxaa))*(2/pi)^2);
8  elseif (xxbb<AA-xxaa)&&(AA-xxaa<xxbb+0.5*aa) %'case 2'
9      zzcc=120*pi./((4*bb./(AA-aa))+(4*aa./(BB-bb))+(8*(log(AA./(AA-aa))-log(AA./(BB-bb)))
        /pi));
10     RReq=(aa/(2*xxaa^2))+((2/pi)^2)*((1/xxbb)-(1/xxaa)))+(4/(pi*xxaa))*log((AA-xxaa)/xxbb
        )+((8/(AA*pi^2))+(4/(pi*xxaa)))*log(xxaa/(AA-xxaa));
11     RReq=RReq+(((1/xxbb)-(1/xxaa))*(2/pi)^2);
12 elseif (AA-xxaa<xxbb) %'case 3'
13     zzcc=120*pi./((4*bb./(AA-aa))+(4*aa./(BB-bb))+(8*log((AA+aa)./(AA-aa))/pi));
14     RReq=(aa/(2*xxaa^2))+(4/(pi^2))*((1/xxbb)-(1/(AA-xxbb)))+((8/(AA*pi^2))+(4/(pi*xxaa)
        ))*log((AA-xxbb)/xxbb);
15     RReq=RReq+(((1/xxbb)-(1/(xxbb+aa)))*(2/pi)^2);
16 else 'there is a problem: the parameters don t fulfill case 1, 2 or 3!!'
17 end
18 RReq=RReq+(bb/(2*xxbb^2));
19 RReq=RReq+((bb/(2*xxbb^2))*(bb/(bb+2*xxbb))^2);
20 RReq=RReq+(0.5*aa*(aa/(xxaa*AA))^2);
```

# C. PSI Beam Line Study

Input file for TRANSPORT analysis: misalignment of a single quadrupole

```
/250 MeV p-beam from Cyclotron to AMA1/
(analysis of measurement results of 3 nov 09)
(Hliste 18 Mar 2005)
0
15. 11.0 /MEV/ .001 ;
15. 1.0 /MM/ .1 ;
15. 6.0 /PM/ .1 ;
-1. 4.8 3.46 8.52 6.25 0. 0.01 729. /BEAM/ ;
-12. -0.921 0. 0. 0. 0. -0.975 0. 0. 0. 0. 0. 0. 0. 0. 0. /CORR/ ;
-16. 16. 50. ;
1. 0. 0. 0. 0. 0. 0. 729. /BEAM/ ;
12. 0. 0. 0. 0. 0. 0. 0. 0. 0. 0. 0. 0. 0. 0. 0. /CORR/ ;(special beam for misalignment)
3. 0.0 /SJ1/; (STEERER IN YOKE)
3. 1.058 /SMA1/;(STEERER OUT OF YOKE)
3. 0.326 /KMA1/ ;
3. 0.0823 ;(COLLIMATOR 1)
3. 0.0 /MAP1/ ;
3. 0.0 /MAP2/ ;
3. 0.09 ;
3. 0.0 /MAP3/ ;
3. 0.0 /MAP4/ ;(BEAM MONITOR 1-2-3-4)
3. 0.3165 ;
5. 0.35 -2.84 50. /QMA1/ ;
8. 0. 0. -0.45 0. 0. 0. 100. /ALGN/;
3. 0.312;
5. 0.35 0.0 50. /QMA2/ ; (4 druple 1-2)
6. 1.0 45.0 3.0 22.0 /AMAK/;
3. 0.233;
3. 0.05 /AMAK/;
-7. 0. 15.0 0. 15.0 0. 0. /Kick/ ;
3. 0.05 /AMAK/ ;
3. 0.05 /AMAK/;
3. 0.05 /AMAK/;
3. 0.233;
6. 1.0 45.0 3.0 22.0 /AMAK/;(KICKER MAGNET 1)
5. 0.35 0. 50. /QMA3/ ;(4 druple 3)
3. .6345 /KMA2/;
```

```
3.  .0815  ;(COLLIMATOR 2)
6.  1.  2.5  3.  2.5  /MAP5/  ;
3.  0.0  /MAP5/  ;
3.  0.0  /MAP6/  ;
−13.  8.;
SENTINEL
 /∗PLOT∗/
−1
SENTINEL
SENTINEL
```

Input file for TRANSPORT analysis: misalignment of quadrupoles and profile monitors

```
/250 MeV p−beam from Cyclotron to first magnet of Gantry1/
(reproduction of measurement results of 3 dec 09 after survey results)
(Hliste 18 Mar 2005)
0
15.  11.0  /MEV/  .001  ;
15.  1.0  /MM/  .1  ;
15.  6.0  /PM/  .1  ;
−1.  4.8  3.46  8.52  6.25  0.  0.01  729.  /BEAM/  ;
−12.  −0.921  0.  0.  0.  0.  −0.975  0.  0.  0.  0.  0.  0.  0.  0.  0.  /CORR/  ;(with MMAC2?)
−16.  16.  50.  ;
1.  0.  0.  0.  0.  0.  729.  /BEAM/  ;
12.  0.  0.  0.  0.  0.  0.  0.  0.  0.  0.  0.  0.  0.  0.  0.  /CORR/  ;(special beam for misalignment)
3.  0.0   /SJ1/; (STEERER IN YOKE)
3.  1.058   /SMA1/;(STEERER OUT OF YOKE)
3.  0.326  /KMA1/  ;
3.  0.0823  ;(COLLIMATOR 1)
7.  −0.10  −0.1  1.18  −0.48  0.  0.  /Kick/  ;
3.  0.0  /MAP1/  ;
3.  0.0  /MAP2/  ;
3.  0.09  ;
3.  0.0  /MAP3/  ;
3.  0.0  /MAP4/  ;(BEAM MONITOR 1−2−3−4)
3.  0.3165  ;
−5.  0.35  −6.3127  50.  /QMA1/  ;
7.  −0.11  0.  −0.45  0.  0.  0.  ;
5.  0.35  0.0  50.  /QMA1/  ;
7.  0.11  0.  0.45  0.  0.  0.  ;
3.  0.312;
−5.  0.35  6.6131  50.  /QMA2/  ;
7.  −0.11  0.  −0.51  0.  0.  0.  ;
5.  0.35  0.0  50.  /QMA2/  ; (4druple 1−2)
7.  0.11  0.  0.51  0.  0.  0.  ;
6.  1.0   45.0   3.0   22.0  /AMAK/;
3.  0.233;
3.  0.05  /AMAK/;
−7.  0.  15.0  0.  15.0  0.  0.  /Kick/  ;
3.  0.05  /AMAK/  ;
−7.  0.  0.  0.  0.  0.  0.   /Kick/;
3.  0.05  /AMAK/;
−7.  0.  0.  0.  0.  0.  0.   /Kick/;
3.  0.05  /AMAK/;
−7.  0.  0.  0.  0.  0.  0.   /Kick/;
3.  0.233;
6.  1.0   45.0   3.0   22.0  /AMAK/;(KICKER MAGNET 1)
−5.  0.35  −5.4142  50.  /QMA3/  ;
7.  0.0  0.  −0.61  0.  0.  0.  ;
5.  0.35  2.88  50.  /QMA3/  ;(4druple 3)
7.  0.0  0.  0.61  0.  0.  0.  ;
3.  0.6345   /KMA2/;
3.  0.0815  ;(COLLIMATOR 2)
6.  1.  2.5  3.  2.5  /MAP5/  ;
3.  0.0  /MAP5/  ;
3.  0.0  /MAP6/  ;
7.  0.19  0.0  −0.49  0.00  0.  0.  /Kick/  ;(mmap 5 reading)
−13.  8.;
SENTINEL
 /∗PLOT∗/
```

```
−1
SENTINEL
−1
  SENTINEL
  SENTINEL
```

Input file for TURTLE analysis

```
( analysis on measurement varying KMA3 position and observing MMAP9−10)
500000
16. 190. 0. 100. /newF/ ;
15. 11.0 /MEV/ .001 ;
15. 1.0 /MM/ .1 ;
(beam card : 2 sigma values or use 16. 20. = homog distr )
1. 6.0 145. 6.0 145. 0.0  0. 445. /xxl/ ;
50. 1. −5. 5. 0.1 /X_i/;
−50. 2. −120. 120. 2.5 /Xp_i/;
50. 3. −5. 5. 0.1 /Y_i/;
−50. 4. −120. 120. 2.5 /Yp_i/;
−50. 6. −20. 20. 0.5 /dP_i/;
3. 0.000 ;   ( location of virtual source )
3. 0.0017 ;  (end plane of degrader to KMA3 entrance )
50. 1. −5. 5. 0.1 /KMA3/ ;
50. 3. −5. 5. 0.1 /KMA3/ ;
6. 1. 6.5 3. 6.5 /KMA3/ ;( pos5 )
−6. 1. 0.5 3. 0.5 /KMA3/ ;( pos6 )
−6. 1. 2.5 3. 2.5 /KMA3/ ;( pos1 )
−6. 1. 1.5 3. 1.5 /KMA3/ ;( pos3 )
50. 1. −5. 5. 0.1 /KMA3/ ;
50. 3. −5. 5. 0.1 /KMA3/ ;
3. 0.075 ;
50. 1. −5. 5. 0.1 /KMA3/ ;
50. 3. −5. 5. 0.1 /KMA3/ ;
−6. 1. 3.14 3. 3.14 /KMA3/ ;( pos3 )
−6. 1. 4.14 3. 4.14 /KMA3/ ;( pos1 )
6. 1. 8.14 3. 8.14 /KMA3/ ;( pos5 )
−6. 1. 2.14 3. 2.14 /KMA3/ ;( pos6 )
50. 1. −5. 5. 0.1 /KMA3/ ;
50. 3. −5. 5. 0.1 /KMA3/ ;
3. 0.0045 ;
7. 0. 0. −1. 0. 0. ; (beam shift − misalignment )
6. 1. 6.5 3. 6.5 /KMA4/ ;
3. 0.250 ;
6. 1. 12.5 3. 12.5 /KMA4/ ;
7. 0. 0. 1. 0. 0. ; (beam shift − misalignment )
50. 1. −5. 5. 0.1 /KMA4/ ;
50. 3. −5. 5. 0.1 /KMA4/ ;
3. 0.656 ;
3. 0.0443 /MAP9/ ; (and MMAP10)
50. 1. −5. 5. 0.1 /MP9/;
50. 3. −5. 5. 0.1 /MP10/;
16. 180. 3. 0. /OUT3/ ; ( write particle coordinates to FOR003. out )
SENTINEL  ()
SENTINEL  ()
```

Matlab script to read output from profile monitor reading

```matlab
1  function outputM=read_MMAP_AG( filename )
2  input_fileM=filename ;
3  fil=fopen ( input_fileM , 'r ' );  %open data file
4  fileCCL=fscanf ( fil , '%c ' );    %put all the content of the file in a string
5  outputM (1) . name='Comment    =';  outputM (2) . name='Profile      =';
6  outputM (3) . name='pmType     =';  outputM (4) . name='Status       =';
7  outputM (5) . name='Direction  =';  outputM (6) . name='Sensitivity =';
8  outputM (7) . name='UnitX      =';  outputM (8) . name='UnitY        =';
9  outputM (9) . name='NumPoints  =';  outputM (10) . name='FirstPoint  =';
10 outputM (11) . name='Step       =';  outputM (12) . name='P            ='; %peak point
11 outputM (13) . name='4Sn        =';  outputM (14) . name='4Sr          =';
12 outputM (15) . name='BH         =';  outputM (16) . name='BY           =';
```

```
13  outputM(17).name='BF              ='; outputM(18).name='ydata';
14  outputM(19).name='xdata';
15    for i=1:length(outputM)-2
16  k=strfind(fileCCL,outputM(i).name);   %find position of the variable
17  fseek(fil,k+length(outputM(i).name),-1);   %put index on the ending position of the
        variable
18  if (i==1)||(i==2)||(i==3)||(i==7)||(i==8)     outputM(i).value=fgetl(fil);
19  else outputM(i).value=str2double(fgetl(fil));
20  end end
21  k=findstr(fileCCL,'#'); %read data from there on
22  outputM(18).value=[]; fseek(fil, k+1,-1);
23  while(feof(fil)==0)
24      outputM(18).value=[outputM(18).value str2num(fgetl(fil))];
25  end
26  fclose(fil);          %close the input file
27  step=outputM(11).value; firstpoint=outputM(10).value;
28  nbpoints=outputM(9).value;
29  outputM(19).value=[firstpoint:step:firstpoint+step*(nbpoints-1)];
```

### Matlab script to read output from 'harfen' profile monitor reading

```
1   function outputH=read_harf_AG(filename, profilename)
2   input_fileH=filename; filH=fopen(input_fileH,'r');  %open data file
3   fileH=fscanf(filH,'%c');    %put all the content of the file in a string
4    outputH(1).name='device';   outputH(2).name='Streifen';
5    outputH(3).name='xUnit';   outputH(4).name='position';
6    outputH(5).name='width';   outputH(6).name='nTraces';
7    outputH(7).name='pointsPerTrace';   outputH(8).name='timeBetweenTraces';
8    outputH(9).name='yUnit';   outputH(10).name='ydata';
9   outputH(10).value=[];
10  outputH(1).value=profilename; k=findstr(fileH,outputH(1).value);
11  fseek(filH,k,-1); fgetl(filH); %skip the first line with the name
12  % read the data from the profile monitor, line by line
13   temp=fgetl(filH); outputH(3).value=temp(end-2:end);
14   temp=get_nos(temp); outputH(2).value=temp.numbers(1);
15   temp=fgetl(filH); temp=get_nos(temp);
16   outputH(4).value=temp.numbers;
17   temp=fgetl(filH); temp=get_nos(temp);
18   outputH(5).value=temp.numbers; temp=fgetl(filH);
19   outputH(6).value=str2num(temp(11:13));
20   outputH(7).value=str2num(temp(29:31));
21   outputH(8).value=str2num(temp(50:56));
22   temp=fgetl(filH); k=strfind(temp,'units');
23   outputH(9).value=temp(k+7:end-1); j=1;
24   while(j<=outputH(6).value)
25   temp=fgetl(filH); temp=get_nos(temp);
26   outputH(10).value=[outputH(10).value; temp.numbers];
27   j=j+1; end
28   close; fclose(filH);
```

### Matlab script to calculate the centroid from beam profile

```
1    input_file='xxx\xxx.dat';   fit_window_left= xxxx;% in proportion to peak value
2    fit_window_right= xxxx;   weight_factor=xxx;
3   %importance to give to central values in the fit, others are set to 1
4    inputM=read_MMAP_AG(input_file);
5    xM=inputM(19).value;   yM=inputM(18).value;
6    xM2=[];   yM2=[];   k=[];   l=[];
7   for i=1:size(yM,2)-1
8       j=size(yM,2)-i+1;
9       if (yM(i+1)~=yM(i)) k=[k;i]; end;
10          if(yM(j-1)~=yM(j)) l=[j; l]; end;
11  end
12  k=[k; size(yM,2)]; l=[1; l];
13  for i=1:size(k)
14      temp=round(0.5*(k(i)+l(i)));
15   yM2=[yM2 yM(temp)];   xM2=[xM2 xM(temp)];
16  end
17  % w is a weight parameter used for the fitting: setting
```

```
18  w=ones(1,length(yM2));
19  temp1=min(find(yM2> fit_window_left*max(yM2)));
20  temp2=max(find(yM2>fit_window_right*max(yM2)));
21  w(temp1:temp2)=w(temp1:temp2)*weight_factor;
22    a4 = 0.25*inputM(14).value; %4Sr
23    a3 = inputM(12).value; %P
24    a2 = max(yM);
25    a1 = mean(yM(1:10));
26    a0M = [a1,a2,a3,a4];
27  lsqMw = @(a) sum(w.*((yM2 - (a(1)+a(2).*exp(-(xM2-a(3)).^2./(2*a(4)^2))))).^2));
28   aMw = fminsearch(lsqMw,a0M);
29   fitMw=aMw(1)+aMw(2)*exp(-(xM-aMw(3)).^2/(2*aMw(4)^2));
```

<div align="center">Matlab script to calculate the centroid from 'harfen' beam profile</div>

```
1   input_file='xxx\xxx.txt'; profile='XXXX';
2   % INSERT WEIGHT FACTOR FOR CENTRAL VALUES IN GAUSSIAN FIT
3   % (first and last data points have a weight of 1)
4   weight_factor=xxx;
5   %fit_window_left= 0.;% in proportion to peak value
6   %fit_window_right= 0.;
7   inputH=read_harf_AG(input_file, profile);
8   xH=inputH(4).value; yH=inputH(10).value;
9   %data file is read: position values are stored in "xH" variable, current
10  %values are stored in "yH" values
11  i=1; centroid=[]; centroid_fit=[];
12  while (i<=inputH(6).value)
13  centroid=[centroid; sum(xH.*yH(i,:))/sum(yH(i,:))];
14    a4 = sqrt(sum(yH(i,:).*((xH-centroid(i)).^2))/sum(yH(i,:))); %4Sr
15    a3 = xH(round(median(find(yH(i,:)==max(yH(i,:)))))); %P
16    a2 = max(yH(i,:));
17    a1 = min(yH(i,:));
18    a0H = [a1,a2,a3,a4];
19  w=ones(1,length(yH(i,:)));
20  temp1=2; temp2=length(yH(i,:))-1;
21  w(temp1:temp2)=w(temp1:temp2)*weight_factor;
22  lsqHw = @(a) sum(w.*((yH(i,:) - (a(1)+a(2).*exp(-(xH-a(3)).^2./(2*a(4)^2)))).^2));
23  aHw = fminsearch(lsqHw,a0H);
24  fitHw=aHw(1)+aHw(2)*exp(-(xH-aHw(3)).^2/(2*aHw(4)^2));
25  centroid_fit=[centroid_fit; aHw(3)];
```

<div align="center">Matlab script to extract numbers from strings</div>

```
1   function g=get_nos(s)
2   %%% code kindly given by Rossana Bonomi (CERN)
3   %%%  g=get_nos(s);
4   %%%  This function reads the input string s and converts it to numbers
5   %%%  (if possible) or strings otherwise. Seperators are ' ',\t,\n,\r,[,].
6   %%%  The output format is a struct, made of:
7   %%%  g.numbers          % a list of all numbers found
8   %%%  g.s_no             % the number of strings found
9   %%%  g.s(i).s           % the individual strings (i is in [1, g.s_no])
10  ss=s; gg.numbers=[]; gg.s_no=0;
11  %%% convert any seperator to a space
12  seperators=[' ',')','(',sprintf('%c',[9,13,10,91,93])];
13  for i=1:length(seperators),
14    ss=strrep(ss,seperators(i),' ');
15  end;
16  %%% convert double seperators in a single one
17  while (strfind(ss,'  ')),
18    ss=strrep(ss,'  ',' ');
19  end;
20  %%% if input string ends with a seperator, it will be removed
21  if (length(ss) && ss(length(ss))==' ')
22      ss(length(ss))='';
23  end;
24  %%% converting string ss
25  if (length(ss)),
26    f=[0,strfind(ss,' '),length(ss)+1];
```

```
27      for  i=1:length(f)−1,
28        sx=ss(f(i)+1:f(i+1)−1);        fx=str2num(sx);
29        if  length(fx),
30          gg.numbers=[gg.numbers,fx];
31        else
32          gg.s_no= gg.s_no+1; gg.s(gg.s_no).s=sx;
33        end;  %%  fx  is  a  number
34      end;
35    end;  %%  if  (length(ss))
36    %%  return  values
37    g=gg;
```

# CURRICULUM VITAE

agaronna@cern.ch / agaronna@gmail.com
27 years old, Italian

| EDUCATION | |
|---|---|
| 2008-2011 | **PhD student** in Physics at the **Swiss Federal Institute of Technology in Lausanne (EPFL)**<br>- Research in the field of **Medical Physics,** carried out at **European Organization for Nuclear Research (CERN)**, in collaboration with the **Paul Scherrer Institute** (PSI), the **TERA Foundation** and private companies.<br>Skills: *Particle accelerator and beam line design (Magnet, Radiofrequency, Beam Optics)* |
| 2002-2007 | **MSc** and **BSc** in **Engineering Physics** at **EPFL** (overall grade **5.2/6**)<br>- Exchange year at the **Royal Institute of Technology (KTH)** in Sweden.<br>- **Teaching** and **Laboratory Assistant**, Summer Internship at the **Italian National Institute for Nuclear Physics (INFN)** in Rome<br>- Courses in Management and Economics at the Lausanne Business School (HEC).<br>Skills: *Experimental techniques in Particle Physics and Cellular Biophysics, Numerical Simulation* |
| 1990-2002 | **French High School Diploma in Science and International Studies** (**'**Baccalauréat Scientifique à Option Internationale') with honours ('mention bien')<br>- French schools in Paris, Rome and Geneva. |
| **PUBLICATIONS** | - Garonna, A. et al., *JINST*, Vol. 5, C09004, pp.19, 2010.<br>- Amaldi, U. et al., *NIMA*, Vol.620 (2-3), p.563-577, 2010.<br>- Garonna, A., *IPAC10 Proc.*, p.552-554, 2010.<br>- Co-author for *LINAC10, XB10* and *IWAA2006* Conference Proceedings. |
| **PROFESSIONAL EXPERIENCE** | - Intern at Vermilion Partners Ltd in **Shanghai (China): market research** and **corporate advisory** document preparation (reports, presentations, meeting minutes) for a leading multinational investing in China (2007).<br>- Internship at **CERN**, development of a **user interface software** for position monitoring (2006). Project completed with success within the deadline of 3 months. |
| **LANGUAGE SKILLS** | - **French** and **Italian** (mother tongue).<br>- Fluent in **English** (TOEFL and Cambridge Advanced Certificate).<br>- Fair knowledge of **German** (studied at school and university).<br>- Notions of **Mandarin**, **Russian** and **Swedish.** |
| **COMPUTING SKILLS** | - **Programming** in C++, Matlab, PVSS, Tcl/Tk and Fortran.<br>- Software packages: MS Office, Labview, Vector Fields OPERA, Mathematica ... |